technische universität
dortmund

Dissertation

Iron containing compounds of the inner Earth: X-ray Raman scattering from ambient to extreme conditions

zur Erlangung des Doktorgrades der Naturwissenschaften
der Fakultät Physik der Technischen Universität Dortmund

eingereicht von:

Alexander Nyrow

Juni 2014

Contents

Table of contents I

List of figures VI

List of tables XI

1. Introduction 1

2. Spectroscopy of core-level excitations by X-ray Raman scattering 4
2.1. Interaction of X-rays with matter . . . 4
2.2. X-ray absorption spectroscopy . . . 6
2.3. Inelastic X-ray scattering . . . 7
2.4. X-ray Raman scattering . . . 9
2.5. Experimental aspects . . . 11
2.6. High pressure XRS experiments . . . 13

3. Calculation of core-level excitations in 3d transition metal oxides 18
3.1. Single-particle model . . . 18
3.1.1. Atom including one electron . . . 18
3.1.2. Multi-electron systems . . . 20
3.2. Atomic multiplet theory . . . 20
3.2.1. Term symbols . . . 22
3.2.2. Matrix elements . . . 23
3.3. Ligand field multiplet theory . . . 25
3.3.1. Crystal field Hamiltonian . . . 26
3.3.2. Crystal field parameters . . . 27
3.4. Charge transfer effects . . . 28
3.5. Calculation of core-level excitations using the CTM4XAS code . . . 30
3.5.1. $3d^6$ configuration . . . 32
3.5.2. $3d^5$ configuration . . . 34

4. Experimental stations for X-ray Raman scattering experiments 37
4.1. Beamline 20-ID-B at the Advanced Photon Source . . . 37
4.2. Beamline ID16 at the European Synchrotron Radiation Facility . . . 39
4.3. Beamline BL12XU at SPring-8 . . . 40
4.4. Beamline P01 at PETRA III . . . 41

5. Sample characterization **43**
5.1. Samples used for X-ray Raman scattering experiments 43
5.2. Sample characterization by X-ray diffraction 45

6. Commissioning of beamline P01 at PETRA III: First XRS experiments **48**
6.1. Determination of the local coordination in SiO_2 polymorphs 48
6.2. Sensitivity of the Si $L_{2/3}$-edge on the oxidation state of silicon 51
6.3. Momentum transfer dependence of the Mg $L_{2/3}$-edge in MgO 51

7. Determination of the oxidation state of iron using Fe $L_{2/3}$-edge X-ray Raman scattering spectroscopy **54**

8. Quantitative determination of the oxidation state and local coordination of iron by Fe $M_{2/3}$-edge XRS spectroscopy **60**
8.1. Data treatment and background subtraction 61
8.2. Momentum transfer dependence of the Fe $M_{2/3}$-edge 63
8.3. Impact of the oxidation state and local coordination on the Fe $M_{2/3}$-edge 65
8.4. Quantitative determination of the iron oxidation state in glasses 69
8.5. Detection limits and summarizing remarks 70

9. Pressure induced high-spin to low-spin transition in FeS **72**
9.1. High pressure diamond anvil cell 72
9.2. Detection of the high-spin to low-spin transition in FeS by Fe $M_{2/3}$-edge XRS spectroscopy 74
9.3. Quantitative determination of the crystal field splitting at high pressure . 78
9.4. Detection limits and outlook 81

10. Portable laser heating setup for inelastic X-ray scattering experiments at beamline P01 of the PETRA III synchrotron radiation facility **83**
10.1. Laser heating of samples in a diamond anvil cell 84
10.2. Portable double-sided laser heating setup for XRS experiments at beamline P01 85
10.2.1. Experimental constrains for the laser heating setup 86
10.2.2. Laser heating optics 87
10.2.3. Temperature control 88
10.2.3.1. Light collecting optics 88
10.2.3.2. Sample imaging 90
10.2.3.3. Temperature measurements 91
10.2.4. Remote control 92
10.3. First performance tests of the laser heating setup 94
10.3.1. Imaging properties of the setup 94
10.3.2. Control of the laser spot size and position 96
10.3.3. Spectrograph calibration and temperature measurement 97
10.4. Concluding remarks 100

11. Conclusion and Outlook **101**

A. Structural changes in amorphous GexSiOy on the way to the nanocrystal formation **103**

B. The 3j- and 6J-symbols **109**

Bibliography **111**

Publication list **131**

Acknowledgments **133**

Eidesstattliche Erklärung **135**

Abstract

Iron is one of the most abundant elements inside the deep Earth. Numerous geologically relevant iron bearing materials are well characterized utilizing minerals obtained e.g. from volcano eruptions. Here, typical geophysical and geochemical properties of iron, especially the oxidation state, local coordination and spin state, are subject of extensive research in order to understand the structural and electronic properties of minerals as well as the mechanism of chemical reactions at extreme conditions. The local chemical and physical properties of iron in minerals can be studied by core-level spectroscopy using sensitive techniques like x-ray absorption or electron energy loss spectroscopy, which are routinely applied to measure absorption edges of elements in compounds. However, these tools cannot be applied at extreme conditions when diamond anvil cells in combinations with external or laser heating are utilized.
X-ray Raman scattering, a non-resonant inelastic X-ray scattering technique, can be used for bulk sensitive studies of low energy absorption edges by hard x-rays. In contrast to x-ray absorption spectroscopy or electron energy loss spectroscopy, X-ray Raman scattering can be applied also using highly absorbing sample environments being a perfect alternative for high pressure high temperature applications. On the way towards extreme conditions, novel measurements of the Fe $L_{2/3}$- and $M_{2/3}$-are performed on pre-characterized geologically relevant materials to prove the capability of such a study as well the sensitivity of the Fe $M_{2/3}$-edge on the oxidation state and the local coordination of iron in compounds. In addition, the momentum transfer dependence of the spectra, which is a special feature of inelastic X-ray scattering, is discussed. The results are subsequently used to obtain quantitative results about the oxidation state of iron in glasses and to study the impact of the local coordination. Furthermore, first in-situ study of the Fe $M_{2/3}$-edge is presented to track the high-spin to low-spin transition in FeS at pressures up to 10 GPa. In combination with atomic multiplet crystal field calculations, in-situ measurements of the Fe $M_{2/3}$-edge can be used to extract quantitative information about the crystal field splitting, the main component of the spin cross-over process. To simulate the conditions of the inner Earth a portable double-sided laser heating setup optimized for inelastic X-ray scattering is designed and constructed in order to provide a possibility to perform high temperature experiments.

List of Figures

2.1. (a): Schematic sketch of an inelastic scattering process. The sample is exposed to X-rays with the wave vector $\mathbf{k}_1$, energy $\hbar\omega_1$ and polarization unit vector $\mathbf{e}_1$. The scattered X-rays leave the sample with the wave vector $\mathbf{k}_2$, energy $\hbar\omega_2$ and polarization unit vector $\mathbf{e}_2$ under the scattering angle 2Θ (see reference [244]). (b): the energy loss from the inelastic scattering process may excite electrons from a core state into non-occupied or continuum states [199]. 5
2.2. Schematic representation of possible electronic excitations which can be measured using IXS at (a) low q and (b) high q. Phonon, electron-hole and plasmon excitations mostly occur for low momentum transfer, while Compton scattering dominates at high momentum transfer [245]. Here, the energy position C marks the centroid of the Compton profile and E is the energy position of a possible absorption edge. The contribution of the core and valence electrons to the total Compton profile is marked by the blue and red line, respectively. 9
2.3. Schematic representation of an XRS spectrometer in (a) Rowland geometry [131] and (b) Laue geomentry [118]. 13

3.1. Illustration of the crystal field effects on the energy levels of a TM atom on the example of (a) an Fe atom, which is surrounded by six O atoms. (b) The ligand field interacts with the $3d_z^2$ and $3d_{x^2-y^2}$ orbitals of Fe while the other 3d orbitals are not affected. (c) The atomic 3d state of Fe is 5-fold degenerated and all states have the same energy in the case of an isolated atom, while the states are split if crystal field is applied. 26
3.2. Calculated Fe $M_{2,3}$-edge for the octahedral coordinated $3d^6$ configuration. The calculated transition patterns (sticks) and the correspondingly convoluted spectra show the influence of the Slater-Condon parameters (a) and the crystal field splitting (b) on the spectral shape. The spectra are shifted in the intensity for a better overview. 33
3.3. Calculated Fe $M_{2,3}$-edge for the octahedral coordinated $3d^5$ configuration. The calculated transition pattern (sticks) and the correspondingly convoluted spectra show the influence of (a) the Slater-Condon parameters and (b) the crystal field splitting on the spectral shape. The spectra are shifted in the intensity for a better overview. In (c) the spectra from (b) are presented with a focus on the energy region from 49 eV to 53 eV for different 10Dq. (d) shows the impact of charge transfer effects. 35

4.1. Left: Schematics of the LERIX spectrometer [80] including the incident (B) and the transmitted (I) X-ray beam, ionization chambers (C) and (H), as well as analyzer modules for X-ray energy loss measurements in forward (G) and backward (D) scattering, and the helium filled analyzer chamber. Additionally, the path of the incident (red) and scattered (green) beam detected by one analyzer is indicated. Right: a picture of the LERIX spectrometer including the flight path of the incident and scattered radiation. 38
4.2. Left: Setup for measurements of electronic excitations by inelastic X-ray scattering of the beamline ID16 at the ESRF including the sample position, vacuum chamber for analyzer crystals as well as the beam path of incoming (red) and scattered (green) radiation. Right: Arrangement of nine Si analyzer crystals of the multiple-element spectrometer with unmounted vacuum chamber. 39
4.3. Left: Multiple element spectrometer for inelastic X-ray scattering in Rowland geometry. Right: Laue spectrometer for transmission mode experiments. Schematics of both setups is given in figure 2.3. 40
4.4. General layout of beamline P01 at PETRA III including the most important beamline components for IXS experiments: high heat-load double crystal monochromator (DCM), collimating mirrors (CM), and a channel-cut monochromator (CCM). The experimental section can be divided into the experimental hutches 1 (EH1), 2 (EH2), and 3 (EH3), respectively. Here, EH2 is dedicated to inelastic X-ray scattering experiments, especially XRS and RIXS. 41
4.5. Sketch of the spectrometer for inelastic X-ray scattering, which will be installed at beamline P01. The main components are the KB-mirror tank (blue), laser heating setup and an analyzer crystal array (yellow) mounted on a granite block (black). 42

5.1. Segments of the two dimensional X-ray diffraction pattern of FeO, Fe_3O_4, MgO and AOQ-2 (left), as well as Fe_2SiO_4, $FeAl_2O_4$, α-Fe_2O_3 and $FePO_4$ (right), respectively. 45
5.2. Integrated XRD pattern (black) measured on (a) FeO, (b) α-Fe_2O_3, (c) Fe_3O_4, (d) Fe_2SiO_4, (e) $FeAl_2O_4$, (f) $FePO_4$, (g) MgO, and (h) AOQ-2, as well as the corresponding calculated diffraction pattern (blue) [206]. Furthermore, the diffraction pattern of additional compounds Fe (in (a)) and Al (in (e)) (red) is shown. 46

6.1. (a) Si $L_{2/3}$-edge and (b) O K-edge measured on the SiO_2 polymorphs stishovite (red), α-quartz (green) and its glass (black). 50
6.2. Si $L_{2/3}$-edge measured on polycrystalline Si (black) and α-quartz SiO_2 (red) as well as on amorphous SiO powder (blue). 51

6.3. Comparison between the Mg $L_{2/3}$-edge measurements on MgO at (a) low q and (b) high q as well as calculations using FEFF [223, 224]. The high resolution spectrum measured at high q was collected at beamline P01 (PETRA III) while the other spectra were obtained at beamline BL12XU (SPring-8). 52
6.4. Comparison between the Mg $L_{2/3}$-edge measured at beamline P01 with an energy resolution of $\Delta E = 0.5$ eV at $q = 9.1$ Å^{-1} and corresponding FEFF calculation. 52

7.1. First measurements of the Fe $L_{2/3}$-edge on FeO, α-Fe_2O_3, and Fe_3O_4 by XRS and comparison with EELS spectra reported in reference [43]. The spectra are shifted in the intensity for a better overview. 55
7.2. (a): XRS spectra of FeO, α-Fe_2O_3, and Fe_3O_4 as well as a double arctangent background; (b): background corrected spectra with indicated integration ranges; (c): Calculated $I(L_3)/I(L_2)$ fractions as a function of the $Fe^{3+}/Fe_{tot.}$ ratio. 58

8.1. Wide energy loss scans of α-Fe_2O_3 for selected momentum transfers demonstrating momentum transfer dependence of the background. 61
8.2. Comparison between different background subtraction procedures for (a) $q = 1.57$ Å^{-1}, (b) $q = 3.1$ Å^{-1} and (c) $q = 7.62$ Å^{-1} on the example of FeO XRS spectra [204]. 62
8.3. Momentum transfer dependent measurements of the Fe $M_{2/3}$-edge of $^{[6]}Fe^{2+}$ (FeO) and $^{[6]}Fe^{3+}$ (α-Fe_2O_3) in q-ranges (a) 0.8-5.2 Å^{-1}, (b) 5.9-8.5 Å^{-1}, (c) 8.9-10.0 Å^{-1} in comparison with calculations for (d) dipole and (f) ocupole transitions. In addition, a 1:1 superposition of dipole and octupole transitions is presented for both $^{[6]}Fe^{2+}$ and $^{[6]}Fe^{3+}$ in order to model the Fe $M_{2/3}$-edge at intermediate q [204]. 64
8.4. High resolution measurements of the Fe $M_{2/3}$-edge of $^{[6]}Fe^{2+}$ (Fe_2SiO_4), $^{[4]}Fe^{2+}$ ($FeAl_2O_4$), $^{[6]}Fe^{3+}$ (α-Fe_2O_3) and $^{[4]}Fe^{3+}$ ($FePO_4$) at (a) $q = 2.1$ Å^{-1} and (b) $q = 9.1$ Å^{-1} [204]. 66
8.5. (a) Correction scheme of the $FeAl_2O_4$ spectrum by 6% of Fe^{3+} and a comparison between the original and the corrected $^{[4]}Fe^{2+}$ reference spectrum [204]. (b) Comparison between the corrected $^{[4]}Fe^{2+}$ and Fe_2SiO_4 spectra. 68
8.6. Fe $M_{2/3}$-edge measured on glasses RB0-1 (left), AOQ2 (center), and RB0-4 (right) together with fit results using three different approaches [204]. . 70

9.1. General layout (left) and a photograph (right) of a diamond anvil cell. . . 73
9.2. Left: Background subtraction scheme applied to separate the Fe $M_{2/3}$-edge from the background scattering. Right: Pressure dependent measurements of the Fe $M_{2/3}$-edge on FeS by XRS. The spectra collected at 1.7 GPa and 5.3 GPa are shown in the inset separately in order to demonstrate the spectral changes of the absorption edge as the consequence of the structural transition, which occurs at 3.5 GPa [205]. 75

9.3. Left: Differences calculated by subtracting high pressure spectra from the corrected 1.7 GPa spectrum. Right: Pressure dependent total spin transition parameter A(P) calculated using the corrected 1.7 GPa spectrum (blue) and 5.3 GPa spectrum (red) as reference, respectively. The renormalized data measured using XES by Rueff *et al.* [227] is shown (black) for a comparison with XRS results [205]. 77
9.4. Left: Calculations of the Fe $M_{2/3}$-edge using the CTM4XAS package for selected 10Dq. Upper right: experimental spectra collected at 5.3 GPa and 9.5 GPa representative for the HS and LS states in comparison with calculated spectra for 10Dq values obtained by the best fit. Lower right: Spectral difference between the spectra measured at 5.3 GPa and 9.5 GPa (dots) and differences of calculated spectra using three representative LS values and 10Dq = 1.7 eV for HS. 79

10.1. Sketch (left) and photograph (right) of the water cooled DAC holder including a DAC in Böhler-Almax design, copper contacts, and water cooled steel holders mounted on a plate. 87
10.2. Schematics of the double-sided laser heating setup including its components: (LC) laser collimator, safety shutter, (PBC) polarizing beam splitter, (WP) wave plates, (LM) laser mirror, (LL) laser lens, (VLCD1) and (VLCD2) are visible light collection devices in the downstream and upstream direction, respectively, (M1) right angle mirror, (BS1) beam splitter cube, ND1 and ND2 are neutral density filters, (NF) notch filter, (PBS) pellicle beam splitter, (BS2) beam splitter cube, (DM) drilled mirror, (CAM1) and (CAM2) CCD cameras, as well as spectrograph with its CCD chip. 89
10.3. Photograph of the laser heating setup. 90
10.4. Working principle of the spectrometer used for temperature measurements. The picture is taken from the user manual [4]. 92
10.5. Results of the performance test of the imaging optics on the example of a test sample (upper panel) and an FeO loaded DAC (lower panel) from the upstream (right) and downstream (center) site in comparison to a picture taken using a commercial microscope with 10 × magnification. 95
10.6. Laser spot shape taken for the misaligned (left), badly aligned (center) and fine aligned (right) laser optics. 96
10.7. Spectra obtained by the spectrograph in combination with light collecting optics of the laser heating setup for calibration purposes using He, Hg, N_2, and air gas discharge lamps as well as a red laser diode. 97
10.8. Light source spectra as a test for temperature measurements for the downstream (left) and upstream (right) optics, respectively. 98

10.9. Spectra corrected for the contribution of the optics for the downstream (a) and upstream (b) optics, respectively, together with corresponding Planck fits. The fitting range is marked by the yellow area. Additionally, correction function for the downstream and upstream sites are shown in (c). 99

A.1. Temperature dependent measurements of the Si $L_{2/3}$-edge on $Ge_{0.04}SiO_{1.18}$ (a) and $GeSiO_{2.35}$ (b) in comparison with the spectra of crystalline references Si and SiO_2 [203]. 105
A.2. Results of the determination of the contribution of different silicon oxide phases in (d) $Ge_{0.04}SiO_{1.18}$ and (e) $GeSiO_{2.35}$ based on the reference spectra presented in (a) [233]. The estimated total O/Si ratios for both samples are shown in (b) and (c) [203]. 106

List of Tables

2.1. Summary of selected absorption edges measured by X-ray Raman scattering. 15

3.1. Rules for branching calculations for symmetry elements going from SO_3 symmetry to O_h symmetry as can be found in [61]. 27

5.1. Overview about the samples used for the experiments. 47

8.1. $Fe^{3+}/Fe_{tot.}$ ratios extracted from XRS measurements [204]. 70

10.1. Comparison between the expected temperatures and the fit result for upstream and downstream sites, respectively. The standard deviation of the fit results is about 3%. 99

1. Introduction

The Earth bulk is a highly complex thermodynamic system, which is still not completely understood despite of the intensive research. Usually, information about the physical and chemical properties of the Earth's constituents are obtained by seismic observations as well as geophysical or geochemical analysis of natural minerals and rocks. Furthermore, natural samples of deeper Earth can be obtained during volcano eruptions. Their physical and chemical properties reveal very important information about the composition and thermodynamical condition in the inner Earth. Nowadays, in-situ studies at such experimental conditions became feasible and provide unique information about the thermodynamic conditions inside the Earth's core, mantle, and crust.
Iron is one of the most abundant elements in the bulk Earth, which forms minerals e.g. predominantly with light elements (O, Si, Mg, Al) in the Earth's crust and mantle [213]. Especially the Earth's core consists of iron with about 5-10 % and 2-3 % light element inclusions in the liquid outer core and solid inner core, respectively [132, 218, 277, 2, 303]. Thus, iron containing mineral are involved in numerous geological processes inside the Earth's crust and mantle and its chemical and physical properties are responsible for the presence of geodynamo producing the Earth's magnetic field [303]. With increasing depth high pressure (up to about 360 GPa) and temperature (up to 6000 K and more) may initiate significant changes of the local physical and chemical properties of such materials [65]. Especially iron containing compounds may completely change their magnetic and optical properties depending on the oxidation state, local coordination and spin state of iron, e.g. regarding black ferrimagnetic FeO (Fe^{2+}) and dark red ferromagnetic Fe_2O_3 (Fe^{3+}). Such significant changes of the local properties of iron can be particularly observed during the partitioning of Mg-Fe phases or partial melting [328, 329, 207, 130, 315, 177, 257]. Additionally, high pressure leads to a complete disappearance of the magnetic moment in different iron compounds [209, 227, 165, 266, 174] or to several phase transformation [266, 176] at high pressure. Investigations of the local chemical and physical properties of iron in compounds in-situ at extreme conditions (high pressure, high temperature) reveal extremely valuable information about their properties in the Earth's crust, mantle, and core [15, 210, 65]. This knowledge allows to constrain thermodynamic conditions where geologically relevant processes occur in bulk Earth.
Iron containing materials have been subject of numerous studies and their physical and chemical properties are well understood under ambient conditions. Here, e.g. Raman spectroscopy can be applied to extract important information about the molecular composition [48, 313]. Furthermore, X-ray based methods are widely used to determine information about the local atomic and electronic structure of matter. X-ray diffraction is typically used in order to study the long-range atomic order in matter

[71, 139]. Mössbauer spectroscopy is highly sensitive on the magnetic properties of iron and thus to its oxidation state in geologically or technologically relevant compounds [191, 176, 66, 74, 211]. Furthermore, spectroscopy on core-level electrons provides very detailed information about the electron density of states. Here, different absorption edges of iron, e.g. K- [316, 242, 189, 25], L-, or M-edge were measured by X-ray absorption spectroscopy (XAS) [55, 115] or electron energy loss spectroscopy (EELS) [296, 43, 44, 185, 33, 188, 284, 322, 34] and routinely used to determine the oxidation state, local coordination or spin state of iron. In contrast, core-electron excitations can be studied with a very high spatial resolution even on very small samples [94, 200].
Despite of extensive investigations of the local chemical and physical properties of iron in compounds, in-situ studies at extreme conditions are demanding. In order to apply pressure, highly absorbing diamond anvil cells are used, which significantly limits the number of applicable experimental techniques. Optical absorption or Raman spectroscopy can still be used but these techniques are not bulk sensitive and the interpretation of spectra is not straightforward [101]. Mössbauer spectroscopy experiments are very difficult to perform on compounds with a low iron content and the samples must be enriched with ^{57}Fe [258]. Furthermore, a special radiation micro-source is required for very small samples. Fe K-edge (at about 7112 eV) can be measured by XAS bulk sensitively even at extreme conditions conditions but the pre-edge containing information about the oxidation and spin state is very difficult to resolve at non-ambient conditions [318, 197]. Although high sensitivity of the Fe L- (706.8 eV) and M-edge (52.7 eV) on the oxidation state, local coordination, and spin state was demonstrated, XAS and EELS measurements require vacuum condition and are very surface sensitive due to the low energy of the absorption edges and thus are not applicable in-situ at extreme conditions.
X-ray Raman scattering (XRS), an inelastic non-resonant scattering technique, can be used as alternative method in order to measure low energy absorption (below 2 keV) edges by high energy X-rays (typically above 10 keV) bulk sensitively. Therefore, XRS is a very valuable tool in order to measure soft X-ray absorption edges at extreme conditions, even using highly absorbing environment [245, 203, 268, 228]. Although XRS was successfully employed for high pressure applications [241, 246, 12, 178, 235, 11, 172, 291, 228, 268, 292] systematic studies of absorption edges of iron have not been reported so far. In this thesis, XRS will be used in order to analyze the Fe $L_{2/3}$- and Fe $M_{2/3}$-edge on different geologically relevant compounds to reveal the oxidation state and local coordination at ambient conditions. Furthermore, atomic multiplet model employing charge transfer and crystal field effects will be used to describe the spectral shape of the Fe $M_{2/3}$-edge to extract valuable information about the crystal field splitting of 3d states, responsible for the local chemical properties of iron. Subsequently, a systematic in-situ high pressure study of the Fe $M_{2/3}$-edge will be presented in order to analyze the high-spin to low-spin transition in FeS and calculations will be applied to determine the crystal field splitting at high pressure. To extend the studies at ambient and high pressure conditions to realistic conditions present in the inner Earth, samples have to be exposed to both high pressure and high temperature. Therefore, a portable double-sided laser heating setup was constructed for the inelastic X-ray scattering beamline P01 at the synchrotron radiation facility PETRA III. Such laser heating setup provides a unique possibility to

perform in-situ high pressure high temperature experiments at conditions of deep Earth. The outline of this thesis is as follows: Chapter 2 gives a brief overview about the theoretical background of inelastic non-resonant X-ray scattering with a focus on X-ray Raman scattering. Chapter 3 describes the theory of the calculation of core-level excitations using atomic multiplet, crystal field, and charge transfer effects. Chapter 4 gives a short summary about the experimental stations where experiments within this thesis were performed and the samples used for the experiments are described in chapter 5. A study of different low energy absorption edges of geologically relevant compounds are presented in chapter 6. The study of Fe $L_{2/3}$-edge measurements by XRS on compounds with different/mixed oxidation state is shown in chapter 7 and the algorithm to extract the oxidation state of iron in mixed compounds developed by van Aken *et al.* [295] was transferred to XRS measurements. In chapter 8 first systematic XRS measurements of the Fe $M_{2/3}$-edge on iron compounds is presented in order to study the spectral impact of the different oxidation and coordination states. The general spectral shape of the absorption edge could be understood using the atomic multiplet model employing crystal field effects. Furthermore, the oxidation state and local coordination of iron in unknown glasses could be extracted. Chapter 9 shows a systematic in-situ study of the pressure induced high-spin to low-spin transition in FeS by XRS. In combination with the theoretical model pressure dependence of the crystal field splitting of the 3d states of iron, mechanism responsible for the spin transition, can be extracted. In order to expose materials to high temperature a portable double-sided laser heating optimized for the XRS instrumentation at beamline P01 of the synchrotron radiation facility PETRA III was constructed and is presented in chapter 10. The performance of the new setup was successfully shown, which will provide unique possibility to perform high pressure high temperature XRS experiments in-situ under geologically relevant conditions. A conclusion and outlook are given in section 11.

2. Spectroscopy of core-level excitations by X-ray Raman scattering

Knowledge about the electronic, magnetic and structural properties of materials is crucial for numerous applications. Core-level spectroscopy reveals very important information about the local chemical state of a certain kind of absorber atom. Here, different experimental techniques can be used like XAS or EELS. Especially in the case of light elements (e.g. with the nuclear charge $Z < 14$) the binding energy of the electrons is below 2 keV [287] and the number of available techniques to study low energy absorption edges bulk sensitively becomes very limited. X-ray Raman scattering is an experimental method based on inelastic X-ray scattering, which provides a possibility to measure low energy absorption edges bulk sensitively using X-rays with energy above 6 keV allowing experiments without vacuum conditions. Furthermore, even highly absorbing sample environments can be used due to the high penetration length of the X-rays. After a brief overview about the general interaction of X-rays with matter given in section 2.1, some basic aspects on X-ray absorption spectroscopy will be given in section 2.2. A very brief overview about the inelastic X-ray scattering is presented in section 2.3 followed by a short discussion of the X-ray Raman scattering limit in section 2.4. Subsequently, some remarks on how to measure X-ray absorption edges by X-ray Raman scattering are given in section 2.5 and some current works are presented in section 2.6 to show the capabilities of X-ray Raman scattering for experiments under extreme conditions.

2.1. Interaction of X-rays with matter

A typical scattering process, as illustrated in figure 2.1, can be represented by the interaction of an incoming X-ray beam with a sample. The incoming X-ray wave can be described by its wave vector $\mathbf{k}_1$, energy $\hbar\omega_1$ and polarization unit vector $\mathbf{e}_1$. During the inelastic scattering process, a certain amount of energy and momentum is transferred to the sample and the radiation is scattered into the solid angle element $\mathrm{d}\Omega_2$ with the wave vector $\mathbf{k}_2$, energy $\hbar\omega_2$ and polarization unit vector $\mathbf{e}_2$. The momentum transfer

$$\mathbf{q} = \mathbf{k}_1 - \mathbf{k}_2$$

can be expressed by the equation [248, 3]

$$|\mathbf{q}| = q \approx 2\,|\mathbf{k}_1| \sin(2\Theta/2) = \frac{4\pi}{\lambda} \sin(2\Theta/2) \tag{2.1}$$

in the limit, where the energy transfer

$$\hbar\omega = \hbar\omega_1 - \hbar\omega_2 \tag{2.2}$$

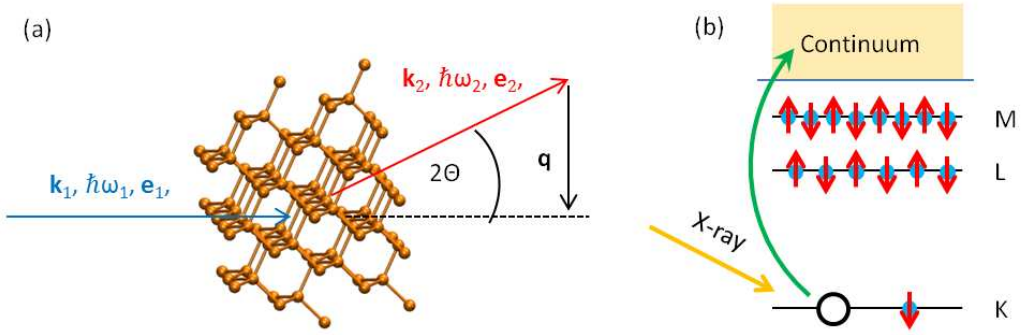

Figure 2.1.: (a): Schematic sketch of an inelastic scattering process. The sample is exposed to X-rays with the wave vector $\mathbf{k}_1$, energy $\hbar\omega_1$ and polarization unit vector $\mathbf{e}_1$. The scattered X-rays leave the sample with the wave vector $\mathbf{k}_2$, energy $\hbar\omega_2$ and polarization unit vector $\mathbf{e}_2$ under the scattering angle 2Θ (see reference [244]). (b): the energy loss from the inelastic scattering process may excite electrons from a core state into non-occupied or continuum states [199].

is significantly smaller than the energy of the incident radiation $\hbar\omega_1$. In an experiment, a control of the quantities $\mathbf{k}_1$, $\hbar\omega_1$, $\mathbf{e}_1$, $\mathbf{k}_2$, $\hbar\omega_2$, $\mathbf{e}_2$ with a sufficient resolution would provide a possibility to study different excitations by choosing the appropriate energy and momentum transfer. The measured experimental quantity in an experiment is proportional to the double differential scattering cross section (DDSCS), which can be described as [245]

$$\frac{\mathrm{d}^2\sigma}{\mathrm{d}\Omega\mathrm{d}\hbar\omega} = \frac{\text{current of photons scattered into the solid angle element } [\Omega, \Omega + \mathrm{d}\Omega] \text{ with the energy } [\hbar\omega_2, \hbar\omega_2 + \mathrm{d}\hbar\omega_2]}{\text{current density of the incident photons} \times \mathrm{d}\Omega \times \mathrm{d}\hbar\omega}$$

To describe the interaction of X-rays with matter, the static Schrödinger equation must be solved. The general Hamiltonian for an electronic system in an electro-magnetic field can be defined by [187, 28, 245]:

$$\begin{aligned}\hat{\mathrm{H}} = &\sum_j \frac{1}{2m}\left(\hat{\mathbf{P}}_j - \frac{e}{c}\hat{\mathbf{A}}(\mathbf{r}_j)\right)^2 + \sum_{i,j}\hat{\mathbf{V}}_{i,j} - \frac{e\hbar}{2mc}\sum_j \hat{\mathbf{s}}_j \cdot \nabla \times \hat{\mathbf{A}}(\mathbf{r}_j) \\ &- \frac{e\hbar}{2(mc)^2}\sum_j \hat{\mathbf{s}}_j \cdot \hat{\mathbf{E}}(\mathbf{r}_j) \times \left(\hat{\mathbf{P}}_j - \frac{e}{c}\hat{\mathbf{A}}(\mathbf{r}_j)\right) \\ &+ \sum_{\mathbf{k}\lambda}\hbar\omega_{\mathbf{k}}(\mathrm{C}^+(\mathbf{k}\lambda)\mathrm{C}(\mathbf{k}\lambda) + \frac{1}{2}).\end{aligned} \tag{2.3}$$

Here, m is the electron mass, e is the elementary electric charge, c is the speed of light, $\mathrm{C}^+(\mathbf{k}\lambda)$ and $\mathrm{C}(\mathbf{k}\lambda)$ are creation and annihilation operators, respectively, and $\hat{\mathbf{s}}_j$ are the Pauli matrices. The first term in equation 2.3 describes an electron j with its momentum $\hat{\mathbf{P}}_j$ in a presence of the photon field $\hat{\mathbf{A}}(\mathbf{r}_j)$ at the position $\mathbf{r}_j$. The second

term corresponds to the potential between two electrons at the positions $\mathbf{r}_i$ and $\mathbf{r}_j$. The third and the forth terms describe magnetic scattering. The last term describes the energy of the photon field with the summation over its modes $\mathbf{k}\lambda$. Here, magnetic interactions are very weak and thus can be neglected and equation 2.3 can be simplified using the commutator $[\hat{\mathbf{P}},\hat{\mathbf{A}}]=0$ to [107, 245]

$$\hat{\mathrm{H}} = \hat{\mathrm{H}}_0 + \hat{\mathrm{H}}_\mathrm{R} + \hat{\mathrm{H}}_\mathrm{Int} \tag{2.4}$$

where

$$\begin{aligned}
\hat{\mathrm{H}}_0 &= \sum_j \frac{1}{2m}\hat{\mathbf{P}}_j^2 + \sum_{i,j}\hat{\mathbf{V}}_{i,j}, \\
\hat{\mathrm{H}}_\mathrm{R} &= \sum_{\mathbf{k}\lambda} \hbar\omega_\mathbf{k}(\mathrm{C}^+(\mathbf{k}\lambda)\mathrm{C}(\mathbf{k}\lambda) + \frac{1}{2}), \\
\hat{\mathrm{H}}_\mathrm{Int} &= \underbrace{\frac{e^2}{2mc^2}\sum_j \hat{\mathbf{A}}^2(\boldsymbol{r}_j)}_{\hat{\mathrm{H}}_{\mathrm{Int},1}} - \underbrace{\frac{e}{mc}\sum_j \hat{\mathbf{A}}(\mathbf{r}_j)\cdot\hat{\mathbf{P}}_j}_{\hat{\mathrm{H}}_{\mathrm{Int},2}}
\end{aligned} \tag{2.5}$$

Here, $\hat{\mathrm{H}}_0$ represents the unperturbed part of the electronic system, $\hat{\mathrm{H}}_\mathrm{R}$ describes the radiation field and $\hat{\mathrm{H}}_\mathrm{Int}$ is the interaction Hamiltonian, which describes both scattering and absorption. However, a fundamental difference between scattering and absorption must be taken into account. During the absorption process an incoming X-ray photon is annihilated and thus absorption can be described by the Hamiltonian $\hat{\mathrm{H}}_{\mathrm{Int},2}$, which is linear in $\hat{\mathbf{A}}(\mathbf{r}_j)$ (and thus in $\mathrm{C}^+(\mathbf{k}\lambda)$ and $\mathrm{C}(\mathbf{k}\lambda)$). In contrast, scattering is a two-photon process, where the incoming X-ray photon is annihilated and a new, scattered photon is created. Thus, the scattering process is described in first order perturbation theory by the Hamiltonian $\hat{\mathrm{H}}_{\mathrm{Int},1}$ containing terms quadratic in $\hat{\mathbf{A}}(\mathbf{r}_j)$.
The experimentally measurable quantity is the double differential scattering cross section (DDSCS), which is proportional to the detected intensity. The DDSCS can be rewritten up to the second order as [245]

$$\frac{\mathrm{d}^2\sigma}{d\Omega d\hbar\omega_2} \propto \left|\langle \mathrm{f}|\hat{\mathrm{H}}_{\mathrm{Int},1}|\mathrm{i}\rangle + \sum_n \frac{\langle \mathrm{f}|\hat{\mathrm{H}}_{\mathrm{Int},2}|\mathrm{n}\rangle\langle \mathrm{n}|\hat{\mathrm{H}}_{\mathrm{Int},2}|\mathrm{i}\rangle}{E_i - E_f}\right|^2 \delta(E_i - E_f) \tag{2.6}$$

The DDSCS describes the probability to find a photon with the energy $d\omega_2$ in the solid angle $d\Omega_2$. Here, the excitation can occur from the initial state $|\mathrm{i}\rangle$ with the energy E_i into the final state $|\mathrm{f}\rangle$ with the energy E_f either directly by the interaction Hamiltonian $\hat{\mathrm{H}}_{\mathrm{Int},1}$ or via an intermediate state $|\mathrm{n}\rangle$ by the Hamiltonian $\hat{\mathrm{H}}_{\mathrm{Int},2}$ [238].

2.2. X-ray absorption spectroscopy

X-ray absorption spectroscopy (XAS) is a well known and widely used technique to measure core-level excitations, which reveal information about the local chemical structure

of a certain type of the absorber atom (e.g. the oxidation state). Furthermore, the local coordination can be extracted from the spectral shape of the absorption edge.
In first order, XAS is dominated by photoexcitation of electrons. The quantity measured in an experiment is proportional to the absorption coefficient given by [63, 61, 223, 245]

$$\mu \propto \sum_f |\langle \mathrm{f}|\hat{\mathbf{P}} \cdot \hat{\mathbf{A}}(\mathbf{r})|\mathrm{i}\rangle|^2 \delta(E_f - E_i - \hbar\omega_1). \tag{2.7}$$

The absorption coefficient is proportional to the probability to excite an electron from the initial state defined by the initial state wave function Ψ_i with the energy E_i into the final state defined by Ψ_f and E_f by the transition matrix, which is proportional to the Hamiltonian $\hat{\mathrm{H}}_{\mathrm{Int},2}$ linear in $\mathbf{A}(\mathbf{r})$. For deep core-electron excitations the XAS spectrum is strongly dominated by dipole excitations. Higher order contribution is reduced by the factor $(Z\alpha)^2$ (Z is the nuclear charge, α is the fine structure constant) and thus can be neglected [223].
During an experiment the sample is exposed to X-rays and the X-ray energy is tuned close to the onset of the binding energy of an electronic state of a certain kind of atom. If the X-ray energy is high enough to excite electrons into an unoccupied state a relaxation of electrons from above the core-hole into the lower non-occupied states occurs and either the intensity of the characteristic fluorescence radiation or the transmitted intensity can be collected as a function of the incident energy. The resulting absorption edge usually shows a significant increase of the intensity when the energy of the incident X-rays crosses the binding energy of an electronic state. An example on how XAS can be used to investigate the local electronic structure is shown on the example of the structural changes in amorphous $\mathrm{Ge}_x\mathrm{SiO}_y$ on the way to nanocrystal formation in appendix A. Furthermore, additional information on XAS can be found e.g. in [146, 223, 3].

2.3. Inelastic X-ray scattering

Inelastic X-ray scattering (IXS) is a very effective experimental technique to get information about the electronic states of an atom. After first experiments in the late 50's and 60's [104, 280], IXS became great attention after third generation synchrotron radiation sources have been opened for experimentalists. In this section, basic principles of IXS will be introduced.
During an interaction event between X-rays and the electron system of a sample, an incoming X-ray beam with the energy E_1 and wave vector $\mathbf{k}_1$ is scattered inelastically. The scattered X-ray beam leaves the sample with the energy E_2 and wave vector $\mathbf{k}_2$. The energy loss, which is transferred to the sample, is used to produce excitation of electrons from an initial state $|\mathrm{i}\rangle$ to a non-occupied final state $|\mathrm{f}\rangle$ according to the selection rule for electronic excitations. To describe the excitation process equation (2.6) can be used. In an IXS experiment, the energy of the incident X-ray beam is usually significantly higher than the energy transfer which is required to produce an excitation ($\mathrm{E}_1 >> \mathrm{E}_i$ and $\mathrm{E}_i \neq \mathrm{E}_f$). Thus, the contribution of $\hat{\mathrm{H}}_{\mathrm{Int},2}$ can be neglected. Related on [245], the vector potential can be written as a function of the creation and annihilation operators

$C^+(\mathbf{k}\lambda)$ and $C(\mathbf{k}\lambda)$ as

$$\begin{aligned}\hat{\mathbf{A}}(\boldsymbol{r}) = \sqrt{\frac{2\pi\hbar c^2}{V\omega_{\boldsymbol{k}}}} \sum_{\boldsymbol{k}\lambda} [&\mathbf{e}(\mathbf{k},\lambda) C(\mathbf{k},\lambda) \exp(i\mathbf{k}\cdot\mathbf{r} - i\omega_{\mathbf{k}} t) \\ &+ \mathbf{e}^*(\mathbf{k},\lambda) C^+(\mathbf{k},\lambda) \exp(-i\mathbf{k}\cdot\mathbf{r} + i\omega_{\boldsymbol{k}} t)].\end{aligned} \tag{2.8}$$

The summation is over all modes of the photon field $\mathbf{k}\lambda$ with the frequency $\omega_{\boldsymbol{k}}$ and λ counts the two polarization states of the field. Finally, the DDSCS of an IXS process can be written using (2.6) and (2.8) as [299, 245]

$$\frac{d^2\sigma}{d\Omega d\hbar\omega_2} = \left(\frac{d\sigma}{d\Omega}\right)_{Th} S(\mathbf{q},\omega) \tag{2.9}$$

with the Thomson scattering cross-section describing the photon-electron coupling

$$\left(\frac{d\sigma}{d\Omega}\right)_{Th} = r_0^2 \left(\frac{\omega_2}{\omega_1}\right) |\mathbf{e}_1 \cdot \mathbf{e}_2^*|^2 , \tag{2.10}$$

where r_0 is the classical electron radius, and the dynamic structure factor

$$S(\mathbf{q},\omega) = \sum_{i,f} p_i |\langle \mathrm{f}| \sum_j e^{i\mathbf{q}\cdot\mathbf{r}_j} |\mathrm{i}\rangle|^2 \delta(E_i - E_f + \hbar\omega) \tag{2.11}$$

Here, $\mathbf{q}$ is the momentum transfer vector and p_i is the probability of the initial state $|\mathrm{i}\rangle$. The delta-function ensures the energy conservation.
Depending on the energy and momentum transferred to a sample system, different categories of IXS can be distinguished [245].

1. If $q \cdot r_c \approx 1$ and $\omega \approx \omega_c$, where r_c is the interparticle distance and ω_c is the plasmon frequency, valence electron excitations occur.

2. Inner-shell excitations can be studied if $q \cdot a < 1$ (dipole excitations) or $q \cdot a \approx 1$ (non-dipole excitations) and $\hbar\omega \approx E_B$, where a is the orbital radius and E_B is the binding energy of an electronic level.

3. Phonon scattering can be observed if $q \cdot d \approx 1$ and $\omega \approx \omega_{ph}$. Here, d is the intraionic distance and ω_{ph} is the phonon frequency.

4. The condition $q \cdot r_c >> 1$ and $\hbar\omega >> E_0$, where E_0 is the characteristic energy of the system, satisfies the impulse approximation and Compton scattering occurs [53].

Figure 2.2 illustrates an IXS spectrum. Phonon scattering usually appears at very low energy transfer. Excitation of the valence band results in a strong maximum at low momentum transfer in the energy transfer region below about 50 eV, which almost completely disappears when going to high momentum transfer. The strong Compton peak predominantly occurs at higher momentum transfer in the energy range of several hundred eV, where the conditions of the impulse approximation are satisfied. Furthermore, an absorption edge can be observed as the result of the excitation of core-electrons from the initial state into the non-occupied final states. The origin and explanation of this IXS category will be discussed in the following section.

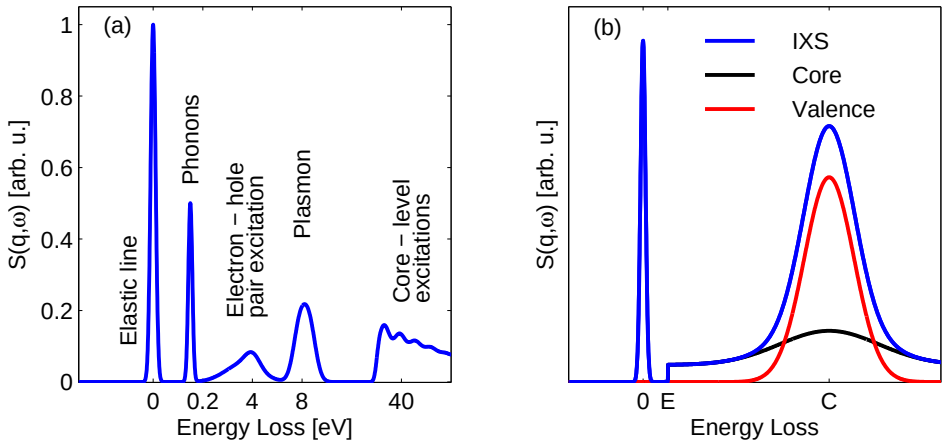

Figure 2.2.: Schematic representation of possible electronic excitations which can be measured using IXS at (a) low q and (b) high q. Phonon, electron-hole and plasmon excitations mostly occur for low momentum transfer, while Compton scattering dominates at high momentum transfer [245]. Here, the energy position C marks the centroid of the Compton profile and E is the energy position of a possible absorption edge. The contribution of the core and valence electrons to the total Compton profile is marked by the blue and red line, respectively.

2.4. X-ray Raman scattering

In the limit of X-ray Raman scattering, predominantly excitations of electrons from a core-shell state into non-occupied higher states occur. In an usual experiment, the energy loss is scanned in the vicinity of the binding energy of an electronic level at a fixed momentum transfer. Here, the binding energy of an electronic state can be measured while the shape of the resulting spectrum contains information about the kind of electronic excitation and the local electronic structure in general. To understand the role of the momentum transfer, equation (2.11) has to be discussed in more detail. In the case only one initial electronic state is taken into account, the dynamic structure factor can be rewritten to [63, 107, 259, 109, 245, 273]

$$S(\mathbf{q},\omega) = \sum_f \left|\langle \mathrm{f}| \sum_j \exp(i\mathbf{q}\cdot\mathbf{r}_j)|\mathrm{i}\rangle\right|^2 \delta(E_i - E_f + \hbar\omega). \tag{2.12}$$

Within the limits of the single electron approximation, where correlation and electron-hole interaction are neglected, the initial state wave function $|\mathrm{i}\rangle$ can be approximated by a Slater determinant which consists of the single electron orbitals ϕ_j and other occupied orbitals $\Psi_\mathbf{j}$. In the final state core electron ϕ_n is excited into a non-occupied state $\Psi_\mathbf{k}$ having the same spin state, so the transition matrix element can be reduced to [187, 245]

$$\langle \mathrm{f}| \sum_j \exp(i\mathbf{q}\cdot\mathbf{r}_j)|\mathrm{i}\rangle = \int \Psi^*_\mathbf{k}(\mathbf{r}) \exp(i\mathbf{q}\cdot\mathbf{r})\phi_n(\mathbf{r}) d^3r \tag{2.13}$$

using $\langle \mathrm{f}| = \Psi^*_\mathbf{k}(\mathbf{r})$ and $|\mathrm{i}\rangle = \phi_\mathbf{k}(\mathbf{r})$. The momentum transfer dependence is described only by the exponential. Using the Taylor expansion, the exponential can be replaced

by [259, 245, 273]

$$e^{i\mathbf{q}\cdot\mathbf{r}} = 1 + i\mathbf{q}\cdot\mathbf{r} + (i\mathbf{q}\cdot\mathbf{r})^2/2 + \dots \tag{2.14}$$

The first term does not contribute due to the orthogonality of the orbitals $\phi_n(\mathbf{r})$ and $\Psi_\mathbf{k}(\mathbf{r})$. For very low momentum transfer ($q \cdot a \leq 1$) the second term dominates and dipole transitions are probed. For higher momentum transfer, the weight of non-dipole transitions increases [148, 193, 259, 245, 273].
Furthermore, the dynamic structure factor can be rewritten using the so called density of states (DOS) approach as [259, 261]

$$S(\mathbf{q},\omega) = \sum_L |M_L(\mathbf{q},E)|^2 \rho_L(E), \tag{2.15}$$

where $\rho_L(E)$ is the electronic density of states, $\mathrm{M}_L(\boldsymbol{q},E)$ are the related transition matrix elements. $L = (l,m)$ denotes the angular momentum channel. It was shown, that the momentum transfer dependence reveals access to the electronic unoccupied partial density of states [193, 272].
All expressions of the dynamic structure factor $S(\mathrm{q},\omega)$ presented above are described in terms of the single electron model. However, especially in the case of transition metals and rare earths, atomic effects including strong interactions between electrons and holes play a major role for X-ray absorption and the dynamic structure factor cannot be understood in terms of the DOS [61]. The equation (2.12) can be used instead and the transition operator $e^{i\mathbf{q}\cdot\mathbf{r}}$ can be rewritten in polar coordinates as a function of spherical harmonics $Y_{k,m}$ [103]

$$e^{i\mathbf{q}\cdot\mathbf{r}} = \sum_{k=0}^{\infty}\sum_{m=-k}^{k} i^k(2k+1)j_k(qr)C_m^{(k)*}(\theta_q,\phi_q)C_m^{(k)}(\theta_r,\phi_r) \tag{2.16}$$

with $C_m^{(k)} = \sqrt{(4\pi/(2k+1))}Y_{k,m}$ employing the $Y_{k,m}$ components in q or r direction, respectively, and $j_k(qr)$ being the k-th order of the spherical Bessel function [109]. This picture simplifies a discussion of the symmetry properties of the transition matrix, which will be very important to interpret the observed spectrum (a detailed discussion will be given in chapter 3). Furthermore, both the initial and final state wave functions $|\mathrm{i}\rangle$ and $|\mathrm{f}\rangle$ can be rewritten as $|\mathrm{i}\rangle = \mathrm{i(r)}$ and $|\mathrm{f}\rangle = \mathrm{f(r)}$, respectively, showing only radial dependence. Inserting equations (2.13) and (2.16) in (2.12) yields

$$S(\mathbf{q},\omega) = \sum_f \sum_{k=0}^{\infty} D_k |\langle \mathrm{f(r)}|j_k(qr)|\mathrm{i(r)}\rangle|^2 \delta(E_i - E_f + \hbar\omega). \tag{2.17}$$

Using equation (2.17) allows to estimate the relative intensity of $S(\mathbf{q},\omega)$ [103]. Any k-th contribution is scaled by the coefficient D_k, which can be extracted from e.g. Hartree-Fock calculations. Exemplary, the special case of excitations from the initial p-states (L=1) to the final d-states (L=2) should be discussed, which describe e.g. the L- or M-absorption edge. Since the initial state wave function is odd and the final state wave function is even under inversion, respectively, the summation index k from equation

(2.17) can be any odd integer in the range $d-p = 1 \leq k \leq p+d = 3$. Thus, only the contributions given by $k = 1$, 3 must be taken into account and the q-dependence of the spherical Bessel function $j_k(qr)$ allows to switch between the dipole ($k = 1$) and octupole ($k = 3$) transitions by scanning the same energy loss range at different scattering angles, i.e. different momentum transfer, according to equation (2.1).
For a very high number of applications X-ray absorption spectroscopy is used to measure dipole electronic excitations, which reveals information about the local chemical surrounding of a kind of atom probed. For low momentum transfer, XRS can be directly compared with XAS. Here, the resulting expression for the dynamic scattering factor can be compared to the general equation for XAS [187, 282, 192]

$$\mathrm{I_{XRS}}(\mathbf{q},\omega) \propto \left|\langle \mathrm{f}|\mathbf{q}\cdot\mathbf{r}|\mathrm{i}\rangle\right|^2 \delta(E_i - E_f + \hbar\omega) \tag{2.18}$$

$$\mathrm{I_{XAS}}(\omega_1) \propto \left|\langle \mathrm{f}|\mathbf{e}\cdot\mathbf{r}|\mathrm{i}\rangle\right|^2 \delta(E_i - E_f + \hbar\omega_1) \tag{2.19}$$

The comparison shows that XRS and XAS become obvious in the case of low momentum transfer if the momentum transfer in XRS plays the same role as the polarization in XAS. Therefore, XRS can be used as very useful alternative to measure absorption edges where XAS cannot be applied [192, 23, 311].

2.5. Experimental aspects

The layout of the experimental setup required to measure core-level electronic excitations by XRS, or IXS in general, is relatively straightforward using the result of theoretical considerations, e.g. the expression for the dynamic structure factor in equation (2.17). In fact, any X-ray source can be used as a probe for an XRS experiment and the momentum and energy of the scattered radiation must be measured. However, both tasks require a relatively advanced setup. A lot of advantages of XRS come with the price of significantly reduced cross section compared to e.g. XAS by a factor of around 10^{-5} [36]. Thus, only 3rd generation synchrotron radiation sources have to be used to exploit the full potential of XRS. The incoming X-ray beam must be collimated using a proper mirror system, monochromatized, and its flux as well as the polarization must be known. The scattered radiation must be collected in a sufficient small solid angle in order to control the momentum transfer and its resolution. Furthermore, the intensity and energy of the scattered radiation must be analyzed with adequate energy resolution [245]. Consequently the following considerations must be done for an XRS experiment:

- The momentum transfer should be fixed.
- The energy of the scattered radiation and thus the energy transfer must be measured with a minimum energy resolution, which is given by the physical properties of a sample (usually 1.5 eV or less).
- The spectrum of the scattered radiation must be measured with a highest possible statistics and signal-to-noise ratio.

Measurement of the energy spectrum of the scattered radiation is probably the most difficult task. The spectrometer must be extremely sensitive and provide an energy resolution of 1.5 eV or less at 10 keV or higher. In general, any detector satisfying this requirements can be used but, however, this kind of detectors are not practicable for such measurements. Thus, the analyzing part of the setup must be split into a spectrometer and a detector [245]. The typical spectrometer is based on a spherically bent Johann type Si$(n, n, 0)$ analyzer crystal with a curvature radius of about 1000 mm [134]. The analyzer is made of an oriented Si$(n, n, 0)$ plate of around 500 μm thickness, which is elastically bent on a spherical substrate using e.g. the anodic bonding technique, reported in [300, 301, 121]. This analyzer crystal focuses the scattered radiation on the detector due to its bent surface. The momentum transfer resolution is given by the lateral size of the crystal with a diameter of around 100 mm [301]. Sometimes, the active area of the analyzer crystal is reduced by shielding the outer area of the analyzer surface by led masks to avoid the reduction of the energy resolution by elastic deformation of the crystal surface on the bent wafer. Furthermore, the sample, analyzer and detector must be arranged in a circle, which is called Rowland geometry as indicated in figure 2.3 (a). This arrangement in combination with the beam size as well as its energy bandwidth strongly influence the focusing properties of the crystal as well as the energy resolution of the experiment [245]. Based on this principle, a real spectrometer can be extended by using more than one analyzer crystal, which provides a possibility to collect the scattered radiation at different solid angles at the same time during one scan [49, 310, 110, 136, 142, 167, 255, 262]. The control of the momentum transfer can be realized by fixing a detector with a small active area at a certain solid angle. After the scattered radiation is energy analyzed the number of counts with a certain energy transfer within a finite bandwidth can be collected by a solid state detector. In general, any energy insensitive detector, e.g. a Si pin diode, can be used [245]. If multiple analyzer crystals are used, one detector for each analyzer must be arranged. Alternatively, an area detector can be used, which allows to separate the signals of different analyzer crystals thus significantly improving the performance of the setup [125, 124]. The experimental statistics and signal-to-noise ratio can be significantly improved by shielding the incident beam path from the source to the sample, so air scattered radiation cannot proceed to the detector. Furthermore, a vacuum environment ($\sim 10^{-3}$ mbar) between the sample and the detector system should be used. Using vacuum is in general not required due to the high energy of incoming X-rays, but is very useful to discriminate air scattering and thus to improve the signal-to-noise ratio.

One of the most important advantages of XRS is a possibility to measure low energy absorption edges by using high energy X-rays. However, the choice of the energy of the incident X-rays is restricted by the properties of the analyzer crystal. Here, the scattering plane of the Si$(n, n, 0)$ surface is the dominating factor. Usually, the sample, analyzer crystal and detector are arranged in Rowland geometry, where the angle between the sample, analyzer crystal and detector is $\theta \approx 87^\circ - 88^\circ$. This angle defines the energy of the Bragg reflection from the analyzer crystal (also called elastic line) as well as the energy resolution. Thus, the available energy range for the incident X-rays can be chosen typically from about 6.46 keV for the Si(4,4,0) reflection to 16.2 keV for the

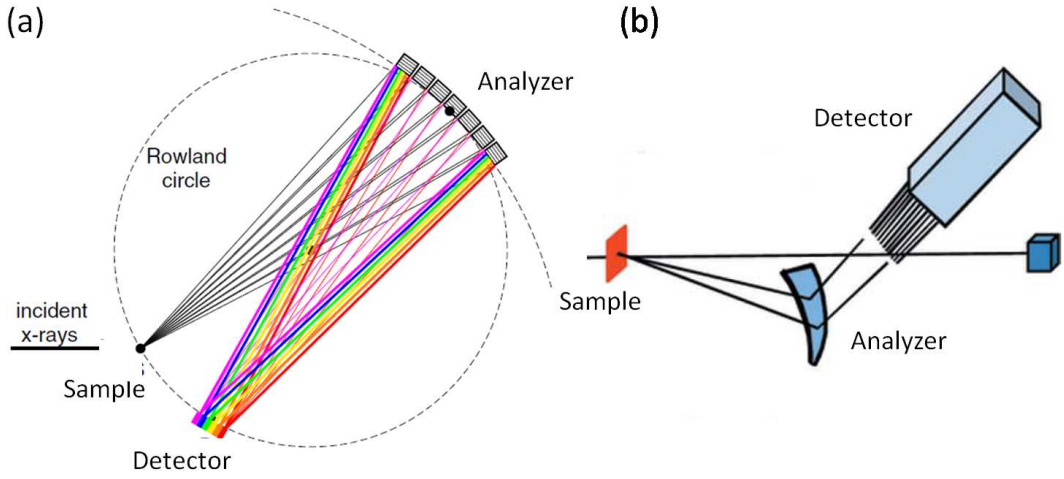

Figure 2.3.: Schematic representation of an XRS spectrometer in (a) Rowland geometry [131] and (b) Laue geomentry [118].

Si(10,10,0) reflection [301].
After the functionality of the spectrometer was explained and the restriction of the energy of incident X-rays was described, two different geometries of energy loss measurements must be distinguished. In the inverse geometry presented in figure 2.3 (a) the position of the sample, spectrometer and detector is kept constant and the energy of the incident X-rays is scanned with respect to the energy of the elastic line and the binding energy of the electronic state to probe. This procedure can be demonstrated on the example of the Si $L_{2/3}$-edge. Here, electrons from the 2p state with the binding energy of $E_B \approx 100$ eV [287] are excited into non-occupied states according to a selection rule. Using e.g. the Si(6,6,0) reflection with the energy of the elastic line at $E_0 = 9.69$ keV, the energy of the incident X-rays must be scanned in a typical range of $\pm$ 30-40 eV around $E_0 + E_B$ and the scattered, energy analyzed intensity must be measured [301]. Furthermore, bent analyzer crystals have unique optical properties, which, in combination with a pixel detector, can be used to perform tomography imaging including chemical bonding contrast analysis without sample rotation [126]. In Laue geometry, which is illustrated in figure 2.3 (b), the energy of incident photons is constant and the analyzer angle is scanned. This geometry is preferred for high energy applications where the efficiency of the bent analyzer crystals drops [245, 118].

2.6. High pressure XRS experiments

After the discovery of the unique potential of X-ray Raman scattering [187, 282] this technique was established as very valuable alternative for applications where other core-level spectroscopic techniques cannot be applied [285, 247, 289, 245]. A summary of

selected absorption edges measured by X-ray Raman scattering are summarized in table 2.1.

Element	Absorption edge	Sample system	Reference
He	K	He gas	[335]
Li	K	metallic Li	[280, 281, 192, 42, 148, 193, 17, 183]
		LiF	[17, 260]
		$LiBH_4$	[183]
		LiC_6	[17]
		Li_2O_2	[45]
		Li_3N	[79]
Be	K	Be	[280, 281, 282, 192, 42]
		BeO	[260]
B	K	BN	[308, 180, 89]
		B_4C	[72]
		MgB_2	[175]
		$Mg_{0.83}Al_{0.17}B_2$	[175]
		$C_2B_{10}H_{12}$	[81]
		$LiBH_4$	[183]
C	K	Graphite	[280, 281, 282, 289, 192, 290, 42, 226, 17]
		C_{60}	[226]
		Diamond	[280, 42, 260, 226, 80, 88]
		CO_2	[129]
		LiC_6	[17]
		$C_2B_{10}H_{12}$	[81]
		Aromatic hydrocarbons and polyfluorene	[232]
		$LiBH_4/C$	[183]
N	K	BN	[180]
		N_2	[231, 129]
		N_2O	[231]
O	K	Liquid H_2O	[35, 24, 311, 22, 222]
		Ice	[35, 311, 22, 76, 220]
		MgO	[81]
		LiCl solution	[137]
		Tetrahydrofuran clathrates	[52, 159]
		Different alcohols	[221]
		SiO_2	[87]
		N_2O	[231]
		$NaReO_4$	[37]

		Li_2O_2	[45]
		$La_{0.6}Sr_{0.4}CoO_3$	[75]
	L_1	MgO	[77]
F	K	LiF	[106]
Na	K	Albite and glasses	[268]
		NaCl	[194]
		NaF	[194]
	$L_{2/3}$	Na	[269, 273]
Mg	L_1	MgO	[77]
	$L_{2/3}$	Mg	[78, 80, 273]
	$L_{2/3}$	MgO	[77]
Al	$L_{2/3}$	Al	[78]
Si	$L_{2/3}$	Si	[269, 273, 274]
		SiO_2	[86, 274, 87]
		SiO	[270, 73, 233]
		Ge_xSiO_y	[203]
		Albite	[268]
Sc	L and M	Sc_2O_3	[42]
Ti	$L_{2/3}$	$Li_{4+x}Ti_5O_{12}$	[98]
V	M	V_2O_3	[42]
		V_2O_5	[42]
		VPO	[42]
Mn	$M_{2/3}$	MnO	[102]
Ba	$N_{4/5}$	Ba	[271]
		Albite and glasses	[268]
		Ba_8Si_{46}	[269, 275]
La	$N_{4/5}$	$La_{0.6}Sr_{0.4}CoO_3$	[75]
		$LaPO_4$	[103]
Ce	$N_{4,5}$	Ce	[36]
		$CePO_4$	[103]
		CeO_2	[103, 102]
Pr	$N_{4,5}$	Pr	[36]
Nd	$N_{4,5}$	Nd	[36]

Table 2.1.: Summary of selected absorption edges measured by X-ray Raman scattering.

The advantage of the high energy and thus high penetration length of incident X-rays was also recognized as a huge advantage for experiments using highly absorbing sample environments. In the particular case of high pressure experiments use of diamond anvil cells (DAC) is indispensable to achieve pressures of several hundred GPa [323, 166, 100, 70, 171]. The diamonds used in such an experiment have a height of 1-2 cm, which must be penetrated by X-rays. Assuming a height of 1.3 mm and a density

of 3.5 g/cm, the transmission[1] for 10 keV X-rays is about 40%. However, the binding energy of the electrons of the most light elements is significantly lower than 10 keV and XAS experiments are not feasible if a DAC is used. Thus, XRS is often the only technique, which allows to measure X-ray absorption edges of light elements at high pressure. The first systematic high pressure study using core-level excitations measured by IXS was performed on solid Helium by Schülke *et al.* and Schell *et al.* in 1995 at the synchrotron radiation source HASYLAB/DESY [241, 246]. The study contributed to the investigation of the quantum nature of the atomic structure of He at 61.5 MPa [245]. The results could be confirmed by Arms *et al.* by an experiment with an improved energy resolution and statistics at the APS [12, 11, 172] at even higher pressure. Subsequently, numerous studies were performed at high pressure in order to investigate structural and electronic phase transitions e.g. in Si [292], Ba_8Si_{46} [293], boron [180, 155, 156, 157] or lithium [156] containing compounds.
Investigations of the local chemical structure of materials are of great interest especially in the field of Geology [154]. Here, studies of the physical and chemical properties of materials at high pressure can reveal very important information about relevant minerals and processes under conditions of the deep Earth. Lee *et al.* (2008) investigated pressure induced changes of the local coordination in $MgSiO_3$ glass at the oxygen K-edge and pressures up to 39 GPa [158]. Comparable studies were performed on silicate [164, 86] and germanium [160] glasses.
The feasibility of in-situ XRS studies at high pressure and high temperature were demonstrated using externally heated diamond anvil cells [243] on the example of an NS3 melt at 230 MPa and 600°C [268]. This cell in combination with XRS was used to study the microscopic structure of water at temperature and pressure conditions close to the supercritical point [228]. Water is, without any doubt, one of the most complicated and controversially discussed substances in condensed matter sciences [18]. Although numerous experimental methods were used to investigate the properties of water at the atomic scale, e.g. neutron or X-ray diffraction [265, 111, 122, 217], small angle scattering [219, 123, 264], and several spectroscopic techniques [311, 312, 22, 123, 201], the local structure of water still remains under controversial discussion [24, 41, 173]. The main point of the discussion is whether the microscopic structure of ambient water may be understood as a liquid with homogenous density [47, 69, 264] or as an inhomogeneous mixture of two phases with a distorted hydrogen-bond structure, which is surrounded by a less dense patches with tetrahedral coordination [312, 123, 122]. Oxygen K-edge spectra measured over a large pressure-temperature range show significant differences of the spectral weight, where the spectra change from water-like shape at low pressure and low temperature to a gas-like shape at high pressure and temperature conditions. However water-like contribution can be found in the spectra even beyond the critical point. The study shows a clear evidence of a homogenous microscopic structure of water, at least at the subnanometer scale. Theoretical analysis based on XRS spectra calculated from ab initio molecular dynamics simulations snapshots allow a deeper inside into the local chemical properties of water. The structure at ambient conditions predominantly

[1] Source: http://henke.lbl.gov/optical_constants/filter2.html

consists of species with four H-bonds and five oxygen neighbors with a distance of around 3.6 Å. If the pressure-temperature conditions increase along the vapor pressure curve, the average number of H-bonds drops to 0.6 at 600 °C and 134 MPa. However, no clustering of these models could be found over the entire pressure - temperature range. This study contributes to the investigation of the microscopic structure of water at high pressure and high temperature conditions, which are hardly accessible by other techniques providing a benchmark for further studies using alternative theoretical background.

3. Calculation of core-level excitations in 3d transition metal oxides

Modeling of X-ray absorption spectra is a very important issue to extract quantitative information from the experimental data. During the last decades different approaches like FEFF [224], FDMNES [135], Wien2K [251], STOBE [144, 145], GW [13] or Bethe-Salpeter approach [302] have been proposed to calculate absorption edges for several materials. However, the single electron picture often breaks down for core-level spectroscopy of strongly correlated systems like transition metals (TM) or rare earth (RE) compounds. Typically, the ligand absorption edge is usually reproduced well by the common single particle models but the TM and RE absorption edges are not. DOS approach does not yield adequate results to be compared with the L- or M- edge spectra of TM and RE [61]. In the final state, partially filled core and valence states can be found, which leads to a strong overlap between the core and valence state wave functions. This is an atomic effect and the proper final states can be found after p- and d- vector coupling resulting in multiplet effects not included into the single particle scheme. A consequence of this atomic multiplet effect is the crystal field effect, which describes the energy differences between different occupations in the 3d band leading to a splitting of energy levels due to a strong core-hole potential.
In the following, a very short introduction to the one particle model is presented in section 3.1. Sections 3.2, 3.3 and 3.4 give an overview on basic aspects of the code used to calculate TM oxide's absorption edges including atomic multiplet, crystal field and charge transfer effects, respectively. In section 3.5, the graphical user interface and the calculation procedure is presented in more detail. Calculations of the Fe $M_{2/3}$-edge for Fe^{2+} and Fe^{3+} are presented and discussed sections 3.5.1 and 3.5.2, respectively.

3.1. Single-particle model

In this section, a brief overview on how to describe atomic orbitals within the single-particle picture is presented, strongly based on reference [54]. The approach will be applied first to an atom including only one electron with a subsequent extension for multi-electron systems.

3.1.1. Atom including one electron

In order to calculate an X-ray absorption spectrum for an atom including one electron, the time independent Schrödinger equation

$$\hat{H}_0\Psi = E\Psi \tag{3.1}$$

must be solved. In this case the Hamiltonian can be defined as

$$\hat{\mathrm{H}}_0 = -\frac{\hbar^2}{2m}\boldsymbol{\nabla}^2 + V(\mathbf{r}), \tag{3.2}$$

which describes a free particle in a potential $V(\mathbf{r})$. The Hamiltonian can be transferred in spherical coordinates and the Schrödinger equation reads in atomic units as:

$$\left[-\frac{1}{\mathrm{r}}\frac{\partial^2}{\partial \mathrm{r}^2}\mathrm{r} + \frac{1}{\mathrm{r}^2}\mathbf{L}^2 + V(\mathbf{r})\right]\Psi = \mathrm{E}\Psi, \tag{3.3}$$

where $\mathbf{L}$ is the angular momentum operator. As long as Ψ is an eigenfunction of $\mathbf{L}^2$ and L_z, the relation

$$\mathbf{L}^2\Psi = \left[\mathrm{r}\frac{\partial^2}{\partial \mathrm{r}^2}\mathrm{r} - \mathrm{r}^2 V(\mathrm{r}) + \mathrm{r}^2\mathrm{E}\right]\Psi = l(l+1)\Psi \tag{3.4}$$

in combination with the central field potential

$$V(\mathbf{r}) = -\frac{2Z}{\mathrm{r}}, \tag{3.5}$$

r measured in Bohr units, can be used to find the wave function Ψ. In this case, the Schrödinger equation can be solved by separating the wave function into a radial, angular and spin part

$$\Psi = \Psi_{n,l,m_l,m_s}(r,\theta,\phi,s_z) = \frac{1}{\mathrm{r}}\mathrm{P}_{n,l}(\mathrm{r})\cdot \mathrm{Y}_{l,m_l}(\theta,\phi)\cdot\sigma_{m_s}(\mathrm{s_z}) = |n,l,m_l,m_s\rangle. \tag{3.6}$$

The spherical harmonics $\mathrm{Y}_{l,m_l}(\theta,\phi)$ in equation (3.6) represent the angular part of the wave function, $\sigma_{m_s}(\mathrm{s_z})$ is a spin function and $\frac{1}{\mathrm{r}}\mathrm{P}_{n,l}(\mathrm{r})$ contains the radial dependence. According to equations (3.3) and (3.4), the Hamiltonian only depends on the magnitude of the radius r and shows no angular or spin dependence. Using the potential given in equation (3.5) and eliminating the angular and spin contribution, the Schrödinger equation can be simplified to

$$\left[-\frac{\partial^2}{\partial \mathrm{r}^2} + \frac{l(l+1)}{\mathrm{r}^2} + \frac{2Z}{\mathrm{r}}\right]\mathrm{P}_{n,l}(\mathrm{r}) = \mathrm{E}\mathrm{P}_{n,l}(\mathrm{r}) \tag{3.7}$$

The function $\mathrm{P}_{nl}(\mathrm{r})$ provides a complete solution of the one-electron problem neglecting relativistic corrections and can be calculated either analytically or using numerical approaches. Basically, every electronic state of an atom can be described by only two quantum numbers within the one-electron model, namely, the principal quantum number n and the orbital angular momentum quantum number l. The following section deals with a solution of the Schrödinger equation for atoms with more than one electron.

3.1.2. Multi-electron systems

The Hamiltonian for a multi-electron system can be defined as

$$\hat{\mathrm{H}}_0 = -\sum_i \frac{\hbar^2}{2m}\nabla_i^2 + \sum_i V(\mathbf{r}_i), \tag{3.8}$$

i being the electrons number [54, 61]. To solve the Schrödinger equation for a multi-electron system the approximation method developed by Slater [256] and extended by Condon [51] will be applied to derive the multi-electron wave function. The procedure is based on the expansion of an unknown wave function ψ by a complete set of known orthonormal basis functions Ψ_b and their contributions y_b^k:

$$\Psi = \sum_b y_b^k \Psi_b. \tag{3.9}$$

In an atom with N electrons, the electrons interact with each other through the Coulomb repulsion and the positions of each electron must be reflected in the basis functions Ψ_b. However, the electron-electron repulsion is neglected within the one-electron model and only the electrostatic field of the nuclei is taken into account. Including the central-field model, the one-electron wave function given in equation (3.6) can be used for each i-th electron, resulting in

$$\phi_i(\mathbf{r}_i) = \frac{1}{\mathrm{r}}\mathrm{P}_{n_i,l_i}(\mathrm{r}) \cdot \mathrm{Y}_{l_i,m_{l_i}}(\theta,\phi) \cdot \sigma_{m_{s_i}}(\mathrm{s}_{i_z}), \tag{3.10}$$

where $\mathbf{r}_i$ denotes the electron position (r,ϕ,θ) with respect to the spin orientation s and the position of the nuclei. In the next step, the one-electron wave functions of N electrons can be combined to the wave function of an N-electron system. The final many-particle wave function Ψ must include the wave function of every single electron of the system. Furthermore, Ψ must be zero according to Pauli's exclusion principle, if any two electrons with the same quantum numbers occur. Finally, Ψ is given by the Slater determinant [54]

$$\Psi = \frac{1}{\mathrm{N}!^{1/2}} \begin{vmatrix} \phi_1(\mathbf{r}_1) & \phi_1(\mathbf{r}_2) & \cdots & \phi_1(\mathbf{r}_N) \\ \phi_2(\mathbf{r}_1) & \phi_2(\mathbf{r}_2) & \cdots & \phi_2(\mathbf{r}_N) \\ \vdots & \vdots & \ddots & \vdots \\ \phi_N(\mathbf{r}_1) & \phi_N(\mathbf{r}_2) & \cdots & \phi_N(\mathbf{r}_N) \end{vmatrix} \tag{3.11}$$

The wave function Ψ includes the complete information about the whole electronic system of an atom with N electrons described by the wave functions $(\phi_1,\ldots,\phi_N)$.

3.2. Atomic multiplet theory

Atomic multiplet effects play a major role when modeling absorption edges of TM and RE and result from the interaction of the core-hole and the electron wave functions in

the final state of an absorption process. This interaction leads to an increase of the number of excitations allowed significantly affecting the shape of an absorption edge. The investigation of the so called multiplet splitting became a hot topic after it was discovered on 3d TMs by Kotani and Toyazawa (1974) [147]. In this section, only very basic aspects of the multiplet effects will be presented while more detailed information can be found e.g. references [54, 61].
In section 3.1.1, the wave function within the single-particle model was derived from the Schrödinger equation employing the Hamiltonian defined in equation (3.8). To include atomic multiplet effects a new Hamiltonian $\hat{\mathrm{H}}_{\mathrm{Atom}}$ must be defined. The starting point of the approach is to use the one-electron Hamiltonian $\hat{\mathrm{H}}_0$ and to extend it by two additional terms, the electron-electron repulsion $\hat{\mathrm{H}}_{\mathrm{ee}}$ and the spin-orbit coupling $\hat{\mathrm{H}}_{\mathrm{so}}$, which are given by [54, 61]

$$\hat{\mathrm{H}}_{\mathrm{Atom}} = \hat{\mathrm{H}}_0 + \underbrace{\sum_{<i,j>} \frac{e^2}{\mathrm{r}_{ij}}}_{\hat{\mathrm{H}}_{\mathrm{ee}}} + \underbrace{\sum_{i=1}^{N} \zeta(\mathbf{r}_i) l_i s_i}_{\hat{\mathrm{H}}_{\mathrm{so}}} . \tag{3.12}$$

Here, the kinetic energy of the i-th electron in the electric field of a nuclei is given by the first two terms, $\hat{\mathrm{H}}_{\mathrm{ee}}$ describes the repulsion between two electrons and the sum is over all pairs $< i, j >$ of the electronic distances r_{ij} with $i \neq j$. For $\hat{\mathrm{H}}_{\mathrm{so}}$ the sum is over all electrons, l_i and s_i are the orbital momentum and spin quantum number, respectively, and

$$\zeta(\mathbf{r}_i) = \frac{\alpha^2}{2} \frac{1}{\mathrm{r}} \left(\frac{\mathrm{dV}}{\mathrm{dr}} \right) \tag{3.13}$$

is the coupling strength between two particles with the distance r, α is the fine structure constant and V is the central field potential given in equation 3.5 [54].
In the next step, the electron-electron interaction and spin-orbit coupling given by the Hamiltonians $\hat{\mathrm{H}}_{\mathrm{ee}}$ and $\hat{\mathrm{H}}_{\mathrm{so}}$, respectively, must be taken into account to calculate the electronic structure according to the atomic multiplet model. As the one electron part of the Hamiltonian in (3.12) is the same for all electrons, it can be neglected for the calculation. The excitations caused by the electron-electron repulsion and spin-orbit coupling can then be calculated relatively to a constant energy position with respect to the one electron part. In general, one could rewrite the one electron Hamiltonian to an average Hamiltonian and use the electron repulsion and spin-orbit coupling as perturbation. However, especially the electron repulsion is too large to be treated as perturbation. It might be possible to separate the spherical average of the electron-electron interaction from the non-spherical part instead. Consequently, $\hat{\mathrm{H}}_{\mathrm{ee}}$ can be rewritten as

$$\hat{\mathrm{E}}'_{\mathrm{ee}} = \hat{\mathrm{H}}_{\mathrm{ee}} - \left\langle \hat{\mathrm{H}}_{\mathrm{ee}} \right\rangle = \sum_{<i,j>} \frac{e^2}{\mathbf{r}_{ij}} - \left\langle \sum_{<i,j>} \frac{e^2}{\mathbf{r}_{ij}} \right\rangle , \tag{3.14}$$

where $\langle\rangle$ denotes the expectation value. Within this formalism, $\hat{\mathrm{E}}'_{\mathrm{ee}}$ determines the energy positions of the different terms within the atomic configuration [61]. In the following an algorithm to calculate the number and energy positions of the possible transitions will be presented.

3.2.1. Term symbols

Term symbols describe the symmetry of an electronic state. To calculate an absorption spectrum term symbols of the initial and final states must be calculated first. Subsequently, only combinations of the symmetries of the initial and final state, which satisfy a selection rule (for dipole or other transitions), are taken into account to calculate the transition pattern [61].
A single electron can be completely described by a set of quantum numbers (see equation (3.6), small and capital letters are used for single- and multi-electron states, respectively), which are the orbital angular momentum quantum number l ($l = 0,\ 1,\ 2,\ \ldots$), the spin angular momentum quantum number s ($s = 1/2$), the total angular momentum quantum number j with the values $l + s$ and $l - s$, the magnetic quantum number m_l ($m_l = -l, -l+1, \ldots, l$), the spin magnetic quantum number m_s ($m_s = -s, -l+1, \ldots, s$) and the total magnetic quantum number m_j ($m_j = -j,\ -l + 1,\ \ldots,\ j$).
New quantum numbers must be introduced to describe a two-electron system including electrons with the quantum numbers l_1,s_1 and l_2,s_2, which are the total orbital angular momentum quantum number L ($l_1 - l_2 \leq L \leq l_1 + l_2$, steps of 1), the total spin quantum number S (0 or 1 in this case) and the total angular momentum quantum number J ($|L - S| \leq J \leq L + S$, steps of 1).
For multi-electron systems the same quantum numbers (L, S, J) can be used. Every configuration can be described by a term symbol ${}^{2S+1}L_J$, where the orbital angular momentum is indicated by the spectroscopic notation S (for $L = 0$), P (for $L = 1$), D (for $L = 2$), F (for $L = 3$), etc. This quantity is also called a symmetry of a state. Furthermore, all terms with the same L and S have the same energy level, which is $(2L + 1)(2S + 1)$-fold degenerate. In the presence of spin-orbit coupling, the degeneration level changes to $(2J + 1)$. The quantity $2S + 1$ is called spin multiplicity and the related terms are labeled singlet ($S = 0$), doublet ($S = 1/2$), triplet ($S = 1$), quartet ($S = 3/2$), etc. [54, 61].
The procedure to obtain term symbols for different configurations can be shown on some simple examples. A single s electron ($l = 0$, $s = 1/2$) is given by ${}^2\mathrm{S}_{1/2}$. To describe a p electron ($l = 1$, $s = 1/2$) two term symbols are required due to the fact that the total angular momentum quantum number can have two values ($j = 1/2$, $j = 3/2$), resulting in term symbols ${}^2\mathrm{P}_{1/2}$ and ${}^2\mathrm{P}_{3/2}$ [56].
The term symbols for two electrons in different orbitals ($n_1 \neq n_2$), e.g. $2\mathrm{p}^1 3\mathrm{p}^1$ ($l_1 = 1$, $s_1 = 1/2$, $l_2 = 1$, $s_2 = 1/2$), can be obtained by calculating the possible values for L ($L = 0,\ 1,\ 2$) and S ($S = 0,\ 1$). For $L = 0$ and $S = 0$ only $J = 0$ is possible, resulting in the term symbol ${}^1\mathrm{S}_0$. A similar result can be obtained for $L = 0$, $S = 1$, and $J = 1$ leading to the term symbol ${}^3\mathrm{S}_1$. For $L = 1$ and $S = 0$ the total angular momentum quantum number can only be $J = 1$ thus resulting in the term symbol ${}^1\mathrm{P}_1$. The picture changes slightly if $L = 1$ and $S = 1$. Here, J can be any integer between 0 and 2 resulting in three term symbols ${}^3\mathrm{P}_0$,${}^3\mathrm{P}_1$, and ${}^3\mathrm{P}_2$. The same situation appears for $L = 2$ and $S = 1$, which leads to the J values of $J = 1,\ 2,\ 3$, again resulting in three term symbols, namely ${}^3\mathrm{D}_1$,${}^3\mathrm{D}_2$, and ${}^3\mathrm{D}_3$. Together with the term symbol ${}^1\mathrm{D}_2$ for $L = 2$, $S = 0$, and $J = 2$, the electronic configuration $2\mathrm{p}^1 3\mathrm{p}^1$ can be described by a total of 10 term symbols in the

presence of spin-orbit coupling. If the term symbols are sorted by their J values, there are two term symbols with $J = 0$, four term symbols with $J = 1$, three term symbols with $J = 2$, and one term symbol with $J = 3$. Thus, the total degeneracy of the $2p^1 3p^1$ configuration can be estimated to $(2 \times 1) + (4 \times 3) + (3 \times 5) + (1 \times 7) = 36$. Special attention should be paid to a configuration with two electrons in the same shell, e.g. the $2p^2$ configuration. Here, the same degree of degeneration can be found as for the $2p^1 3p^1$ configuration. However, due to the Pauli's exclusion principle, the first electron can still occupy six states but the second electron can occupy only five states, leading to a degeneration degree of $6 \times 5 = 30$. Assuming the fact, that the sequence of the electrons does not play any role, the degeneracy must be divided by two leading to 15 possible states [56, 61].
The situation becomes considerably more complicated when the number of electrons exceeds two. In this case, the degeneracy is given by [61]

$$\binom{10}{n} = \frac{10!}{(10-n)!n!}. \tag{3.15}$$

The term symbols and the degeneracy for all electronic configurations including p and d electrons are tabulated in [61].
Now, the shape of an X-ray absorption spectrum can be estimated. Equation (2.19) shows, that calculation of the transition matrix elements is crucial to calculate the absorption probability. In the particular case of XAS, the transition matrix is dominated by the dipole component, which restricts transitions to those with $\Delta J = \pm 1$ or 0 excluding $J' = J = 0$. A simple calculation can be shown on the example of the L-edge of the Sc^{3+} atom. Here, an electron from the closed p-shell is excited into an empty 3d state. The respective initial and final state configurations are $3d^0$ and $2p^5 3d^1$. The initial state can be described by a single term symbol $^1S_0$, while the term symbols $^3P_0$, $^1P_1$, $^3P_1$, $^3D_1$, $^1D_2$, $^3P_2$, $^3D_2$, $^3F_2$, $^1F_3$, $^3D_3$, $^3F_3$, and $^3F_4$ belong to the final state. The transition matrix element, which is proportional to the XAS intensity, can be rewritten as

$$I_{XAFS} \propto \left|\langle 2p^5 3d^1 | \mathbf{r} | 3d^0 \rangle\right|^2 \tag{3.16}$$

or expressed by the respective term symbols

$$I_{XAFS} \propto \left|\langle {}^{1,3}\mathrm{PDF} | \mathbf{r} | {}^1S_0 \rangle\right|^2. \tag{3.17}$$

The dipole properties of the transition operator allow only transition from the initial $^1S_0$ symmetry to the final states with $J = 1$, which restricts the possible final state term symbols to $^1P_1$, $^3P_1$, and $^3D_1$. Thus, the resulting spectrum is given by a linear combination of three maxima.

3.2.2. Matrix elements

If the number and the symmetry of states of an atomic configurations were found, matrix elements based on Hamiltonian used in equation (3.12) can be used to calculate the energy splitting and intensity of allowed transitions. The calculation of the matrix

elements is not straightforward and thus, only a brief overview is given in this section. More detailed description can be found e.g. in [54, 61].
The general Hamiltonian includes the electron-electron interaction $\hat{\mathrm{H}}_{\mathrm{ee}}$ and the spin-orbit coupling $\hat{\mathrm{H}}_{\mathrm{so}}$

$$\hat{\mathrm{H}}_{\mathrm{ee}} + \hat{\mathrm{H}}_{\mathrm{so}} = \sum_{<i,j>} \frac{e^2}{\mathrm{r}_{ij}} + \sum_{i=1}^{N} \zeta(\mathbf{r}_i) l_i s_i. \tag{3.18}$$

First, matrix elements resulting from the electron-electron interaction are discussed [61]. Due to the fact, that $\hat{\mathrm{H}}_{\mathrm{ee}}$ commutates with L^2, S^2, L_z and S_z, all off-diagonal elements are zero. The general equation for matrix element calculation of two-electron wave functions can be written as [61]

$$\left\langle {}^{2S+1}L_J \middle| \frac{e^2}{\mathbf{r}_{12}} \middle| {}^{2S+1}L_J \right\rangle = \sum_k f_k F^k + \sum_k g_k G^k. \tag{3.19}$$

Here, the radial parts F^k and G^k of $\hat{\mathrm{H}}_{\mathrm{ee}}$ were separated using the Wigner-Eckart theorem [314, 68] and the radial part of the Hamiltonian was expanded. The angular parts f_k and g_k can be written in terms of 3j- and 6J-symbols to [61]

$$\begin{aligned} f_k &= (2l_1+1)(2l_2+1)(-1)^L \begin{pmatrix} l_1 & k & l_1 \\ 0 & 0 & 0 \end{pmatrix} \begin{pmatrix} l_2 & k & l_2 \\ 0 & 0 & 0 \end{pmatrix} \begin{Bmatrix} l_1 & l_2 & L \\ l_2 & l_1 & k \end{Bmatrix} \\ g_k &= (2l_1+1)(2l_2+1)(-1)^S \begin{pmatrix} l_1 & k & l_2 \\ 0 & 0 & 0 \end{pmatrix} \begin{pmatrix} l_1 & k & l_2 \\ 0 & 0 & 0 \end{pmatrix} \begin{Bmatrix} l_1 & l_2 & L \\ l_1 & l_2 & k \end{Bmatrix}. \end{aligned} \tag{3.20}$$

The values of k can be found using the triangle conditions of the 3j-symbols. It can be shown, that for f_k, k must be an even integer ranging from 0 to two times the lowest l (otherwise, one of the $3j$-symbols is 0). For g_k, k is even if $l_1 + l_2$ is even and k is odd if $l_1 + l_2$ is odd. The maximum value is $l_1 + l_2$. Furthermore, g_k is not defined if both electrons are inside the same orbital ($l_1 = l_2$) [54]. More details about 3j- and 6J-symbols can be found in appendix B.
A very simple example can be given on the 1s2s ($1s^1 2s^1$) configuration (one 1s and one 2s electron). According to the notation presented in section 3.2.1 this configuration includes the term symbols $^1\mathrm{S}_0$ (singlet) and $^3\mathrm{S}_1$ (triplet). The respective energies can be calculated using

$$\begin{aligned} \left\langle {}^1\mathrm{S} \middle| \frac{e^2}{\mathbf{r}_{12}} \middle| {}^1\mathrm{S} \right\rangle &= \mathrm{F}^0(1\mathrm{s}2\mathrm{s}) + \mathrm{G}^0(1\mathrm{s}2\mathrm{s}), \\ \left\langle {}^3\mathrm{S} \middle| \frac{e^2}{\mathbf{r}_{12}} \middle| {}^3\mathrm{S} \right\rangle &= \mathrm{F}^0(1\mathrm{s}2\mathrm{s}) - \mathrm{G}^0(1\mathrm{s}2\mathrm{s}). \end{aligned} \tag{3.21}$$

The triplet state $^3\mathrm{S}_1$ is threefold degenerate and the average energy of the configuration is F^0(1s2s)-1/2 G^0(1s2s). F^0 and G^0 are the Slater-Condon parameters for the direct Coulomb repulsion and the Coulomb exchange interaction, respectively. The energy difference for this configuration is therefore $2{\cdot}\mathrm{G}^0$(1s2s) [61].

For more than two electrons the picture becomes significantly more complicated. Here, the three-electron wave function with the quantum numbers LS can be generated from a series of two-electron wave functions with quantum numbers L_1S_1 using so called coefficients of fractional parentage $C^{LS}_{L_1S_1}$. Subsequently, the equation for the Slater-Condon parameters must be modified by replacing the 6J-symbol from equation (3.20) by normalized $U^{(k)}_{L'LS}$ matrix elements [61]

$$\begin{aligned} f_k &= (2l+1)^2(-1)^L \begin{pmatrix} l & k & l \\ 0 & 0 & 0 \end{pmatrix}^2 \left[\frac{1}{2L+1} \sum_{L'} \left(U^{(k)}_{L'LS}\right)^2 - \frac{n}{2l+1} \right], \\ U^{(k)}_{L'LS} &= \sum_{L_1S_1} (-1)^{L_1+L+k+l} \sqrt{(2L+1)(2L'+1)} C^{LS}_{L_1S_1} C^{L'S}_{L_1S_1} \begin{Bmatrix} L & K & L' \\ l & L_1 & l \end{Bmatrix}. \end{aligned} \tag{3.22}$$

The values of $U^{(k)}_{L'LS}$ for different electronic configurations are tabulated in [54].
Spin-orbit coupling is included into the Hamiltonian (3.12) by

$$\hat{\mathrm{H}}_{\mathrm{so}} = \sum_{i=1}^{N} \zeta(\mathbf{r}_i) l_i s_i. \tag{3.23}$$

So far only electron-electron interaction was concerned. Now spin-orbit coupling can occur for the initial as well as for the final state and leads to the occurrence of non-diagonal elements in the energy matrix. As a consequence, the states involved into the calculation split and the excitation pattern becomes significantly more complicated [54, 61].

3.3. Ligand field multiplet theory

Due to the interaction between the electronic wave function of the p- and d- states atomic multiplet effects significantly affect the electronic structure of an atom. However, a solid usually consists of more than one atom and coordination effects cannot be neglected. The starting point of the ligand field multiplet (LFM) theory is the approximation of the TM compound by a TM atom surrounded by a distribution of discrete charges, which mimic local atomic environment. Although only a first order approximation, this approach successfully explains a large number of experimental findings [97, 62, 150, 91, 14]. According to the atomic multiplet theory, the 3d state of a single TM atom, e.g. for a TM in a gas phase, is 5-fold degenerate. If the same atom is surrounded by six neighbors (e.g. 6 negative point charges) placed equidistant on three axes, the 3d states loose their degeneracy due to the interaction between the electrons inside the 3d orbitals and the neighbors and the five 3d states are split in energy (see figure 3.1). In the following, the theoretical aspects of the LFM theory are briefly discussed according to [61].

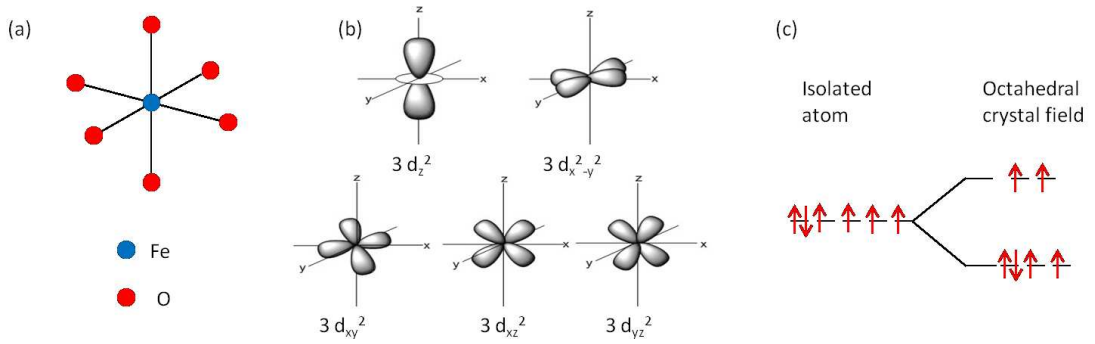

Figure 3.1.: Illustration of the crystal field effects on the energy levels of a TM atom on the example of (a) an Fe atom, which is surrounded by six O atoms. (b) The ligand field interacts with the $3d_z^2$ and $3d_{x^2-y^2}$ orbitals of Fe while the other 3d orbitals are not affected. (c) The atomic 3d state of Fe is 5-fold degenerated and all states have the same energy in the case of an isolated atom, while the states are split if crystal field is applied.

3.3.1. Crystal field Hamiltonian

The starting point is a modification of the Hamiltonian given in equation (3.12) by an additional term describing the crystal field effects. Within the LFM theory, the modified Hamiltonian reads as

$$\hat{\mathrm{H}}_{\mathrm{LFM}} = \hat{\mathrm{H}}_{\mathrm{Atom}} + \hat{\mathrm{H}}_{\mathrm{CF}}. \tag{3.24}$$

with

$$\hat{\mathrm{H}}_{\mathrm{CF}} = e\phi(\mathbf{r}). \tag{3.25}$$

The crystal field part of the LFM Hamiltonian is given by a product of the electronic charge e and the potential $\phi(\mathbf{r})$ created by the nearest neighbors. The potential $\phi(\mathbf{r})$ can be expressed by an expansion into spherical harmonics Y_{LM}

$$\phi(\mathbf{r}) = \sum_{L=0}^{\infty} \sum_{M=-L}^{L} \mathbf{r}^L A_{LM} Y_{LM}(\Psi, \phi). \tag{3.26}$$

Here, A_{LM} is a scaling factor for certain spherical harmonics. In the next step, the crystal field part can be treated as perturbation and the matrix elements of $\phi(\mathbf{r})$ with respect to the 3d orbitals $\langle 3\mathrm{d}|\phi(\mathbf{r})|3\mathrm{d}\rangle$ must be determined. Again, the matrix elements can be separated into spherical and radial parts. The radial part describes the strength of the crystal field interaction and the spherical part can be expressed in terms of the Y_{LM} symmetry. For e.g. two 3d electrons, Y_{LM} can be simplified to Y_{2m}, and the spherical part of $\phi(\mathbf{r})$ can be written in terms of 3j- symbols to

$$\langle Y_{2m_2}|Y_{LM}|Y_{2m_1}\rangle = (-1)^{m_2}\sqrt{15(2L+1)/4\pi}\begin{pmatrix} 2 & L & 2 \\ -m_2 & M & m_1 \end{pmatrix}\begin{pmatrix} 2 & L & 2 \\ 0 & 0 & 0 \end{pmatrix}. \tag{3.27}$$

SO_3	L	O_h (Butler)	O_h (Muliken)
S	0	0	A_1
P	1	1	T_1
D	2	$2+\widehat{1}$	$E+T_2$
F	3	$\widehat{0}+1+\widehat{1}$	$A_2+T_1+T_2$
G	4	$0+1+2+\widehat{1}$	$A_1+E+T_1+T_2$

Table 3.1.: Rules for branching calculations for symmetry elements going from SO_3 symmetry to O_h symmetry as can be found in [61].

The second 3j- symbol is zero unless L = 0, 2, or 4, which simplifies the crystal field potential for 3d electrons to

$$\phi(\mathbf{r}) = A_{00}Y_{00} + \sum_{M=-2}^{2} \mathbf{r}^2 A_{2M}Y_{2M} + \sum_{M=-4}^{4} \mathbf{r}^4 A_{4M}Y_{4M}. \tag{3.28}$$

The term $A_{00}Y_{00}$ defines a constant shift of the atomic states and thus can be neglected for further calculations. After the matrix elements for the initial and final states have been calculated according to a certain selection rule, the matrix elements must be branched accordingly.

3.3.2. Crystal field parameters

The LFM theory, which describes the effect of the local surrounding on the atomic properties of a TM, makes use of an extremely simplified approximation of the local coordination. This model can only succeed if the system is strongly determined by symmetry considerations and group theory can be applied [54, 56, 61]. In the octahedral symmetry, the TM atom is surrounded by six neighbors, which are placed on the three Cartesian axes, or in other words, on the six faces of a cube centered on the TM atom, building an octahedral field. In the tetrahedral symmetry, the eight neighbors are positioned in the eight corners of the same cube, building a cubic field. Both symmetries belong to the O_h group, which is a subgroup of the atomic SO_3 group. The branching ratios between the atomic states to symmetry states within a ligand field can be directly obtained from the Muliken notation. Table 3.1 summarizes symmetry transformations from the SO_3 symmetry group to the O_h group expressed in Butler and in Muliken notation [39, 61]. The atomic S state branches to the A_1 symmetry, which means, that the S orbital is completely symmetric under all transformations. The P state branches to the T_1 symmetry indicating that a two-fold rotation around the x-axis inverts the orbital, etc. In general, the branching ratio between any transformation can be obtained from the Butler notation.
Apparently the only important branching ratio term in the O_h symmetry is X_{40}, which strongly relates to the crystal field splitting of the 3d states, 10Dq, using

$$X_{40} = 1/18 \times \sqrt{30} \cdot 10\text{Dq} \approx 0.304 \cdot 10\text{Dq}. \tag{3.29}$$

In tetragonal symmetry (D_{4h}), three parameters must be used which are defined as

$$\begin{aligned} Dq &= 1/6 \cdot 30^{-1/2} \cdot X_{400} - 7/30 \cdot 42^{-1/2} \cdot X_{420} \\ Ds &= -70^{-1/2} \cdot X_{220} \\ Dt &= -2/5 \cdot 42^{-1/2} \cdot X_{420} \end{aligned} \tag{3.30}$$

The energy levels of different electronic configurations as a function of 10Dq are tabulated in so called Tanabe-Sugano diagrams and the splitting pattern of a certain symmetry for each electronic configuration is presented as a function of the crystal field strength [279].
Crystal field effects split the 3d states into t_{2g} and e_g states and the splitting is given by the parameter 10Dq. In presence of an octahedral coordination, the t_{2g} states are lower in energy. The t_{2g} and e_g states are further split by the so called Stoner exchange J. The Stoner exchange describes the repulsion of the electrons with two parallel spins within t_{2g} or e_g states and is given by a linear combination of Slater-Condon parameters J=(F_2+F_4)/14. It can be shown, that configurations $3d^4$, $3d^5$, $3d^6$, and $3d^7$ can have a second ground state. In the ground state, the $3d^6$ configuration consists of three spin-up electrons in the t_{2g} state and two spin-up electrons in the e_g state. Additionally, one spin-down electron occupies one t_{2g} state. The total spin is maximized according to the Hundt's rule and this state is called high-spin state. In the low-spin state, the $3d^6$ configuration consists of three spin-up and three spin-down electrons in the t_{2g}, while the e_g states are empty. This state can be achieved if the Stoner exchange and thus the repulsion of the electrons with the same spin is too high to keep the high-spin state configuration. The transition from the high-spin to the low-spin state occurs if the crystal field splitting exceeds the value of approximately 2J. Assuming J $\approx$ 0.8 eV the spin transition point can be estimated to the 10 Dq value of 1.6 eV. Similar situation can be found for the $3d^5$ configuration with the transition point at 3J [61].

3.4. Charge transfer effects

The important role of multiplet effects on the transition pattern of a TM has been shown compared to a single electron picture. Here, the strong interaction between the wave functions of electrons and holes leads to a significantly higher number of transitions allowed by the selection rules. The presence of a crystal field results in a branching of the symmetries, which makes the transition pattern significantly more complicated. All this models are based on the fact, that the number of charges in the initial and final states is the same. However, some compounds can show metal-like behavior allowing charge transfer from a TM atom to a ligand or to another metal atom (and vice versa). This effect can be described by the so called charge transfer multiplet (CTM) theory, which is based on the Hubbard model. Although the application of the charge transfer multiplet theory can reveal very useful information on the electronic structure of a compound only a brief, qualitative overview will be given in this section due to the fact, that CTM effects are very difficult to observe by absorption spectroscopy. The reason is, that the

presence of charge transfer results in a weak satellite peak in the absorption edge. The high intrinsic broadening of the absorption edge may lead to the fact, that the weak charge transfer satellite is completely smoothed by the main excitation maximum and is thus not directly observable by XAS. Here, other experimental techniques (e.g. XPS or RIXS) must be used which are more sensitive to the charge fluctuation between the initial and final states [61].
The CTM theory allows to include electron hopping from the TM atom to the ligand or from the ligand to the TM atom, which increases the number of the possible initial and final states. Within both the atomic multiplet theory and ligand field multiplet theory the initial state can be described by the symbol $3d^n$. If charge transfer effects are taken into account, a set of new initial states must be included. Assuming a transfer of an electron from the ligand to the TM atom, the total electron number in the TM atom increases by one and a hole in the ligand site occurs. This configuration can be described as $3d^{n+1}\underline{L}$ ($\underline{L}$ indicating a hole in the ligand site). The next step of this procedure is the configuration $3d^{n+2}\underline{L}^2$. In general, any alike configuration must be taken into account, but two configurations are enough for the most applications. Similarly, the final state configuration $2p^5 3d^{n+2}\underline{L}$ and alike must be added to the final state $2p^5 3d^{n+1}$ known from the atomic multiplet theory. Due to the interaction between the initial and final states application of the CTM theory significantly increases the number of possible transitions for a certain configuration compared to the atomic multiplet theory in the presence of crystal field effects [61].
According to the single impurity Anderson model, the CTM effects can be calculated by only a few number of parameters, which are the on-site *dd* Coulomb repulsion U_{dd} (describing the potential needed to overcome to move an electron from one TM atom to the next TM atom) and the charge transfer energy Δ, also known from the Hubbard model, the hybridization energy $V(\Gamma)$ between the ligand p- and TM d- states and the core hole potential $-U_{dc}$. Here, U_{dc} is usually larger than U_{dd} by 1-2 eV. Furthermore, the largest core hole potential can be related to the deepest core state. Furthermore, $-U_{dc}$ only affects the 3d states and the interaction between the core holes and valence electrons is neglected. For calculations, the following rules are used [61]:

- The 2p3d Slater-Condon parameters are obtained from the atomic calculation.
- The spin-orbit coupling between the 2p and 3d states is taken into account.
- The crystal field strength value 10Dq is assumed to be the same for all initial states.
- The energy difference between two configurations is called charge transfer energy given by $\Delta_f = \Delta + U_{dd} - U_{dc}$. For XAFS, Δ_f is smaller than Δ by 1-2 eV.
- The hopping energy $V(\Gamma)$ is the same for the initial and final states.

The absorption edge can be calculated within the LFM model using the following matrices:

$$I_{\mathrm{XAS},1} \propto \left|\langle 2\mathrm{p}^5 3\mathrm{d}^{n+1}|\mathrm{T}_1(\mathrm{ED})|3\mathrm{d}^n\rangle\right|^2, \tag{3.31}$$

$$E_{\mathrm{INIT},1} = \langle 3\mathrm{d}^n|\mathrm{H}_{\mathrm{LFM}}|3\mathrm{d}^n\rangle, \tag{3.32}$$

$$E_{\mathrm{FINAL},1} = \langle 2\mathrm{p}^5 3\mathrm{d}^{n+1}|\mathrm{H}_{\mathrm{LFM}}|2\mathrm{p}^5 3\mathrm{d}^{n+1}\rangle. \tag{3.33}$$

Subsequently, the CTM effects include another set of matrix elements given by

$$I_{\mathrm{XAS},2} \propto \left|\langle 2\mathrm{p}^5 3\mathrm{d}^{n+2}\underline{\mathrm{L}}|\mathrm{T}_1(\mathrm{ED})|3\mathrm{d}^{n+1}\underline{\mathrm{L}}\rangle\right|^2, \tag{3.34}$$

$$E_{\mathrm{INIT},2} = \langle 3\mathrm{d}^{n+1}\underline{\mathrm{L}}|\mathrm{H}_{\mathrm{LFM}}|3\mathrm{d}^{n+1}\underline{\mathrm{L}}\rangle, \tag{3.35}$$

$$E_{\mathrm{FINAL},2} = \langle 2\mathrm{p}^5 3\mathrm{d}^{n+2}\underline{\mathrm{L}}|\mathrm{H}_{\mathrm{LFM}}|2\mathrm{p}^5 3\mathrm{d}^{n+2}\underline{\mathrm{L}}\rangle. \tag{3.36}$$

The two initial and final states are coupled by monopole transitions (i.e. hybridization) given by the mixing Hamiltonian $\mathrm{H}_{\mathrm{MIX}} = \sum_\nu V(\Gamma)(a^*_{d\nu}a_\nu + a^*_\nu a_{d\nu})$ adding new matrix elements [61]

$$M_{\mathrm{INIT},1;\mathrm{INIT},2} = \langle 3\mathrm{d}^{n+1}\underline{\mathrm{L}}|\mathrm{H}_{\mathrm{MIX}}|3\mathrm{d}^n\rangle, \tag{3.37}$$

$$M_{\mathrm{FINAL},1;\mathrm{FINAL},2} = \langle 2\mathrm{p}^5 3\mathrm{d}^{n+2}\underline{\mathrm{L}}|\mathrm{H}_{\mathrm{MIX}}|2\mathrm{p}^5 3\mathrm{d}^{n+1}\rangle. \tag{3.38}$$

An absorption edge within the CTM model can be calculated by solving the equations (3.31)-(3.38). The term average energy changes to $2\Delta + U_{dd}$, if the $3\mathrm{d}^{n+2}\underline{\mathrm{L}}^2$ is added to the calculation. In application of the CTM theory with positive values of Δ the CTM effects lead to a contraction of the multiplet structure and to formation of weak satellite peaks in the spectrum. This effect is a special feature of XAS, which is a neutral spectroscopy technique according to the equal number of charge of the initial and final state. Thus, the screening of charge transfer effects is weak independent on whether the multiplet effects are present or not. With the values of e.g. $\mathrm{t}_{2\mathrm{g}}$ hopping energy of 1.0 eV and $\Delta = 1$ eV CTM satellite peaks with the intensity of around 20 % of the total intensity can occur. However, typical values for TM oxides suppress the CTM satellite intensity to less than 6 % of the maximum intensity. Furthermore, even a strong variation of the charge transfer parameters reveals only minor changes of the charge transfer peak structure [61]. However, some examples exist with the large CTM effects showing a strong contribution to the absorption edge, e.g in the case of iron cyanides [119].

3.5. Calculation of core-level excitations using the CTM4XAS code

One of the first theoretical observations of multiplet effects in solids were done by Williams (1966) [319], followed by Nakai and co-workers [195]. Shin *et al.* [253] could attribute experimental spectra to a certain multiplet structure. Based on theoretical description of multiplet [147, 105, 254, 278], crystal field [39], and charge transfer effects [147] Thole *et al.* developed a code [286], which allowed to perform systematic L- and

M-edge studies on different TM compounds [59, 58, 297, 298].
Stavitski and de Groot developed a program package employing a graphical user interface, which allows to perform calculations of electronic excitations [267]. The package based on the codes by Cowan and Thole consists of two programs CTM4XAS and CTM4RIXS and was originally developed to simulate TM L-edges but also calculation of 1s, 2s, 3s, 2p, 3p XAS, EELS, and XPS spectra is possible. Furthermore 1s2p and 1s3p XES spectra can be modeled. CTM4RIXS allows additional calculation of two dimensional RIXS plane. In contrast to the most ab initio codes presented at the beginning of chapter 3 CTM4XAS is a semi-empirical code, which significantly improves the run time [127]. In the following, input parameters to calculate a transition pattern to simulate absorption edges using CMT4XAS will be explained.
After selecting an electronic configuration, which includes all $3d^n$, $4d^n$, and $5d^n$ TM ions, the initial and final state configurations are loaded and an absorption edge must be chosen. The graphical user interface allows to control the scaling factors for the F_{pd}, F_{dd} and G_{pd} values, which describe the coupling between the d electrons and between the core and d electrons given by the Slater-Condon parameters F^2 and F^4 for direct Coulomb repulsion as well as G^2 and G^4 for exchange interaction. The scaling factors can be set to any value between 0 and 1.5, where 1 means a reduction of the Slater-Condon parameters to 80% of their atomic values, which was found out to be reasonable for TMs by experiments. Furthermore, the scaling factors for the spin-orbit coupling for core and valence electrons can be chosen separately. The centroid energy position of the transition pattern calculations is obtained from [287].
Calculation on the basis of the atomic multiplet theory can be extended by crystal field effects subsequently by choosing one of the available point group symmetries, which are restricted to the O_h (octahedral), D_{4h} (tetragonal), and C_4 (4-fold) symmetries. Furthermore, the crystal field splitting parameter 10Dq is defined as the energy gap between the T_{2g} and E_g states in the particular case of the O_h symmetry, neglecting all atomic parameters. For the other symmetries, additional crystal field parameters Dq, Dt, and Ds as defined in equation (3.30) can be used [263]. Furthermore, setting different crystal field parameters for the initial and final states is possible. An additional exchange field M can be included to study the impact of magnetic effects, e.g. important for X-ray magnetic circular dichroism studies. Although the tetrahedral symmetry is not implemented into the program, such calculations can also be done with the same settings as for the O_h symmetry but with negative value for the crystal field splitting. For the octahedral coordination the T_{2g} states are lower in energy than the E_g states and the opposite is the case for the tetrahedral symmetry. Thus, the change in sign only defines the energy position of the d-states relative to each other.
Charge transfer effects can be controlled by three parameters presented in section 3.4, which are the charge transfer energy Δ between the $3d^n$ and $3d^{n+1}\underline{L}$ configurations, and U_{dd} and U_{pd} define the Hubbard U parameters for the valence and core-valence interactions, respectively. Additionally, four hopping terms are defined for different symmetries, namely $T(b_1)$, $T(a_1)$, $T(b_2)$, T(e), which relate to the x^2-y^2, z^2, xy, and xz/yz orbitals, respectively. In the particular case of the Oh symmetry, $T(b_1)$ and $T(a_1)$, as well as $T(b_2)$ and T(e), must be equal, due to the E and T_2 symmetry properties, respectively

[267].
The result of a calculation of electronic excitations employing atomic multiplet, ligand field and charge transfer theory is a transition pattern with a certain number of sticks, which have a different intensity according to their degeneracy. For a comparison with a measured absorption edge, the experimental resolution must be taken into account. Furthermore, the finite lifetime of the excited state, so called core-hole lifetime, broadens the stick pattern. Thus, the calculated pattern can be convoluted with a Gaussian and a Lorentzian function with a certain width (full-width-half-maximum, FWHM) to simulate the effect of the experimental resolution and core-hole lifetime, respectively. In the following, the capabilities of the code as well as the impact of different parameters important for the calculations are demonstrated on the examples of $3d^6$ (Fe^{2+}) and $3d^5$ (Fe^{3+}) configurations [267].

3.5.1. $3d^6$ configuration

The configuration $3d^6$ is representative for Fe^{2+}. To show the influence of different parameters on the shape of the absorption edge, calculations of the Fe $M_{2,3}$-edge were performed for octahedral coordination. Within this conditions, the initial state $3d^6$ includes 34 term symbols and 210 states (according to equation (3.15) and reference [61]) with the ground state $^5D_4$. The final state $3p^53d^7$ can be described by 110 term symbols and 270 states. With respect to the total angular momentum quantum number of the initial ground state term symbol ($J = 4$), only transitions employing final state term symbols with $J = 3$ (24 states), $J = 4$ (18 states) and $J = 5$ (11 states) are allowed by the selection rule for dipole transitions. Thus, the resulting transition pattern consists of 53 peaks with different intensities [61].

Figure 3.2 (a) shows the impact of the Slater-Condon parameters (SCP) on the shape of the transition patterns (sticks). The calculated transition patterns were convoluted with a Lorentzian function (FWHM of 0.2 eV) and a Gaussian function (FWHM of 0.2 eV) to simulate the peak broadening due to the finite core-hole life-time and a feasible experimental resolution, respectively. The bottom transition pattern shows only one stick at around 52.7 eV resulting in one maximum for the SCP values set to zero. In this case, multiplet effects are neglected and the single stick represents the well known $p - d$ transition within the single-electron model. The spectral shape becomes more rich of features, if the SCP's are scaled to 24% of their atomic values. Here, four sticks with an intensity of higher than 1% of the maximum peak intensity can be found, resulting in a double-peak shaped absorption spectrum with its maxima at 52.2 eV and 53.4 eV. With increasing SCP values significant changes of the transition patterns can be found resulting in a larger splitting of the two peaks. Here, the position of the first maximum shifts to 50.9 eV and the maximum of the higher peak moves to 55.1 eV. Furthermore, a third maximum can be found at around 54.3 eV, if the SCP's are set to 80% of the respective atomic values (blue spectrum). This scaling factor is typically used for calculations of X-ray absorption spectra for TM compounds and will serve as starting model for further calculations. Spin-orbit coupling (green spectrum, core-valence and valence-valence spin-orbit coupling parameters were both scaled to 1) allows more than 36 transition

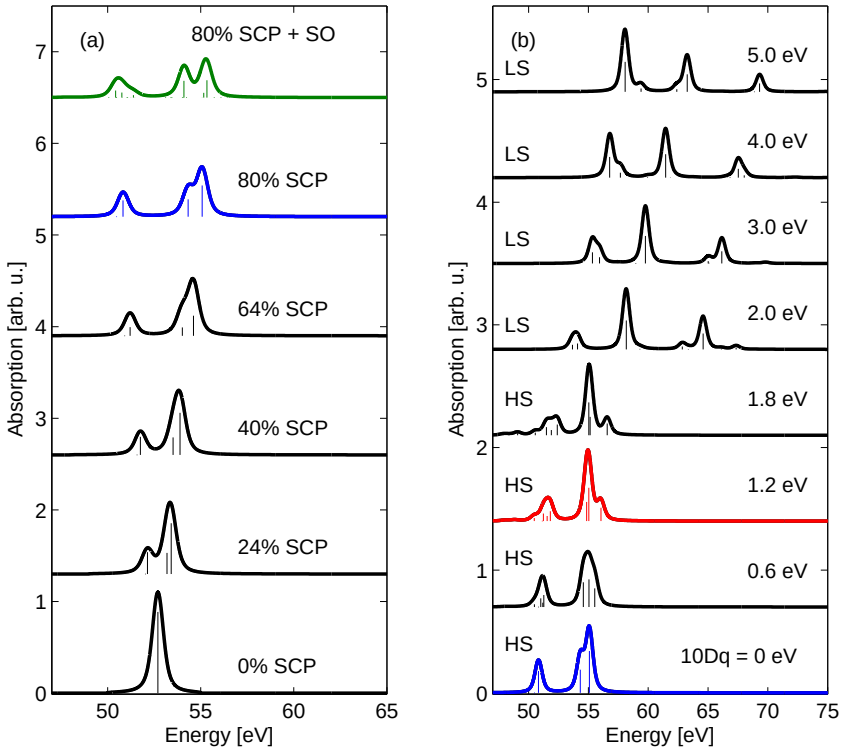

Figure 3.2.: Calculated Fe $M_{2,3}$-edge for the octahedral coordinated $3d^6$ configuration. The calculated transition patterns (sticks) and the correspondingly convoluted spectra show the influence of the Slater-Condon parameters (a) and the crystal field splitting (b) on the spectral shape. The spectra are shifted in the intensity for a better overview.

sticks for SCP set to 80% of the atomic values. A broad, asymmetric maximum can be found at around 50.6 eV together with two well separated maxima at 54.1 eV and 55.3 eV, respectively, in the corresponding spectrum. A comparison between the blue and the green spectrum shows, that spin-orbit coupling affects the shape of the absorption edge. However, electron-electron repulsion is typically much larger compared to spin-orbit coupling can be neglected for calculation of the Fe $M_{2,3}$-edges for most applications [287].

The presence of a cubic crystal field splits the 3d states into five different states. According to Hundt's rules, all t_{2g} and e_g states are occupied by one spin-up electron and an additional spin-down electron can be found in one of the t_{2g} states resulting in $S = 2$. The ground state of this high-spin state is given by the $^5T_2$ symmetry. In the low-spin state the symmetry is $^1A_1$ and all t_{2g} are fully occupied, while the e_g states remain unoccupied leading to $S = 0$. Additionally, an "intermediate" spin state is possible with the occupation $t_{2g}^5 e_g^1$. To demonstrate the impact of the crystal field splitting on the transition pattern and resulting absorption spectrum, the calculations employing octahedral

ligand field were performed for different values for the crystal field splitting (10Dq) and the results are presented in figure 3.2 (b). The starting point is the blue spectrum with SCP scaled to 80% of the respective atomic values and no crystal field effects (the same as the blue spectrum in figure 3.2 (a)). Setting the crystal field splitting to 0.6 eV leads to a branching of states allowing significantly more transitions resulting in a more complicated transition pattern. The only change between the spectrum with 10Dq=0 eV and 10Dq=0.6 eV is the smearing of the strongest maximum at around 55.1 eV and a shoulder at 54.3 eV to a single broad maximum. However, if the crystal field splitting is increased to 1.2 eV (red spectrum in figure 3.2 (b)), which is actually a realistic value for Fe^{2+} in octahedral environment [60], the transition pattern shows significant variation. Here, the spectrum is dominated by an intense and relatively sharp maximum at about 55.0 eV with a shoulder at 56.0 eV and a weaker and broad maximum at 51.6 eV. Weak but still observable changes can be found if the crystal field splitting is set to 1.8 eV. Here, the energy splitting between the strong maximum at 55.0 eV and its shoulder becomes higher. Furthermore, the broad maximum at around 51.6 eV is split and a high number of weak transition sticks result in an additional spectral feature in the region from 48 eV to 50 eV.
If 10Dq exceeds 1.8 eV a transition from the high-spin state to the low-spin state occurs. The change of the ground state symmetry from $^5T_2$ to $^1A_1$ leads to dramatic changes of the transition pattern as well as the absorption spectrum. The spectrum for 10Dq=2.0 eV shows three well separated maxima at 54.0 eV, 58.2 eV and 64.6 eV, respectively. If the position of the X-ray absorption spectrum is defined by the energy position of the strongest maximum, the high-spin to low-spin transition results in a peak shift of approximately 3.2 eV demonstrating a high potential of the Fe $M_{2,3}$-edge for applications where the spin transition must be studied. With increasing crystal field splitting even more pronounced spectral changes can be observed. Besides the continuous shift to higher energy. The shape of the main maxima at 58.2 eV and 64.6 eV, respectively, shows only weak changes but the peak splitting is increased. More pronounced changes can be found in the low-energy region of the spectrum. Here, two transition sticks can be found at 53.7 eV and 54.0 eV with comparable intensity for 10Dq=2.0 eV. With increasing crystal field splitting, the intensity ratio of the transitions changes dramatically resulting in a very strong maximum at 58.1 eV with a weak shoulder at 59.4 eV for 10Dq=5.0 eV
Calculations presented in figure 3.2 demonstrate a high sensitivity of the Fe $M_{2,3}$-edge on atomic multiplet and ligand field effects for the $3d^6$ configuration. In the following, similar calculations will be shown for another important electronic configuration $3d^5$ for iron containing compounds.

3.5.2. $3d^5$ configuration

$3d^5$ is the representative configuration for Fe^{3+}. After a detailed discussion of the effect of the atomic multiplet and ligand field theory on the Fe $M_{2,3}$-edge was given in section 3.5.1 on the example of the $3d^6$ configuration, only very indicative calculations will be presented in this section.

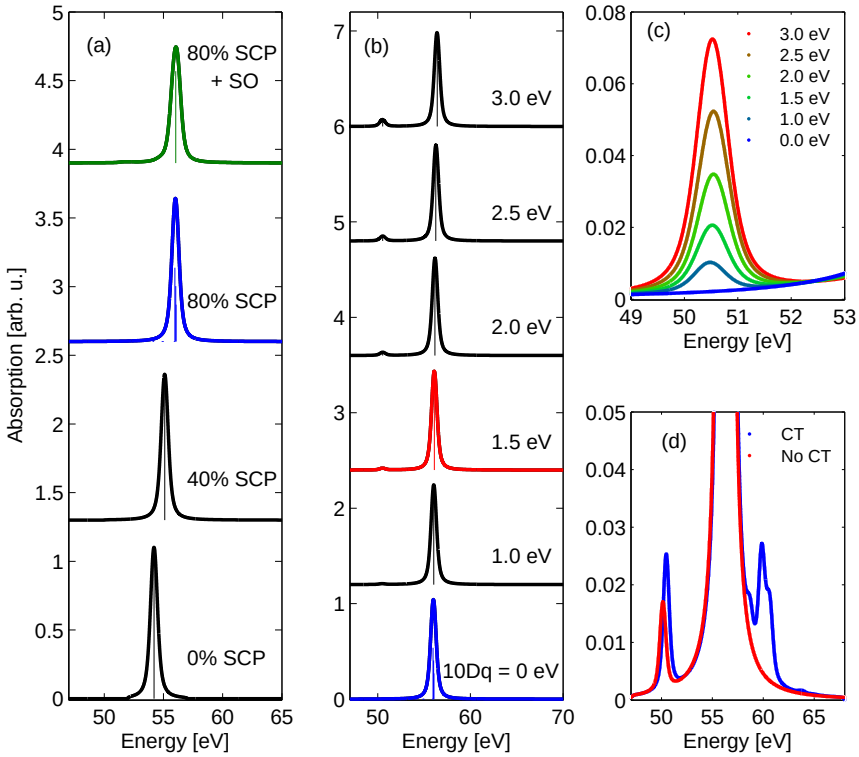

Figure 3.3.: Calculated Fe $M_{2,3}$-edge for the octahedral coordinated $3d^5$ configuration. The calculated transition pattern (sticks) and the correspondingly convoluted spectra show the influence of (a) the Slater-Condon parameters and (b) the crystal field splitting on the spectral shape. The spectra are shifted in the intensity for a better overview. In (c) the spectra from (b) are presented with a focus on the energy region from 49 eV to 53 eV for different 10Dq. (d) shows the impact of charge transfer effects.

The initial state $3d^5$ is described by 37 term symbols and 252 levels and all t_{2g} as well as e_g states are occupied by one electron each. The final state $3p^53d^6$ is given by 180 term symbols and 1260 levels. The atomic ground state is given by $^6S_{5/2}$ and thus, only 110 transitions into the final states with $J = 3/2, 5/2, 7/2$ are allowed. In the presence of the octahedral ligand field the symmetry of the high-spin and low-spin states (the t_{2g} states are occupied by 5 electrons while the e_g states remain empty) is given by $^6A_1$ and $^2T_2$, respectively.

Figure 3.3 (a) shows Fe $M_{2/3}$-edges calculated for the $3d^5$ configuration using different SCP values. If the SCP values are set to zero the spectrum is described by only one excitation at 54.2 eV within the single-particle model, similar to the $3d^6$ configuration. The same can be found if the SCP values are set to 40% of the respective atomic values, but the transition is shifted to higher energy. For SCP=80% 28 sticks with the intensity higher than 1% of the maximum intensity contribute to the spectrum. The absorption

edge is dominated by 3 strong transitions. However, the energy positions are very close to each other and the convoluted spectrum shows, again, only one maximum at 56.3 eV (blue line). Spin-orbit coupling (green line) affects the transition pattern and results in a slightly increased FWHM. Crystal field effects significantly modify the transition pattern but similar to the atomic multiplet effects, only minor changes can be found in the overall absorption edge spectra (3.3 (b)). To emphasize crystal field induced changes, the spectra are plotted in figure 3.3 (c) for the energy range from 49 eV to 53 eV. Increasing crystal field splitting results in a peak at around 50.5 eV. Although the maximum growths with increasing 10 Dq, the peak intensity is below 8% of the maximum intensity even for the very high 10Dq value of 5.0 eV.
In very specific cases, e.g. for Fe_2O_3, charge transfer may contribute to the absorption edge. De Groot *et al.* measured the Fe $L_{2/3}$-edge and obtained the charge transfer parameters by comparing experimental spectra with calculations. The extracted parameters are: SCP of 90% of their atomic values, 10Dq=1.5 eV, ionic crystal field splitting of 1.2 eV with an additional energy splitting of 0.3 eV due to the difference of hopping energies of the t_{2g} and e_g states with the respective energies of 1.0 eV and 2.0 eV [307, 60]. The same parameters were used to calculate the Fe $M_{2/3}$-edge for the same electronic configuration. The calculated spectrum can be found in figure 3.3 (d) together with the spectrum, where charge transfer is not included. Both spectra show identical spectral shape of the main maximum and only subtle differences in the energy region from 48 eV to 52 eV and from 58 eV to 63 eV can be observed. However, the intensity of the both satellite features is below 3% compared to the peak intensity of the spectra.
In order to simulate high q effects of X-ray Raman scattering ($k = 3$) the same scheme but with modified selection rules ($\Delta J = \pm 2$ instead of $\Delta J = 0, \pm 1$) can be applied.

4. Experimental stations for X-ray Raman scattering experiments

Measurements of low-energy absorption edges by X-ray Raman scattering presented in this thesis require high flux X-ray sources due to the small cross-section of an inelastic scattering event. Thus, all experiments relevant for this thesis were carried out at third generation synchrotron radiation facilities APS, ESRF, SPring-8, and PETRA III. After the basic principles to perform an X-ray Raman scattering experiment were discussed in section 2.5, the setups of beamlines BL12XU (SPring-8), 20-ID-B (APS), and ID16 (ESRF), which are dedicated to inelastic X-ray scattering, will be presented in the following and their unique advantages will be discussed. Furthermore, new beamline for inelastic X-ray scattering P01 at the synchrotron radiation facility PETRA III will be presented including first measurements of low energy X-ray absorption edges performed using this setup.

4.1. Beamline 20-ID-B at the Advanced Photon Source

The experimental station 20-ID-B is located in sector 20 of the Advanced Photon Source (APS) at the Argonne National Laboratory, Argonne, IL, USA. A 2.4 m long undulator is used as X-ray source. The X-rays are monochromatized using a Si(1,1,1) monochromator, subsequently focused by toroidal mirrors to 500 μm (H) $\times$ 400 μm (V) and the intensity of the incident X-rays is monitored by a gas ionization chamber. Measurements of X-ray Raman spectra were performed in inverse geometry using the LERIX[1] spectrometer [80]. Here, 19 bent Si(n,n,n) analyzer crystals are arranged in Rowland geometry with a radius of 97.5 cm covering the scattering angle range from 9° to 171° with angular steps of 9°. Each analyzer crystal focuses scattered X-rays to a NaI scintillation detector placed below the sample. The spectrometer plane is mounted perpendicular to the polarization direction of the X-rays allowing measurements also at scattering angles close to 90°. This analyzer crystal arrangement provides access to a scattering angle range of almost 180° and thus is ideally suitable for experiments where the momentum transfer dependence of absorption edges is the main point of interest. Detailed description of the LERIX spectrometer can be found in [80].
For the measurements relevant for this thesis two different analyzer reflections were used. Fe $L_{2/3}$-edge was measured using 19 bent Si analyzer crystals employing the Si(4,4,4) reflection. The energy position of the elastic line is close to 7.92 keV. In combination with the Si(1,1,1) monochromator, an overall energy resolution of 1 eV can be achieved

[1] Low Energy Resolution Inelastic X-ray scattering

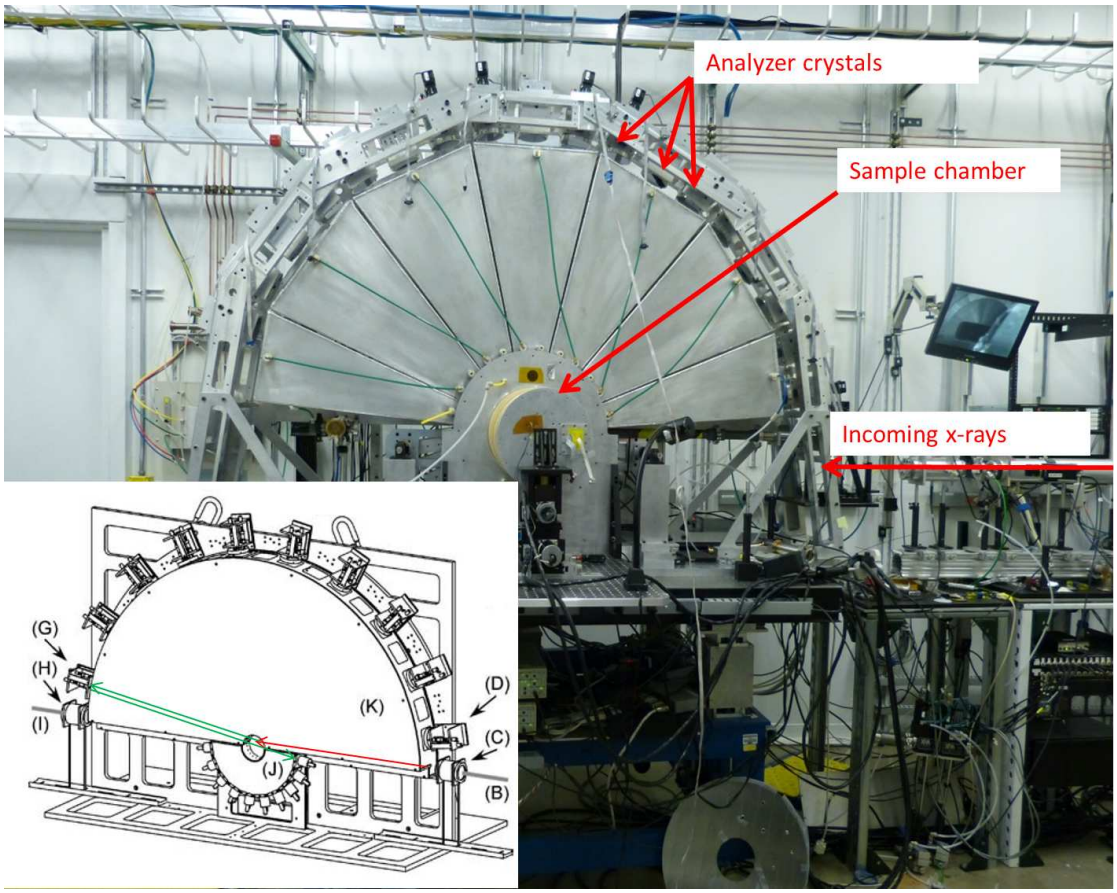

Figure 4.1.: Left: Schematics of the LERIX spectrometer [80] including the incident (B) and the transmitted (I) X-ray beam, ionization chambers (C) and (H), as well as analyzer modules for X-ray energy loss measurements in forward (G) and backward (D) scattering, and the helium filled analyzer chamber. Additionally, the path of the incident (red) and scattered (green) beam detected by one analyzer is indicated. Right: a picture of the LERIX spectrometer including the flight path of the incident and scattered radiation.

and the incident X-ray energy was scanned from about 8.58 keV to 8.68 keV to match the energy loss position of the Fe $L_{2,3}$-edge from 660 eV to 760 eV. The momentum transfer dependence of the Fe M-edge was studied with the same setup but using Si (5,5,5) analyzer reflection at 9.89 keV and an overall energy resolution of approximately 1.5 eV. The incident energy was scanned from 9.92 keV to 10.04 keV corresponding to the energy loss range from 30 eV to 150 eV at the Fe $M_{2/3}$-edge.

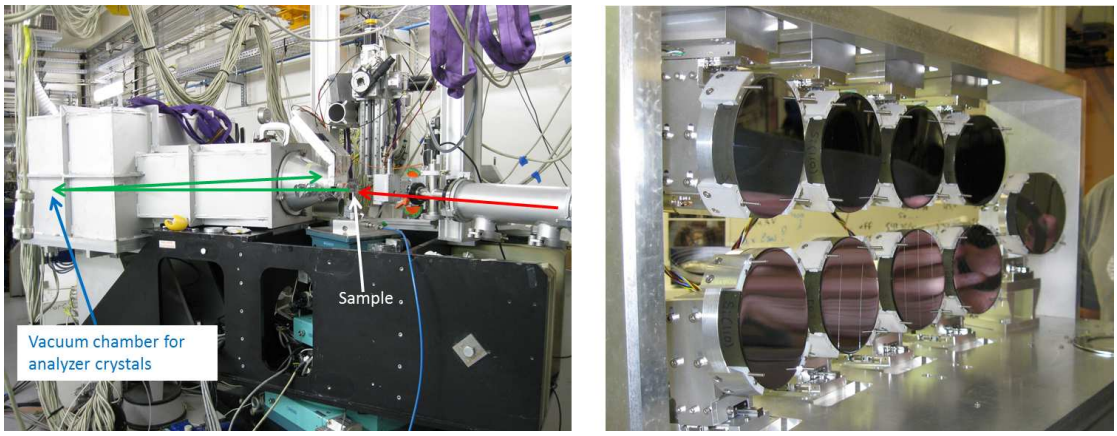

Figure 4.2.: Left: Setup for measurements of electronic excitations by inelastic X-ray scattering of the beamline ID16 at the ESRF including the sample position, vacuum chamber for analyzer crystals as well as the beam path of incoming (red) and scattered (green) radiation. Right: Arrangement of nine Si analyzer crystals of the multiple-element spectrometer with unmounted vacuum chamber.

4.2. Beamline ID16 at the European Synchrotron Radiation Facility

Beamline ID16 of the European Sychrotron Radiation Facility (ESRF) in Grenoble, France, was a state of the art inelastic X-ray scattering beamline until it was replaced by the new generation beamline ID20 as a part of the ESRF upgrade program. The X-rays are produced by three U35 undulators and a double crystal Si(1,1,1) monochromator is used to tune the X-ray energy [301]. The energy bandwidth of the X-rays can be further improved by a four crystal channel cut monochromator using the Si(2,2,0) or Si(4,4,0) reflection. The beam size can be focussed by Rh coated toroidal mirrors to 130 μm (H) $\times$ 50 μm (V). A Si pin diode fixed in front of the spectrometer allows measurements of the incident X-ray beam intensity. The spectrometer is designed in Rowland geometry (1 m radius) and consists of nine Si(n,n,0) analyzer crystals arranged in an array as indicated in figure 4.2. The whole array can be moved in the angular range from 35° to 135° on the plane perpendicular to the polarization plane of the X-rays. Especially at high scattering angle, where XRS spectra show only a weak dependence on the momentum transfer, several spectra at comparable q can be measured by only one scan and summed up, increasing the statistical accuracy of the experimental data. Furthermore, a Maxipix area detector (256 $\times$ 256 pixels with a pixel size of 55 μm $\times$ 55 μm) is used to measure the intensity of the scattered radiation. More detailed information on the spectrometer can be found in reference [301]. The data presented in this thesis was measured employing the Si(6,6,0) reflection at 9.69 keV and a Si(2,2,0) channel cut monochromator. Furthermore, led masks with a centered hole (80 mm diameter) were adapted to the analyzer crystals to discriminate the signal from the edge of the analyzers, improving the total energy resolution to 0.7 eV. Fe M-edge measurements were performed in inverse geometry by

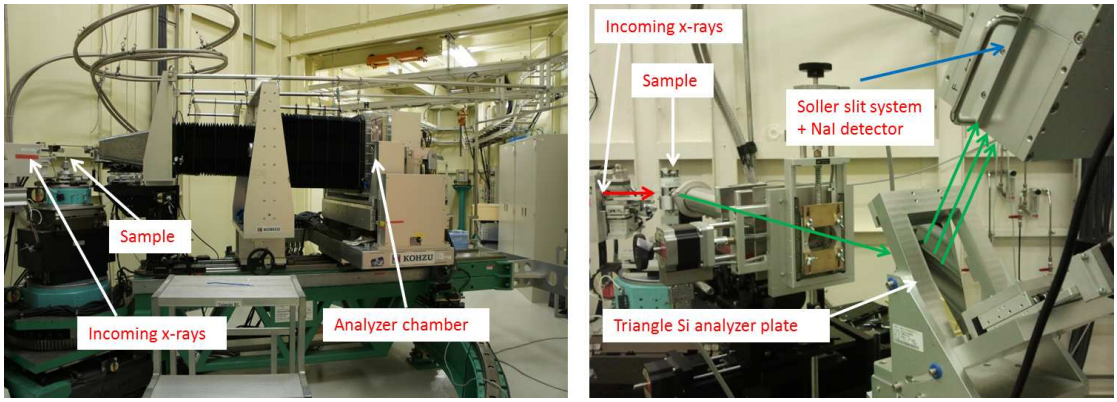

Figure 4.3.: Left: Multiple element spectrometer for inelastic X-ray scattering in Rowland geometry. Right: Laue spectrometer for transmission mode experiments. Schematics of both setups is given in figure 2.3.

scanning the incident X-ray energy from 9.73 keV to 9.76 keV corresponding to the energy loss region from 40 eV to 70 eV to match the energy onset of the Fe $M_{2,3}$-edge.

4.3. Beamline BL12XU at SPring-8

For the inelastic X-ray scattering beamline BL12XU (operated by the National Synchrotron Radiation Research Center Taiwan) at the synchrotron radiation facility SPring-8 in Hyogo, Japan, a 4.5 m long undulator with a period length of 32 mm is used as X-ray source. The X-ray energy is defined by a Si(1,1,1) double crystal monochromator. Additionally, a Si(2,2,0) channel cut monochromator can be used to further reduce the energy bandwidth. A collimating mirror coated with Si (for 5-12 keV) and Pt (for 12-30 keV) is installed to focus the beam size to 120 μm (H) $\times$ 75 μm (V) [40]. The intensity of the incident X-rays is monitored by an ionization chamber. The inelastic scattering spectrometer in Rowland geometry (figure 4.3, left) with a variable circle radius between 1 m and 3 m (for the experiments presented in this thesis the radius was set to 2 m) includes three spherically bent Si(n,n,0) analyzer crystals, six diced Si(n,n,0) analyzer crystals and a Si pin-diode as a detector. The spectrometer is built in a similar design as the spectrometer at ID16 of the ESRF (see figure 4.2). The measurements of low energy absorption edges by XRS were carried out using the Si(6,6,0) reflection at 9.69 keV. The overall energy resolution was 1.4 eV using the bent analyzer crystals without channel cut monochromator and around 0.5 eV using diced analyzer crystals in combination with the Si(220) channel cut monochromator. This setup was used in order to measure the Mg $L_{2/3}$-edge in MgO by scanning the incident energy from 9.692 keV to 9.802 keV in order to match the energy loss region from 2 eV to 112 eV.
Beamline BL12XU was recently extended by a new spectrometer. The spectrometer employing a bent Si(n,n,0) analyzer plate operates in transmission mode and in Laue geometry (see section 2.5 for more details). The distance between the sample and the analyzer was set to 1 m and a NaI detector together with a Soller slit system was used

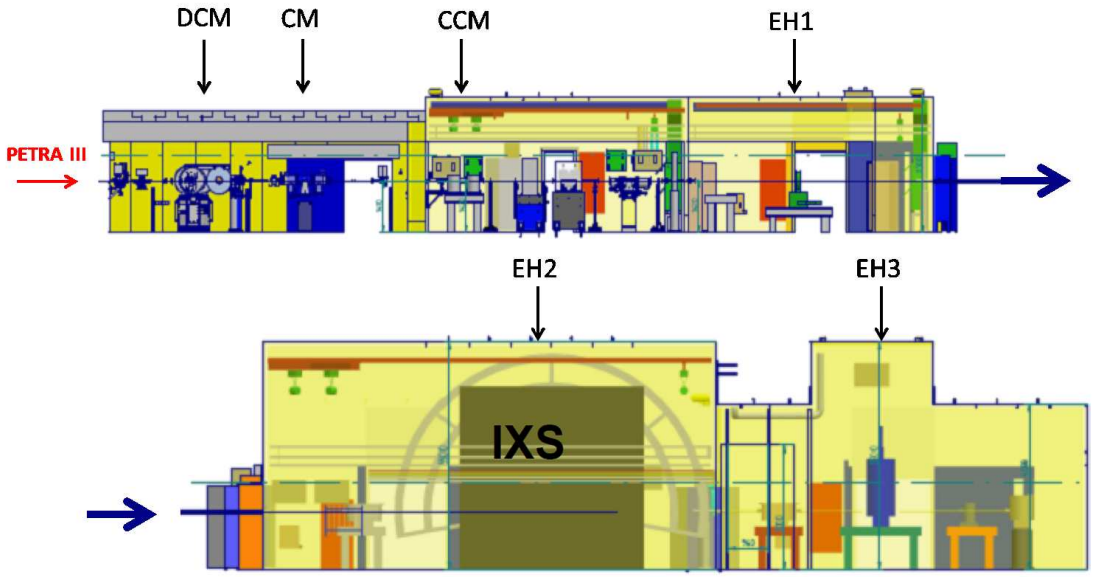

Figure 4.4.: General layout of beamline P01 at PETRA III including the most important beamline components for IXS experiments: high heat-load double crystal monochromator (DCM), collimating mirrors (CM), and a channel-cut monochromator (CCM). The experimental section can be divided into the experimental hutches 1 (EH1), 2 (EH2), and 3 (EH3), respectively. Here, EH2 is dedicated to inelastic X-ray scattering experiments, especially XRS and RIXS.

to measure the intensity of the scattered and energy analyzed radiation in transmission mode (figure 4.3, right). For XRS experiments using the Laue spectrometer the same X-ray source can be used as for the Rowland setup. Using a Si(220) channel cut monochromator and the Si(12,12,0) reflection of the analyzer plate at 19.46 keV an overall energy resolution of 1.4 eV was achieved. Furthermore, a Kirkpatrick-Baez mirror system [141] is used to focus the beam to 30 μm (H) $\times$ 30 μm (V). The energy loss is scanned by tuning the analyzer energy at a fixed incident energy of 19.46 keV [118].

4.4. Beamline P01 at PETRA III

The beamline P01 of the synchrotron radiation facility PETRA III (6 GeV electron energy) is divided in two sections, which are dedicated to Mössbauer spectroscopy and resonant and non-resonant inelastic X-ray scattering. The general layout of the beamline is presented[2] in figure 4.4. Due to a very low cross section of the experiments, two 5 meter long undulators (about 150 periods per undulator, 32 mm period length) are used as X-ray source, followed by a high heat-load Si(311) double crystal monochromator. This monochromator is optimized for higher energy resolution compared to the Si(111) double crystal monochrmomators typically used. The monochromator is followed by

[2]Figures 4.4 and fig:10.1.2 were provided by Fran-Uwe Dill (DESY).

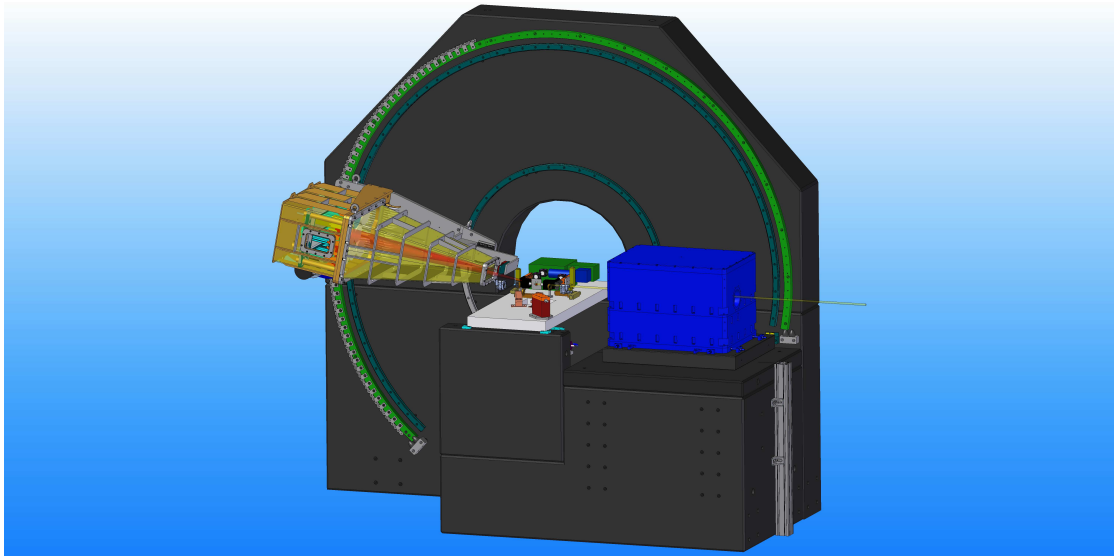

Figure 4.5.: Sketch of the spectrometer for inelastic X-ray scattering, which will be installed at beamline P01. The main components are the KB-mirror tank (blue), laser heating setup and an analyzer crystal array (yellow) mounted on a granite block (black).

bent collimating toroidal mirrors, which reduce the beam size to about 150 μm $\times$ 150 μm (H $\times$ V). Later on, Kirkpatrick-Baez mirrors will be installed to reduce the beam size to about 3 $\times$ 3 μm (H $\times$ V). The central component of the setup is the XRS spectrometer, which is sketched in figure 4.5. The spectrometer is designed in Rowland geometry (1 meter circle radius) in vertical plane such a way, that the scattering radiation is analyzed by Si(n,n,0) analyzer crystals over a solid angle from about 15° to 170°. The spectrometer is similar to that installed at beamline 20-ID at the APS (see setion 4.1 for a detailed description) but using 12 analyzer crystals and a Medipix detector. During the measurements an energy resolution of 0.5 eV could be achieved.

5. Sample characterization

In order to study the oxidation state, local coordination, and spin state of iron in compounds some representative samples were chosen for experiments. Section 5.1 gives an overview on the samples used for XRS measurements. Furthermore, the preparation procedures and the results of the sample characterization will be compiled. In section 5.2, detailed results of the sample characterization by means of X-ray diffraction are summarized.

5.1. Samples used for X-ray Raman scattering experiments

In order to study the feasibility of the Fe $L_{2/3}$- and $M_{2/3}$-edge measurements FeO, α-Fe_2O_3 and Fe_3O_4 were chosen as reference compounds. Powdery samples with trace metal basis of 99.9 %, 99.995 % and 99.99 %, respectively, were purchased from Sigma Aldrich. FeO ($^{[6]}Fe^{2+}$, space group $Fm3m$, corresponding to the mineral wustite[1]) and α-Fe_2O_3 ($^{[6]}Fe^{3+}$, $R\bar{3}c$, corresponding to the mineral hematite) were chosen as reference compounds for Fe^{2+} and Fe^{3+} in octahedral coordination, respectively. Furthermore, Fe_3O_4 (corresponding to magnetite) was used to represent a compound where both Fe^{2+} and Fe^{3+} can be found. The composition of Fe_3O_4 is given by $^{[6]}Fe^{2+}$, $^{[6]}Fe^{3+}$ and $^{[4]}Fe^{3+}$ (tetrahedral Fe^{3+}) with equal fractions [50].
For a quantitative determination of the oxidation state of iron and its local coordination spectra on well characterized reference compounds must be performed. Concerning geologically relevant iron containing minerals, iron predominantly occurs as Fe^{2+} or Fe^{3+}, where the iron atoms are surrounded by ligand atoms or molecules. Here, tetrahedral and octahedral coordination are preferred. Thus, the measurements are focused on four reference compounds, which represent these important iron species. Synthetically prepared Fe_2SiO_4 ($^{[6]}Fe^{2+}$, $Pbnm$, corresponding to fayalite) was used and characterized by Dr. M. Wilke utilizing Fe K-edge XANES spectroscopy, which allows to extract the contribution of iron with different oxidation state and coordination to an unknown compound on the basis of the centroid position and the shape of the Fe K pre-edge [316]. No evidence of Fe^{3+} containing inclusions was found for Fe_2SiO_4. Tetrahedral Fe $^{2+}$ is represented by $FeAl_2O_4$ ($Fd\bar{3}m$, corresponding to the mineral hercynite). A detailed description of the preparation and characterization of this sample is given in reference [7]. Analytical grade powders of $Al(OH_3)$, MgO, and Fe_2O_3 were used as starting materials for the preparation process. The powders were treated using a flux-growth method

[1]Natural minerals may have a non stoichiometric composition and/or spatial inhomogeneities. Impurities also cannot be excluded. Hence, synthetic samples were used, that can be attributed to the corresponding mineral.

described in reference [6]. The resulting powder was subsequently annealed to different temperatures between 900 °C and 1200 °C in a CO_2:H_2 gas mixture with the 2:1 fraction in order to vary the oxygen fugacity. The composition of the final sample powder was extracted by electron micro-probe analysis (EMP) resulting in 44.7±0.2 % FeO and 55.5±0.4 % Al_2O_3. In addition, the $Fe^{2+}/Fe_{tot.}$ ratio was estimated to 0.96 and 0.94 by Mössbauer spectroscopy and EMP, respectively. Furthermore, 15% of the Fe^{2+} content is octahedrally coordinated.
As octahedral Fe^{3+} standard the same α-Fe_2O_3 sample was used as described above. $FePO_4$, iron(III) phosphate ($^4Fe^{3+}$, $P3_121$, corresponding to rodolicoite) with berlinite-like structure ($AlPO_4$) was synthesized by annealing of p.A.-grade $FePO_4$-hydrate in air and used as a reference with tetrahedral Fe^{3+}. Here, Fe K-edge XANES results do not show any indication of Fe^{2+}. In addition to the crystalline reference samples, three synthetically prepared glasses were used for quantitative determination of the $Fe^{3+}/Fe_{tot.}$ ratio by XRS. Two glasses (RB0-1 and RB0-4) with a composition of a transitional alkalic basalt from Iceland [288] were synthesized at 1350 °C and two different oxygen fugacities. The starting composition of the sample was 14.38±0.21 wt% FeO, 47.88±0.20 wt% SiO_2, 13.22±0.16 wt% Al_2O_3, 9.04±0.08 wt% CaO, 4.68±0.08 wt% Na_2O, 4.04±0.10 wt% TiO_2 and 3.23±0.06 wt% MgO. Furthermore, Fe-doped haplogranitic glass AOQ-2 was synthesized and its composition resulting in 8.4±0.2 wt% Fe_2O_3, 72.9±0.5 wt% SiO_2, 10.8±0.2 wt% Al_2O_3, 4.5±0.1 wt% K_2O and 3.4±0.2 wt% Na_2O was determined by EMP [317] after the preparation process. Sample characterization by optical polarization microscopy reveals no indication of clustering effects or other optical inhomogeneities of the glasses. Furthermore, the $Fe^{3+}/Fe_{tot.}$ ratios of the glasses were estimated by Mössbauer spectroscopy [321] to 0.83±0.04, 0.63±0.04 and 0.16±0.04 for RB0-1, AOQ-2 and RB0-4, respectively.
Measurements of the Fe $M_{2/3}$-edge under high pressure were performed on synthetic FeS powder ($P6\overline{2}c$, corresponding to the mineral troilite). X-ray diffraction analysis did not reveal any crystalline impurities or formation of single crystals[2].
Additional measurements of low energy absorption edges were performed on the most abundant elements of the deep Earth as a part of the commissioning of the new inelastic X-ray scattering beamline P01 at the synchrotron radiation facility PETRA III. Here, the impact of the coordination in Si-O networks in quartz (Si is surrounded by four O atoms), stishovite (6-fold coordination) and glass (distorted 4-fold coordination) at the Si $L_{2/3}$- and O K-edge was studied. Therefore, SiO_2 quartz powder on the 99.995 % trace metal basis was obtained from Sigma Aldrich. Commercially available SiO_2 glass was used as a second reference. The same glass served as starting material for stishovite synthesis, which was formed by treating the glass at 15 GPa and 1800 °C. The resulting spectra were compared with the spectra of polycrystalline Si powder (Sigma Aldrich, 99.95% trace metal basis) and SiO powder (see reference [73] for more details on the preparation process). Additionally, MgO powder (Sigma Aldrich, 99.99% trace metal basis) was used for test measurements of the Mg $L_{2/3}$-edge.

[2]Private communication with Prof. Dr. J. S. Tse

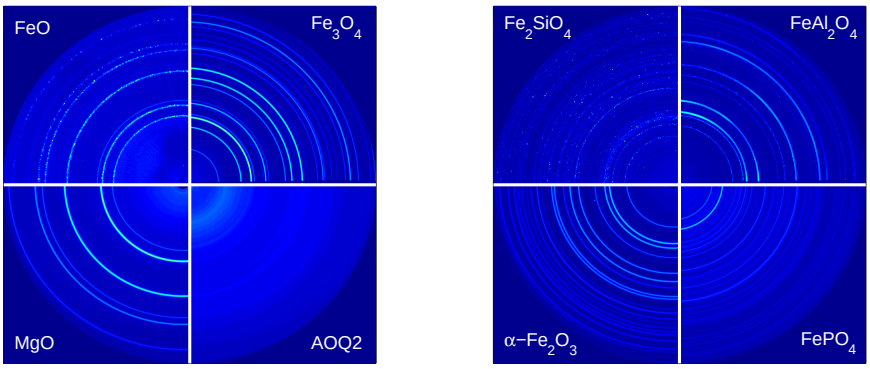

Figure 5.1.: Segments of the two dimensional X-ray diffraction pattern of FeO, Fe_3O_4, MgO and AOQ-2 (left), as well as Fe_2SiO_4, $FeAl_2O_4$, α-Fe_2O_3 and $FePO_4$ (right), respectively.

5.2. Sample characterization by X-ray diffraction

The samples used within this thesis were characterized by means of X-ray diffraction (XRD). XRD is very sensitive to the long-range order of matter and thus very useful as a fingerprinting technique in order to identify crystalline phases in matter [38, 306, 3]. The experiment was conducted at beamline BL9 [151] of the synchrotron radiation facility DELTA (Dortmund, Germany), which is dedicated to elastic X-ray scattering, e.g. X-ray diffraction, X-ray reflectivity or small-angle X-ray scattering. The measurements were performed using 27 keV X-rays. A MAR345 imaging plate detector was used to collect the data.

The collected two dimensional images of the X-ray diffraction pattern of FeO, Fe_3O_4, MgO, AOQ-2, Fe_2SiO_4, $FeAl_2O_4$, αFe_2O_3 and $FePO_4$ are presented in figure 5.1. Every sample shows a unique diffraction pattern according to its composition and crystal structure. In general, three different kind of diffraction pattern can be observed. The diffraction pattern measured on Fe_3O_4, MgO, $FeAl_2O_4$, α-Fe_2O_3 and $FePO_4$ show a clear formation of Debye-Scherrer rings. This is typical for a powdery sample without any preferred orientation of single larger crystallites. In the diffraction pattern obtained from FeO and Fe_2SiO_4 similar Debye-Scherrer rings can be found, but the intensity distribution is not homogenous. Hence, some larger single crystals can be found with a preferred orientation. In order to match the relative peak intensities of the calculated spectra the samples must be rotated during the experiment in order to neglect the crystal orientation and e.g. Rietveld analysis can be applied in order to obtain detailed quantitative information about the crystal structure and relative fractions of different phases. In contrast, the pattern of AOQ-2 glass shows only one broad structure, which is typical for amorphous samples.

For a more detailed data analysis the measured XRD pattern were integrated over the whole azimuthal angle of the detector plane for each scattering angle 2Θ using the software package FIT2D [108]. The resulting diffraction pattern are presented in figure 5.2

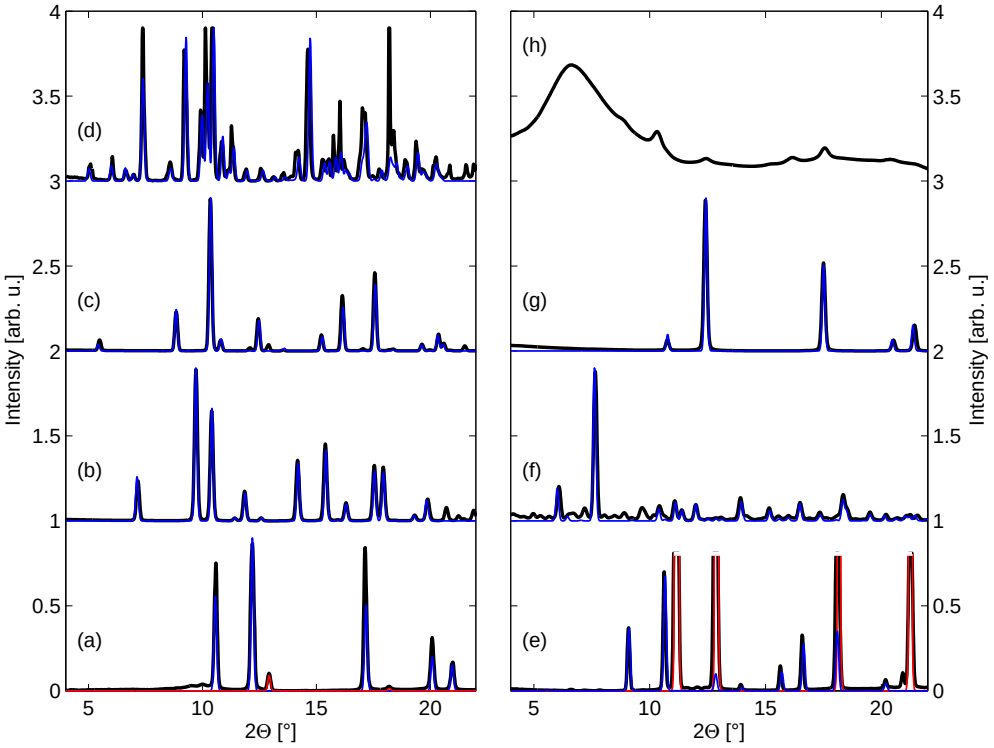

Figure 5.2.: Integrated XRD pattern (black) measured on (a) FeO, (b) α-Fe_2O_3, (c) Fe_3O_4, (d) Fe_2SiO_4, (e) $FeAl_2O_4$, (f) $FePO_4$, (g) MgO, and (h) AOQ-2, as well as the corresponding calculated diffraction pattern (blue) [206]. Furthermore, the diffraction pattern of additional compounds Fe (in (a)) and Al (in (e)) (red) is shown.

together with theoretical calculation based on the crystal structures given in section 5.1. All sample except of AOQ-2 show several strong peaks indicating a crystalline structure of the samples. The diffraction pattern of FeO shows a very good agreement with the calculated FeO pattern, but two additional diffraction peaks at about 12.9 ° and 18.2 ° cannot be attributed to FeO. These peaks fit very well to the typical Fe structure (α-iron, $Im3m$). Thus, the FeO sample is contaminated by about 3% of elemental Fe, which must be critically assessed concerning the XRS measurements. In contrast, the XRD pattern of α-Fe_2O_3, Fe_3O_4 are well reproduced by the calculated spectra indicating a strongly crystalline and homogenous sample structure confirming the phase purity. The diffraction pattern of Fe_2SiO_4 shows a reasonable agreement compared to the calculated spectrum. Although all calculated peaks can be identified in the experimental pattern, the intensity of distinct peaks differ from the calculation. This is an effect of the certain orientation of the crystallites in the Fe_2SiO_4 thus modifying the intensity of single peaks. A similar trend can be found for $FeAl_2O_4$ and $FePO_4$. In the pattern of $FeAl_2O_4$ addi-

tional peaks can be found originating from the aluminum sample holder due to the fact, that the horizontal X-ray size was larger than the sample. In $FePO_4$ some unidentified peaks can be found in the angle region below 10 °. Although the typical rodolicoite-like $FePO_4$ structure is still conserved, impurities by other phases cannot be excluded. The absolute intensity of the peaks caused by unknown phases is less than 1 %. Finally, the XRD pattern of AOQ-2 shows only one strong and broad maximum at around 6.6 °, stressing the glassy structure of the sample. Furthermore, some very weak peaks can be found indicating Fe_3O_4 impurities with a relative contribution of about 3%. An overview about the samples used for the experiments within this thesis is given in table 5.1.

Sample	Oxidation state	Local coordination
FeO	2+	octahedral
α-Fe_2O_3	3+	octahedral
Fe_3O_4	mixed	mixed
Fe_2SiO_4	2+	octahedral
$FeAl_2O_4$	2+	mixed
$FePO_4$	3+	tetrahedral
RB0-1	mixed	mixed
RB0-4	mixed	mixed
AOQ2	mixed	mixed
FeS	2+	octahedral
MgO	2+	octahedral
SiO_2 glass	4+	tetrahedral
SiO_2 quartz	4+	tetrahedral
SiO_2 stishovite	4+	octahedral

Table 5.1.: Overview about the samples used for the experiments.

6. Commissioning of beamline P01 at PETRA III: First XRS experiments

In this section first results using a preliminary version of the XRS spectrometer installed at P01 will be presented. For this purpose different samples were used in order to study the feasibility of such measurements of low energy absorption edge for several geologically relevant elements, e.g. silicon, oxygen, and magnesium. At this early stage, 6 Si(n,n,0) analyzer crystals and one Medipix detector were installed in the spectrometer. This setup was used for measurements of well known standards as well as to study the oxidation state of iron in unknown glasses presented in section 8.4. In the following, measurements of the Si $L_{2/3}$- and O K-edge on SiO_2 glass and its crystalline polymorphs α-quartz and stishovite will be presented in section 6.1. Additionally, the potential of the Si $L_{2/3}$-edge in order to study the oxidation state in mixed state compounds will be demonstrated in section 6.2. Finally, test measurements of the Mg $L_{2/3}$-edge on MgO will be shown and discussed in section 6.3.

6.1. Determination of the local coordination in SiO_2 polymorphs

Oxygen and silicon are the most common materials in the deep Earth [116, 27] and knowledge about the local electronic properties of silica glasses at high pressure is crucial in order to understand e.g. the incorporation of water molecules into the silica networks at extreme conditions, relevant for magma formation [190]. Despite of intensive studies the local structure in silica glasses at high pressure is still controversially discussed due to the high complexity of the glass structure. For pressures up to 10 GPa a non reversible density increase was observed on cost of a collapse of voids in the glass, which is accompanied by changes of ring structures [116] and a decrease of the Si-O-Si bonding angle leading to a coordination change from 4-fold to 6-fold at pressures up to 20 GPa [320]. However, in-situ XRD studies reveal controversial results concerning the pressure range where the structural transformation occurs [179, 128]. Due to the low binding energy of the electrons in silicon and oxygen XRS is the only feasible technique for measurements of e.g. oxygen K-edge and Si L-edge in order to study the local electronic and chemical properties in compounds under extreme conditions. Lin *et al.* performed in-situ XRS measurements of the O K-edge in silica glass at pressures up to 51 GPa [164]. Here, significant spectral changes of the O K-edge were found in the energy loss region between 535 eV and 545 eV, which allows to distinguish between the quartz-like and stishovite-like local electronic structure of Si in the glass. Thus, a structural

transition from 4-fold to 6-fold coordination at pressures between 10 GPa and 22 GPa was concluded and a conservation of the stishovite-like structure (6-fold coordination) up to 41 GPa was shown. Based on this study Fukui *et al.* performed Si $L_{2/3}$-edge measurements by XRS at comparable experimental conditions [85]. The spectral features of the Si $L_{2/3}$-edge indicative for quartz- or stishovite-like structures were manifested on the basis of polycrystalline polymorphs. The measurements were performed with a very good energy resolution of 0.3 eV at ambient conditions and strong spectral differences between the two structures could be observed. In addition to the experiment the partial DOS for the SiO_2 structures stishovite, quartz, penta-SiO_2 and hp-cristobalite was calculated using the WIEN2K package and compared with the experimental results. In contrast to the results obtained by Lin *et al.* the authors found no indication for a structural transition from the 4-fold to the 6-fold coordination in the SiO_2 glass even at pressures up to 74 GPa. This is a surprising result due to the fact that formation of crystalline stishovite was observed experimentally at room temperature already below 7 GPa [1]. Furthermore, this transformation is predicted theoretically for pressures above 15 GPa [162]. Fukui *et al.* claim that the experimentally obtained partial DOS does not show the shape of the DOS calculated for stishovite, but partial formation of 5-fold coordination could be found at high pressure. The discrepancy from the results obtained at the O K-edge are explained by the fact that the local electronic structure in quartz may become stishovite-like as a consequence of high pressure, with respect to the results by Lin *et al.*, but a change of the local coordination cannot be directly concluded. However, the measurements of the Si $L_{2/3}$-edge at high pressure were performed with an energy resolution of 2.0 eV and the statistical accuracy of the measurements may suppress pressure induced changes of the spectra. Thus, simultaneous in-situ measurements of both O K-edge and Si $L_{2/3}$-edge with significantly improved energy resolution and statistical accuracy together with theoretical calculations might clarify changes of the local structure of Si in SiO_2 glasses at high pressure.

In order to study the feasibility of possible measurements at high pressure, test measurements of the O K-edge and Si $L_{2/3}$-edge on SiO_2 glass and its quartz and stishovite polymorphs were performed. The spectra were taken in 1.5 hours in the case of the Si $L_{2/3}$-edge and 8.5 hours in the case of the O K-edge, respectively. The background was subtracted from the raw spectra by fitting a linear function to the pre-edge region of the Si $L_{2/3}$-edge. For the O K-edge a Lorentzian function was used instead in order to subtract the contribution of the Compton scattering. The resulting spectra are presented in figure 6.1. The spectral shape of the Si $L_{2/3}$-edge of SiO_2 glass shows a maximum at 108.5 eV and a pre-edge feature with its maximum at about 105.9 eV. Furthermore, a broad but weak maximum between 114 eV and 116 eV can be observed. The spectrum of α-quartz SiO_2 shows a Si $L_{2/3}$-edge very similar to that of the corresponding glass, but the edge is shifted by about 0.2 eV to higher energy loss. Furthermore, the pre-edge maximum appears slightly broader and can be found at 106.5 eV, which agrees well with earlier results [73, 233, 203]. The spectral shape changes significantly in the case of stishovite demonstrating the huge effect of the change between 4-fold to 6-fold Si coordination. The spectrum shows an extremely intense and sharp maximum at 107.1 eV followed by two weaker and broader features at about 110.3 eV and 113.5 eV, which

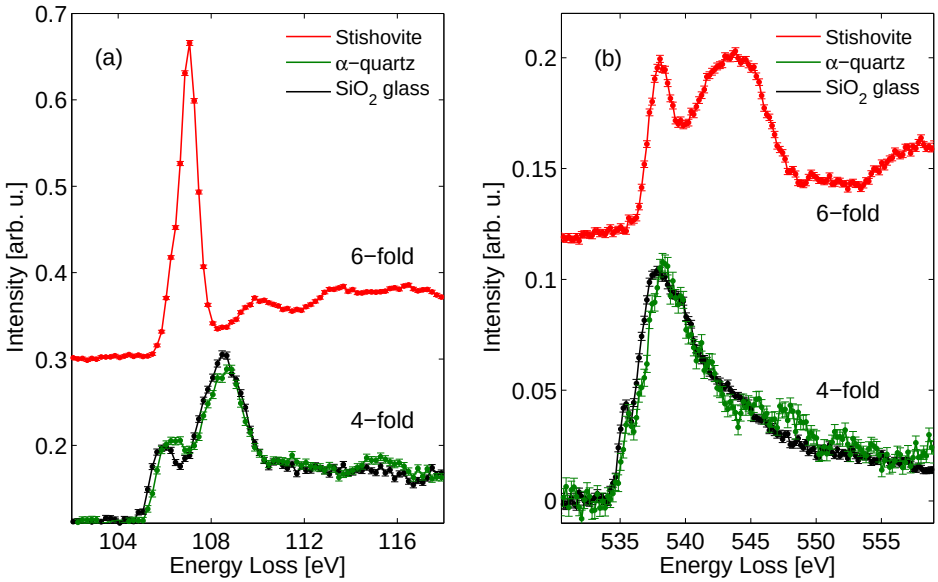

Figure 6.1.: (a) Si $L_{2/3}$-edge and (b) O K-edge measured on the SiO_2 polymorphs stishovite (red), α-quartz (green) and its glass (black).

is completely different to the spectrum of α-quartz and glass. The general trends are in agreement with those obtained by Fukui *et al.* [85].
Subsequently, similar measurements were performed at the O K-edge on the same samples. The O K-edge of the glassy SiO_2 shows a broad and strongly asymmetric maximum at about 537.8 eV and a pre-edge feature at 535.5 eV. The spectrum of α-quartz SiO_2 is very similar compared to the spectrum of glass, but shifted by about 0.2-0.3 eV to higher energy losses. The picture significantly changes for stishovite. Here, the main asymmetric maximum can be found at about 543.8 eV together with an almost same intense pre-peak at 538 eV. Thus, remarkable spectral differences of the O K-edge can be found according to the local coordination in SiO_2, similar to the results of the Si $L_{2/3}$-edge, showing the great potential of simultaneous measurements of both absorption edges in SiO_2 glasses in-situ at high pressure. Furthermore, comparable results found at the O K-edge for GeO_2 glass at high pressure [160] show the relevance of such studies. The quality of the results obtained using the preliminary setup of beamline P01 shows great perspectives for experiments under extreme condition employing the XRS spectrometer in its final version. Simultaneous in-situ measurements of the O K- and Si L-edge may reveal important information about pressure induced changes of the local coordination in SiO_2 glass.

6.2. Sensitivity of the Si $L_{2/3}$-edge on the oxidation state of silicon

To test the beamline performance, measurements of the Si $L_{2/3}$-edge were performed on crystalline Si, SiO_2 quartz and amorphous SiO [233]. These samples are very suitable reference compounds, because comparable XRS measurements are available [73, 233]. The scientific interest on this kind of compounds as well as potential applications are discussed in detail in appendix A and in reference [203]. Thus, comparable measurements were performed at beamline P01 in order to prove the feasibility of such measurements. First Si $L_{2/3}$-edges on Si, SiO and SiO_2 measured at beamline P01 are shown in figure 6.2. The spectra of Si and SiO_2 were taken in 1.5 hours while measurements on SiO were obtained in 6 hours.

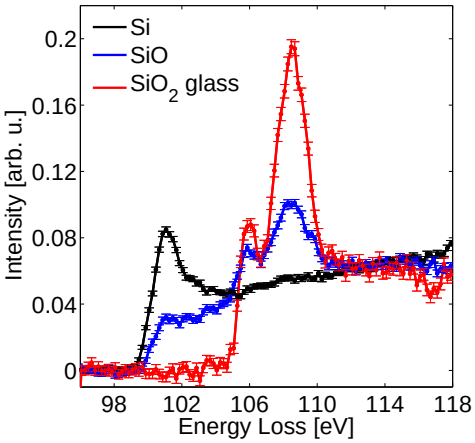

Figure 6.2.: Si $L_{2/3}$-edge measured on polycrystalline Si (black) and α-quartz SiO_2 (red) as well as on amorphous SiO powder (blue).

The shape of the Si $L_{2/3}$-edges of Si can be characterized by a single maximum at 101 eV with the edge onset at about 99.8 eV, which is in good agreement with the literature [287]. In contrast, the Si $L_{2/3}$-edges on SiO_2 show a narrower maximum at 108.7 eV and a pre-edge feature at about 106.5 eV. Furthermore, a broad maximum between 114 eV and 116 eV can be observed. Both spectra show a very good agreement compared to other results measured at beamline 20-ID of the APS [73, 233] and beamline ID16 of the ESRF [203]. The spectrum of SiO shows a featureless intensity increase in the energy range between 99 eV and 101 eV. Furthermore, an additional structure can be found at higher energy, which shows a shape very similar to that of SiO_2. Conclusively, the spectrum of SiO can be reproduced by a superposition of the spectra of Si and SiO_2 with an additional contribution between 103 eV and 106 eV, which is due to silicon sub-oxides [73, 233, 203]. Thus, new beamline P01 provides very good experimental conditions for prospective measurements on analogous samples concerning the energy resolution and the available flux, very promising for future experiments on more complicated samples.

6.3. Momentum transfer dependence of the Mg $L_{2/3}$-edge in MgO

Another very important low Z element involved in numerous minerals is magnesium [325, 8, 158]. Here, bulk sensitive measurements of the Mg $L_{2/3}$-edge (at about 49.50 eV, [287]) might be of major interest. Thus, feasibility tests of such measurements were performed at beamlines P01 (PETRA III, 1 hour acquisition time) and BL12XU

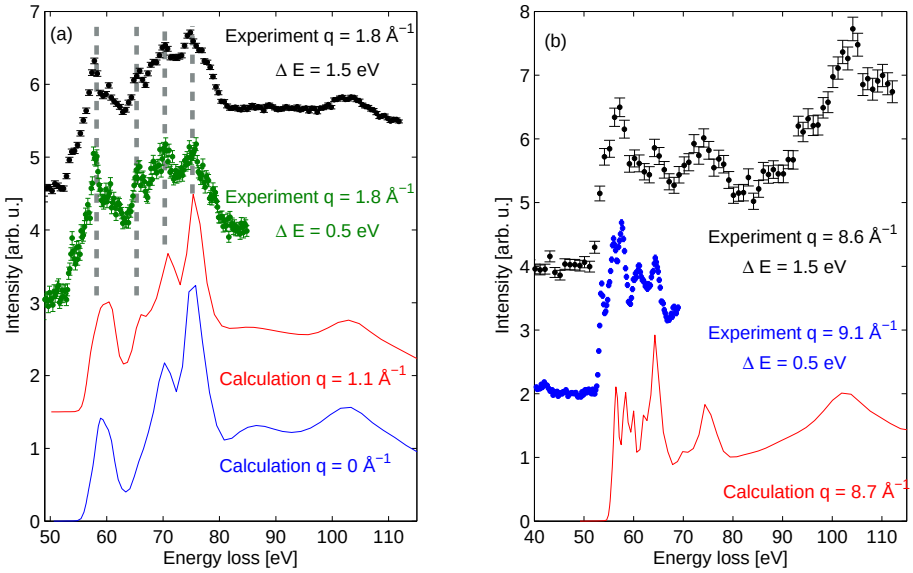

Figure 6.3.: Comparison between the Mg $L_{2/3}$-edge measurements on MgO at (a) low q and (b) high q as well as calculations using FEFF [223, 224]. The high resolution spectrum measured at high q was collected at beamline P01 (PETRA III) while the other spectra were obtained at beamline BL12XU (SPring-8).

(SPring-8, 2 hours acquisition time). The Mg $L_{2/3}$-edge spectra of MgO are presented in figure 6.3 for low q ($q = 1.7$ Å^{-1}) and high q ($q = 8.6$ Å^{-1} and $q = 9.1$ Å^{-1}) together with FEFF calculations at similar q. At low q the energy onset of the absorption edge can be found at about 54.8 eV and the spectrum shows sharp maxima at 57.8 eV, 65.8 eV, 70.4 eV, and 74.8 eV followed by a broad but weaker maximum at about 103 eV. A comparison between FEFF calculation for $q = 0.0$ Å^{-1} and $q = 1.1$ Å^{-1} show a weak but non negligible momentum transfer dependence. The experimentally obtained spectrum shows a very good agreement with the calculation for $q = 1.1$ Å^{-1} but the first peak after the edge onset is not reproduced. Furthermore, no significant variation between the spectra measured with an energy resolution of 0.5 eV and 1.5 eV can be observed. At high q the onset of the Mg $L_{2/3}$-edge can be found at about 53.0 eV, corresponding to an energy shift of 1.8 eV compared to low q, and the spectrum shows again several sharp maxima but at 53.6 eV, 56.0 eV, 57.6 eV 61.2 eV, and 64.4 eV. Additionally, a broad maximum

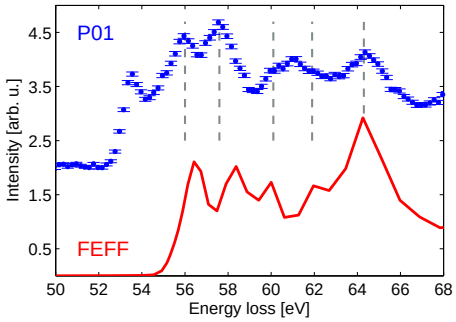

Figure 6.4.: Comparison between the Mg $L_{2/3}$-edge measured at beamline P01 with an energy resolution of $\Delta E = 0.5$ eV at $q = 9.1$ Å^{-1} and corresponding FEFF calculation.

can be found at about 104.1 eV. However, the spectrum measured with the energy resolution of 0.5 eV (figure 6.4) shows significantly more features compared to the spectrum obtained with the energy resolution of 1.5 eV, in contrast to the conclusion found at low q. The spectral shape of the calculated spectrum can be described by a series of sharp features at very similar positions as the experimental ones and only the maximum found at 53.6 eV in the experiment is missing in the calculation. Although the relative intensities of the features differ between the experiment and the calculation, a good general agreement between the experiment and theory can be found. Conclusively, measurements of the Mg $L_{2/3}$-edge at both high and low q reveal very detailed information about the local electronic structure of Mg, feasible with an energy resolution of 0.5 eV. Due to the spectrum rich on features, Mg $L_{2/3}$-edge might be a very sensitive tool in order to study the oxidation state and local coordination of Mg in compounds. The results obtained by XRS show a very good agreement with EELS data [133]. Future improvement of the theoretical model, e.g. using Bethe-Salpeter calculation, may provide a deeper insight into the local electronic structure of Mg in compounds [208] i.e. core hole (excitonic) effects that significantly influences the edge onset.

7. Determination of the oxidation state of iron using Fe $L_{2/3}$-edge X-ray Raman scattering spectroscopy

Measurements of the Fe $L_{2/3}$-edge is a widely used method to study the local electronic properties of iron in compounds. The binding energy of the 2p electrons is about 707 eV [287], depending on the compound. Thus, the Fe $L_{2/3}$-edge is easily accessible by several experimental techniques. Besides XMCD studies [250], numerous XAS and EELS investigations have been performed during the last decades to investigate the local atomic and electronic structure of several iron containing compounds relevant e.g. for geology [295, 83, 177], physics [55, 60, 119, 182, 150, 95], biology [304, 21], catalysis [113, 112, 114, 115], and materials science [32, 305]. The progress in data processing in order to extract the oxidation state of iron expressed by the quantity $Fe^{3+}/Fe_{tot.}$ will be summarized in the following.

The Fe $L_{2/3}$-edge is separated into the Fe L_3-edge at around 707 eV and the Fe L_2-edge at about 720 eV [283, 149, 216, 92]. The energy difference between the L_3- and L_2-edge is around 13 eV and is a result of the spin-orbit coupling, which splits the 2p states into $2p_{3/2}$ and $2p_{1/2}$ [295, 61]. The local chemical structure of iron can be studied by means of the position, shape, and energy splitting of the Fe $L_{2/3}$-edge. Due to very high impact of the local chemical environment of iron on its electronic structure, systematic studies of the Fe $L_{2/3}$-edge can be used as fingerprinting technique to identify the oxidation, coordination, and spin state of iron in a compound. However, measurements at geologically relevant conditions are rare. XAS and EELS cannot be applied due to the low energy of the probing radiation. Thus, XRS may be an alternative to measure the Fe $L_{2/3}$-edge at high pressure. Although the X-ray energy can be set to 10 keV or more, a significant fraction of the incoming radiation will be absorbed by the diamonds of a diamond anvil cell. Furthermore, the comparably high energy loss region, which has to be scanned to match the Fe $L_{2/3}$-edge, significantly reduces the cross section. Despite of all the experimental challenges XRS is the only experimental technique, which can be used to measure the Fe $L_{2/3}$-edge at geologically relevant conditions. Thus, the first step is to show the feasibility of such an experiment using samples with a high Fe content under normal conditions.

The experiment was performed at the beamline 20-ID-B of the synchrotron radiation source APS (see section 4.1 for more details). To demonstrate the impact of the oxidation state on the shape of the Fe $L_{2/3}$-edge, FeO and α-Fe_2O_3 were chosen as reference compounds for octahedrally coordinated Fe^{2+} ($^{[6]}$Fe2+) and Fe^{3+} ($^{[6]}Fe^{3+}$). Furthermore, Fe_3O_4 was used as an example for an iron containing sample with a mixed oxidation

state. XRS spectra were acquired for 2 hours (FeO) and 5 hours (α-Fe_2O_3 and Fe_3O_4), respectively, and were normalized to the intensity of the incoming radiation. Due to the negligible q-dependence, the signals of all 19 analyzer crystals were summed up to increase the statistical accuracy of the measurements. Subsequently, a constant background fitted to the pre-edge region was subtracted and the spectra were normalized to the integral intensity between 700 eV and 728 eV.

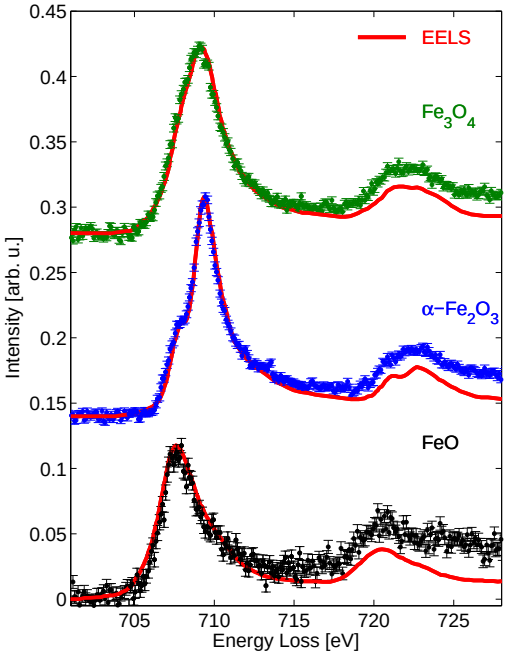

Figure 7.1.: First measurements of the Fe $L_{2/3}$-edge on FeO, α-Fe_2O_3, and Fe_3O_4 by XRS and comparison with EELS spectra reported in reference [43]. The spectra are shifted in the intensity for a better overview.

The resulting spectra are presented in figure 7.1. For a better comparison with EELS data [43], all XRS spectra were shifted by 0.3 eV to lower energy to match the peak positions of the Fe $L_{2/3}$-edge measured by EELS. The spectrum of FeO shows a strong asymmetric Fe L_3-edge with its maximum at 707.8 eV and its energy onset, corresponding to the inflexion point, at around 706.5 eV. The Fe L_2-edge shows an even more asymmetric shape with its maximum at about 720.4 eV and energy onset at 719.3 eV. The edge splitting due to spin-orbit coupling is 12.8 $\pm$ 0.2 eV, which is in good agreement with the value 12.9$\pm$0.2 eV found in reference [50]. A more precise description of the spectral features of the $L_{2/3}$-edge of FeO is difficult due to the statistical accuracy of the measurements. Significant modifications of the Fe $L_{2/3}$-edge can be observed with a change of the oxidation state of iron from $^{[6]}Fe^{2+}$ to $^{[6]}Fe^{3+}$. Here, the maximum of the Fe L_3-edge can be found at 709.5 eV. Additionally, a pre-edge feature, wich is clearly separated from the main maximum, can be found at around 708.0 eV. The spectral shape of the Fe L_2-edge can be described by a broad asymmetric feature with its maximum at around 723.1 eV. The inflexion points of the Fe L_3- and Fe L_2-edge are 707.1 eV and 720.3 eV, respectively. The splitting of the Fe $L_{2/3}$-edge of 13.2 $\pm$ 0.2 eV is in very good agreement with the value of 13.2$\pm$0.1 given in literature [50, 295]. The spectral shape of the Fe $L_{2/3}$-edge of Fe_3O_4 shows two characteristic maxima at the position of the Fe L_3- and Fe L_2-edge, respectively. The features show less structure compared to FeO and Fe_2O_3. However, the energy position of the spectral features of Fe_3O_4 cover the energy range where the absorption edges of both references can be found.

The results given above show the feasibility of bulk sensitive measurements of the Fe

$L_{2/3}$-edge on three different geologically relevant materials. For interpretation of the XRS spectra, they are compared with earlier EELS measurements. Calvert *et al.* performed a systematic EELS study of the Fe $L_{2/3}$-edge on numerous minerals, including wustite (FeO), hematite (α-Fe_2O_3) and magnetite (Fe_3O_4) [43]. A comparison between the EELS spectra by Calvert *et al.* and the XRS data is given in figure 7.1 showing a very good agreement between the results of both experimental techniques. Although the experimental resolution of the EELS spectra (ΔE = 0.7 - 0.8 eV) is slightly better compared to the energy resolution of the XRS experiment (ΔE = 1.0 eV), the EELS spectra exactly reproduce the spectral features of the XRS measurements in the energy region of the Fe L_3-edge for all samples. Small differences between the spectra can be found in the energy region of the Fe L_2-edge, which can be explained by the lower statistical accuracy of the XRS measurements. Stronger discrepancy between the EELS and XRS results can be observed regarding the intensity ratio between the Fe L_3-edge ($I(L_3)$) and the Fe L_2-edge ($I(L_2)$). While the normalized spectra overlap at the maximum of the L_3-edge, all L_2-edge spectra measured by EELS are less intense by up to 30 % (in the case of FeO). This difference might be a result of different background subtraction procedures applied to the EELS and XRS data, respectively. The background of the EELS spectra was simulated by a polynomial $A \cdot E^{-r}$ (A and r are fitting parameters), while only a constant background subtraction was performed for the XRS data. Despite of the small variation in the total intensity, the overall agreement between the EELS and the XRS spectra is very good. This is a surprising result considering the origin of the measurements. EELS measurements are usually performed under experimental conditions where the scattering angle, and thus the momentum transfer, is favorably minimized to increase the cross-section. This geometry restricts the electronic transitions, which mainly define the shape and position of the absorption edge, to the dipole transitions. In contrast, the whole solid angle can be used to detect the scattered intensity in an XRS experiment, thus allowing dipole forbidden transitions. The XRS spectra shown in figure 7.1 are an average over the whole solid angle range, corresponding to the momentum transfer range from 0.7 Å to 8.7 Å. The access to higher momentum transfer allows to distinguish between dipole and non-dipole transitions, which is a special feature of XRS [245, 274, 103]. However, despite of the average over a huge momentum transfer range, the spectral shape of the Fe $L_{2/3}$-edge shows a very good agreement with the dipole-like EELS measurements demonstrating the fact, that the contribution of the non-dipole excitations to the Fe $L_{2/3}$-edge is negligible even at high momentum transfer.
Despite of the experimental challenge, measurements of the Fe $L_{2/3}$-edge by XRS can be assumed as highly useful in order to study the oxidation state of iron in minerals. An overview of several algorithms to extract the oxidation state of iron in minerals is given in reference [43] and their advantages and limitations are discussed. Although numerous methods are applicable [169, 93, 295, 294], most of them have several common properties. The advantage of the Fe $L_{2/3}$-edge in terms of the data analysis is the fact, that its energy position is far away from the other excitations, e.g. valence band excitations, which can be found in the low energy loss region. Thus, background subtraction procedure is relatively straight forward minimizing the systematic error of the measurements. To obtain accurate results, the contribution of the p to d excitations must be separated

from the contribution of the excitations into the continuum states by using a double arctangent function [295, 43]. Subsequently, the white line intensity ratio between the Fe L_3- and the Fe L_2-edge ($I(L_3)/I(L_2)$) can be related to the $Fe^{3+}/Fe_{tot.}$ ratio of a mineral with an unknown oxidation state of iron. Additionally, two reference samples (Fe^{2+} and Fe^{3+}) should be measured for calibration purpose. Finally, different routines can be applied to the resulting spectra to calculate the $Fe^{3+}/Fe_{tot.}$ ratio. Garvie and Buseck [93] propose to use a superposition of the spectra of two references to model the spectrum of a mixed state compound [93]. This algorithm is restricted to the references, as well as minerals with unknown $Fe^{3+}/Fe_{tot.}$ ratio, with the same end members. Different end members might significantly affect the shape of the absorption edge thus revealing ambiguous results [43]. Van Aken *et al.* [295] use the double arctangent - background corrected spectra to calculate the integral intensity of the Fe L_3- and the L_2-edge of a sample assuming the $I(L_3)/I(L_2)$ fraction to be proportional to the $Fe^{3+}/Fe_{tot.}$ ratio [295]. Similar to the method of Garvie and Buseck, this method is also restricted to the use of references as well as unknown compounds with the same coordination of iron. A change of the coordination might lead to a shift of the maxima contributing to the absorption edge and the inflexion points of the double arctangent function would be at the wrong energy position, leading to inaccurate results. The next step to optimize the fitting procedure is to use the corrected spectra and to fit a series of analytical functions, e.g. Gaussian profiles, to fit the shape of the Fe $L_{2/3}$-edge. The position, relative intensity and the full width at half maximum of the single profiles contain information about the $Fe^{3+}/Fe_{tot.}$. This algorithm may be applicable to samples independent on the kind of end member and coordination [169, 294]. However, several profiles must be used to fit the Fe $L_{2/3}$-edge resulting in a comparable high number of free parameters.
The potential of the algorithms described above was substantially shown on the basis of EELS data and can also be used for the XRS spectra presented in figure 7.1. Due to the improvable statistical accuracy especially of the FeO reference sample, fitting of analytical functions to the maxima contributing to the Fe $L_{2/3}$-edge would not yield satisfying results due to a high number of free parameters. Thus, the algorithm developed by van Aken *et al.* [295] can be applied to the XRS spectra as an example in order to prove its potential to extract the $Fe^{3+}/Fe_{tot.}$ ratio using the XRS results.

After subtracting a constant background from the Fe $L_{2/3}$-edge of FeO, α-Fe_2O_3 and Fe_3O_4 a double arctangent function must be used to separate the 2p to 3d excitations from the continuum excitations. Therefore, the slope of the double arctangent-like function is set to 1, the inflexion points are fixed to 708.65 eV and 721.65 eV, according to the instructions given in [295]. Subsequently, the edge steps are fitted to the intensity difference between the pre- and post-edge of the L_3- and L_2-edge, respectively. An example of the background fitting procedure is shown in figure 7.2 (a). The background corrected spectra can be used to calculate the $I(L_3)/I(L_2)$ fractions for all samples. Here, van Aken *et al.* [295] propose to calculate $I(L_3)$ and $I(L_2)$ by integrating the spectral intensity within two energy windows with a width of 2 eV. Here, energy ranges from 708.5 eV to 710.5 eV and from 719.5 eV to 721.7 eV were found to be reasonable considering the positions of the respective maxima of the spectral intensity (see figute 7.2 (b)). Van Aken *et al.* [295] calculated the $I(L_3)/I(L_2)$ fractions as a function of the $Fe^{3+}/Fe_{tot.}$

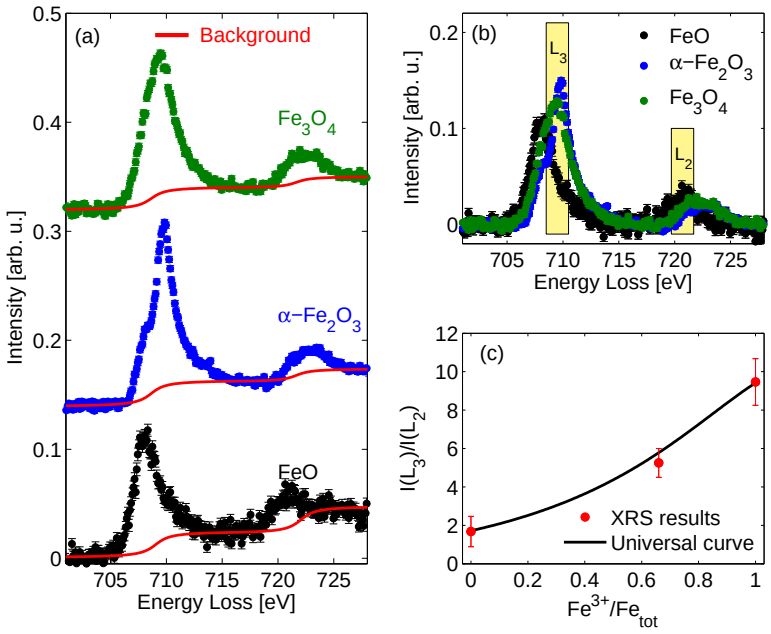

Figure 7.2.: (a): XRS spectra of FeO, α-Fe_2O_3, and Fe_3O_4 as well as a double arctangent background; (b): background corrected spectra with indicated integration ranges; (c): Calculated $I(L_3)/I(L_2)$ fractions as a function of the $Fe^{3+}/Fe_{tot.}$ ratio.

ratio for a series of samples with a systematic increase of the $Fe^{3+}/Fe_{tot.}$ ratio. Here, a polynomial relation was found, which is given by

$$\frac{I(L_3)}{I(L_2)} = \frac{1}{a \cdot x^2 + b \cdot x + c} - 1, \tag{7.1}$$

with $a = 0.183 \pm 0.011$, $b = -0.455 \pm 0.015$, and $c = 0.368 \pm 0.005$, x being the $Fe^{3+}/Fe_{tot.}$ ratio. Equation 7.1 can be used as a universal curve to determine the $Fe^{3+}/Fe_{tot.}$ ratio of an unknown compound by measuring the Fe $L_{2/3}$-edge and calculating the $I(L_3)/I(L_2)$ fraction. To prove the applicability of the universal curve by van Aken *et al.* [295] on XRS measurements, the $I(L_3)/I(L_2)$ fractions calculated for a priori characterized samples can be plotted as a function of the well known $Fe^{3+}/Fe_{tot.}$ ratio. The results can be found in figure 7.2 (c). Here, a good agreement between the quantities extracted from the XRS spectra and the universal curve can be found. The differences between the XRS and EELS measurements as a consequence of different background subtraction procedures as shown in figure 7.1 seem to be equalized by a subtraction of the contribution of the continuum excitations. Despite of the relatively large errorbars, the $I(L_3)/I(L_2)$ fractions calculated for the reference spectra for Fe^{2+} and Fe^{3+} fit very well to the universal curve. The $I(L_3)/I(L_2)$ fraction for the mixed state sample Fe_3O_4 can also be found on the universal curve within the calculated errorbar. The main contribution to a deviation compared to the universal curve is given by the composition of the Fe_3O_4, consisting of

$^{[6]}Fe^{2+}$, $^{[6]}Fe^{3+}$, and $^{[4]}Fe^{3+}$ with identical fractions. However, the universal curve was calculated on the basis where all samples contain different $Fe^{3+}/Fe_{tot.}$ ratios but with the same coordination [50]. Nevertheless, a very good overall agreement between the universal curve and the results on the basis of XRS measurements can be found.
In this section, first measurements of the Fe $L_{2/3}$-edge on three representative samples relevant for geological applications by XRS are presented. Although the statistical accuracy of the measurements must be improved to obtain quantitative results on the $Fe^{3+}/Fe_{tot.}$ ratios in unknown minerals, the feasibility of such measurements was shown. Furthermore, the efficiency of one possible algorithm to extract the $Fe^{3+}/Fe_{tot.}$ in minerals was successfully tested stressing the great potential of Fe $L_{2/3}$-edges measured by XRS for future applications in order to extract quantitative information about the oxidation state and local coordination of iron in minerals.

8. Quantitative determination of the oxidation state and local coordination of iron by Fe $M_{2/3}$-edge XRS spectroscopy

The potential of bulk sensitive XRS measurements in order to extract the oxidation state of iron in mixed compounds was shown on the example of the Fe $L_{2/3}$-edge in chapter 7. Here, changes of the oxidation state from Fe^{2+} to Fe^{3+} result in a shift of the absorption edge of around 1.5 eV. The strong edge shift allows very precise determination of the oxidation state of iron in unknown species. Furthermore, the Fe $L_{2/3}$-edge is known to be very sensitive on weak variation of the local coordination [60]. This sensitivity can be used to study the local environment of iron in unknown materials. A disadvantage of the Fe $L_{2/3}$-edge is the high binding energy of the 2p electrons of around 707 eV. Here, the scattering cross section drops with increasing energy loss leading to relatively low intensity. Although the feasibility of such measurements was successfully shown the counting time may increase dramatically if the Fe $L_{2/3}$-edge will be measured at extreme conditions using e.g. diamond anvil cell.
Here, measurements of the Fe $M_{2/3}$-edge (excitations from the 3p initial state into final d states) might be an adequate alternative. The binding energy of the 3p electrons is about 52.7 eV [287] and the cross section is comparably high [296]. Although the Fe $M_{2/3}$-edge can be routinely measured by XANES or EELS, systematic studies of materials using the Fe $M_{2/3}$-edge are very rare. The Fe $M_{2/3}$-edge shows strong changes related to the oxidation state [297, 296] but its shape is relatively broad and featureless due to the comparably high intrinsic broadening. Thus, in contrast to the changes of the oxidation state, strong changes of the local coordination result in very weak modifications of the absorption edge [56, 322]. Although the potential of the Fe $M_{2/3}$-edge measurements as a possible tool for quantitative extraction of the oxidation state of iron in compounds was already shown [296], systematic bulk sensitive studies of the Fe $M_{2/3}$-edge are very rare and have not been accomplished utilizing XRS, which can be used also at in-situ conditions.
In this chapter an algorithm for quantitative determination of the $Fe^{3+}/Fe_{tot.}$ ratio in iron compounds of unknown composition is presented. Due to the lack of comparable measurements first data treatment and background subtraction is exemplified in section 8.1. Furthermore, the contribution of dipole and non-dipole excitations to the total shape of the Fe $M_{2/3}$-edge is discussed in section 8.2. Subsequently, reference materials for the most prominent iron species for geological applications are studied and results are presented. The impact of the oxidation state and local coordination on the Fe $M_{2/3}$-edge and a novel approach to extract the $Fe^{3+}/Fe_{tot.}$ ratio in glasses will be discussed

in section 8.3 and 8.4, respectively. Finally, detection limits as well as limitations of the approach will be critically assessed in section 8.5. A summary of this chapter can be found in reference [204]

8.1. Data treatment and background subtraction

X-ray Raman scattering measurements are usually performed using high energy X-rays, typically at above 10 keV. Thus, several excitation processes contribute to the IXS spectrum, as discussed in section 2.3. Representative q dependent IXS measurements are presented in figure 2.2 where all excitation processes involved in an IXS spectrum are shown. Usually, an absorption edge is strongly overlapped by the contribution of the electron-hole pair or plasmon excitations (low q) and Compton scattering (high q). Within the XRS regime these excitation can be assumed as background, which must be separated from the absorption edge. Due to the fact, that in a real spectrum the intensity of the background scattering can be higher by several orders of magnitude compared to the intensity of the absorption edge, the background subtraction procedure must be performed very carefully. Here, the background can be approximated by an analytical function and its contribution must be subtracted from the XRS spectrum [274, 76]. Alternatively, the background must be estimated based on theoretical calculations. In any case, a critical assessment of the background subtraction procedure must be done. Otherwise, it will remain unclear whether the spectral changes of the absorption edge result from direct changes of the electronic levels to be studied or from the change of the background. This point gains special importance if measurements at high pressure are performed using a DAC. Here, the scattering on diamonds significantly contributes to the background scattering, which may show a pressure dependence. To clarify the impact of the background scattering to the total IXS spectrum, the variation of the energy loss spectrum of α-Fe_2O_3 with momentum transfer is shown in figure 8.1. The spectra measured for

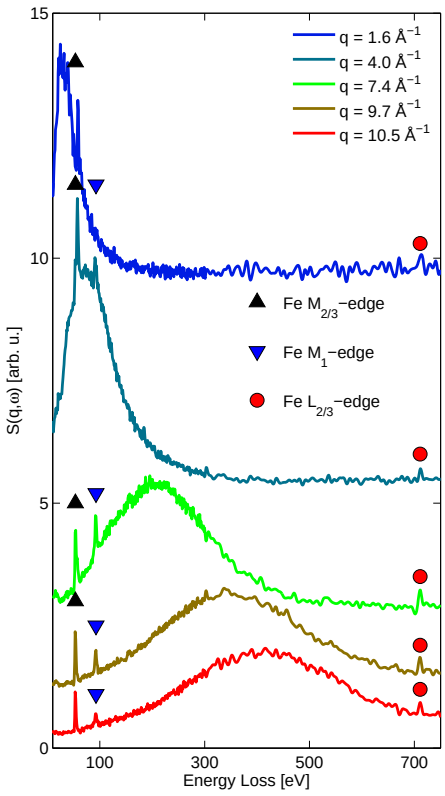

Figure 8.1.: Wide energy loss scans of α-Fe_2O_3 for selected momentum transfers demonstrating momentum transfer dependence of the background.

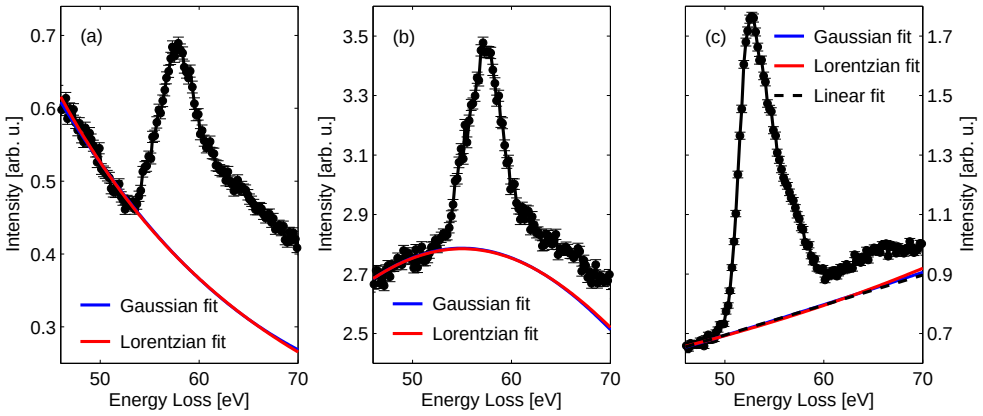

Figure 8.2.: Comparison between different background subtraction procedures for (a) $q = 1.57$ Å^{-1}, (b) $q = 3.1$ Å^{-1} and (c) $q = 7.62$ Å^{-1} on the example of FeO XRS spectra [204].

all momentum transfers can be characterized by more or less intensive, narrow maxima at around 711 eV and 92 eV corresponding to the Fe $L_{2/3}$-edge and Fe M_1-edge, respectively. In addition, a third maximum can be found at different q-dependent positions between 53 eV and 58 eV, corresponding to the Fe $M_{2/3}$-edge. The absorption edges are strongly overlapped by background scattering, which changes with q. At $q = 1.6$ Å^{-1} the background scattering contribution can be described by an asymmetric maximum. Here, the Fe $M_{2/3}$-edge can be found at the right tail of the electron-hole excitation spectrum with a rather complicated shape and the intensity of the background scattering is almost 1.5 times higher than the intensity of the XRS signal. At $q = 4.0$ Å^{-1} the background spectrum becomes slightly broader and less intensive but its spectral shape becomes more complicated. Furthermore, the XRS signal in the low energy loss region can be found exactly on the top of the background contribution. In this case, background subtraction might be significantly more difficult, as discussed by Sternemann *et al.* [274]. Here, the origin of the spectral features of the Fe $M_{2/3}$-edge, which might be mixed with the spectral shape of the background scattering, is unclear. With increasing q the contribution of the background scattering becomes wider but less intense. For $q = 7.4$ Å^{-1}, $q = 9.7$ Å^{-1}, and $q = 10.5$ Å^{-1} the Fe $M_{2/3}$-edge can be found on the left tail of the Compton profile, which is the dominating spectral feature at high momentum transfers. Thus, the Fe $M_{2/3}$-edge spectrum becomes less influenced by the background scattering with increasing q. At the highest q the intensity of the Fe $M_{2/3}$-edge is higher by a factor of 3.3 compared to the background intensity.

For a reliable background subtraction the q-dependence of the XRS spectra can be separated in three regions: (I) at low q the absorption edge to be measured can be found at the right tail of the intense electron-hole excitation spectrum. The absorption edge should be far enough from the background maximum such a way that the spectral shape of the XRS signal is not significantly affected by background features. Here, the background can be simulated either by a Gaussian [76] or by a Lorentz function [274]; (II)

At intermediate q, where the absorption edge can be found close to the top of the background peak, systematic background approximation is challenging. The shape of the background is rather complicated and approximation by an analytical function is difficult [274]; (III) At high q the background is dominated by Compton scattering and the absorption edge can be found on the left tail of the background maximum, which becomes wider and shifts to higher energy with increasing q. Here, the background can be simulated using Gaussian function. Another background subtraction approach is proposed by Sternemann *et al.* [274]. Here, theoretical Hartree-Fock calculations of the Compton profile [26] can be used and directly subtracted from the spectra. This routine reveals reasonable results on the example of the q-dependence of the Si $L_{2/3}$-edge [274]. The result of different background subtraction procedures is shown on the example of the Fe $M_{2/3}$-edge of FeO at $q = 1.57$ Å^{-1}, $q = 3.1$ Å^{-1}, and $q = 7.62$ Å^{-1} representative for low, intermediate, and high q, respectively. Figure 8.2 (a) compares background simulation by a Gaussian and a Lorentzian function fitted to the pre-edge region of the low q spectrum. Both background functions show a very similar shape and only minor variations can be found at energy loss values close to 70 eV. This result manifests the fact that both Gaussian and Lorentzian background are reasonable if only a short energy loss region of some tenths of eV is the point of interest. A similar result can be obtained for the intermediate q presented in Figure 8.2 (b). Figure 8.2 (c) shows the same procedure for a high q spectrum. Here, similar trend using the Gaussian and Lorentzian background approximation can be observed. Additionally, a linear background can be used.

8.2. Momentum transfer dependence of the Fe $M_{2/3}$-edge

The momentum transfer dependence of the Fe $M_{2/3}$-edge was studied for the reference compounds FeO and α-Fe_2O_3 representative for $^{[6]}Fe^{2+}$ and $^{[6]}Fe^{3+}$, respectively. A detailed information about the samples used for this experiment is given in section 5.1. The experiment was performed at beamline PNC/XSD 20-ID of the Advanced Photon Source (see chapter 4.1 for more information). The q-dependent spectra were background corrected by fitting a Gaussian function to the pre-edge region. The resulting spectra for a large q-range from 0.8 Å^{-1} to 10.0 Å^{-1} are presented in figure 8.3 (a)-(c) showing clear differences between Fe^{2+} and Fe^{3+} in the energy region from 54 eV to 60 eV as well as a strong q dependence. For $q < 2$ Å^{-1} the spectrum of FeO is dominated by a strong maximum at 58 eV and a pre-edge maximum at 55 eV. In contrast, the spectrum of α-Fe_2O_3 shows only one maximum at about 58 eV and a weak pre-edge maximum at 52.6 eV. Thus, significant differences of the spectral shape between Fe^{2+} and Fe^{3+} can be observed at low q, in the dipole limit ($k = 1$ in equation 2.17). Significant spectral changes occur with increasing q and thus increasing contribution of octupole transitions ($k = 3$). The changes manifest in an intensity increase in the energy region below 55 eV and a weaker edge jump, which can be related to a weaker contribution of continuum excitations. The spectra hardly change for large q. Here, the spectrum of FeO shows a strong asymmetric maximum at 52 eV with a weaker shoulder at higher energy loss.

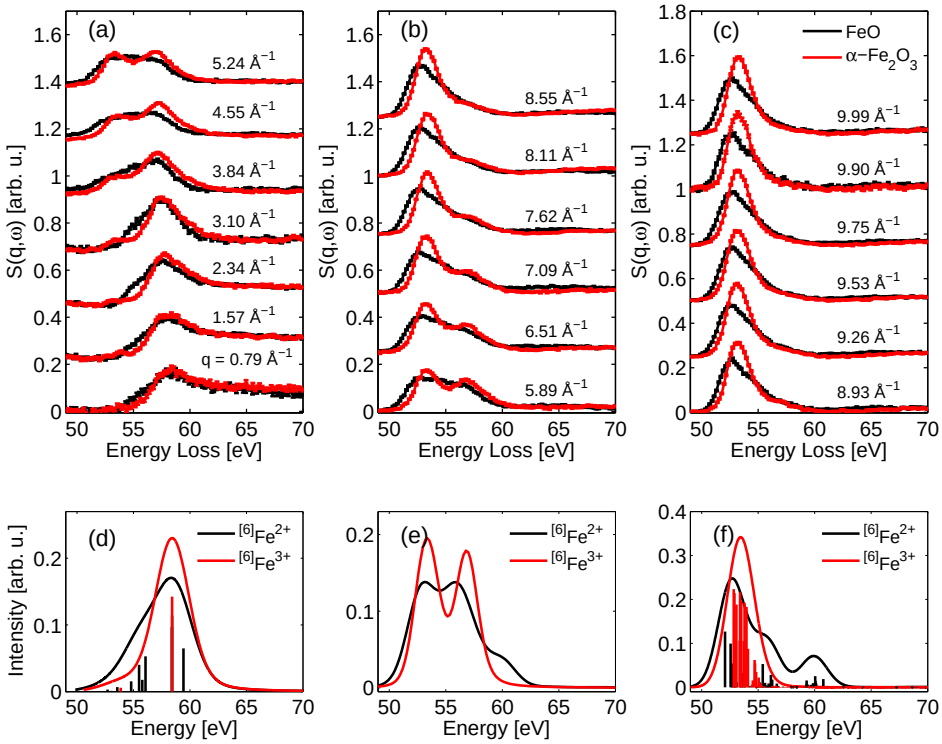

Figure 8.3.: Momentum transfer dependent measurements of the Fe $M_{2/3}$-edge of $^{[6]}Fe^{2+}$ (FeO) and $^{[6]}Fe^{3+}$ (α-Fe_2O_3) in q-ranges (a) 0.8-5.2 Å^{-1}, (b) 5.9-8.5 Å^{-1}, (c) 8.9-10.0 Å^{-1} in comparison with calculations for (d) dipole and (f) ocupole transitions. In addition, a 1:1 superposition of dipole and octupole transitions is presented for both $^{[6]}Fe^{2+}$ and $^{[6]}Fe^{3+}$ in order to model the Fe $M_{2/3}$-edge at intermediate q [204].

The spectrum of Fe_2O_3 again shows a peak at 53.5 eV and a weak second maximum at 57 eV.

Atomic multiplet calculations in the dipole limit ($k = 1$) [297] including crystal field effects [56, 57] were performed using the CTM4XAS package [267]. Moreover, calculations of the octupole contribution ($k = 3$) were carried out by S. Huotari[1] and Ch. J. Sahle[2] on the basis of the Cowan code included into the CTM4XAS package. All spectra were calculated using the same crystal field parameters as reported by de Groot (*et al.*) [60], but the Slater-Condon parameters were reduced to 64% of their atomic values to get a better agreement with the experimental data. The spin-orbit coupling was set to zero [287]. For a better comparison with the experiment the calculated transition pattern was convoluted with a Gaussian (FWHM of 1.5 eV) and a Lorentzian (FWHM of 0.6 eV) function in order to match the experimental resolution and the natural broadening

[1]S. Huotari, Department of Physics, University of Helsinki, P.O. Box 64, 00014 Helsinki, Finland
[2]Ch. J. Sahle, European Synchrotron Radiation Facility, 38043 Grenoble Cedex, France

of the spectra [84]. The spectra of Fe^{2+} and Fe^{3+} calculated for $k = 1$ and $k = 3$ are presented in figure 8.3 (d) and (f). All spectral features of the experimental results are adequately resembled by the calculation except of the calculated high energy loss maximum for $k = 3$, which is overestimated in case of $^{[6]}Fe^{2+}$ and is missing for $^{[6]}Fe^{3+}$. Although the overall agreement between the experiment and theory is remarkable, the atomic multiplet model is only a first order approximation for calculation of the spectrum of a solid. The theoretical results show that high q spectra are strongly dominated by $k = 3$ transition while low q spectra can be well reproduced by $k = 1$ calculations. Especially the low q features appear slightly broader in the experiment, which might be due to the fact, that continuum excitations are not considered into the calculations [229, 252]. The intermediate q spectra are well represented by a linear superposition of spectra calculated for $k = 1$ and $k = 3$ in a certain fraction. Here, e.g. the spectral shape of the measurement at $q = 5.89$ Å^{-1} can be well reproduced by a 1:1 superposition of $k = 1$ and $k = 3$ spectra for both Fe^{2+} and Fe^{3+} as indicated in figure 8.3 (e).
The understanding of the q-dependence of the Fe $M_{2/3}$-edge has two major implications on further studies. Both the experimental and the theoretical results show a strong sensitivity of the Fe $M_{2/3}$-edge at high and low momentum transfer. However, the spectral features indicative for the oxidation state are better resolved at high momentum transfer. Furthermore, the q-dependence becomes negligible for $q > 9$ Å^{-1}. Due to the absence of the q-dependence, several spectra collected at different but sufficiently high q can be summed up, which dramatically increases the statistical accuracy of the spectra.

8.3. Impact of the oxidation state and local coordination on the Fe $M_{2/3}$-edge

Knowledge about the momentum transfer dependence of the XRS spectra is crucial in order to optimize challenging measurements of the Fe $M_{2/3}$-edge. However, measurements presented above reveal momentum transfer regions, where the spectra are dominated either by dipole or by octupole excitations. The spectra in the intermediate q range, where both dipole and octupole contributions can be found, are difficult to analyze. Furthermore, this q range overlaps with the momentum transfer region, where the XRS signal can be found rather on top of the very intense background scattering and reliable background subtraction is challenging. Thus, characterization of unknown iron containing species should be performed at $q \leq 2$ Å^{-1} (low q) or $q \geq 9$ Å^{-1} (high q). Momentum transfer dependent measurements of samples with different oxidation state of iron show clear spectral differences resulting either in an additional pre-peak in the Fe^{2+} spectrum at low q or in a significantly broader and more asymmetric main maximum for the same sample at high q compared to Fe^{3+}. However, geologically relevant iron containing species may differ not only in their oxidation state but also in their local coordination. Therefore, the impact of the local coordination on the shape of the Fe $M_{2/3}$-edge of Fe^{2+} and Fe^{3+} in octahedral and tetrahedral coordination will be studied at low and high q in the following.

Fe $M_{2/3}$-edge measurements were performed at two selected q values of 2.1 Å^{-1} and 9.1

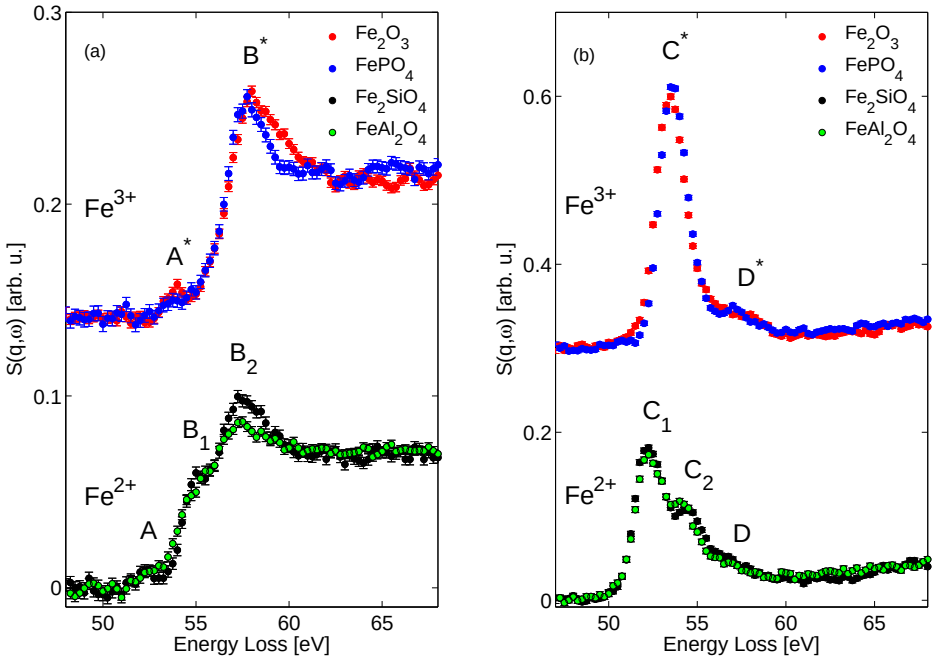

Figure 8.4.: High resolution measurements of the Fe $M_{2/3}$-edge of $^{[6]}Fe^{2+}$ (Fe_2SiO_4), $^{[4]}Fe^{2+}$ ($FeAl_2O_4$), $^{[6]}Fe^{3+}$ (α-Fe_2O_3) and $^{[4]}Fe^{3+}$ ($FePO_4$) at (a) $q = 2.1$ Å^{-1} and (b) $q = 9.1$ Å^{-1} [204].

Å^{-1} at beamline ID16 of the European Synchrotron Radiation Facility. Experimental details are given in section 4.2. The energy resolution was 0.7 eV, which is close to the natural broadening of the spectral features of 0.6 eV [84]. Lorentzian and linear background subtraction were applied to low and high q spectra, respectively. Four different compounds, namely Fe_2SiO_4, $FeAl_2O_4$, α-Fe_2O_3 and $FePO_4$, representative for $^{[6]}Fe^{2+}$,$^{[4]}Fe^{2+}$,$^{[6]}Fe^{3+}$,$^{[4]}Fe^{3+}$, respectively, were measured. The resulting spectra are presented in figure 8.4. The spectra measured at low q (a) and high q (b) confirm the spectral changes due to the oxidation state discussed in section 8.3, but more spectral features could be resolved due to improved energy resolution. The spectral shape of the Fe $M_{2/3}$-edge of the $^{[6]}Fe^{2+}$ species at low q (figure 8.4 (a)) can be characterized by two maxima at 54.5 eV and 57.3 eV (features B_1 and B_2). Additionally, a weak pre-feature at 52.8 eV (feature A) can be observed. The Fe $M_{2/3}$-edge of the $FeAl_2O_4$ sample containing 85% $^{[4]}Fe^{2+}$ shows a very similar spectral shape compared to $^{[6]}Fe^{2+}$, but the features B_1 and B_2 appear broader and shifted by about 0.2 eV to higher energies. Moreover, the pre-edge feature A is less pronounced. The results conclude small but distinct coordination related spectral differences of the Fe $M_{2/3}$-edge between octahedrally and tetrahedrally coordinated iron in Fe_2SiO_4 and $FeAl_2O_4$.
The spectra of Fe^{3+} with octahedral and tetrahedral coordination can be characterized by a strong excitation maximum B* and a weak pre-edge feature A*. In the case of $^{[6]}Fe^{3+}$

B* can be found at 58.0 eV and A* at about 53.5 eV. In the case of $^{[4]}Fe^{3+}$ a sharper main peak B* can be observed together with a broader and weaker pre-edge features A*. The spectral features observed for $^{[4]}Fe^{3+}$ are in good agreement with XAS results obtained for $FePO_4$ [322]. Conclusively, strong spectral changes for different oxidation states could be observed, but only small but distinct changes due to local coordination could be found. Thus, determination of the local coordination might be difficult at low q.

The spectral shape of the Fe $M_{2/3}$-edge changes completely at high q. The spectra of the octahedral and tetrahedral Fe^{2+} can be described by a strong maximum C_1 at 52.3 eV and a second maximum C_2 at 54.0 eV. Furthermore, a weak but comparably broad maximum D appears in the higher energy loss region. The spectra do not reveal strong differences due to different coordination.

The high q spectra of Fe^{3+} compounds (figure 8.4 upper right) exhibit a strong maximum C* at 53.5 eV accompanied by a weak but broad shoulder D*. The energy position of the main excitation maximum C* corresponds to the energy position of the weak pre-edge feature A* in the low q spectra of Fe^{3+} compounds, while the energy position of the weak shoulder D* (57.5 eV) is very similar to the position of the main excitation maximum B*. Thus, the pre-edge feature A* of the low q spectra might originate from the weak but not negligible contribution of octupole transitions to the low q spectra, which are dominated by dipole positions. Similarly, the weak maximum D* in high q spectra might be the result of a weak contribution of dipole excitations to the high q spectra, which are dominated by octupole transitions.

The remarkable spectral differences of the Fe $M_{2/3}$-edge according to the oxidation state of iron could be reproduced by high resolution measurements. At low q the main excitation maxima B_2 for Fe^{2+} and B* for Fe^{3+} can be found almost at the same energy position. However, the relative intensity of the pre-edge maximum B_1 is about 55 % in the case of Fe^{2+} while such a feature is absent for Fe^{3+}. This result can be used in order to determine the $Fe^{3+}/Fe_{tot.}$ ratio in unknown samples, as proposed by van Aken *et al.* [296]. At high q the spectral shape of the absorption edge changes dramatically but the main trends are similar. While the spectra of Fe^{2+} can be described by a twin-peak structure, the single maximum of Fe^{3+} can be found at energy transfer values right between the both Fe^{2+} peaks. These spectral differences can be used in order to study the oxidation state of iron in minerals at high q.

In contrast to the oxidation state effects, the coordination leads to weaker modifications of the spectral shape of the Fe $M_{2/3}$-edge. At low q, the difference of the coordination from octahedral to tetrahedral manifests in a weak energy shift of about 0.2 eV for Fe^{2+} while the spectral features B_1 and B_2 become broader in the case of the tetrahedral coordination. For Fe^{3+} the changes due to the coordination can be described by a broader main excitation maximum B* and a more pronounced pre-edge feature A*. Especially the interpretation of the pre-edge feature A* is very difficult. This maximum can become broader and less intensive if the octahedra in Fe^{3+} become distorted [322]. Hence, measurements with improved statistics and energy resolution are required in order to adequately resolve feature A*. In contrast, the spectral features at high q become very sharp, intense and thus very distinct. This is possibly due to the fact, that the contribu-

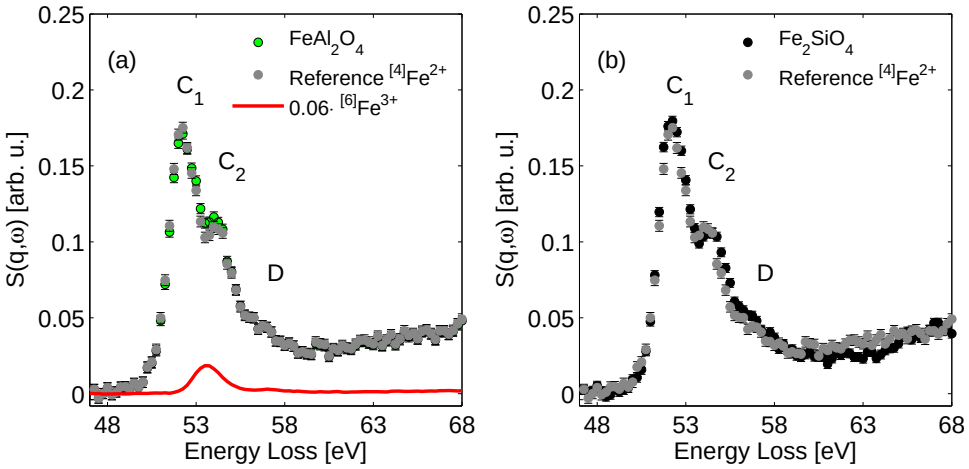

Figure 8.5.: (a) Correction scheme of the $FeAl_2O_4$ spectrum by 6% of Fe^{3+} and a comparison between the original and the corrected $^{[4]}Fe^{2+}$ reference spectrum [204]. (b) Comparison between the corrected $^{[4]}Fe^{2+}$ and Fe_2SiO_4 spectra.

tion of continuum excitations is significantly weaker compared to low q and coordination effects are at least the same strong as at low q. The coordination effects may be described by an energy shift of around 0.25 eV between the octahedral and tetrahedral coordination for Fe^{3+}. In the case of Fe^{2+}, the feature C_2 is slightly shifted to lower energy loss values for $FeAl_2O_4$ compared to Fe_2SiO_4.
Based on the results revealed by high resolution measurements of the Fe $M_{2/3}$-edge by XRS, measurements at high q might be preferable in order to determine the $Fe^{3+}/Fe_{tot.}$ ratio in unknown samples. Here, the spectral features are stronger and sharper while changes according to the oxidation state and coordination are similar as for low q. However, an important advantage of high q measurements is the comparably low momentum transfer dependence for $q \geq 9$ Å^{-1}, where the spectra collected at different q can be summed up reducing the acquisition time significantly. Thus, measurements performed on reference compounds Fe_2SiO_4, $FeAl_2O_4$, α-Fe_2O_3 and $FePO_4$ at high q can be used as standards for determining the $Fe^{3+}/Fe_{tot.}$ in unknown minerals.
It should be recalled, that the $FeAl_2O_4$ sample contains about 6% of $^{[6]}Fe^{3+}$. Thus, the spectrum of α-Fe_2O_3 weighted by 0.06 can be subtracted from the $FeAl_2O_4$ spectrum in order to obtain a corrected $^{[4]}Fe^{2+}$ reference. The resulting spectrum in comparison with the original $FeAl_2O_4$ spectrum is presented in figure 8.5 (a). Here, a weak intensity decrease of the maximum C_2 can be observed. Although the subtraction of the Fe^{3+} contribution does not modify the shape of the Fe $M_{2/3}$-edge, the spectral shape is now close to that of $^{[6]}Fe^{2+}$ demonstrating only subtle spectral differences between the both coordination states (see figure 8.5 (b)).

8.4. Quantitative determination of the iron oxidation state in glasses

In this section, an approach will be presented, which allows to obtain quantitative information about the oxidation state and coordination of iron in minerals. Therefore, three glasses (RB0-1, AOQ2, and RBO-4) with different $Fe^{3+}/Fe_{tot.}$ ratios ranging from 0.1 to 0.9 were prepared as discussed in section 5.1. Measurements of the Fe $M_{2/3}$-edge were performed at beamline P01 of the synchrotron radiation facility PETRA III at the same q as the references presented above. The energy resolution was 0.5 eV and the spectra were convoluted with a Gaussian function (0.6 FWHM) in order to match the energy resolution of the references of 0.7 eV.
The spectra measured on the glasses are presented in figure 8.6. In comparison with the spectra of references, which can be found in figure 8.4, the Fe $M_{2/3}$-edge of RB0-1 and AOQ2 show a similar shape compared to the Fe^{3+} references while the RB0-4 spectrum is comparable to those of Fe^{2+} references. Due to strong multiplet effects, the Fe $M_{2/3}$-edge is not significantly overlapped by absorption edges of other light elements contained in the sample, e.g. the Mg L-edge in the RB0 glasses at about 50 eV.
In order to extract quantitative information about the oxidation state and coordination of iron in glasses a linear superposition of the reference samples presented in section 8.3, including the spectra of $^{[6]}Fe^{2+}$, $^{[4]}Fe^{2+}$, $^{[6]}Fe^{3+}$, and $^{[4]}Fe^{3+}$, were fitted to the glass spectra. For this purpose, three different fitting strategies were used:

- (I): In order to extract the $Fe^{3+}/Fe_{tot.}$ ratios of glassy samples spectra of $^{[6]}Fe^{2+}$ and $^{[6]}Fe^{3+}$ will be used as references.
- (II): In the next step only $^{[4]}Fe^{2+}$ and $^{[4]}Fe^{3+}$ references will be used.
- (III): All references will be taken into account.

The fit results can be found in figure 8.6. Although the general shape of the absorption edges of glasses are well reproduced by all fitting strategies, strategy (I) seems to show a better agreement in the case of RB0 glasses rather than (II), while the spectrum of AOQ2 is better reproduced by strategy (II), as can be determined from the coefficients of determination R^2. This result indicates that octahedral coordination of iron is preferred for the RB0 glasses, while tetrahedral coordination is preferred in the case of AOQ2.
The extracted $Fe^{3+}/Fe_{tot.}$ ratios are presented in table 8.1 together with the coefficients of determination for each fit, which allows to make a quantitative description of the agreement between the experimental data and the fits. Furthermore, results of the sample characterization by Mössbauer spectroscopy are shown. The XRS results slightly differ from those obtained by Mössbauer spectroscopy depending on the fitting procedure. The $Fe^{3+}/Fe_{tot.}$ ratios in glasses obtained on the basis of fitting routine (I) show a good agreement with Mössbauer spectroscopy results for the RB0-glasses with respect to the errorbars but the $Fe^{3+}/Fe_{tot.}$ ratio of AOQ2 is overestimated by about 10%. In contrast, the $Fe^{3+}/Fe_{tot.}$ ratios of AOQ2 and RB0-4 are very close to the value obtained by Mössbauer spectroscopy but the $Fe^{3+}/Fe_{tot.}$ ratio of RB0-1 is significantly underestimated. Procedure (III) reveals the best $Fe^{3+}/Fe_{tot.}$ ratios for all glasses compared to

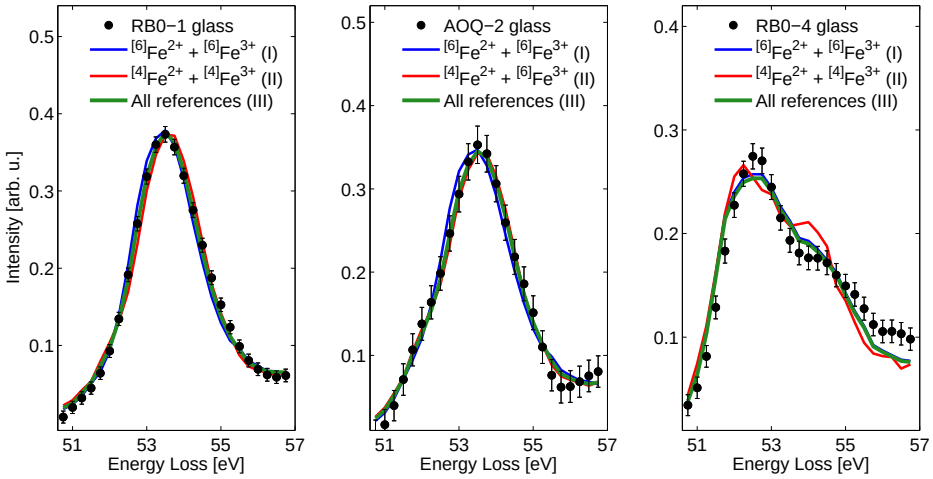

Figure 8.6.: Fe $M_{2/3}$-edge measured on glasses RB0-1 (left), AOQ2 (center), and RB0-4 (right) together with fit results using three different approaches [204].

the results by Mössbauer spectroscopy. Assuming the fact, that the $Fe^{3+}/Fe_{tot.}$ ratio of the RB0-4 glass, which is dominated by Fe^{2+}, is reproduced well by all fitting strategies, the coordination of Fe^{3+} in glasses has a significant impact on the $Fe^{3+}/Fe_{tot.}$ ratio, that can be determined by a linear superposition of reference samples in general. Thus, use of all four references plays a key role in order to obtain reliable $Fe^{3+}/Fe_{tot.}$ ratios in unknown minerals.

	RB0-1 (R^2)	AOQ-2 (R^2)	RB0-4 (R^2)
$Fe^{3+}/\sum$Fe XRS (I)	0.89±0.01 (0.9890)	0.73±0.04 (0.9780)	0.18±0.02 (0.9274)
$Fe^{3+}/\sum$Fe XRS (II)	0.74±0.05 (0.9884)	0.61±0.04 (0.9880)	0.14±0.04 (0.8561)
$Fe^{3+}/\sum$Fe XRS (III)	0.82±0.03 (0.9964)	0.69±0.05 (0.9911)	0.18±0.01 (0.9291)
$Fe^{3+}/\sum$Fe Mössbauer	0.83±0.04	0.63±0.04	0.16±0.04

Table 8.1.: $Fe^{3+}/Fe_{tot.}$ ratios extracted from XRS measurements [204].

8.5. Detection limits and summarizing remarks

In this chapter the feasibility of Fe $M_{2/3}$-edge measurements in iron containing compounds was presented. Furthermore, the momentum transfer of the Fe $M_{2/3}$-edge was discussed in detail for reference samples. The spectral shape of the Fe $M_{2/3}$-edge can be reproduced by q-dependent fraction of dipole and octupole transitions. Subsequently, high resolution measurements were used in order to discuss the impact of different spectral features of the Fe $M_{2/3}$-edge and their dependence on the oxidation state of iron and its local coordination. Therefore, remarkable sensitivity of the Fe $M_{2/3}$-edge could be

found on the oxidation state resulting in an energy shift of the absorption edge of more than 2 eV. Coordination has a weaker impact on the spectral shape of the Fe $M_{2/3}$-edge of Fe^{2+} but an energy shift of 0.2 eV can be observed between tetrahedral and octahedral coordination of Fe^{3+}. Together with the fact, that spectral features in general are sharper and stronger at high q, spectra collected at $q \geq 9$ Å^{-1} can be summed up increasing the statistical accuracy of the measurements. Thus, Fe $M_{2/3}$-edge measured at high q can be used for a quantitative determination of the $Fe^{3+}/Fe_{tot.}$ ratio and the local coordination of iron in unknown species. It was shown, that coordination effects have an impact on the determined $Fe^{3+}/Fe_{tot.}$ ratios. A linear superposition of reference spectra measured on Fe^{2+} and Fe^{3+} standards, both with octahedral and tetrahedral coordination, reveals the best agreement between the fit and the experimental data. The extracted $Fe^{3+}/Fe_{tot.}$ ratio agrees well with the results by Mössbauer spectroscopy. Here, especially the coordination of Fe^{3+} fraction significantly affects the extracted $Fe^{3+}/Fe_{tot.}$ ratios. Thus, this method can be used to quantitatively obtain not only the $Fe^{3+}/Fe_{tot.}$ ratios in unknown minerals but possibly also the coordination of iron in different phases, which contribute to the glass structure. It should be stressed, that this fitting procedure applied on Fe $M_{2/3}$-edges provides a unique tool in order to study the oxidation state of iron and its coordination in geologically relevant minerals bulk sensitively and even using high pressure diamond anvil cell or laser heating, where other experimental techniques cannot be applied.

Despite of all advantages the results obtained by the procedure presented above must be critically assessed. Although the fitting procedure reveals very satisfying results, which have been compared with Mössbauer spectroscopy, the statistical accuracy of the measurements must be improved to reduce the systematic uncertainty of the results. Furthermore, the energy resolution should be improved in order to get quantitative results about the local coordination of iron. The measurements used for this thesis were performed on samples with a comparably high iron amount, which allows to establish the procedure for quantitative determination of the $Fe^{3+}/Fe_{tot.}$ ratio. However, this technique must be tested using samples with the iron amount of natural minerals, which are of greater interest for geological applications. One more criticism of the method presented above is the use of both octahedral and tetrahedral Fe^{2+} and Fe^{3+} references, which automatically excludes the presence of other species. Although the most geologically relevant species are dominated by iron with octahedral or tetrahedral coordination, also a presence of five-fold coordinated species with trigonal bipyramidal symmetry has been proposed [225, 90, 67], but their existence in glasses as well as their relative contribution to the structure of glass is still under discussion. The question how such species can be included into the coordination determination procedure cannot be answered at this point. However, measurements of the Fe $M_{2/3}$-edge by XRS provide a unique tool for a bulk sensitive determination of the local chemical structure of iron in minerals with respect to experimental constrains discussed above.

9. Pressure induced high-spin to low-spin transition in FeS

The application of the Fe $M_{2/3}$-edge measurements by XRS in order to obtain quantitative results about the oxidation state and local coordination of iron in unknown geologically relevant compounds was presented in chapter 8. The high sensitivity of the Fe $M_{2/3}$-edge can be used e.g. for studies of iron partitioning or melting. However, for numerous geological or geochemical in-situ studies the spin state of iron must be revealed. Usually, X-ray diffraction [266], X-ray absorption spectroscopy [196], Mössbauer spectroscopy [177] or fluorescence spectroscopy [174] are used in order to obtain such information. However, these experimental techniques have several limitations concerning their sensitivity or sample treatment and data interpretation is often not unambiguous. Thus, direct investigation of the spin state or even the spin transition in general is still controversially discussed [215, 16]. In this chapter, the sensitivity of the Fe $M_{2/3}$-edge on the spin state of iron is studied. The bulk sensitivity of XRS measurements combined with the new generation high energy setup of the beamline BL12XU installed at the synchrotron radiation facility SPring-8 provides a unique possibility to perform a systematic pressure dependent study of the Fe $M_{2/3}$-edge on FeS in-situ at high pressure, not feasible so far. The diamond anvil cell used for the high pressure experiment is presented in section 9.1 followed by a discussion of spin state dependent spectral features of the Fe $M_{2/3}$-edge in section 9.2. Furthermore, a quantitative approach will be proposed in section 9.3 employing atomic multiplet and crystal field calculations in order to obtain quantitative information about the crystal field splitting 10Dq, the central parameter to describe the spin transition mechanism. Final discussion of the results is given in section 9.3. A summary of the results presented in this chapter can be alternatively found in reference [205]

9.1. High pressure diamond anvil cell

The mechanism in order to expose a sample to high pressure is based on the principle applying very high force on a very small area. The pressure should be transferred to the sample by a material with the highest hardness possible. Thus, polished diamonds trapped between two plates made of stainless steel are frequently used in diamond anvil cells (DAC), where a thin sample is placed between two diamonds. To ensure that the sample remains between the diamonds while pressure is applied, the sample material is filled into the gasket hole, while the gasket, along with the sample, is pressed by the diamonds. The pressure can be tuned by tightening the screws of the outer stainless steel plates and the force is transferred to the gasket material and thus to the sample by

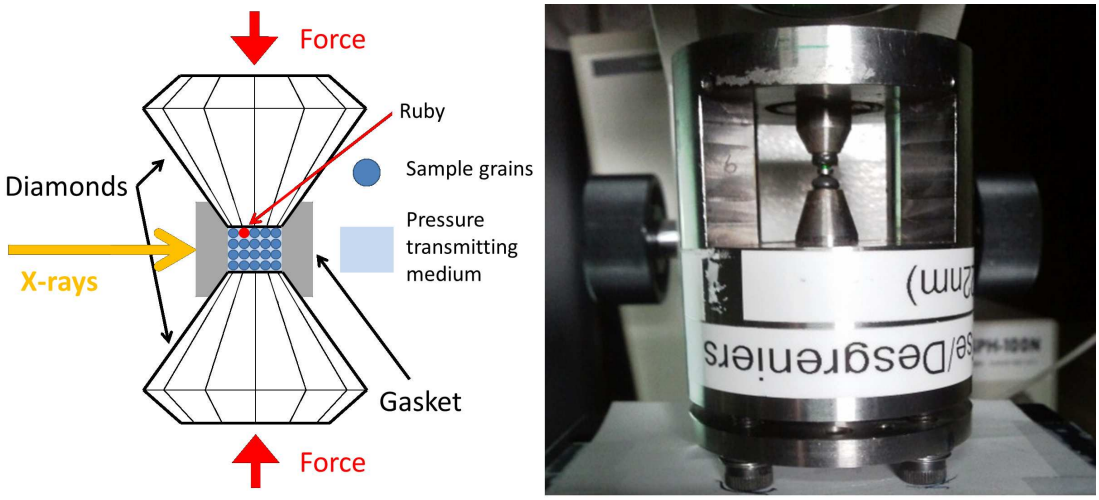

Figure 9.1.: General layout (left) and a photograph (right) of a diamond anvil cell.

the diamonds. The outer diameter of such diamonds is usually about 3-5 mm while the culet size is below 0.5 mm, which allows to apply pressures up to several hundred GPa [323, 166, 100, 70, 171].
Besides of the sample, ruby grains can be loaded into the gasket hole. The lattice parameters of the ruby are very sensitive on pressure changes, which significantly affects the fluorescence spectrum of the ruby material. The fluorescence spectrum usually shows a double peak shape, which shifts to higher wavelengths with increasing pressure. The pressure determination is mostly performed by measuring the wavelength position of the emission line at high pressure. Subsequently, the wavelength shift between the fluorescence line measured at high pressure and that at ambient conditions allows to estimate the pressure inside the sample volume. The relation between the peak shift and pressure is given by the pressure-volume equation of states [170, 330, 331, 171] defined as

$$P(\mathrm{GPa}) = (A/B)\{[1 + (\Delta\lambda/\lambda_0)]^B - 1\},$$

P being the resulting pressure in GPa, A=1904 GPa, B=7.715, $\Delta\lambda$ is the ruby fluorescence shift in nm and λ_0 is the position of the fluorescence maximum at ambient pressure. Additionally, pressure transmitting medium should be loaded into the cell in order to reduce the pressure gradient inside the sample. Here, e.g. nitrogen or helium are widely used.

A sketch of the cell used for this experiment is presented in figure 9.1. Here, two diamonds (outer diameter of about 3 mm, 0.5 mm culet size) are used to apply pressure on synthetic FeS (see section 5.1 for more details on the sample system), which was loaded into a beryllium gasket (3 mm outer diameter, about 1 mm height, hole diameter of 100μm) together with ruby material. Beryllium is relatively transparent for high energy X-rays, which can be coupled through the gasket rather than through the diamonds. This significantly decreases the background signal. Here, FeS was chosen as sample system for the experiment as the high-spin to low spin transition occurs at mod-

erate pressure of about 6.5 GPa [227]. This is relatively low pressure compared to the spin transition pressure observed for other iron containing materials [209, 165, 266, 174]. Furthermore, the spin transition takes place in a very narrow pressure range of about 1 GPa. The local structure of the troilite sample (FeS under ambient conditions) changes to the MnP-like structure at about 3.5 GPa [227]. Furthermore, the spin transition, which is accompanied by a collapse of the magnetic moment [143, 227], goes along with a second structural transition into a monoclinic phase [71]. For this experiment, no pressure medium was used in order to increase the sample volume and to reduce the background scattering for the challenging XRS experiment.

9.2. Detection of the high-spin to low-spin transition in FeS by Fe $M_{2/3}$-edge XRS spectroscopy

The Fe $M_{2/3}$-edge on FeS was measured at high pressure using the Laue spectrometer presented in section 4.3 operating at 19.4 keV. Such a high X-ray energy is required in order to penetrate the gasket and the highly absorbing sample. Pressure dependent measurements of the Fe $M_{2/3}$-edge were performed by coupling the X-rays through the gasket due to its higher transparency for X-rays compared to the diamond at five different pressure points ranging from 1.7 GPa to about 10 GPa in order to study the impact of the structural transition at 3.5 GPa and the spin transition at about 6.5 GPa on the spectral shape of the Fe $M_{2/3}$-edge. The pressure gradient due to absence of the pressure transmitting medium was determined by measuring the optical emission of the ruby at different lateral positions of the sample. The lowest pressure gradient was about 0.2 GPa at 1.7 GPa and the highest pressure gradient was 1.5 GPa at 10.1 GPa. At the same pressure points, the sample thickness dropped from 60 μm to about 40 μm. The spectra were collected with an energy resolution of 1.4 eV in 7 to 12 hours depending on the pressure.

Measurements of the Fe $M_{2/3}$-edge at high pressure are very challenging. While the long counting time of up to 12 hours demand very high stability of the XRS setup and the DAC, the measurement itself must be optimized. Therefore, knowledge about the q-dependence of the background as well as the contribution of dipole and octupole transitions to the overall spectrum as discussed in chapter 8 is indispensable. Thus, the best experimental conditions to measure the Fe $M_{2/3}$-edge at high pressure is in the range $q < 2$ Å^{-1}. Here, the Fe $M_{2/3}$-edge is strongly dominated by dipole transitions ($k = 1$) and the contribution of the electron-hole pair excitation background is comparably low. For this reason, the high pressure experiment was performed at the lowest accessible scattering angle of 2Θ=10° corresponding to $q = 1.7$ Å^{-1}.
Different background subtraction procedures for XRS spectra were presented in section 8.1. Here, a Gaussian function was fitted to the pre-edge region of the Fe $M_{2/3}$-edge and subtracted from the experimental data but also Lorentzian function was found to be reasonable for low q. In the case of FeS loaded in a DAC the signal-to-noise-ratio was significantly weaker, which requires a more careful background treatment. With increasing pressure the sample height converges to the vertical X-ray size resulting in

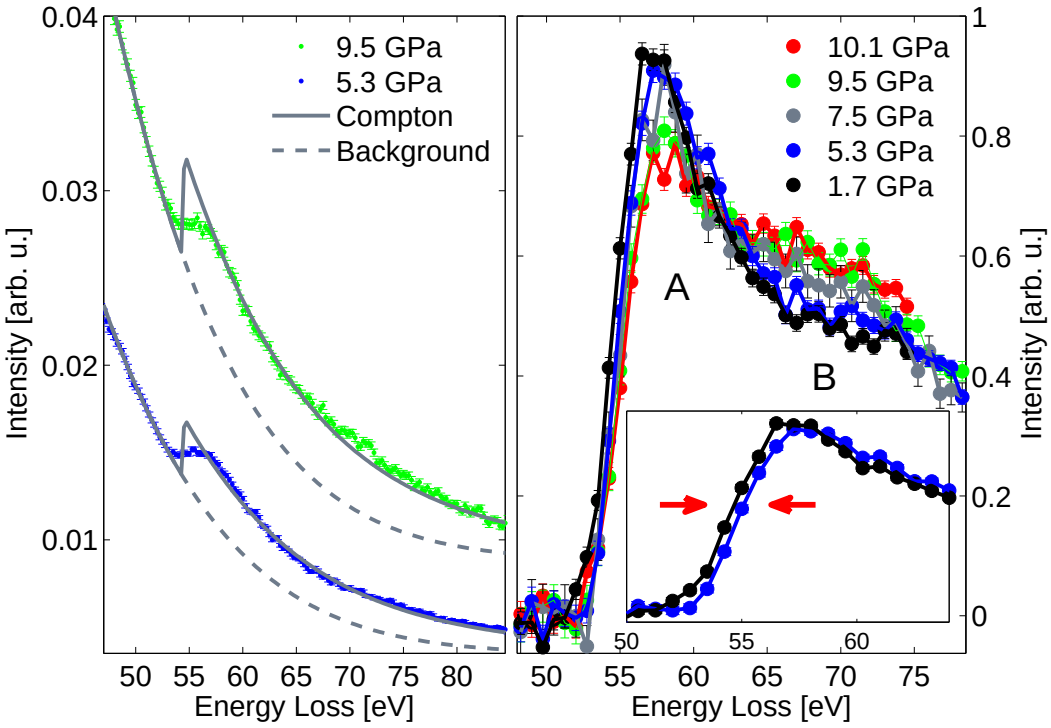

Figure 9.2.: Left: Background subtraction scheme applied to separate the Fe $M_{2/3}$-edge from the background scattering. Right: Pressure dependent measurements of the Fe $M_{2/3}$-edge on FeS by XRS. The spectra collected at 1.7 GPa and 5.3 GPa are shown in the inset separately in order to demonstrate the spectral changes of the absorption edge as the consequence of the structural transition, which occurs at 3.5 GPa [205].

significantly enhanced background contribution by scattering on diamonds. In such a case, again a Gaussian function was found to be sufficient for background subtraction but the corrected data should be compared to the shape of the FeS Compton profile calculated in Hartree-Fock approximation [26] in order to match the edge step of the absorption edge. This background treatment provides a possibility to perform a consistent background subtraction for all pressure dependent spectra, independent on the strength of the contribution by diamond scattering. Thus, Gaussian background was subtracted from the experimental spectra such a way that the edge step is reproduced by the core-electron Compton profile.

The background subtraction scheme is presented for the spectra taken at 5.3 GPa (high-spin) and 9.5 GPa (low-spin) in figure 9.1 (left). Here, the dashed line shows the contribution of the Gaussian function to the background, which simulates the valence electron excitations, while the solid line reproduces the shape of the background function including the Compton contribution of core-electrons. A very good agreement with the experimental data can be found demonstrating the feasibility of the proposed background subtraction procedure but other background functions, e.g. Lorentzian, would

not significantly affect the shape of the corrected spectrum within this scheme.
The background corrected pressure dependent Fe $M_{2/3}$-edges of FeS are presented in figure 9.2 (right). Notably, the spectrum of FeS at the lowest pressure looks very similar to the spectrum of FeO at the comparable q shown in figure 8.2. Consequently, the spectral shape of the Fe $M_{2/3}$-edges is strongly dominated by multiplet effects. Although iron atoms are surrounded by different ligands as long as the coordination is conserved.
The most prominent pressure dependent changes of the spectral shape of the Fe $M_{2/3}$-edge can be found basically in two energy loss regions: (A) the energy loss region from $E_1^A = 51$ eV to $E_2^A = 62$ eV around the energy position of the main excitation maximum and (B) the energy region from $E_1^B = 62$ eV to $E_2^B = 75$ eV. First spectral changes of the Fe $M_{2/3}$-edge can be observed when the pressure is changed from 1.7 GPa to 5.3 GPa. Here, a direct comparison between the spectra measured at these two pressure points (Fig 9.2 left, inset) shows an almost identical spectral shape but an energy shift of about 0.5 eV can be found with increasing pressure. Such spectral changes might be indicative for a change of the local environment due to the structural transition from the troilite (NiAs-related) to the MnP-related local structure, which occurs at about 3.5 GPa [227]. The spin cross-over in FeS takes places at about 6.5 GPa, going along with a structural transition from the MnP-like structure to a monoclinic structure in a very narrow pressure range of about 1 GPa. Indeed, significant spectral changes of the Fe $M_{2/3}$-edge can be observed with increasing pressure between 5.3 GPa and 9.5 GPa. Here, the relative intensity of the main excitation maximum in the energy loss region (A) decreases while a broad asymmetric maximum appears in the energy loss region (B) with increasing pressure. The spectral shape of the Fe $M_{2/3}$-edge measured at 9.5 GPa and 10.1 GPa is very similar indicating the fact, that the HS to LS transition is almost complete at such a high pressure. The spectrum at 7.5 GPa, close to the spin cross-over pressure, can be understood as a superposition of HS (below 6.5 GPa) and LS (significantly above 6.5 GPa) spectra possibly due to the pressure gradient in the sample.

To quantify the pressure related spectral changes due to the spin transition in FeS difference spectra must be calculated by a subtraction of all high pressure spectra from a reference spectrum. Here, the challenge is to separate coordination effects from the pressure dependent changes of the electronic structure, which lead to the spin cross-over. More precise, earlier studies show no indication for the spin transition significantly below 6.5 GPa and the spectral changes, which can be found between 1.7 GPa and 5.3 GPa can be certainly attributed to the structural transition at 3.5 GPa. To discriminate this transition from the spin cross-over the Fe $M_{2/3}$-edge measured at 1.7 GPa was shifted by 0.5 eV to higher energy losses in order to match the energy position of the Fe $M_{2/3}$-edge measured at 5.3 GPa, after the structural transition. Thus, the corrected spectrum measured at 1.7 GPa as well as the 5.3 GPa spectrum can be used as references for further calculations. Shifting of the absorption edges to characteristic energy positions is routinely used also for the data processing of e.g. Fe $L_{2/3}$-and Fe $M_{2/3}$-edges [295, 296]. The spectral differences calculated by subtraction of the high pressure spectra from the corrected 1.7 GPa spectrum are shown in figure 9.3 (left). Again, the most prominent spectral changes can be found in the energy loss regions (A) and (B), as discussed above.

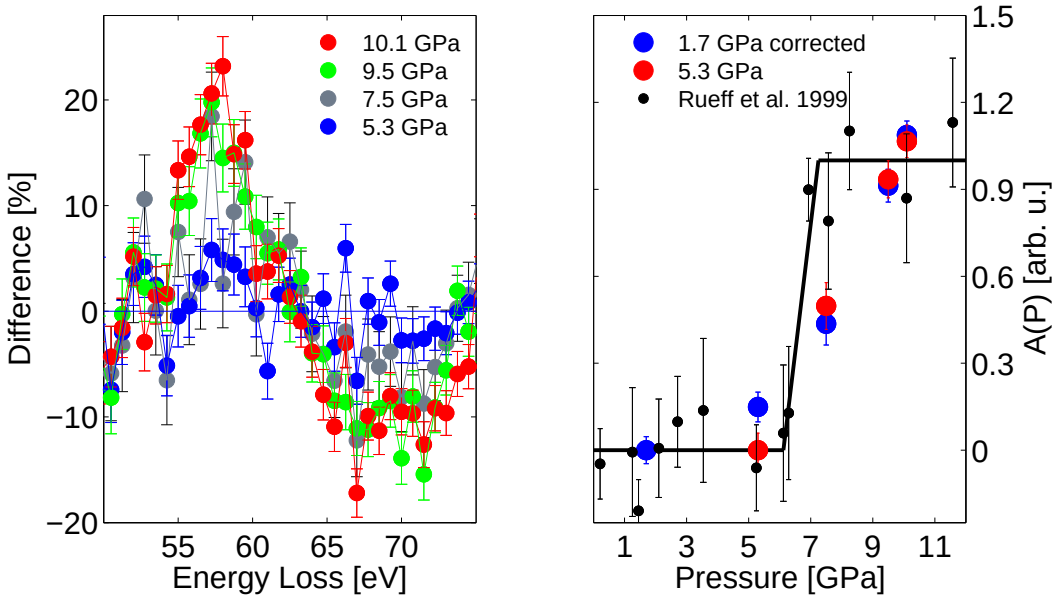

Figure 9.3.: Left: Differences calculated by subtracting high pressure spectra from the corrected 1.7 GPa spectrum. Right: Pressure dependent total spin transition parameter A(P) calculated using the corrected 1.7 GPa spectrum (blue) and 5.3 GPa spectrum (red) as reference, respectively. The renormalized data measured using XES by Rueff *et al.* [227] is shown (black) for a comparison with XRS results [205].

Now, the pressure dependence of the spin cross-over can be quantified using the related spectral changes of the Fe $M_{2/3}$-edge by calculating the integrated intensities A_1 and A_2 of the difference spectra in the related energy loss regions A and B, which can be described by the formula

$$A_{1,2} = \int_{E^1_{A,B}}^{E^2_{A,B}} (I_{\mathrm{Ref}} - I(P))\mathrm{dE},$$

I_{Ref} being a selected reference spectrum and I(P) spectra obtained at higher pressures. The total pressure dependence of the spin cross-over can be described by the total spin transition parameter $A(P)$ given by

$$A(P) = |A_1(P)| + |A_2(P)|.$$

$A(P)$ was calculated using the corrected 1.7 GPa spectrum and the 5.3 GPa spectrum as reference separately. The obtained parameters $A(P)$ for both references are subsequently normalized to zero for the HS state and to 1 for the LS state. The pressure dependence of $A(P)$ calculated using both references is shown in figure 9.3 (right) in comparison with XES results obtained by Rueff *et al.* [227] renormalized in the same manner as $A(P)$. The parameter $A(P)$ calculated for the 1.7 GPa reference shows a significant increase in the pressure range between about 5 GPa and 9 GPa while the values at

above 9 GPa are close to 1 (figure 9.3 right). The results for $A(P)$ are independent on the choice of the reference spectra and are also in agreement with the $A(P)$ found by Rueff *et al.* [227]. The only difference between XES and XRS results can be observed in the spin cross-over pressure range around 6.5 GPa. The data obtained by XES shows a significantly stronger increase in the pressure range from about 6 GPa to about 7 GPa, which is narrower than that obtained by XRS. This pressure range widening is most likely due to the absence of the pressure transmitting medium for the XRS experiment. However, the general trends are well reproduced by the XRS results demonstrating the high sensitivity of the Fe $M_{2/3}$-edge on the spin state of iron.

9.3. Quantitative determination of the crystal field splitting at high pressure

The feasibility of measurements of the Fe $M_{2/3}$-edge at high pressure by XRS as well as its sensitivity to the spin state was demonstrated above. Furthermore, the experimental results can be used to calculate the state of the spin transition as a function of pressure. However, the spin cross-over goes along with a structural transition, which might affect the experimentally obtained Fe $M_{2/3}$-edge. Although structural changes of the local structure of iron do not significantly modify the spectral shape of the Fe $M_{2/3}$-edge, minor changes cannot be excluded thus affecting the pressure dependence of the spectra. In this section a novel approach will be presented to extract the pressure dependent crystal field splitting in Fe. Such a quantitative analysis provides a deeper insight into processes leading to the spin transition.

For this purpose the Fe $M_{2/3}$-edge have been calculated using the multiplet code, which is described in detail in chapter 3. First calculations performed by van der Laan [297] predicted huge spectral changes according to the occupation of the 3d states of iron and thus to its spin state. Thus, similar calculations were done with Slater-Condon parameters scaled to 1.0 (which corresponds to 80% of the atomic values) and the spin-orbit coupling was set to zero. Subsequently, calculations were performed for different 10Dq parameters ranging from 1.0 eV to 5.0 eV. For a better comparison with the experimental data the resulting excitation pattern were convoluted with a Lorenzian function (FWHM of 0.6 eV) and a Gaussian function (FWHM of 1.4 eV) in order to match the natural broadening of the Fe $M_{2/3}$-edge [84] and the experimental resolution, respectively.
The impact of the crystal field splitting 10Dq on the shape of the Fe $M_{2/3}$-edge for Fe^{2+} ($3d^6$ configuration) is discussed in section 3.5.1. The spin transition can be found for 10Dq between 1.8 eV and 1.9 eV. The effect of the crystal field strength can be recalled on the basis of calculations shown in figure 9.4. The HS spectra for 10Dq = 1.0 eV, 1.4 eV and 1.8 eV show only weak changes with increasing 10Dq. The double-peak structure of the HS spectra changes if 10Dq exceeds the crystal field strength of the spin cross-over. Notable changes of the spectral shape can be observed comparing the calculation for the HS and LS states. In the latter case, the absorption edge is dominated by a strong main excitation maximum together with a pre-edge feature and a post-edge maximum. With increasing 10Dq the pre-edge feature shifts to the main excitation maximum and

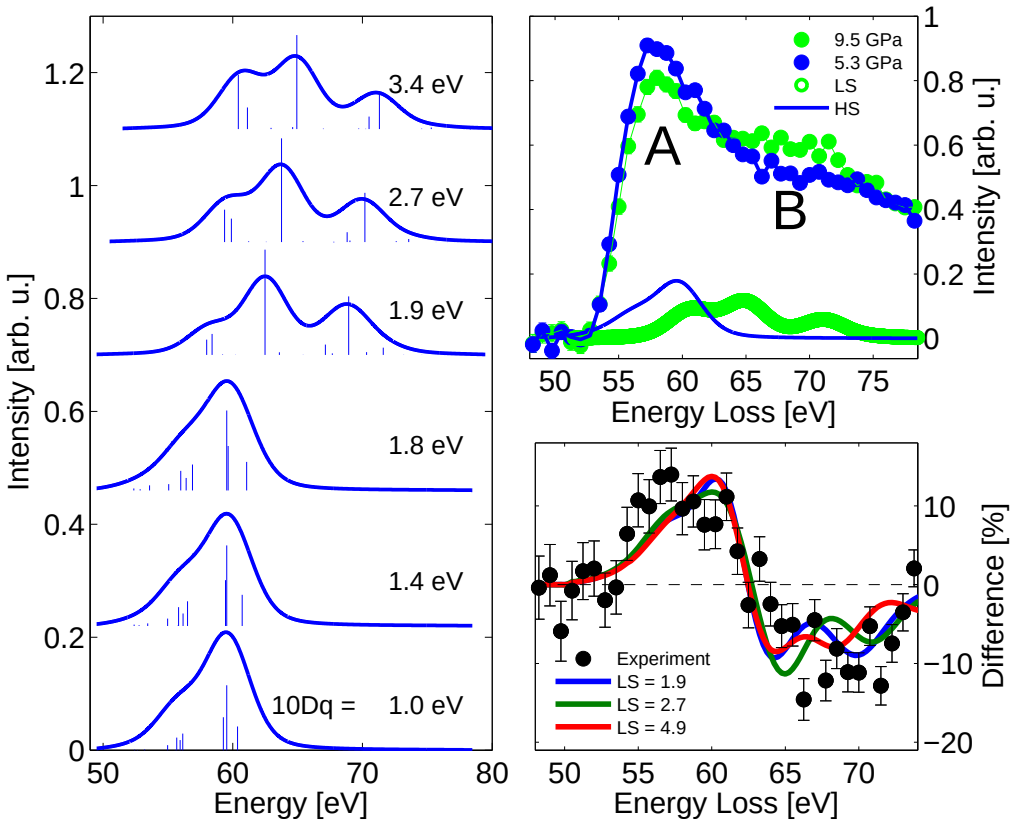

Figure 9.4.: Left: Calculations of the Fe $M_{2/3}$-edge using the CTM4XAS package for selected 10Dq. Upper right: experimental spectra collected at 5.3 GPa and 9.5 GPa representative for the HS and LS states in comparison with calculated spectra for 10Dq values obtained by the best fit. Lower right: Spectral difference between the spectra measured at 5.3 GPa and 9.5 GPa (dots) and differences of calculated spectra using three representative LS values and 10Dq = 1.7 eV for HS.

becomes stronger. Finally, at very high 10Dq (e.g. 3.4 eV), the pre-edge intensity is close to the main excitation maximum.
Although the spectral shape of the HS state shows only minor changes with increasing 10Dq, stronger modifications for the LS state calculations can be observed. Consequently, the determination of the crystal field strength in the HS state might be difficult on the basis of the experimental spectra. However, significant changes for the LS state calculations show a great potential to extract quantitative information about the crystal field strength in the 3d states of iron at high pressure. A satisfying agreement between the calculations and the XRS measurements of the Fe $M_{2/3}$-edge on iron oxides was shown in section 8.2. Additionally, the problem of absence of continuum excitations in the calculations, which might modify the spectral shape of the absorption edge, was

considered. Due to the fact, that the Fe $M_{2/3}$-edge on FeS at high pressure was measured at low q, continuum excitations show a significant contribution to the overall spectra. Thus, a direct comparison of the experimental results with calculations is not possible. Alternatively, the contribution of continuum excitations can be separated from the multiplet contribution if difference spectra are compared with calculations instead. For this approximation no changes of the continuum excitations with increasing pressure are assumed. This constrain is reasonable due to the fact, that all spectra saturate to the same level for high energy losses and the most prominent spectral changes occur between this point and the energy onset of the Fe $M_{2/3}$-edge. Subsequently, the approach to extract quantitative information about the crystal field strength at a given pressure can be described as following:

- In the first step, difference spectrum between an experimental HS spectrum and a LS spectrum must be calculated.
- Difference spectra between all modeled HS and LS spectra must be calculated
- The crystal field strengths of the HS and LS states can be extracted from the pair of calculated spectra, which reveals the best agreement with the experiment

To illustrate the approach, two experimental spectra at 5.3 GPa and at 9.5 GPa, representative for HS and LS state, are analyzed and their difference spectrum is calculated. Subsequently, calculations of the Fe $M_{2/3}$-edge for 10Dq values ranging from 1.0 eV to 5.0 eV in 0.1 eV steps were performed and differences between all possible contributions of HS and LS spectra are calculated. Finally, the difference spectra based on the theoretical model are shifted in energy with respect to the experimental data and fitted to the experimental difference spectra. The 10Dq value in the 3d state of iron in FeS at 5.3 GPa and 9.5 GPa can be obtained from the calculated spectra representing the best fit. The experimentally obtained difference of the 5.3 GPa and 9.5 GPa spectra is compared with the best fit in figure 9.4 (b). The best fit reveals 10Dq values for the selected pressure points of $10Dq^{HS}=1.7^{+0.1}_{-0.7}$ eV for the HS state and $10Dq^{LS}=3.4^{+0.5}_{-0.7}$ eV for the LS state measured at 5.3 GPa and 9.5 GPa, respectively.
The results obtained by the presented approach can be hardly compared with literature value due to the lack of comparable measurements. The crystal field splitting of the 3d states 10Dq is well known in octahedral Fe^{2+} species under ambient conditions. Here, a literature value of 1.2 eV can be found for fayalite [60]. Assuming the fact, that the HS state in FeS was measured at significantly higher pressure than ambient, the result obtained for FeS shows a good agreement to the crystal field splitting in fayalite at ambient conditions with respect to the errorbars. Concerning the LS state, a crystal field splitting of 2.35 eV was reported in $[Fe(tacn)_2]^{2+}$, which is a LS compound even at ambient conditions [120]. The crystal field splitting found for FeS at 9.5 GPa is larger than the crystal field splitting in $[Fe(tacn)_2]^{2+}$ but the measurements on FeS were performed at a pressure, which is significantly higher than the pressure where the spin cross-over occurs. Thus, both HS and LS results seem to be reasonable. However, the results are critically assessed in the nest section.

9.4. Detection limits and outlook

Quantitative results for the crystal field strength of the 3d state in FeS at high pressure were determined by combining Fe $M_{2/3}$-edge by XRS at high pressure and calculations employing atomic multiplet and crystal field effects. Based on the presented approach unique information about the local electronic structure of iron in FeS at in-situ conditions i.e. information about the pressure dependence of the crystal field splitting can be extracted. However, the results are critically assessed. The disadvantage of the theoretical calculations is the fact, that continuum excitations are not considered. Due to the significant contribution of those excitations to the Fe $M_{2/3}$-edge at low q, possible pressure dependent changes of the continuum excitations cannot be excluded, which might affect the extracted multiplet contribution. Thus, calculating spectral differences is only a first order approximation for multiplet contribution extraction. Alternatively, continuum excitations can be simulated by a convolution of the calculations with a Fano function [297]. Use of a Fano function instead of the Lorentzian function in order to simulate the natural broadening of the spectral features lead to an edge-step in the post-edge region but the agreement between the calculated spectra and the experimental data is still poor. Furthermore, a continuous decrease of the Fano line shape does not significantly affect the multiplet extraction.
Another problem is the experimental resolution and the statistical accuracy of the Fe $M_{2/3}$-edges measured by XRS. A better energy resolution in combination with improved statistical accuracy will allow to resolve more spectral features especially in the LS state, which will improve the accuracy of the crystal field splitting extraction approach.
The most important point to improve is the statistical accuracy of the measurements for further studies. Although the feasibility of the XRS measurements as a unique tool to measure low energy absorption edges at high pressure as well as the potential of calculations to extract the crystal field splitting at in-situ conditions were shown, the changes in the difference spectra are very weak even for significant variations of 10Dq. Thus, strong changes of the crystal field result in weak changes of the spectral features. This aspect is illustrated in figure 9.4 (lower right). Here, the experimentally obtained difference spectrum for 5.3 GPa and 9.5 GPa is shown together with calculated differences using 10Dq = 1.7 eV for HS and three 10 Dq values for LS, namely 1.9 eV, 2.7 eV and 4.9 eV. The experimentally obtained difference spectrum is adequately reproduced by calculations but within the statistical accuracy all three calculations may reproduce the spectrum except of that for 10Dq = 4.9 eV, which fits less to the experimental data than the other calculations.
Although both calculations and measurements should be significantly improved, a very important result can be achieved already within the current study when experimentally obtained spectral differences are compared to the calculated ones. Pressure induced HS to LS transition in general can hardly be detected. Thus, predictions about the spin cross-over are usually done on the basis of its consequences, which are a structural transition and an abrupt decrease of lattice parameters (e.g. using XRD) as well as disappeared magnetic moment (e.g. using XES or Mössbauer spectroscopy). However, there is no direct prove whether the structural or magnetic transition are the consequence of the

spin cross-over or vice versa. Furthermore, it is unclear, if the spin cross-over and the structural/magnetic changes appear simultaneously at the same pressure. A comparison of the XRS spectra with calculations presented above show a good agreement although no changes of the local environment is taken into account. The results presented above show a unique possibility to separate structural effects from the spin cross-over and thus might be the first direct prove of the spin transition using a more sophisticated theoretical approach.
Although the progress of the spin transition as a function of pressure can be qualitatively reproduced on the basis of the factor $A(P)$, spectra with significantly improved statistical accuracy and energy resolution are needed in order to obtain accurate results on both spin transition regime and the crystal field splitting at high pressure. The feasibility of such a study could be shown by measurements employing the new high energy spectrometer installed at the beamline ID12XU of the synchrotron radiation facility SPring-8. However, the spectrometer is being developed at the moment and the measurements presented above were performed using a prototype-like setup. In the next future, more and improved analyzers will be available with significantly optimized energy resolution and reduced acquisition time. Alternatively, the new IXS setup of the beamline ID20 of the ESRF can be used, which operates at lower energy but significantly more analyzer crystals are available. Both setups will be new generation facilities for in-situ measurements under extreme conditions. Thus, the approach presented above may have a great potential for this quantitative estimation.

10. Portable laser heating setup for inelastic X-ray scattering experiments at beamline P01 of the PETRA III synchrotron radiation facility

So far materials were studied at ambient conditions and at high pressure using XRS. This is a first step in order to measure low energy absorption edges of iron at thermodynamic conditions of the Earth's crust, mantle or core. However, the temperature, a very important parameter playing a key role in the deep Earth, was not yet included. Depending on the depth, temperatures of more than 5000 K can occur in addition to high pressure [65, 276]. In the last decades, great effort was achieved in high pressure high temperature instrumentation. For temperatures up to about 1000 °C resistive heating can be applied to diamond anvil cells. Here, heating wires and thermocouples are adapted to the diamonds for sample heating and temperature control, respectively [20, 243]. For improved thermal stability and damage prevention of the diamonds the DAC can be adapted in a vacuum chamber or alternatively in an inert gas atmosphere. Such a setup provides a unique possibility to perform XRS experiments under conditions of the Earth's crust with high p/T stability [228, 268].
Higher temperatures cannot be reached by resistive heating due to the lack of thermal stability of the heating material. In this case laser heated DACs are used to achieve temperatures up to 5000 °C or even higher, depending on the laser. Laser heating setups are routinely used in combination with DACs to perform experiments, e.g. in Mössbauer spectroscopy [153, 152], XAS [64, 9, 196], XRD [181, 186, 234] or optical spectroscopy [99, 161] at in-situ conditions of the deep Earth. However, measurements of low energy X-ray absorption edges are not feasible so far due to the fact, that laser heating setups are difficult to adapt to the IXS instrumentation. Thus, a portable double sided laser heating setup was designed on the basis of the laser heating system of Böhler *et al.* [30], which can be installed at the beamline P01 of the synchrotron radiation facility PETRA III. This setup in combination with new generation instrumentation will provide a unique possibility to perform XRS experiments in-situ under high pressure high temperature conditions, relevant especially for geological and geochemical applications.
The layout of beamline P01 was already presented in section 4.4 while this chapter is dedicated to describe the double-sided laser heating setup. The schemes of some relevant existing laser heating setups are summarized in section 10.1 followed by the presentation of the general layout of the laser heating optimized for the XRS instrumentation of beamline P01 in section 10.2. First results of the performance tests are presented in

section 10.3 followed by some concluding remarks in section 10.4.

10.1. Laser heating of samples in a diamond anvil cell

Laser heated DACs are applied to study samples at high pressure and high temperature, typically above 1000°C. The first laser heating setups were successfully used in the 60's [184, 19] and the design was subsequently improved. There are several setups permanently installed at beamlines of different synchrotron radiation facilities. These setups are optimized according to the requirements of certain experimental techniques and thus to related instrumentation allowing to perform experiments e.g. using nuclear resonant scattering (beamline 3-ID, APS [333]) or X-ray diffraction (16-ID, HPCAT at the APS [181]; ID27 at the ESRF [249], BL10XU at SPring-8 [309], P02 at PETRA III [163]). In addition, some portable laser heating setups are designed for multipurpose experiments, e.g. nuclear inelastic scattering [64], Mössbauer spectroscopy [152] or X-ray absorption spectroscopy [30, 64]. In this section the main components and specifics of some selected laser heating setups are presented.
The general layout of a laser heating setup is given by the following requirements:

- (I) Variation of the laser spot position and size on the sample, which defines the heated sample volume and thus the maximum temperature. The temperature gradient strongly depends on the laser profile and thus the lateral power density as well as on the laser stability.

- (II) Optical observation of the sample surface and the laser beam. This is particularly important in order to define the laser spot size in relation to the sample size. If the laser spot is too big the laser might heat the sample gasket thus annealing the diamonds of the DAC, which might lead to the damage of the diamond.

- (III) Temperature measurement, typically by spectral radiometry. Here, the emission spectrum is measured on small surface area of the sample in the hot spot regime. Due to a very strong temperature gradient (about 100°C per μm [30]) the probing radiation, typically X-rays, must coincide with the position of the temperature measurement in order to reduce the systematic error of the measurements. Furthermore, the X-ray spot size should not significantly exceed the area size of the temperature measurement.

A typical layout of a laser heating setup can be illustrated on the example of the portable laser heating system developed by Dubrovinsky and co-workers [64]. The system consists of two major components, which are the laser radiation source and the universal laser heating head (UniHead) originally developed for three dimensional cutting processes. A near-infrared laser ($\lambda = 1064$ nm) with a maximum output power of 100 W was used as source. The laser spot position and size can be controlled by three dimensional translation of the UniHead. The sample emission light is collected by the same UniHead and processed to a spectrograph. According to the properties of the optical components, the temperature measurement is performed on the sample surface element with a radius of

about 5 μm. Furthermore, a camera and illumination devices are coupled to the Uni-Head for the optical observation of the sample surface.
The most stationary setups, which are more or less permanent components of the beamline, provide enhanced stability but require significantly more space. Due to an increased number of components the alignment procedure is more complicated. The most important advantage of a stationary setup is the reduction of the temperature gradient on the sample and high stability. This is one of the most critical point of high temperature applications, as can be demonstrated e.g. on contradictory results on the pressure-temperature phase diagram of iron [31, 240, 326, 5, 239]. Thus, double-sided laser heating is often used at synchrotron radiation sources. Therefore, either two separated lasers are utilized for each side of the sample or a single laser beam is split and separately coupled into the cell. Here, on-axis and off-axis heating can be distinguished depending on the angle between the X-ray beam and the laser radiation. For an off-axis setup the incidence angle of the laser beam relative to the X-rays is about 20°, depending on the optics size [30]. In the case of an on-axis setup the laser is coupled into the DAC parallel to the X-rays by mirrors, which are reflective for visible and infrared light but nearly transparent for X-rays. Here, typically carbon [181, 64] or beryllium mirrors coated with gold or silver [333] are used.
The most critical point of a laser heating setup is the choice of optics in order to transfer the hot spot emission spectrum from the sample surface to the spectrometer. In general, any objective with sufficient magnification can be used. However, chromatic aberrations play a very important role for such a sensitive application and thus, the number of optics must be kept to a minimum. In addition, standard lenses are not adequate especially for temperatures below 1000 K [29]. Thus, two achromatic doublets can be used to replace a conventional objective, where the focal length of the first doublet corresponds to the working distance of the optical device. The focal length ratio between the second and the first doublet gives the total magnification ratio, important to reduce the area of the temperature measurement [30]. In order to avoid chromatic aberrations optical lenses can be replaced by Schwarzfield objectives. A Schwarzfield objective is based on a plano-concave and a plano-convex mirror, which couple the light emission into the spectrograph [249]. However, Schwarzfield objectives are not commercially available for the layout of a typical laser heating system. In addition, the imaging properties of the objective strongly depend on the surface quality of the mirrors [30].

10.2. Portable double-sided laser heating setup for XRS experiments at beamline P01

A general laser heating layout can now be combined using the routines from existing setups with a special requirement, that the setup must fit to the XRS instrumentation of the beamline P01. The experimental constrains important for the laser heating layout are presented in section 10.2.1 followed by a detailed description of the laser heating optics (section 10.2.2), temperature control (section 10.2.3), and remote control of motorized components (section 10.2.4).

10.2.1. Experimental constrains for the laser heating setup

Due to comparably long exposure time for a high pressure XRS experiment of several hours the laser heating must be very robust and stable. Furthermore, the combination of the working distance of the Kirkpatrick-Baez focusing mirrors and the spectrometer limits the width of the whole setup to less than 500 mm. Additionally, the length of the setup is restricted to 1200 mm. In order to increase the stability of the setup and to reduce the temperature gradient the sample material will be heated from both sides by one laser. This configuration provides a possibility to adjust the heating properties separately on both sides reducing the temperature gradient.
Finally, the setup is an optional experimental tool of the beamline. Thus, the beamline staff must be able to remove the laser heating setup from the beamline easily and the laser heating should be operated ex-situ in a laboratory providing a possibility to quench annealed samples and to perform ex-situ XRS measeurements. In the following, the layout of the laser heating setup developed for beamline P01 will be presented. Therefore, the double-sided laser heating setup designed by Boehler *et al.* [30] will be transferred and optimized for the XRS instrumentation at beamline P01.
The laser heating setup components are mounted on a honeycomb-like breadboard made of light aluminum (1200 mm (L) $\times$ 475 mm (W) $\times$ 5.8 mm (H)). For external operation and transport between the optical laboratory and the beamline the whole setup can be mounted on a movable table. The table is equipped by four pneumatic anti-vibration units in order to increase the stability of the setup during the operation in the laboratory. The overall weight of the laser heating including breadboard is about 50 kg. Additionally, a 175 mm (L) $\times$ 175 mm (W) rectangular hole was cut into the breadboard. The laser heating setup can be lifted by a crane such a way, that the beamline goniometer tower fits to the rectangular hole. Thus, the beamline alignment can be performed separately and independent on the laser heating setup.
To anneal samples in a DAC a fiber-pumped single-mode CW Ytterbium laser (YLR-100-AC by IPG) operating in the near-infrared region (λ = 1070 nm) is used. The maximum output power of the laser is 100 Watts with a power instability of about $\pm$1.0 %. The laser can be operated using a standard 220 V plug and no water cooling is required. Thus, this laser is compact, very stable and ideal for transport. The output laser beam with a diameter of 5.5 mm (86% power level) has a nearly Gaussian profile ($M^2 < 1.1$). For a better alignment a guide laser is installed (red diode, output power of 0.5 mW). Furthermore, a DAC holder consisting of two copper contacts and two water cooled steel holders was designed and is available to improve the temperature stability of the sample during the heating process (see figure 10.1).

A sketch and a photograph of the double-sided laser heating setup are presented in figure 10.2 and 10.3, respectively, and the components of the setup are discussed in detail in the following.

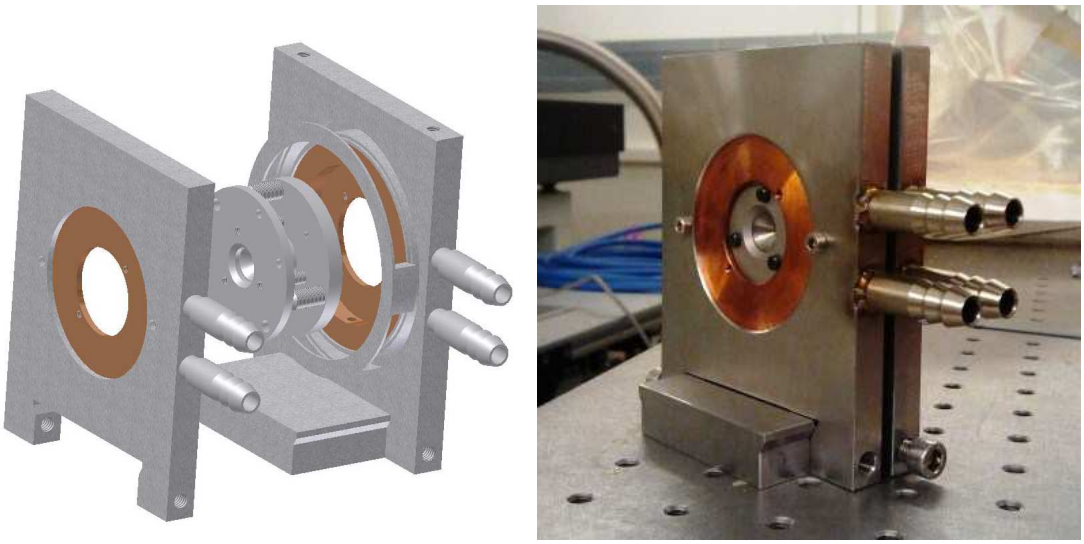

Figure 10.1.: Sketch (left) and photograph (right) of the water cooled DAC holder including a DAC in Böhler-Almax design, copper contacts, and water cooled steel holders mounted on a plate.

10.2.2. Laser heating optics

The laser collimator (LC) is oriented in a 45° angle with respect to the incoming X-ray beam and attached to a laser safety shutter. To provide a possibility to perform double-sided heating the laser beam is split with a ratio of 50:50 using a polarizing beam splitter (PBC). Subsequently, each of the partial laser beams is coupled to the sample from two sites by motorized kinematic mirrors (LM) at an angle of incidence of about 23° and further focused by movable lenses (LL) with a focal length of 100 mm. This off-axis coupling of the laser beam with respect to the X-rays provides the advantage to avoid additional absorption of the X-rays by optical components, which would be positioned in the X-ray beam path otherwise. Furthermore, X-rays and the laser heating optics can be aligned independent on each other and the accessible scattering angle range for inelastic X-ray scattering studies is maximized. The heating power is proportional to the laser power. One specialty of the laser used for this setup is that the minimum output power cannot be regulated below 10% of the maximum output power. Although the laser is split into two parts, even 5% of the maximum laser power is enough to anneal a sample to several hundred degrees, depending on the absorption properties of the material. If the laser spot is not properly aligned, the laser might hit the gasket of the DAC, which may result in the annealing and damage of diamonds. To overcome this problem, a wave plate (WP) is installed in a rotation device for each partial laser beam path. Consequently, the laser power can be further regulated by adjusting the wave plates.

10.2.3. Temperature control

The temperature control of the sample is constrained to only few parameters. The position of the laser spot is crucial to prevent annealing of the sample environment. Thus, the laser spot should be positioned as precise at the center of the sample as possible. Another very important parameter is the laser spot size, which should be kept as small as possible. If the spot size is too large, the temperature gradient on the sample increases due to the Gaussian beam profile. Consequently, the sample environment e.g. the gasket material might be annealed, which may damage the diamonds. Additionally, the control of the laser spot size provides a possibility to reduce the temperature gradient on the both sides of the sample to a minimum. For sample imaging and temperature measurement control several optics must be used to collect the light reflected or emitted by the sample, respectively, which is described in the following.

10.2.3.1. Light collecting optics

The sample emits radiation in the visible and near-infrared wavelength range when annealed to high temperature. Due to the high temperature and to the fact, that the sample is trapped between two diamonds, a mechanical contact to the sample is not possible. Thus, conventional methods to measure the sample temperature, e.g. using thermocouples, cannot be applied. In this case, the emission spectrum in the near-infrared and visible range must be measured and the sample temperature can be extracted by fitting e.g. the black-body radiation described by the Planck's law. Due to aberration effects during the interaction of light with optics, the number of optical components for light collection must be reduced to the minimum. Therefore, two optical devices to collect the emitted light from both sides of the sample are used, similar to those described in reference [30]. Each device consists of a 4 mm pinhole, an achromatic lens doublet with a focal length of 30 mm, a right angle mirror and a second achromatic lens doublet with a focal length of 500 and 400 mm for the upstream (VLCD2) and downstream (VLCD1) site, respectively. The focal length of the first achromatic doublet defines the working distance of the light collecting device while the focal length of the second doublet depends on the distance between the spectrometer entrance and the lens doublet itself. Furthermore, the ratio of the focal lengths of the doublets defines the magnification factor of this optics, important for the optical observation of the sample (13.3× and 16.7× at downstream and upstream site, respectively). The numerical aperture of this setup is 0.07 resulting in an optical resolution of about 4 μm. The collected light from both sides of the sample is combined to a single optical path by the mirror (M1) and the 50:50 beam splitter cube (BS1). The emission may become very strong if the sample is annealed to very high temperature, which may overexpose or even damage the cameras or CCD chip of the spectrograph. Thus, two neutral density filters with the optical density (OD factor) of 2 and 6 (ND1 and ND2, respectively) can be moved into the light path. Additionally, a notch filter is used to protect the optics from the laser radiation (NF).

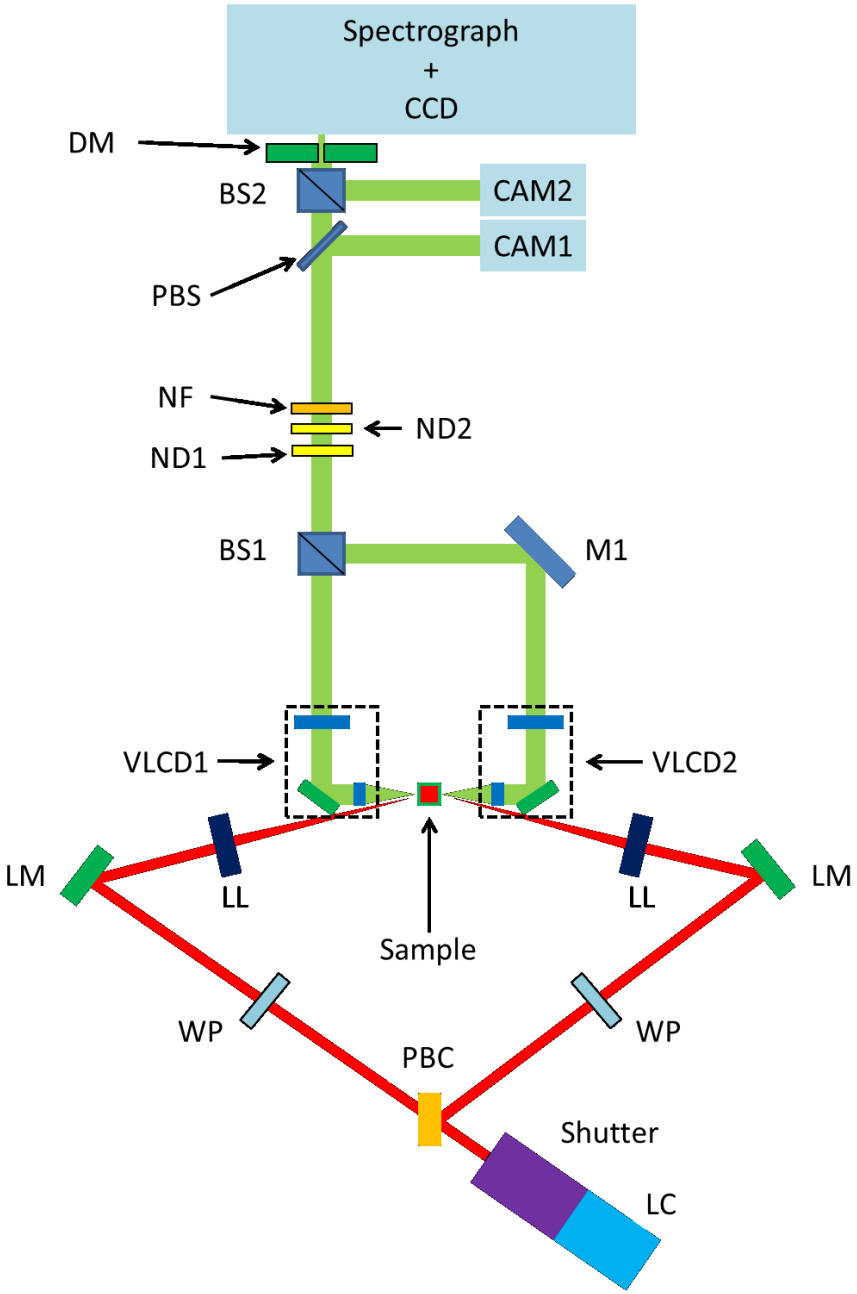

Figure 10.2.: Schematics of the double-sided laser heating setup including its components: (LC) laser collimator, safety shutter, (PBC) polarizing beam splitter, (WP) wave plates, (LM) laser mirror, (LL) laser lens, (VLCD1) and (VLCD2) are visible light collection devices in the downstream and upstream direction, respectively, (M1) right angle mirror, (BS1) beam splitter cube, ND1 and ND2 are neutral density filters, (NF) notch filter, (PBS) pellicle beam splitter, (BS2) beam splitter cube, (DM) drilled mirror, (CAM1) and (CAM2) CCD cameras, as well as spectrograph with its CCD chip.

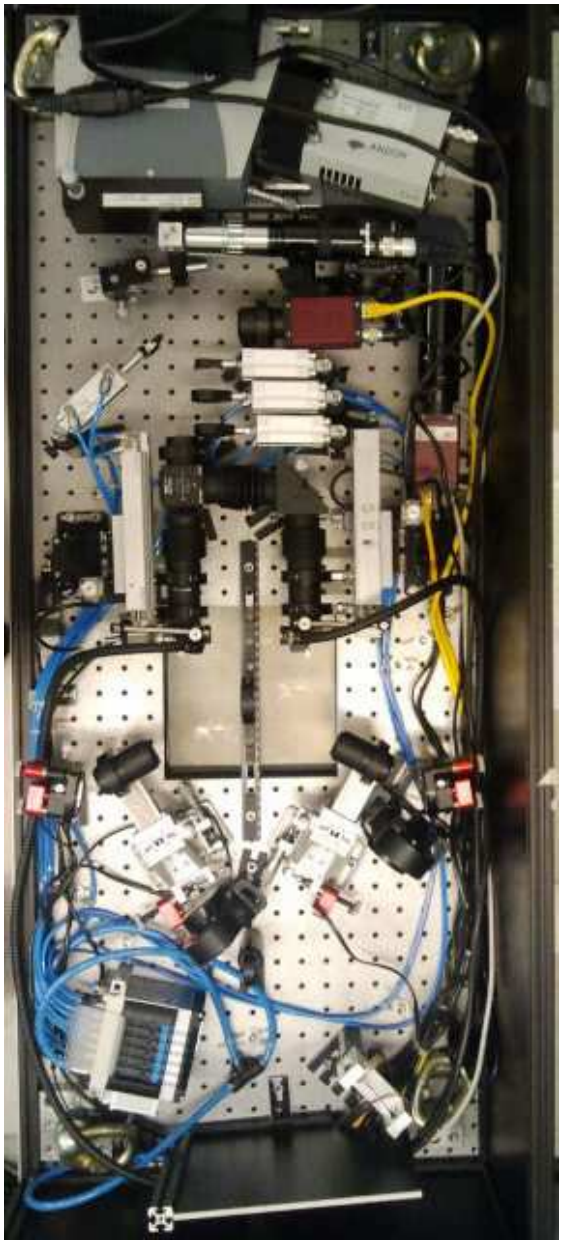

Figure 10.3.: Photograph of the laser heating setup.

10.2.3.2. Sample imaging

The light from both sides is coupled in a single path by the beam splitter cube BS1. After the optical filters a 50:50 pellicle beam splitter (PBS) is installed in combination with the camera (CAM1) for sample imaging purposes. Here, a pellicle beam splitter was chosen due to the fact, that this beam splitter does not significantly modify the position of the transmitted light, in contrast to a beam splitter cube. A disadvantage of

the PBS is a significant spectral modification of the light, which however does not play any role for optical observation. The sample surface is observed by a Manta G-125B/C camera with an integrated SONY CCD chip with an effective chip size of 4.8 mm (H) × 3.6 mm (V) and a maximum resolution of 1292 × 964 pixels, which is sufficient in order to observe a DAC loaded sample. This camera is very compact, easy to use and can be controlled by ethernet connection. In addition, off-axis illumination units on VLCD1 and VLCD2 are used employing a light source KL 2500 LCD (230V) by Schott. This light source generates bright light in the visible range and is thus routinely used for microscopy.

10.2.3.3. Temperature measurements

For temperature measurements the hot spot emission is collected by optical components VLCD1 and VLCD2. The light passes a 50:50 beam splitter cube (BS2) and hits a self-made drilled mirror (DM). The mirror was prepared using a silicon wafer as starting material. The wafer was cut in 5 mm × 5 mm pieces and polished on one side to reduce its thickness to about 80 - 100 μm. As a consequence of the polishing process, the wafer surface became highly reflective and thus the thin silicon wafer can be used as a mirror. Subsequently, a 40 μm hole was drilled by a pulsed laser into the mirror surface[1]. Combined with the magnification factor of the visible light collecting devices VLCD1 and VLCD2 of 13.3 and 16.7 the mirror with the pinhole of 40 μm allows temperature measurements on the sample area with the diameter of about 3.0 μm (downstream) and 2.4 μm (upstream), respectively. This values are very suitable in combination with e.g. a laser spot size of about 40 - 50 μm and an X-ray size of below 5 μm. The light reflected by the mirror is coupled by the beam splitter BS2 into a camera (CAM2), which is adapted with a Mitutoyo objective (20× magnification, 20 mm working distance) and a Zoom6000 right angle tube. Here, the same Manta G-125B/C camera is used as for the sample imaging and the setup is aligned with respect to the mirror surface. This instrumentation allows in-situ observation of the hot spot on the sample and thus the laser spot position and size. Subsequently, the devices VLCD1 or VLCD2 should be moved so that the hot spot center appears exactly at the position of the mirror pinhole. Consequently, the light emitted by the sample passes through the pinhole into the spectrometer and is collected by a CCD camera. For this part of the setup a DU420A detector is used in combination with a Shamrock SR-163 spectrograph (163 mm focal length). The detector contains an air cooled 26.6 mm × 6.7 mm CCD chip (1024 × 255 pixels with a single pixel size of 26 μm × 26 μm), which is a very sensitive low-noise detector. The spectrograph is adapted with a grating with 300 lines/mm and a blaze of 500 nm. Furthermore, a variable vertical slit is mounted on the spectrometer entrance. The principle of the temperature measurement procedure is illustrated in figure 10.4. The center of the hot spot taken on the sample area with a diameter of about 2 - 3 μm passes the drilled mirror DM and the spectrometer entrance slit. The sample emission is refracted into its spectral components by the grating and subsequently projected on

[1]Laser drilling was performed by PD Dr. M. Wilke, Deutsches GeoForschungsZentrum, Section 3.3, Potsdam, D-14473, Germany

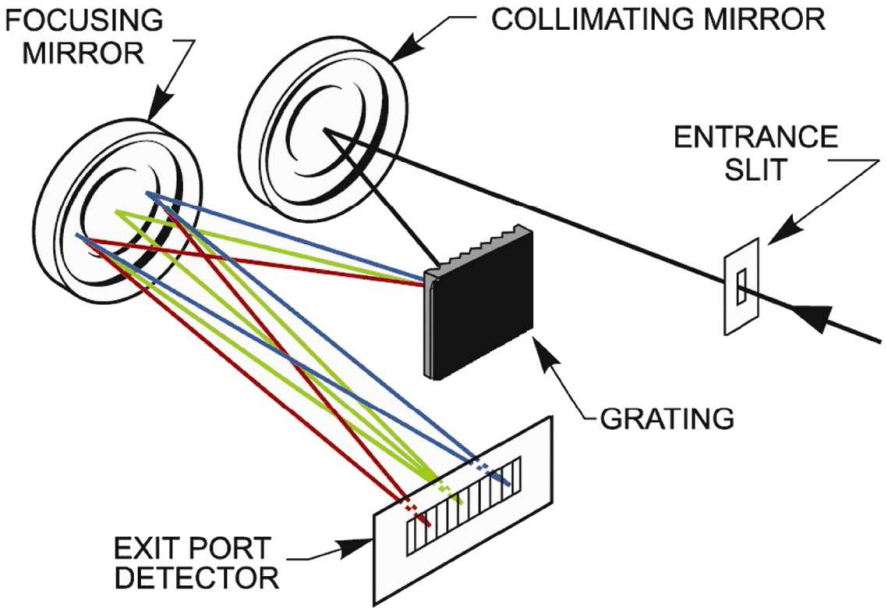

Figure 10.4.: Working principle of the spectrometer used for temperature measurements. The picture is taken from the user manual [4].

the CCD chip. The spectrograph provides a resolution of about 1 nm in the wavelength range between 300 nm and 825 nm [4].

10.2.4. Remote control

According to the safety precautions at a synchrotron an X-ray beam shutter can be opened after the experimental hutch was interlocked. During the measurements, nobody is allowed to enter the hutch. Thus, all relevant components of the laser heating setup must be remotely controlled from outside. In this section a short overview about the motorized components is given.
The laser can be completely operated remotely by PETRA III in-house communication system, which includes changing between the infrared and the guide laser, switching the lasers and the modulation, and regulation of the laser power (between 10% and 100 %). The laser radiation is split by the polarizing beam splitter PBC in two partial beams. Each beam is regulated on the sample by tilt and pitch movements of the mirror LM and a translation of the laser lens LL. Additionally, the laser power is regulated by the rotation device RD. Therefore, two actuators motorized by picomotors (obtained from Newport) are adapted to the laser mirror allowing to tilt and pitch the mirror within the angle range of 3° (0.7 μrad angular resolution). A translation picomotor actuator (25.4 mm translation range, 30 nm resolution) from the same series is attached to the translation stage of the laser lens. This devices are slightly more expensive compared to the conventional stepper motors, but they are optimized for high stability applications and provide a smaller step size. The motorized actuators can be operated using

a 6-axis iPico driver in combination with a joystick. The joystick interface allows to switch between any pair of motors and two motors can be moved separately or even simultaneously. Due to an available gear mechanism the motors can be easily moved with different speed. During the laser heating operation the joystick can be connected to the iPico driver from the users cabin by ethernet. Each rotation device is equipped with a 2-phase stepper motorized actuator (travel range of 360°, 1° step size). This motorized components including 6 picomotors and 2 stepper motors allow a complete control of the laser beam size, position, and power.
In order to measure the spectrum of the sample emission as well as for optical sample observation the visible light collection devices VLCD1 and VLCD2 must be moved in three dimensions in order to find the sample center and to align the focal distance of the devices to the sample surface. Furthermore, the devices must be pushed to the sample observation position for optical observation and temperature measurements. Otherwise, they must be pushed away from the sample to prevent blocking of incoming or scattering X-rays. For precise three dimensional movements the optical devices are mounted on XYZ stages. One stepper motor is adapted to the actuator of each translation stage (model 8MT184-13 XYZ, 13 mm translation range with a resolution of 1.25 μm, purchased from Standa). These motorized actuators are very compact, stable, comparably cheap, and can be remotely controlled via the PETRA III in-house communication system or Beckhoff drive.
In order to push the optical devices to the sample observation position and away, additional motors are required. The translation movement must be fast and extremely reproducible. Otherwise, temperature measurements would be performed at different sample surface positions after each cycle. Conventional stepper motors are to slow for this operation and would be very expensive due to the high required translation range. Thus, a pneumatic stage with 80 mm translation range is used, which is mounted between each optical device and the XYZ stage. This translation stage (DGSL-8-80-P1A by Festo) is compact and its reproducibility is increased to about 1 μm by shock absorbing units. Thus, the optical devices can be moved away from the sample observation position in about 1 second. Due to the advantages of pneumatic device concerning the speed of movements and their stability the filters ND1 and ND2, the notch filter NF, and the pellicle beam splitter PBS are mounted on pneumatic cylinders with a square-shaped rod and a translation range of 40 mm. This devices push the filters into the light path and away within less than 1 second. All pneumatic devices are adapted with proportionality plug valve, which allows to tune the speed of movements. Furthermore, all devices are connected to a control valve. The control valve is a central device, which connects the pneumatic stages and cylinders to the source of compressed air. Furthermore, the control valve can be connected to the Beckhoff drive for remote control of the pneumatic devices.
Another motorized device is the Zoom6000 objective, which allows to tune the magnification factor by a dc motor. Therefore, a driver and the related software package are available. However, this movement is not required for laser heating operation.
Finally, the beam splitter cube BS2 is fixed on a compact XYZ stage in order to align the camera CAM2 to the surface of the mirror DM. Furthermore, the laser lenses LL are

mounted on XYZ translation stages with one motorized axis as described above. The lens position vertical and horizontal to the laser beam can be aligned by micrometer screws.
After a pre-alignment, the whole laser heating setup can be operated remotely controlled from outside of the experimental hutch, as prescribed by safety requirements. The laser spot position, size, and power can be aligned by a total amount of 6 picomotors and 2 stepper motors. The visible light collecting devices can be pushed to the sample observation position and 8 cm away by 2 pneumatic translation stages and the fine alignment can be performed by two motorized XYZ stages resulting in 6 additional stepper motors. Furthermore, PBS, the ND and notch filters can be moved in the light path by 4 pneumatic cylinders. Thus, the laser heating can be operated by a total of 8 stepper motors, 6 picomotors and 6 pneumatic devices.

10.3. First performance tests of the laser heating setup

After the general layout of the double-sided laser heating setup was described, first performance tests were performed and the results of the imaging properties (section 10.3.1), control of the laser spot (section 10.3.2), and spectrograph calibration (section 10.3.3) are presented.

10.3.1. Imaging properties of the setup

In order to test the performance of the imaging components of the laser heating setup pictures of the test sample surface were taken from upstream and downstream site using the respective light collecting devices VLCD2 and VLCD1 and the components M1, BS1, PBS and CAM1. The pictures taken from the cross-hairs on the test sample surface are shown in the upper panel of figure 10.5 in comparison with a picture taken by a commercial microscope. In the microscope picture (left) a sharp white line of the cross-hairs can be observed. The color distribution on the surface of the black anodized plate is non-homogenous and color blobs can be observed on the surface of the cross-hairs. This becomes even more clear regarding the picture taken from the downstream site with a higher magnification of 13×. Here, the center of the cross-hairs is presented. Again, the white cross-hairs can be clearly separated from the black background and white blobs of the cross-hairs can be observed. A similar picture can be obtained from the upstream site (right) with even higher magnification of 17×. Both pictures, upstream and downstream, show consistent structure of the test sample surface and were taken in a sufficient time of 1 second.
After the successful performance test of the imaging components of the laser heating setup the test sample was replaced by a DAC loaded with FeO. Here, the contrast between the sample and the gasket material is pure and thus more difficult to resolve. In addition, the second lens of VLCD1 was replaced to decrease the magnification of this device to 10× for a better comparison with the microscope picture. The results of the DAC sample imaging are shown in the lower panel of figure 10.5. The picture taken by the microscope shows a well resolved shape of the diamond facets as well as the

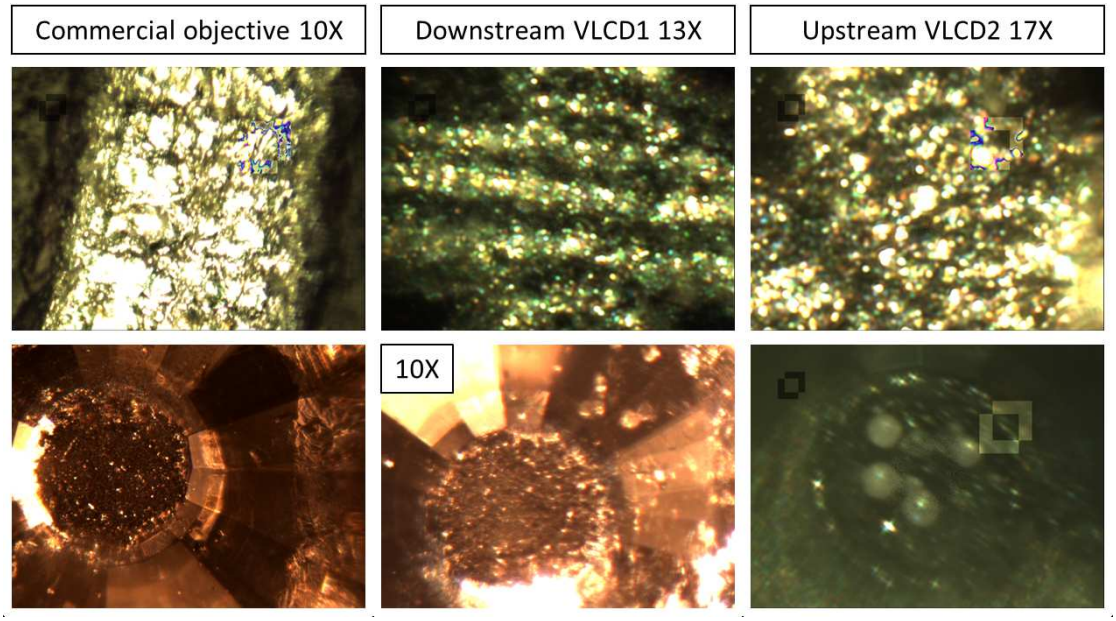

Figure 10.5.: Results of the performance test of the imaging optics on the example of a test sample (upper panel) and an FeO loaded DAC (lower panel) from the upstream (right) and downstream (center) site in comparison to a picture taken using a commercial microscope with 10 × magnification.

diamond imprint into the gasket. Furthermore, gasket hole filled with dark FeO powder can be observed. Here, even single powder grains of the sample can be resolved and the gasket seems to be moved out of the center of diamond culets during the DAC loading. A similar picture can be obtained using VLCD1 from downstream site compared to the microscope picture. Here, a contrast between the gasket hole contour and the powdery sample grains is visible, but the picture seems to be over-saturated by illumination light. This is due to the fact, that the illumination unit was installed on-axis in the microscope and off-axis at this early test stage of the laser heating setup. Different coupling schemes of the illumination result in stronger light reflexion by the diamond surfaces thus decreasing the imaging properties of the setup. Furthermore, very simple optics with a minimum number of optical components is used for the laser heating setup, while expensive anti-reflection coated components are used for the microscope objective. This of cource significantly enhances the imaging properties. However, the imaging properties of the laser heating setup provide sufficient contrast in order to distinguish between the diamond facets and culet surface, gasket material and powdery sample even in the case the gasket and the sample have a similar color. Consequently, VLCD2 generates pictures from the upstream site of the sample of very similar quality as VLCD1, but with a slightly higher magnification (17×). Larger bright and less resolved structures in the picture are the big ruby grains. Conclusively, the laser heating setup provides a possibility for real-time optical observation of the sample surface from two sides in very sufficient quality for high temperature experiments.

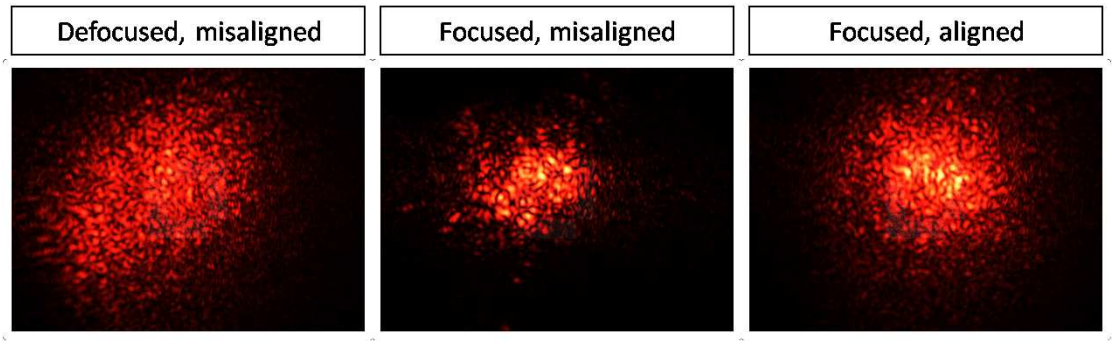

Figure 10.6.: Laser spot shape taken for the misaligned (left), badly aligned (center) and fine aligned (right) laser optics.

10.3.2. Control of the laser spot size and position

Alignment of the laser components can be performed on the basis of the successful performance test of the imaging optics. After the laser collimator, safety beam shutter, and the polarizing beam splitter are installed, the laser mirrors are used to couple the laser on the center of the test sample cross-hairs at the minimum possible angle of incidence of about 23°. It should be minimized in order to decrease the temperature gradient of the sample during the high temperature experiments as well as to reduce reflections of the laser light by the surface of diamonds. Finally, laser lenses should be installed such a way, that their surfaces are perpendicular to the incoming laser beam. This is particularly important in order to reduce the minimum laser spot size. For this test using a red laser pointer instead of the high power laser ($\lambda = 692$ nm), wave plates are not required due to the very low power of the guide laser and the analysis was performed only for the downstream site of the sample. The alignment of the upstream site is done in a similar way.
After the pre-alignment of the laser part described in section, first pictures of the laser spot on the surface of the test sample are shown in figure 10.6. The left picture shows the laser spot on the surface of the white cross-hairs of the test sample immediately after the pre-alignment of the laser heating optics. According to the chip size of the camera and the magnification of VLCD1 the laser spot size (FWHM) can be estimated to about 130 μm (V) $\times$ 110 μm (H). The brightness is distributed non-homogeneously due to the blob formation of the white color of the cross-hairs surface. Furthermore, the area with the highest brightness is not centered on the laser spot. The background scattering can be reduced by moving the lens along the laser beam according to the focal length of the lens. Here, the laser spot size (figure 10.6, center) decreases to about 113 μm (V) $\times$ 90 μm (H), but the brightness is still distributed non-uniformly. A huge increase of the laser spot quality can be achieved after the optimization of the lens orientation to the laser beam. Therefore, two alignment disks made of frosted glass with a 1 mm hole in the center were mounted in front and behind the laser lens. Subsequently, the lens was rotated until the laser beam could pass both holes of the alignment disks. Such a way, the lens orientation could be optimized resulting in a significant improvement of

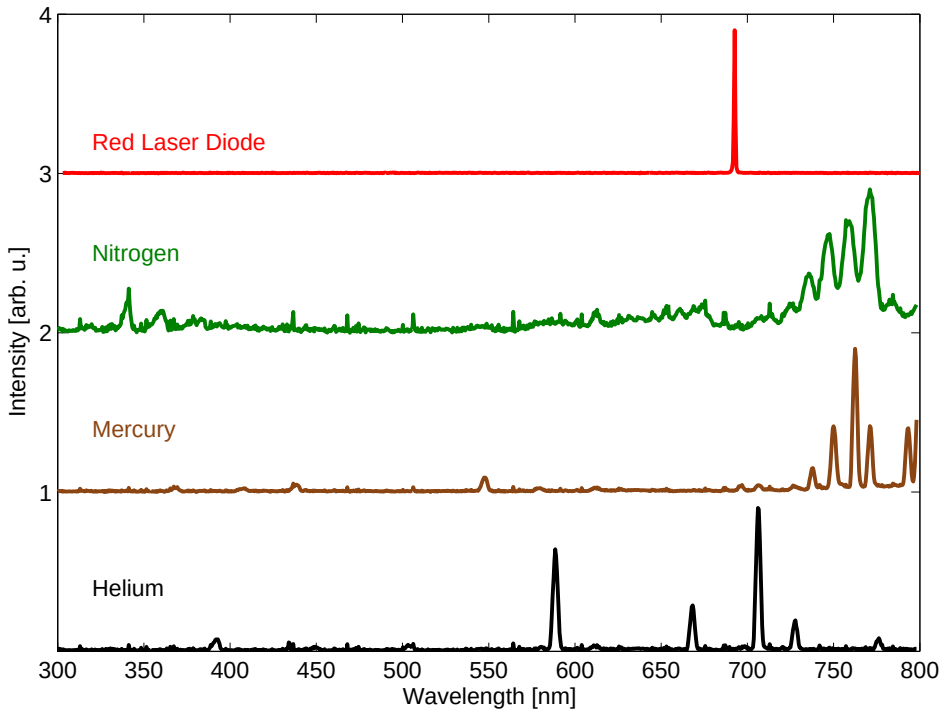

Figure 10.7.: Spectra obtained by the spectrograph in combination with light collecting optics of the laser heating setup for calibration purposes using He, Hg, N_2, and air gas discharge lamps as well as a red laser diode.

the laser spot quality (figure 10.6, right). Here, the laser spot appears larger compared to the picture obtained using a misaligned lens, which is only due to a longer acquisition time. However, the brightness distribution of the laser spot unambiguously improved and is now very symmetric and relatively isotropic. Furthermore, optimization of the lens orientation decreases the laser spot size to about 60 μm, which is required for high temperature experiments.

10.3.3. Spectrograph calibration and temperature measurement

After the imaging and laser optics were aligned the spectrograph calibration was performed. Therefore, gas discharge calibration lamps loaded with helium, mercury, and nitrogen were used. The emission spectra reveal characteristic maxima well known for a certain gas. For the spectrograph calibration the test sample was replaced by the calibration lamps and the spectra are presented in figure 10.7 together with the laser spectrum measured during the alignment procedure described in section 10.3.2. The laser spectrum shows a distinct line at 692 nm in an excellent agreement with the wavelength of the laser diode. Furthermore, spectra of He, Hg, and N_2, gas discharge lamps were collected within acquisition times of 10 seconds or less. Here, all characteristic

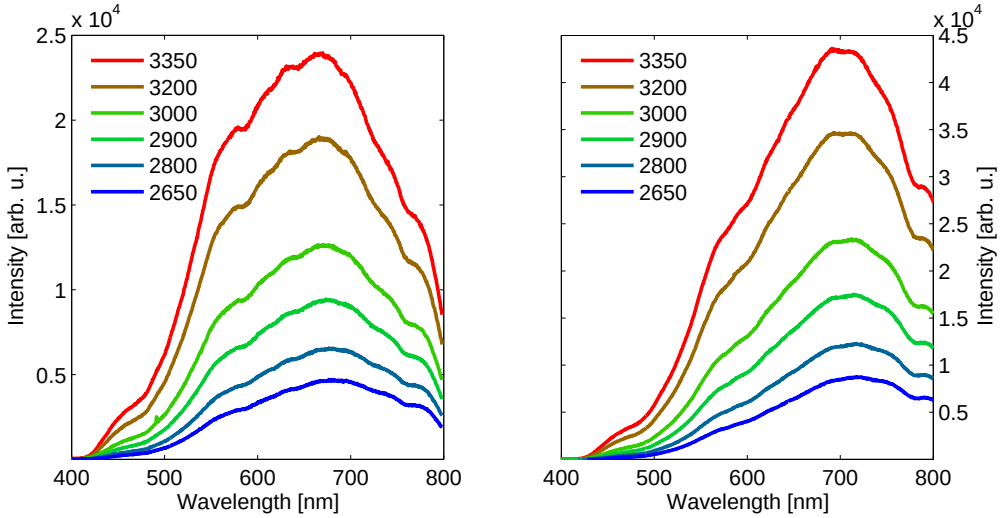

Figure 10.8.: Light source spectra as a test for temperature measurements for the downstream (left) and upstream (right) optics, respectively.

maxima of the related gases could be identified at correct wavelength positions according to the information provided by the manufacturer. Thus, performance of the optical components involved into the emission measurements is very reasonable for further tests.

After the successful spectrograph calibration measurements first temperature measurements on both upstream and downstream sites were performed. For the first test the light source used as illumination unit replaced the sample. The temperature of the emitted light can be changed by a variation of the input voltage of the lamp in distinct steps and the temperature is displayed on the monitor of the light source. The laser heating optics could be aligned to the illumination fiber in about 5 minutes. The resulting background corrected spectra for the upstream and downstream sites are presented in figure 10.8. The spectra show a good statistical accuracy for both upstream and downstream sites and have a very similar shape with an additional stronger maximum at about 700 nm for the upstream site. Here, one more mirror is used compared to the downstream site and the maximum may be caused by the chromatic aberrations produced by the mirror coating. Notably, the spectra measured for all temperatures show no similarity to a Planck function. Thus, the spectra are strongly dominated by the contribution of the optical elements rather than by the black body radiation. Therefore, the optical response of the components must be separated from the sample emission. For this purpose, the spectrum obtained for 2650 K was used as reference. This correction procedure is, of course, a strong approximation and is not appropriate for later experiments. Here, a spectrum of a well characterized calibration lamp must be used as reference. However, for the first test the assumption will be done, that the coldest light temperature is exactly 2650 K. The correction function of the optical components to extract the Planck spectrum can be calculated by dividing the experimentally obtained spectrum by a calculated spectrum for the same temperature. Typically Planck's law is used to calculate

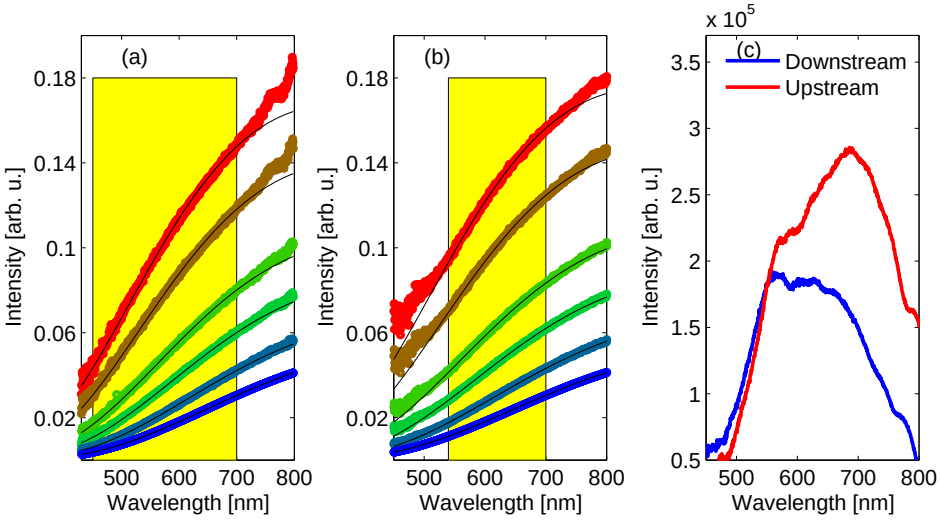

Figure 10.9.: Spectra corrected for the contribution of the optics for the downstream (a) and upstream (b) optics, respectively, together with corresponding Planck fits. The fitting range is marked by the yellow area. Additionally, correction function for the downstream and upstream sites are shown in (c).

$T_{Expected}$ [K]	2800	2900	3000	3200	3350
$T_{Upstream}$ [K]	2775	2917	3045	3238	3357
$T_{Downstream}$ [K]	2766	2904	3027	3211	3327

Table 10.1.: Comparison between the expected temperatures and the fit result for upstream and downstream sites, respectively. The standard deviation of the fit results is about 3%.

the black body emissivity, which is proportional to the experimental intensity, given by

$$I(\lambda, T) \propto \frac{c_1 \cdot \epsilon(\lambda)/\lambda.^5}{e^{c_2/(\lambda \cdot T)} - 1},$$

where $c_1 = 3.7418 \cdot 10^{-16}$ Wm^2, c_2=0.014388 Km, and $\epsilon(\lambda)$ is the emissivity with a weak wavelength dependence, which will be neglected in the following. The emissivity is 1 for a perfect black body and lower for other samples [181].

Subsequently, all spectra corrected for the contribution of the optical components are shown in figure 10.9. In contrast to the raw spectra, the shape of the corrected spectra look very similar to the Planck function. Finally, the temperature is obtained by fitting a Planck function to each spectrum using temperature as free parameter in the wavelength range from 450 to 700 nm and from 540 to 700 nm for the downstream and upstream sites, respectively. The agreement between the experimental and calculated spectra is very good in the wavelength range where the fit is performed and the resulting temperatures for the downstream and upstream sites show a very good agreement compared to the expected temperature values (table 10.1). Thus, reliable temperature measurements can be performed using the laser heating setup already at this early test phase.

10.4. Concluding remarks

In this chapter portable double-sided laser heating setup designed for the inelastic X-ray scattering beamline P01 at PETRA III was presented and results of the successful performance tests are shown. For further operation, the laser diode used for the first tests will be replaced by the high power laser and its remote control unit will be adapted to the internal communication system of PETRA III. Subsequently, wave plates, not used for the tests, will be installed and tested. Although the imaging properties of the laser heating setup were tested successfully on-axis illumination will still improve the contrast of the picture. Furthermore, this kind of illumination might be essential for transparent samples. The most important modification is to decrease the distance between the drilled mirror and the spectrometer entrance, which was about 10 mm during the tests. This improvement will further enhance the resolution of the spectrograph and reduce the systematic error of the measurements.
After the optimization of the laser heating setup first high temperature test will be done. Therefore, e.g. a tungsten foil with a well known melting temperature of 3695 K will be annealed to very high temperature and the measured melting temperature will be compared to the theoretical value. Subsequently, the setup will be installed at the beamline P01 and XRS measurements at high pressure and high temperature can be performed in order to study low energy absorption edges of geologically relevant melts [237, 236].

11. Conclusion and Outlook

The aim of this thesis was to exploit the capabilities of XRS to perform systematic studies of low energy absorption edge of iron in compounds at high pressure/temperature. X-ray Raman scattering measurements were performed at the Fe $L_{2/3}$-edge on different iron oxides and an algorithm to determine the $Fe^{3+}/Fe_{tot.}$ ratio in minerals and glasses, so far applicable for EELS measurements, was transferred to the X-ray Raman scattering results. Furthermore, a systematic study of the Fe $M_{2/3}$-edge on different geologically relevant materials was presented and the momentum transfer dependence of the XRS spectra was explained utilizing atomic multiplet calculations employing crystal field effects. Furthermore, high sensitivity of the Fe $M_{2/3}$-edge on the oxidation state and local coordination of iron in compounds was demonstrated and its great potential for quantitative extraction of the $Fe^{3+}/Fe_{tot.}$ ratio in unknown glasses was shown. Subsequently, first systematic measurements of the Fe $M_{2/3}$-edge in-situ at high pressure were performed in order to reveal the spin state of iron. In combination with calculations the high-spin to low-spin transition at high pressure could be directly proved. Furthermore, a novel approach to extract quantitative information on the crystal field splitting of the 3d states of iron for the high-spin and low-spin state at in-situ conditions was introduced. However, the impact of the temperature cannot be neglected to match the thermodynamic conditions of the inner Earth. On the way to perform this experiment at high pressure and high temperature conditions, a portable double-sided laser heating setup optimized for X-ray Raman scattering experiments at beamline P01 of the synchrotron radiation facility PETRA III was developed, which allows to anneal samples to temperatures above 3000 K. Its components and functionality were successfully tested. The results presented in this thesis can serve as a basis for prospective systematic in-situ studies of the oxidation state, local coordination and spin state of iron in compounds at conditions of the deep Earth. Therefore, general changes of the spectral shape of the Fe $M_{2/3}$-edge can be directly attributed to modifications of the oxidation state, local coordination, and spin state. Additionally, a theoretical approach was proposed, which in principle allows to extract quantitative information on the crystal field splitting. This basic knowledge can be used in order to study iron partitioning in mixed compounds at extreme conditions. Furthermore, a more systematic in-situ study of the pressure induced high-spin to low-spin transition will be performed on siderite. Siderite ($FeCO_3$) is a natural mineral relevant for geological applications and only few studies of the spin cross-over are available [174]. Here, Fe $M_{2/3}$-edge might provide more direct prove of the spin transition and the limits of the theoretical approach will be tested. Furthermore, the double-sided laser heating setup opens access to completely new experimental possibilities in combination with the new spectrometer for X-ray Raman scattering at beamline P01 of PETRA III. So far, no measurements of low energy absorption edges of

iron have been reported at high pressure and high temperature conditions. Thus, this setup provides exciting possibilities to study iron partitioning, changes of the oxidation state and local coordination, and spin transition at extreme conditions. This information may be the next step in order to constrain thermodynamic conditions, at which minerals are formed inside the bulk Earth [237, 236].

A. Structural changes in amorphous GexSiOy on the way to the nanocrystal formation

Silicon oxide based compounds play an important role for numerous materials science and industrial applications due to its unique electronic properties, e.g. in photovoltaic [324, 332] or as a candidate for light emitting device components [10, 168] and fast and stable non-volatile flash memory devices [46, 140, 214]. Several studies are available, which focus on the investigation of physical properties of Ge nanocrystal in different matrices. [96, 198, 138, 334]. However, especially Ge nanocrystals embedded in a SiO_x matrix ($x \approx 2$) are of the greatest interest for the application due to a high difference of the dielectric constant between Ge and SiO_2 [140, 168, 214]. Here, bulk amorphous Ge_xSiO_y can serve as starting material, which can be synthesized by e.g. dc magnetron sputtering [327, 336], sol-gel method [117, 202] or chemical vapor deposition [82, 212]. Ge nanocrystals can be subsequently produced by annealing the starting material in a certain inert gas, e.g. nitrogen, argon or hydrogen. The size, shape and density of the nanocrystals is significantly affected by preparation and annealing conditions. Although matrix nanocrystals are extensively investigated, information about processes leading to the formation of nanocrystals is very rare but crucial in order to tune the properties of the material [230, 337] but bulk sensitive studies of temperature induced changes of the local structure in ternary Ge_xSiO_y are very challenging. Usually, several experimental techniques must be combined in order to obtain a complete picture about the local electronic structure. Routinely, XRD or visible Raman spectroscopy are used to reveal the formation of Ge crystallites and their local chemical environment. Subsequently, the local chemical environment of Si is concluded from the information found for Ge-sites of such a sample assuming a constant sample composition during the annealing process. This is due to the fact, that bulk sensitive study of the local structure of Si is very difficult. Here, XRS provides a very valuable alternative to study the local chemical environment of the Si-rich part by measuring e.g. the Si $L_{2/3}$-edge at high temperature. The feasibility of such measurements and a capability to distinguish between different oxidation states of Si ranging from 0^+ to 4^+ is demonstrated within this thesis and in reference [203]. Here two sample, namely $Ge_{0.04}SiO_{1.18}$ (sample A) and $GeSiO_{2.35}$ (sample B) were prepared by evaporating Si, SiO_2, Ge, and GeO_2 precursors at different conditions. Detailed information on sample preparation and characterization can be found in reference [203]. Subsequently, 1 μm thick layers deposited on a molybdenum substrate were annealed to different temperatures up to 1100 °C in nitrogen and argon atmosphere. The inert gases are used in order to conserve the sample stoichiometry

[230, 337]. Temperature induced changes of the local structure in Ge_xSiO_y was studied by XAS at the Ge K-edge. The binding energy of the 1s electrons of Ge is at about 11.103 keV [287] thus allowing bulk sensitive XAS measurements. Due to the different composition of samples A and B completely different changes of the local structure at high temperature can be observed. The composition of sample A is strongly dominated by Ge^{0+} (SiGe) with a small amount of Ge^{4+} (GeO_2). Furthermore, occurrence of Ge in intermediate oxidation states (Ge^{1+}, Ge^{2+}, and Ge^{3+}, so called sub-oxides [233]) cannot be excluded but its concentration is below the detection limits. No significant changes of the local structure of Ge could be observed after annealing up to 550 °C. Here, Ge still predominantly appears in the Ge^{0+} and Ge^{4+} clusters, which are embedded in a silica matrix. At higher temperatures up to 1100 °C significant changes of the local structure of Ge occur resulting in an increase of the contribution of Ge^{0+} on costs of a reduction of Ge^{4+}. This reaction is initiated by an increased mobility of atoms at high temperature and the Ge^{4+} contribution is probably reduced by unsaturated Si content of the sample due to the fact, that the SiO_2 configuration if preferred compared to the GeO_2 configuration according to its lower configuration energy (ΔH_{SiO_2} = -902 kcal/mol; ΔH_{GeO_2} = -538 kcal/mol [337]). As a consequence of a low Ge amount ($x \approx 0.04$), SiGe cluster formation occurs already after the preparation process and Ge sub-oxide formation is suppressed due to the oxygen deficit on the Si-site ($y < 2$). Additional Ge cluster formation could be observed driven by a GeO_2 reduction by the unsaturated silica matrix at temperatures between 550 °C and 1100 °C. In the case of sample B the native state after the preparation process is again dominated by Ge^{0+} with a lower Ge^{4+} fraction but here, significant amount of Ge sub-oxides occurs due to a higher Ge content in sample B ($x \approx 1$). In contrast to sample A significant changes of the local structure of Ge could be observed already at temperatures above 300 °C. Here, a phase separation according to the reaction $GeO_x \rightarrow Ge + GeO_2$ can be observed, well known from binary GeO_x compounds [230, 336, 337]. The phase separation end between 600 °C and 700 °C and only Ge and GeO_2 can be found on the Ge-sites. At higher temperatures above 700 °C GeO_2 is further reduced by the silica matrix, similar to the process found for sample A. In addition, XRD results reveal a formation of Si nanocrystals with a mean size of (2.4 ± 0.2) nm in sample A after annealing at 1000 °C. In sample B Ge nanocrystal formation can be found with a mean size of (2.3 ± 0.2) nm at temperatures above 700 °C, which increases up to (23.9 ± 2.4) nm at about 1000 °C [203].

The local electronic structure of Ge could be determined by XAS at the Ge K-edge and the temperature induced formation of Ge (or SiGe) could be studied. The understanding of processes leading to the nanocrystal formation are essential in order to tune the properties of nanocrystals. However, the luminescent properties of Ge_xSiO_y are extremely affected by the composition of the silica matrix. Similar systematic study of the local structure of Si is required in order to understand temperature induced silica matrix formation, which embeds semiconductor nanocrystals. Furthermore, the matrix is usually assumed to be dominated by pure SiO_2, which though depends on the sample composition. Here, especially the presence of sub-oxides might be dominant at low and intermediate temperatures, which can be hardly screened experimentally. In such a case, measurements of the Si $L_{2/3}$-edge by XRS reveal bulk sensitive and reliable information

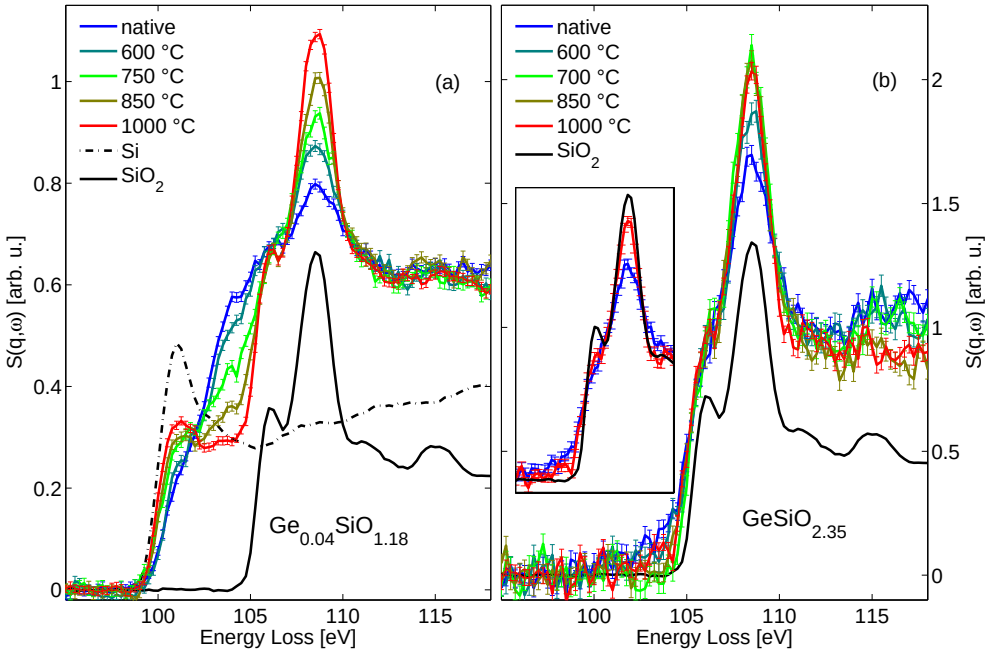

Figure A.1.: Temperature dependent measurements of the Si $L_{2/3}$-edge on $Ge_{0.04}SiO_{1.18}$ (a) and $GeSiO_{2.35}$ (b) in comparison with the spectra of crystalline references Si and SiO_2 [203].

about the composition of the SiO_y matrix at different temperatures, hardly accessible by other experimental methods [73, 233].

A systematic study of the Si $L_{2/3}$-edge on the same samples A and B in order to study temperature induced changes of the local electronic structure of the silica matrix is presented in figure A.1. The spectrum of the as-prepared sample A shows a significantly different spectral shape compared to the reference spectra measured on polycrystalline Si and SiO_2. The spectrum of pure Si shows a typical absorption edge at about 99.7 eV, which is in good agreement with the literature [287], while the spectral shape of SiO_2 was discussed in section 6.1. The spectral shape of the as-prepared sample A shows no sharp features and can be described by a continuously increasing intensity with a maximum at 108 eV rather than a superposition of the Si (Si^{0+}) and SiO_2 (Si^{4+}) reference spectra. Thus, the local structure of the SiO_y matrix is strongly dominated by Si sub-oxides (Si^{1+}, Si^{2+}, and Si^{3+}) for $y \approx 1.18$ according to earlier results on binary SiO [73, 233]. Very strong spectral changes of the single broad and structureless maximum can be found at the Si $L_{2/3}$-edge with increasing temperature. The spectral shape of the Si $L_{2/3}$-edge at the highest temperature of about 1000 °C is changed and can be described by a superposition of pure Si^{0+} and Si^{4+} and only a negligible contribution of sub-oxides can be observed. Thereby, temperature induced SiO_y matrix formation is driven by a formation of Si and SiO_2 on costs of a reduction of sub-oxides, which

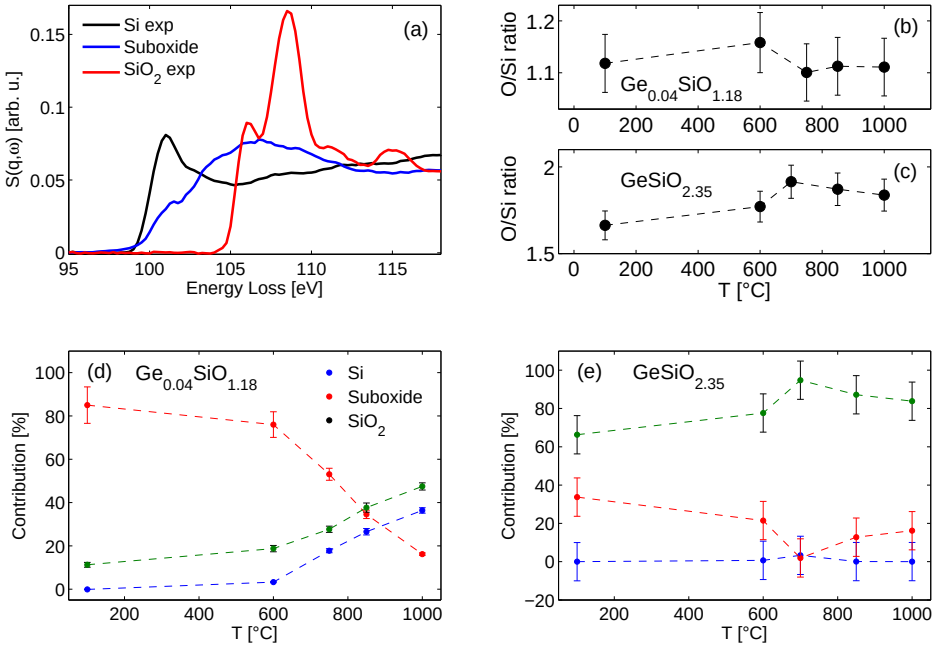

Figure A.2.: Results of the determination of the contribution of different silicon oxide phases in (d) $Ge_{0.04}SiO_{1.18}$ and (e) $GeSiO_{2.35}$ based on the reference spectra presented in (a) [233]. The estimated total O/Si ratios for both samples are shown in (b) and (c) [203].

can be described by the reaction $SiO_y \rightarrow Si + SiO_2$. In contrast, sample B ($y \approx 2.35$) shows a spectral shape in its as-prepared state very similar to SiO_2 together with a very small contribution of sub-oxides, while no intensity is observed at the vicinity of the Si $L_{2/3}$-edge indicative for elemental Si. At temperatures above 600 °C the spectral weight in the energy loss region of the sub-oxide contribution becomes lower but still not negligible even at the highest temperature of 1000 °C. This is supported by the fact, that the pre-edge shoulder, which can be found in the SiO_2 spectrum, is present but strongly suppressed in the spectrum of sample B at 1000 °C. Therefore, the Si-sites of the sample B are strongly dominated by SiO_2 with a weak amount of sub-oxides and the contribution of sub-oxides is significantly reduced with increasing temperature. The matrix tends to become SiO_2-like but still small but not negligible amount of sub-oxides is present.

Although the temperature behavior of the silica matrix in Ge_xSiO_y with different compositions could be studied on the way to nanocrystal formation adequately, even more quantitative information about the fractions of single oxidation states can be obtained from the experimental data. Therefore, reference spectra of Si, SiO_2 and sub-oxides were fitted to the spectra of samples A and B annealed to different temperatures. Unfortunately, pure sub-oxide reference samples are very difficult to prepare and thus were not available for the experiment. Thus, atomic structure of a Si cluster embedded in SiO_2

was calculated using molecular dynamics (MD) simulations and the spectrum of sub-oxides was calculated on the basis of the interface between the Si cluster and the SiO_2 matrix [233]. This model was already successfully applied in order to study the local electronic structure of SiO [231]. Using these spectra as references allows to determine the temperature behavior of the O/Si fraction in order to study the GeO_2 reduction by Si as well as the composition of the Si oxide matrix.
Results obtained from the fit of reference spectra for Si^{0+}, Si^{4+} and sub-oxides (figure A.2 (a)) in the energy loss region between 97 and 113 eV reveal very important information about the temperature behavior of the O/Si fraction at the Si-sites in order to conclude the O/Ge ratio at the Ge-sites. In the case of sample A the determined O/Si ratio is 1.12 ± 0.03 (figure A.2 (b)), which remains constant with increasing temperature with respect to the errorbars. This result is in very good agreement with the sample stiochiometry of the $Ge_{0.04}SiO_{1.18}$ sample. The O/Si ratio obtained for sample B is 1.85 ± 0.06 (figure A.2 (c)), which significantly differs from the sample composition of $GeSiO_{2.35}$. Based on the O/Si ratio of 1.85 ± 0.06 at Si-sites for sample B the O/Ge ratio of 0.50 ± 0.06 at Ge-sites can be followed from the sample stiochiometry. Neglecting the Ge sub-oxide contribution a O/Ge ratio of 0.38 ± 0.05 can be obtained from the Ge K-edges, which is in qualitative agreement. The reason for the difference is the fact, that the spectrum calculated on the basis of MD simulation is only a first order approximation. Furthermore, the Si/SiO_2 cluster was calculated for SiO_y with $y = 1$, which is different from the composition of the sample B ($y = 1.18$) and the calculated spectra might be not fully representative especially for the sub-oxides dominated as-prepared sample B.
The fitting procedure allows to extract relative fractions of the oxidation states Si^{0+}, Si^{4+} and sub-oxides. The as-prepared sample A is strongly dominated by Si sub-oxides and its relative fraction can be estimated to about 80%, as shown in figure A.2 (d). This value is significantly higher than a contribution of about 40 % found in amorphous SiO [231], which might be due to different sample preparation conditions. The sub-oxide contribution drops to about 16 % at 1000 °C while the Si^{0+} and Si^{4+} contributions increase up to 36 % and 48 %, respectively. This is a clear indication of the temperature induced phase separation. However, absolute values might be not representative due to the fact, that the MD simulations are only an approximation and the absolute values might be overestimated but general trends are still reliable. An increase of the O/Si fraction at Si-sites due to the reduction of GeO_2 cannot be observed probably due to a low amount of Ge in sample A. The same fitting procedure applied to sample B reveals a Si content of less than 2 % independent on the temperature (figure A.2 (e)). The as-prepared sample is dominated by about 66 % of SiO_2 with an additional sub-oxide fraction of around 33 %. With increasing temperature the SiO_2 content increases up to 84 % while the sub-oxide contribution drops to about 16 %.
Temperature induced phase separation and nanocrystal formation could be observed by XRD, XAS at the Ge K-edge and XRS at the Si $L_{2/3}$-edge. Only a combination of three experimental techniques provides a complete picture about the processes leading to silica matrix embedded Ge nanocrystals. Here, especially XRS provides a deep insight into the mechanism of the matrix formation, hardly accessible by other techniques. Although

knowledge about the phase separation and GeO_2 reduction at the Ge-sites could be extracted from XAS measurements, XRS results provide quantitative information about the temperature related behavior of the local structure of the silica matrix. The Ge-sites of the sample with oxygen deficit ($Ge_{0.04}SiO_{1.18}$) are strongly dominated by SiGe and GeO_2 clusters surrounded by Si sub-oxide dominated matrix. After annealing to above 700 °C a phase separation of Si sub-oxides in Si and SiO_2 occurs. Subsequently, Si formed during the phase separation is used to bond oxygen atoms from GeO_2 clusters resulting in SiO_2 and Ge. The GeO_2 reduction is complete at above 1000 °C. In samples with oxygen excess ($GeSiO_{2.35}$) Ge sub-oxides are reduced in the temperature range from 300 °C to about 700 °C while fractions of Ge and GeO_2 increase. Subsequently, GeO_2 is reduced by the silica matrix at temperatures above 700 °C resulting in Ge nanocrystals embedded by an SiO_2 matrix.

B. The 3j- and 6J-symbols

In chapter 3.2.2, a brief overview is given on how to calculate relative energies of electronic levels according to the atomic multiplet model. Therefore, term symbols for every multi-electron symmetry state must be determined and combined with the Hamiltonian, which describes the electron-electron interaction. Subsequently, the angular parts of the matrix elements f_k and g_k must be calculated. In the simple case of two electrons, the parameters f_k and g_k are given by

$$\begin{aligned} f_k &= (2l_1+1)(2l_2+1)(-1)^L \begin{pmatrix} l_1 & k & l_1 \\ 0 & 0 & 0 \end{pmatrix} \begin{pmatrix} l_2 & k & l_2 \\ 0 & 0 & 0 \end{pmatrix} \begin{Bmatrix} l_1 & l_2 & L \\ l_2 & l_1 & k \end{Bmatrix} \\ g_k &= (2l_1+1)(2l_2+1)(-1)^S \begin{pmatrix} l_1 & k & l_2 \\ 0 & 0 & 0 \end{pmatrix} \begin{pmatrix} l_1 & k & l_2 \\ 0 & 0 & 0 \end{pmatrix} \begin{Bmatrix} l_1 & l_2 & L \\ l_1 & l_2 & k \end{Bmatrix}. \end{aligned} \tag{B.1}$$

For f_k, k must be an even number ranging from 0 to two times the lowest l (otherwise, one of the $3j$-symbols is 0). For g_k, k is even if $l_1 + l_2$ is even and k is odd if $l_1 + l_2$ is odd. The maximum value is $l_1 + l_2$. Furthermore, g_k is not present if both electrons are inside the same orbital. To calculate the $3j$- and $6J$-symbols for a certain problem, following expressions can be used.
The 3j- symbol is a function of six arguments and is defined as

$$\begin{aligned} &\begin{pmatrix} j_1 & j_2 & j_3 \\ m_1 & m_2 & m_3 \end{pmatrix} \equiv \delta_{m_1+m_2+m_3,0}(-1)^{j_1-j_2-m_3} \\ &\times \Big[\tfrac{(j_1+j_2-j_3)!(j_1-j_2+j_3)!(-j_1+j_2+j_3)!(j_1-m_1)!(j_1+m_1)!(j_2-m_2)!(j_2+m_2)!(j_3-m_3)!(j_3+m_3)!}{(j_1+j_2+j_3+1)!}\Big]^{1/2} \\ &\times \textstyle\sum_k \frac{(-1)^k}{k!(j_1+j_2-j_3-k)!(j_1-m_1-k)!(j_2+m_2-k)!(j_3-j_2+m_1+k)!(j_3-j_1-m_2+k)!}. \end{aligned} \tag{B.2}$$

Here, the summation integer k can be estimated using the relation $\max(0,\ j_2 - j_3 - m_1,\ j_1 - j_3 + m_2) \le k \le \min(j_1 + j_2 - j_3,\ j_1 - m_1,\ j_2 - m_2)$.
The 6J- symbol can be written as

$$\begin{aligned} &\begin{Bmatrix} j_1 & j_2 & j_3 \\ l_1 & l_2 & l_3 \end{Bmatrix} \equiv \Delta(j_1,j_2,j_3)\Delta(j_1,l_2,l_3)\Delta(l_1,j_2,l_3)\Delta(l_1,l_2,j_3) \\ &\times \textstyle\sum_k \Big[\frac{(-1)^k(k+1)!}{(k-j_1-j_2-j_3)!(k-j_1-l_2-l_3)!(k-l_1-j_2-l_3)!(k-l_1-l_2-j_3)!} \\ &\times \tfrac{1}{(j_1+j_2+l_1+l_2-k)!(j_2+j_3+l_2+l_3-k)!(j_3+j_1+l_3+l_1-k)!}\Big], \end{aligned} \tag{B.3}$$

where

$$\Delta(abc) = \Big[\frac{(a+b-c)!(a-b+c)!(-a+b+c)!}{(a+b+c+1)!}\Big]^{1/2}. \tag{B.4}$$

and the summation integer k covers the range defined by $\max(j_1+j_2+j_3,\ j_1+l_2+l_3,\ l_1+j_2+l_3,\ l_1+l_2+j_3) \leq\ k\ \leq \min(j_1+j_2+l_1+l_2,\ j_2+j_3+l_2+l_3,\ j_3+j_1+l_3+l_1)$. Now, the matrix elements for different two-electron configurations can be calculated using equations (3.19), (3.20) and (B.2)-(B.4). In section 3.2.2 values for the matrix elements for the 1s2s configuration were presented, which can now be calculated in detail.

The $1s^1 2s^1$ configuration can be devided into the $^1S_0$ and $^3S_1$ symmetry states. For both, $l_1 = l_2 = 0$. Thus, $k_{min} = k_{max} = k = 0$. Furthermore, the electrons are not in the same shell and only f_0 and g_0 are present. According to equations (B.2)-(B.4), f_0 and g_0 can be calculated for the $^1S_0$ state as

$$\begin{aligned} f_0 &= 1 \cdot \begin{pmatrix} 0 & 0 & 0 \\ 0 & 0 & 0 \end{pmatrix} \begin{pmatrix} 0 & 0 & 0 \\ 0 & 0 & 0 \end{pmatrix} \begin{Bmatrix} 0 & 0 & 0 \\ 0 & 0 & 0 \end{Bmatrix} = 1 \\ g_0 &= 1 \cdot \begin{pmatrix} 0 & 0 & 0 \\ 0 & 0 & 0 \end{pmatrix} \begin{pmatrix} 0 & 0 & 0 \\ 0 & 0 & 0 \end{pmatrix} \begin{Bmatrix} 0 & 0 & 0 \\ 0 & 0 & 0 \end{Bmatrix} = 1. \end{aligned} \tag{B.5}$$

For $^3S_1$, f_0 is the same but the total spin quantum number is equal to 1. Thus, g_0 is

$$g_0 = (-1) \cdot \begin{pmatrix} 0 & 0 & 0 \\ 0 & 0 & 0 \end{pmatrix} \begin{pmatrix} 0 & 0 & 0 \\ 0 & 0 & 0 \end{pmatrix} \begin{Bmatrix} 0 & 0 & 0 \\ 0 & 0 & 0 \end{Bmatrix} = -1. \tag{B.6}$$

The angular parts obtained for the $1s^1 2s^1$ configuration are the same as those presented in equation (3.21).

Bibliography

[1] M. Akaogi, H. Yusa, K. Shiraishi, and T. Suzuki. Thermodynamic properties of α-quartz, coesite, and stishovite and equilibrium phase relations at high pressures and high temperatures. *Journal of Geophysical Research: Solid Earth*, 100(B11):22337 – 22347, 1995. [49]

[2] D. Alfè, M. J. Gillan, and G. D. Price. Ab initio chemical potentials of solid and liquid solutions and the chemistry of the Earth's core. *The Journal of Chemical Physics*, 116(16):7127 – 7136, 2002. [1]

[3] J. Als-Nielsen and D. McMorrow. *Elements of Modern X-ray Physics*. Wiley, 2011. [4, 7, 45]

[4] Andor Technology. User guide for the Shamrock SR-163 spectrograph. `http://www.lot-qd.de/files/downloads/andor/en/ms_sr163manual_deen01.pdf`, 2008. [IX, 92]

[5] D. Andrault, G. Fiquet, M. Kunz, F. Visocekas, and D. Häusermann. The Orthorhombic Structure of Iron: An in Situ Study at High-Temperature and High-Pressure. *Science*, 278(5339):831–834, 1997. [85]

[6] G.A. Andreozzi. *Periodico di mineralogia: Synthetic spinel in the (Mg,Fe^{2+},Zn)(Al,Fe^{3+})$_2O_4$ system*, volume 68. Consiglio nazionale delle ricerche (Italy), 1999. [44]

[7] G.A. Andreozzi and S. Lucchesi. Intersite distribution of Fe^{2+} and Mg in the spinel (sensu structo)-hercynite series by single-crystal X-raydiffraction. *American Mineralogist*, 87:1113 – 1120, 2002. [43]

[8] R. J. Angel and J. M. Jackson. Elasticity and equation of state of orthoenstatite, $MgSiO_3$. *American Mineralogist*, 87:558 – 561, 2002. [51]

[9] G. Aquilanti, S. Pascarelli, O. Mathon, M. Muñoz, O. Narygina, and L. Dubrovinsky. Development of micro-XANES mapping in the diamond anvil cell. *Journal of Synchrotron Radiation*, 16(3):376 – 379, May 2009. [83]

[10] M. Ardyanian, H. Rinnert, X. Devaux, and M. Vergnat. Structure and photoluminescence properties of evaporated GeO_x thin films. *Applied Physics Letters*, 89(1), 2006. [103]

[11] D. A. Arms, T. J. Graber, A. T. Macrander, R. O. Simmons, M. Schwoerer-Böhning, and Y. Zhong. Excitons in bulk liquid ^{4}He. *Phys. Rev. B*, 71:233107, 2005. [2, 16]

[12] D. A. Arms, R. O. Simmons, M. Schwoerer-Böhning, A. T. Macrander, and T. J. Graber. Exciton dispersion and electronic excitations in hcp ^{4}He. *Phys. Rev. Lett.*, 87:156402, 2001. [2, 16]

[13] F. Aryasetiawan and O. Gunnarsson. The GW method. *Reports on Progress in Physics*, 61(3):237, 1998. [18]

[14] D. Asakura, M. Okubo, Y. Mizuno, T. Kudo, H. Zhou, K. Amemiya, F. M. F. de Groot, J.-L. Chen, W.-C. Wang, P.-A. Glans, C. Chang, J. Guo, and I. Honma. Electron delocalization in cyanide-bridged coordination polymer electrodes for Li-ion batteries studied by soft x-ray absorption spectroscopy. *Phys. Rev. B*, 84:045117, 2011. [25]

[15] J. Badro, G. Fiquet, F. Guyot, J.-P. Rueff, V. V. Struzhkin, G. Vankó, and G. Monaco. Iron Partitioning in Earth's Mantle: Toward a Deep Lower Mantle Discontinuity. *Science*, 300(5620):789–791, 2003. [1]

[16] J. Badro, V. V. Struzhkin, J. Shu, R. J. Hemley, H.-k. Mao, C.-c. Kao, J.-P. Rueff, and G. Shen. Magnetism in FeO at Megabar Pressures from X-Ray Emission Spectroscopy. *Phys. Rev. Lett.*, 83:4101 – 4104, 1999. [72]

[17] M. Balasubramanian, C. S. Johnson, J. O. Cross, G. T. Seidler, T. T. Fister, E. A. Stern, C. Hamner, and S. O. Mariager. Fine structure and chemical shifts in nonresonant inelastic x-ray scattering from Li-intercalated graphite. *Applied Physics Letters*, 91(3), 2007. [14]

[18] P. Ball. Water - an enduring mystery. *Nature*, 452(7185):291–292, 2008. [16]

[19] W. A. Bassett. The birth and development of laser heating in diamond anvil cells. *Review of Scientific Instruments*, 72(2):1270 – 1272, 2001. [84]

[20] W. A. Bassett. High pressure-temperature aqueous systems in the hydrothermal diamond anvil cell (HDAC). *European Journal of Mineralogy*, 15(5):773 – 780, 2003. [83]

[21] N. Bergmann, S. Bonhommeau, K. M. Lange, S. M. Greil, S. Eisebitt, F. M. F. de Groot, M. Chergui, and E. F. Aziz. On the enzymatic activity of catalase: an iron L-edge X-ray absorption study of the active centre. *Phys. Chem. Chem. Phys.*, 12:4827–4832, 2010. [54]

[22] U. Bergmann, A. Di Cicco, P. Wernet, E. Principi, P. Glatzel, and A. Nilsson. Nearest-neighbor oxygen distances in liquid water and ice observed by x-ray raman based extended x-ray absorption fine structure. *The Journal of Chemical Physics*, 127(17):174504, 2007. [14, 16]

[23] U. Bergmann, P. Glatzel, and Cramer S. P. Bulk-sensitive XAS characterization of light elements: from X-ray Raman scattering to X-ray Raman spectroscopy. *Microchemical Journal*, 71(2 & 3):221 – 230, 2002. [11]

[24] U. Bergmann, Ph. Wernet, P. Glatzel, M. Cavalleri, L. G. M. Pettersson, A. Nilsson, and S. P. Cramer. X-ray Raman spectroscopy at the oxygen K edge of water and ice: Implications on local structure models. *Phys. Rev. B*, 66:092107, 2002. [14, 16]

[25] A. J. Berry, G. M. Yaxley, A. B. Woodland, and G. J. Foran. A XANES calibration for determining the oxidation state of iron in mantle garnet. *Chemical Geology*, 278(1 - 2):31 – 37, 2010. [2]

[26] F. Biggs, L.B. Mendelsohn, and J.B. Mann. Hartree-fock compton profiles for the elements. *Atomic Data and Nuclear Data Tables*, 16(3):201 – 309, 1975. [63, 75]

[27] N. Binggeli and James R. Chelikowsky. Structural transformation of quartz at high pressures. *Nature*, 353(6342):344 – 346, 1991. [48]

[28] M. Blume. Magnetic scattering of x rays (invited). *Journal of Applied Physics*, 57(8):3615–3618, 1985. [5]

[29] R. Boehler. High-pressure experiments and the phase diagram of lower mantle and core materials. *Reviews of Geophysics*, 38(2):221 – 245, 2000. [85]

[30] R. Boehler, H. G. Musshoff, R. Ditz, G. Aquilanti, and A. Trapananti. Portable laser-heating stand for synchrotron applications. *Review of Scientific Instruments*, 80(4):045103, 2009. [83, 84, 85, 86, 88]

[31] R. Boehler, N. von Bargen, and A. Chopelas. Melting, thermal expansion, and phase transitions of iron at high pressures. *Journal of Geophysical Research: Solid Earth*, 95(B13):21731 – 1736, 1990. [85]

[32] S. Bonhommeau, N. Pontius, S. Cobo, L. Salmon, F. M. F. de Groot, G. Molnar, A. Bousseksou, H. A. Durr, and W. Eberhardt. Metal-to-ligand and ligand-to-metal charge transfer in thin films of Prussian blue analogues investigated by X-ray absorption spectroscopy. *Phys. Chem. Chem. Phys.*, 10:5882–5889, 2008. [54]

[33] E. Boulard, N. Menguy, A. Auzende, K. Benzerara, H. Bureau, D. Antonangeli, A. Corgne, G. Morard, J. Siebert, J. Perrillat, F. J. Guyot, and G. Fiquet. Experimental investigation of the stability of Fe-rich carbonates in the lower mantle. *Journal of Geophysical Research*, 117:B02208, 2012. [2]

[34] F. Bourdelle, K. Benzerara, O. Beyssac, J. Cosmidis, D. R. Neuville, Jr. Brown, G. E., and E. Paineau. Quantification of the ferric/ferrous iron ratio in silicates by scanning transmission X-ray microscopy at the Fe $L_{2,3}$ edges. *Contributions to Mineralogy and Petrology*, 166(2):423 – 434, 2013. [2]

[35] D. T. Bowron, M. H. Krisch, A. C. Barnes, J. L. Finney, A. Kaprolat, and M. Lorenzen. X-ray Raman scattering from the oxygen K edge in liquid and solid H_2O. *Phys. Rev. B*, 62:R9223–R9227, 2000. [14]

[36] J. A. Bradley, K. T. Moore, G. van der Laan, J. P. Bradley, and R. A. Gordon. Core and shallow-core d- to f-shell excitations in rare-earth metals. *Phys. Rev. B*, 84:205105, 2011. [11, 15]

[37] J. A. Bradley, P. Yang, E. R. Batista, K. S. Boland, C. J. Burns, D. L. Clark, S. D. Conradson, S. A. Kozimor, R. L. Martin, G. T. Seidler, B. L. Scott, D. K. Shuh, T. Tyliszczak, M. P. Wilkerson, and L. E. Wolfsberg. Experimental and Theoretical Comparison of the O K-Edge Nonresonant Inelastic X-ray Scattering and X-ray Absorption Spectra of $NaReO_4$. *Journal of the American Chemical Society*, 132(39):13914–13921, 2010. [14]

[38] W. H. Bragg and W. L. Bragg. The reflection of x-rays by crystals. *Proceedings of the Royal Society of London. Series A*, 88(605):428–438, 1913. [45]

[39] P.H. Butler. *Point group symmetry applications: methods and tables*. Plenum Press, 1981. [27, 30]

[40] Y. Q. Cai, P. Chow, C. C. Chen, H. Ishii, K. L. Tsang, C. C. Kao, K. S. Liang, and C. T. Chen. Optical Design and Performance of the Taiwan Inelastic X-Ray Scattering Beamline (BL12XU) at SPring-8. *AIP Conference Proceedings*, 705(1):340–343, 2004. [40]

[41] Y. Q. Cai, H.-K. Mao, P. C. Chow, J. S. Tse, Y. Ma, S. Patchkovskii, J. F. Shu, V. Struzhkin, R. J. Hemley, H. Ishii, C. C. Chen, I. Jarrige, C. T. Chen, S. R. Shieh, E. P. Huang, and C. C. Kao. Ordering of Hydrogen Bonds in High-Pressure Low-Temperature H_2O. *Phys. Rev. Lett.*, 94:025502, 2005. [16]

[42] W. A. Caliebe. *Inelastic X-Ray Scattering with High Energy Resolution*. dissertation, Christian-Albrechts Universität zu Kiel, 1997. [14, 15]

[43] C. C. Calvert, A. Brown, and R. Brydson. Determination of the local chemistry of iron in inorganic and organic materials. *Journal of Electron Spectroscopy and Related Phenomena*, 143(2 - 3):173 – 187, 2005. [VIII, 2, 55, 56, 57]

[44] L. Cavé, T. Al, D. Loomer, S Cogswell, and L. Weaver. A STEM/EELS method for mapping iron valence ratios in oxide minerals. *Micron*, 37(4):301 – 309, 2006. [2]

[45] Maria K. Y. Chan, Eric L. Shirley, Naba K. Karan, Mahalingam Balasubramanian, Yang Ren, Jeffrey P. Greeley, and Tim T. Fister. Structure of Lithium Peroxide. *The Journal of Physical Chemistry Letters*, 2(19):2483–2486, 2011. [14, 15]

[46] T. C. Chang, F.-Y. Jian, S.-C Chen, and Y.-T. Tsai. Developments in nanocrystal memory. *Materials Today*, 14(12):608 – 615, 2011. [103]

[47] G. N.I. Clark, C. D. Cappa, J. D. Smith, R. J. Saykally, and T. Head-Gordon. The structure of ambient water. *Molecular Physics*, 108(11):1415–1433, 2010. [16]

[48] S. P. Jr. Clark. Absorption spectra of some silicates in the visible and near infrared. *American Mineralogist*, 42:732–742, 1957. [1]

[49] E. Collart, A. Shukla, F. Gélébart, M. Morand, C. Malgrange, N. Bardou, A. Madouri, and J.-L. Pelouard. Spherically bent analyzers for resonant inelastic X-ray scattering with intrinsic resolution below 200 meV. *Journal of Synchrotron Radiation*, 12(4):473–478, 2005. [12]

[50] C. Colliex, T. Manoubi, and C. Ortiz. Electron-energy-loss-spectroscopy near-edge fine structures in the iron-oxygen system. *Phys. Rev. B*, 44:11402 – 11411, 1991. [43, 55, 59]

[51] E.U. Condon and G.H. Shortley. *The Theory of Atomic Spectra*. Cambridge University Press, 1935. [20]

[52] H. Conrad, F. Lehmkühler, C. Sternemann, A. Sakko, D. Paschek, L. Simonelli, S Huotari, O. Feroughi, M. Tolan, and K. Hämäläinen. Tetrahydrofuran Clathrate Hydrate Formation. *Phys. Rev. Lett.*, 103:218301, 2009. [14]

[53] M. J. Cooper. Compton scattering and electron momentum determination. *Reports on Progress in Physics*, 48(4):415, 1985. [8]

[54] R.D. Cowan. *The Theory of Atomic Structure and Spectra*. Los Alamos series in basic and applied sciences. University of California Press, 1981. [18, 20, 21, 22, 24, 25, 27]

[55] J. P. Crocombette, M. Pollak, F. Jollet, N. Thromat, and M. Gautier-Soyer. X-ray-absorption spectroscopy at the Fe $L_{2,3}$ threshold in iron oxides. *Phys. Rev. B*, 52:3143 – 3150, 1995. [2, 54]

[56] F. M. F. de Groot. Multiplet effects in x-ray spectroscopy. *Coordination Chemistry Reviews*, 249(1-2):31–63, 2005. Synchrotron Radiation in Inorganic and Bioinorganic Chemistry. [22, 23, 27, 60, 64]

[57] F. M. F. de Groot. Ligand and metal x-ray absorption in transition metal complexes. *Inorganica Chimica Acta*, 361(4):850 – 856, 2008. [64]

[58] F. M. F. de Groot, J. C. Fuggle, B. T. Thole, and G. A. Sawatzky. 2p x-ray absorption of 3d transition-metal compounds: An atomic multiplet description including the crystal field. *Phys. Rev. B*, 42:5459–5468, 1990. [31]

[59] F. M. F. de Groot, J. C. Fuggle, B. T. Thole, and G. A. Sawatzky. $L_{2,3}$ x-ray-absorption edges of d^0 compounds: K^+, Ca^{2+}, Sc^{3+}, and Ti^{4+} in Oh (octahedral) symmetry. *Phys. Rev. B*, 41:928–937, 1990. [31]

[60] F. M. F. de Groot, P. Glatzel, U. Bergmann, P. A. van Aken, R. A. Barrea, S. Klemme, M. Hävecker, A. Knop-Gericke, W. M. Heijboer, and B. M. Weckhuysen. 1s2p Resonant Inelastic X-ray Scattering of Iron Oxides. *The Journal of Physical Chemistry B*, 109(44):20751–20762, 2005. [34, 36, 54, 60, 64, 80]

[61] F. M. F. De Groot and A. Kotani. *Core level spectroscopy of solids*. CRC Press, 2008. [XI, 7, 10, 18, 20, 21, 22, 23, 24, 25, 27, 28, 29, 30, 32, 54]

[62] C. De Nadaï, A. Demourgues, J. Grannec, and F. M. F. de Groot. $L_{2,3}$ x-ray absorption spectroscopy and multiplet calculations for KMF_3 and K_2NaMF_6 (M=Ni,Cu). *Phys. Rev. B*, 63:125123, 2001. [25]

[63] S. Doniach, P. M. Platzman, and J. T. Yue. X-Ray Raman Scattering in Metals. *Phys. Rev. B*, 4:3345–3350, 1971. [7, 9]

[64] L. Dubrovinsky, K. Glazyrin, C. McCammon, O. Narygina, E. Greenberg, S. Übelhack, A. I. Chumakov, S. Pascarelli, V. Prakapenka, J. Bock, and N. Dubrovinskaia. Portable laser-heating system for diamond anvil cells. *Journal of Synchrotron Radiation*, 16(6):737 – 741, Nov 2009. [83, 84, 85]

[65] T. S. Duffy. Mineralogy at the extremes. *Nature*, 451(7176):269 – 270, 2008. [1, 83]

[66] R.A. Dunlap, D.A. Eelman, and G.R. MacKay. A Mössbauer effect investigation of correlated hyperfine parameters in natural glasses (tektites). *Journal of Non-Crystalline Solids*, 223(1 - 2):141 – 146, 1998. [2]

[67] Jackson W. E., F. Farges, M. Yeager, P. A. Mabrouk, S. Rossano, G. A. Waychunas, E. I. Solomon, and G. E. Jr Brown. Multi-spectroscopic study of Fe(II) in silicate glasses: Implications for the coordination environment of Fe(II) in silicate melts. *Geochimica et Cosmochimica Acta*, 69(17):4315 – 4332, 2005. [71]

[68] C. Eckart. The Application of Group theory to the Quantum Dynamics of Monatomic Systems. *Rev. Mod. Phys.*, 2:305 – 380, 1930. [24]

[69] N. J. English and J. S. Tse. Density Fluctuations in Liquid Water. *Phys. Rev. Lett.*, 106:037801, Jan 2011. [16]

[70] M. I. Eremets, A. G. Gavriliuk, N. R. Serebryanaya, I. A. Trojan, D. A. Dzivenko, R. Boehler, H. K. Mao, and R. J. Hemley. Structural transformation of molecular nitrogen to a single-bonded atomic state at high pressures. *The Journal of Chemical Physics*, 121(22):11296–11300, 2004. [15, 73]

[71] Y. Fei, C. T. Prewitt, H.-k. Mao, and C. M. Bertka. Structure and Density of FeS at High Pressure and High Temperature and the Internal Structure of Mars. *Science*, 268(5219):1892 – 1894, 1995. [2, 74]

[72] Y. Feng, G. T. Seidler, J. O. Cross, A. T. Macrander, and J. J. Rehr. Role of inversion symmetry and multipole effects in nonresonant x-ray Raman scattering from icosahedral B_4C. *Phys. Rev. B*, 69:125402, 2004. [14]

[73] O. M. Feroughi, C. Sternemann, Ch. J. Sahle, M. A. Schroer, H. Sternemann, H. Conrad, A. Hohl, G. T. Seidler, J. Bradley, T. T. Fister, M. Balasubramanian, A. Sakko, K. Pirkkalainen, K. Hämäläinen, and M. Tolan. Phase separation and Si nanocrystal formation in bulk SiO studied by x-ray scattering. *Applied Physics Letters*, 96(8):081912, 2010. [15, 44, 49, 51, 105]

[74] G. Fierro, G. Moretti, G. Ferraris, and G. B. Andreozzi. A Mössbauer and structural investigation of Fe-ZSM-5 catalysts: Influence of Fe oxide nanoparticles size on the catalytic behaviour for the NO-SCR by C3H8. *Applied Catalysis B: Environmental*, 102(1 - 2):215 – 223, 2011. [2]

[75] T. T. Fister, D. D. Fong, J. A. Eastman, H. Iddir, P. Zapol, P. H. Fuoss, M. Balasubramanian, R. A. Gordon, K. R. Balasubramaniam, and P. A. Salvador. Total-Reflection Inelastic X-Ray Scattering from a 10-nm Thick $La_{0.6}Sr_{0.4}CoO_3$ Thin Film. *Phys. Rev. Lett.*, 106:037401, 2011. [15]

[76] T. T. Fister, K. P. Nagle, F. D. Vila, G. T. Seidler, C. Hamner, J. O. Cross, and J. J. Rehr. Intermediate-range order in water ices: Nonresonant inelastic x-ray scattering measurements and real-space full multiple scattering calculations. *Phys. Rev. B*, 79:174117, 2009. [14, 61, 62]

[77] T. T. Fister, G. T. Seidler, J. O. Cross, J. J. Rehr, and J. A. Soininen. Measurement of the Full XAFS Spectrum of MgO Using Nonresonant Inelastic X-ray Scattering. *AIP Conference Proceedings*, 882:156–158, 2007. [15]

[78] T. T. Fister, G. T. Seidler, C. Hamner, J. O. Cross, J. A. Soininen, and J. J. Rehr. Background proportional enhancement of the extended fine structure in nonresonant inelastic x-ray scattering. *Phys. Rev. B*, 74:214117, 2006. [15]

[79] T. T. Fister, G. T. Seidler, E. L. Shirley, F. D. Vila, J. J. Rehr, K. P. Nagle, J. C. Linehan, and J. O. Cross. The local electronic structure of α-Li_3N. *The Journal of Chemical Physics*, 129(4), 2008. [14]

[80] T. T. Fister, G. T. Seidler, L. Wharton, A. R. Battle, T. B. Ellis, J. O. Cross, A. T. Macrander, W. T. Elam, T. A. Tyson, and Q. Qian. Multielement spectrometer for efficient measurement of the momentum transfer dependence of inelastic x-ray scattering. *Review of Scientific Instruments*, 77(6):063901, 2006. [VII, 14, 15, 37, 38]

[81] T. T. Fister, F. D. Vila, G. T. Seidler, L. Svec, J. C. Linehan, and J. O. Cross. Local Electronic Structure of Dicarba-closo-dodecarboranes $C_2B_{10}H_{12}$. *Journal of the American Chemical Society*, 130(3):925–932, 2008. [14]

[82] S. Foss, T.G. Finstad, A. Dana, and A. Aydinli. Growth of Ge nanoparticles on SiO_2/Si interfaces during annealing of plasma enhanced chemical vapor deposited thin films. *Thin Solid Films*, 515(16):6381 – 6384, 2007. Proceedings of Symposium J on Synthesis Processing and Characterization of Nanoscale Functional Oxide Films - {EMRS} 2006 {EMRS} 2006 - Symposium J. [103]

[83] D. J. Frost, F. Langenhorst, and P. A. van Aken. Fe-Mg partitioning between ringwoodite and magnesiowüstite and the effect of pressure, temperature and oxygen fugacity. *Physics and Chemistry of Minerals*, 28(7):455–470, 2001. [54]

[84] J. C. Fuggle and S. F. Alvarado. Core-level lifetimes as determined by x-ray photoelectron spectroscopy measurements. *Phys. Rev. A*, 22:1615 – 1624, 1980. [65, 66, 78]

[85] H. Fukui, S. Huotari, D. Andrault, and T. Kawamoto. Oxygen K-edge fine structures of water by x-ray Raman scattering spectroscopy under pressure conditions. *The Journal of Chemical Physics*, 127(13):134502, 2007. [49, 50]

[86] H. Fukui, M. Kanzaki, N. Hiraoka, and Y. Q. Cai. Coordination environment of silicon in silica glass up to 74 gpa: An x-ray Raman scattering study at the silicon *L* edge. *Phys. Rev. B*, 78:012203, 2008. [15, 16]

[87] H. Fukui, M. Kanzaki, N. Hiraoka, and Y.Q. Cai. X-ray Raman scattering for structural investigation of silica/silicate minerals. *Physics and Chemistry of Minerals*, 36(3):171–181, 2009. [14, 15]

[88] S. Galambosi, J. A. Soininen, K. Nygård, S. Huotari, and K. Hämäläinen. Symmetry of the $1s$ core exciton in diamond studied using x-ray Raman scattering. *Phys. Rev. B*, 76:195112, 2007. [14]

[89] S. Galambosi, L. Wirtz, J. A. Soininen, J. Serrano, A. Marini, K. Watanabe, T. Taniguchi, S. Huotari, A. Rubio, and K. Hämäläinen. Anisotropic excitonic effects in the energy loss function of hexagonal boron nitride. *Phys. Rev. B*, 83:081413, 2011. [14]

[90] L. Galoisy, G. Calas, and Arrio M.A. High-resolution XANES spectra of iron in minerals and glasses: structural information from the pre-edge region. *Chemical Geology*, 174(1 - 3):307 – 319, 2001. 6th International Silicate Melt Workshop. [71]

[91] P. Gambardella, S. Stepanow, A. Dmitriev, J. Honolka, F. M. F. de Groot, M. Lingenfelder, S. S. Gupta, D. D. Sarma, P. Bencok, S. Stanescu, S. Clair, S. Pons, N. Lin, A. P. Seitsonen, H. Brune, J. V. Barth, and K. Kern. Supramolecular control of the magnetic anisotropy in two-dimensional high-spin Fe arrays at a metal interface. *Nat Mater*, 8(3):189–193, 2009. [25]

[92] L. A. J. Garvie, A. J. Craven, and R. Brydson. Use of electron-energy loss near-edge fine structure in the study of minerals. *American Mineralogist*, 79(5-6):411–425, 1994. [54]

[93] Laurence A. J. Garvie and Peter R. Buseck. Ratios of ferrous to ferric iron from nanometre-sized areas in minerals. *Nature*, 396(6712):667 – 670, 1998. [56, 57]

[94] C. Gauthier, V. A. Solé, R. Signorato, J. Goulon, and E. Moguiline. The ESRF beamline ID26: X-ray absorption on ultra dilute sample. *Journal of Synchrotron Radiation*, 6(3):164 – 166, May 1999. [2]

[95] B. Gilbert, J. E. Katz, J. D. Denlinger, Y. Yin, R. Falcone, and G. A. Waychunas. Soft X-ray Spectroscopy Study of the Electronic Structure of Oxidized and Partially Oxidized Magnetite Nanoparticles. *The Journal of Physical Chemistry C*, 114(50):21994–22001, 2010. [54]

[96] P. K. Giri, S. Bhattacharyya, Satchi Kumari, Kaustuv Das, S. K. Ray, B. K. Panigrahi, and K. G. M. Nair. Ultraviolet and blue photoluminescence from sputter deposited Ge nanocrystals embedded in SiO_2 matrix. *Journal of Applied Physics*, 103(10):103534, 2008. [103]

[97] P. Glatzel, U. Bergmann, F. M. F. de Groot, and S. P. Cramer. Influence of the core hole on K emission following photoionization or orbital electron capture: A comparison using MnO and $^{55}Fe_2O_3$. *Phys. Rev. B*, 64:045109, 2001. [25]

[98] T. Gog, G. T. Seidler, D. M. Casa, M. H. Upton, J. Kim, S. Stoupin, K. P. Nagle, M. Balasubramanian, R. A. Gordon, T. T. Fister, S. M. Heald, T. Toellner, J. P. Hill, D. S. Coburn, Y.-J. Kim, A. H. Said, E. E. Alp, W. Sturhahn, H. Yavaş, C. A. Burns, and H. Sinn. Momentum-resolved Resonant and Nonresonant Inelastic X-ray Scattering at the Advanced Photon Source. *Synchrotron Radiation News*, 22(6):12–21, 2009. [15]

[99] A. F. Goncharov and J. C. Crowhurst. Raman Spectroscopy under Extreme Conditions. *Journal of Low Temperature Physics*, 139(5 - 6):727 – 737, 2005. [83]

[100] A. F. Goncharov, E. Gregoryanz, R. J. Hemley, and H.-k. Mao. Spectroscopic studies of the vibrational and electronic properties of solid hydrogen to 285 GPa. *Proceedings of the National Academy of Sciences*, 98(25):14234–14237, 2001. [15, 73]

[101] A. F. Goncharov and V. V. Struzhkin. Raman spectroscopy of metals, high-temperature superconductors and related materials under high pressure. *Journal of Raman Spectroscopy*, 34(7-8):532–548, 2003. [2]

[102] R. A. Gordon, M. W. Haverkort, S. Sen Gupta, and G. A. Sawatzky. Orientation-dependent x-ray Raman scattering from cubic crystals: Natural linear dichroism in MnO and CeO_2. *Journal of Physics: Conference Series*, 190(1):012047, 2009. [15]

[103] R. A. Gordon, G. T. Seidler, T. T. Fister, M. W. Haverkort, G. A. Sawatzky, A. Tanaka, and T. K. Sham. High multipole transitions in NIXS: Valence and hybridization in 4f systems. *EPL*, 81(2):26004, 2008. [10, 15, 56]

[104] K. Das Gupta. Smekal-Raman Type Modified X-Ray Scattering. *Phys. Rev. Lett.*, 3:38 – 40, 1959. [7]

[105] R. P. Gupta and S. K. Sen. Calculation of multiplet structure of core p -vacancy levels. II. *Phys. Rev. B*, 12:15–19, 1975. [30]

[106] K. Hämäläinen, S. Galambosi, J. A. Soininen, Eric L. Shirley, J.-P. Rueff, and A. Shukla. Momentum dependence of fluorine K-edge core exciton in LiF. *Phys. Rev. B*, 65:155111, 2002. [15]

[107] K Hämäläinen and S Manninen. Resonant and non-resonant inelastic x-ray scattering. *Journal of Physics: Condensed Matter*, 13(34):7539, 2001. [6, 9]

[108] A. P. Hammersley, S. O. Svensson, M. Hanfland, A. N. Fitch, and D. Hausermann. Two-dimensional detector software: From real detector to idealised image or two-theta scan. *High Pressure Research*, 14(4-6):235 – 248, 1996. [45]

[109] M. W. Haverkort, A. Tanaka, L. H. Tjeng, and G. A. Sawatzky. Nonresonant Inelastic X-Ray Scattering Involving Excitonic Excitations: The Examples of NiO and CoO. *Phys. Rev. Lett.*, 99:257401, 2007. [9, 10]

[110] J.-L. Hazemann, O. Proux, V. Nassif, H. Palancher, E. Lahera, C. Da Silva, A. Braillard, D. Testemale, M.-A. Diot, I. Alliot, W. Del Net, A. Manceau, F. Gélébart, M. Morand, Q. Dermigny, and A. Shukla. High-resolution spectroscopy on an X-ray absorption beamline. *Journal of Synchrotron Radiation*, 16(2):283–292, 2009. [12]

[111] T. Head-Gordon and M. E. Johnson. Tetrahedral structure or chains for liquid water. *Proceedings of the National Academy of Sciences*, 103(21):7973–7977, 2006. [16]

[112] W. M. Heijboer, A. A. Battiston, A. Knop-Gericke, M. Havecker, H. Bluhm, B. M. Weckhuysen, D. C. Koningsberger, and F. M. F. de Groot. Redox behaviour of over-exchanged Fe/ZSM5 zeolites studied with in-situ soft X-ray absorption spectroscopy. *Phys. Chem. Chem. Phys.*, 5:4484–4491, 2003. [54]

[113] W. M. Heijboer, A. A. Battiston, A. Knop-Gericke, M. Hävecker, R. Mayer, H. Bluhm, R. Schlögl, B. M. Weckhuysen, D. C. Koningsberger, and F. M. F. de Groot. In-Situ Soft X-ray Absorption of Over-exchanged Fe/ZSM5. *The Journal of Physical Chemistry B*, 107(47):13069–13075, 2003. [54]

[114] W. M. Heijboer, P. Glatzel, K. R. Sawant, R. F. Lobo, U. Bergmann, R. A. Barrea, D. C. Koningsberger, B. M. Weckhuysen, and F. M. F. de Groot. Kβ-Detected XANES of Framework-Substituted FeZSM-5 Zeolites. *The Journal of Physical Chemistry B*, 108(28):10002–10011, 2004. [54]

[115] W.M. Heijboer, D.C. Koningsberger, B.M. Weckhuysen, and F.M.F. de Groot. New frontiers in X-ray spectroscopy in heterogeneous catalysis: Using Fe/ZSM-5 as test-system. *Catalysis Today*, 110(3 - 4):228 – 238, 2005. [2, 54]

[116] R. J. Hemley, H. K. Mao, P. M. Bell, and B. O. Mysen. Raman Spectroscopy of SiO_2 Glass at High Pressure. *Phys. Rev. Lett.*, 57:747 – 750, 1986. [48]

[117] E. J. Henderson, C. M. Hessel, and J. G. C. Veinot. Synthesis and Photoluminescent Properties of Size-Controlled Germanium Nanocrystals from Phenyl Trichlorogermane-Derived Polymers. *Journal of the American Chemical Society*, 130(11):3624 – 3632, 2008. [103]

[118] N. Hiraoka, H. Fukui, H. Tanida, H. Toyokawa, Y. Q. Cai, and K. D. Tsuei. An X-ray Raman spectrometer for EXAFS studies on minerals: bent Laue spectrometer with 20keV X-rays. *Journal of Synchrotron Radiation*, 20(2):266–271, 2013. [VI, 13, 41]

[119] R. K. Hocking, E. C. Wasinger, F. M. F. de Groot, K. O. Hodgson, B. Hedman, and E. I. Solomon. Fe L-Edge XAS Studies of $K_4[Fe(CN)_6]$ and $K_3[Fe(CN)_6]$: A Direct Probe of Back-Bonding. *Journal of the American Chemical Society*, 128(32):10442–10451, 2006. [30, 54]

[120] R. K. Hocking, E. C. Wasinger, Y.-L. Yan, F. M. F. de Groot, F. A. Walker, K. O. Hodgson, B. Hedman, and E. I. Solomon. Fe L-Edge X-ray Absorption Spectroscopy of Low-Spin Heme Relative to Non-heme Fe Complexes: Delocalization of Fe d-Electrons into the Porphyrin Ligand. *Journal of the American Chemical Society*, 129(1):113 – 125, 2007. [80]

[121] A.-P. Honkanen, R. Verbeni, L. Simonelli, M. Moretti Sala, G. Monaco, and S. Huotari. Study on the reflectivity properties of spherically bent analyser crystals. *Journal of Synchrotron Radiation*, 21(1):104–110, 2014. [12]

[122] C. Huang, K. T. Wikfeldt, D. Nordlund, U. Bergmann, T. McQueen, J. Sellberg, L. G. M. Pettersson, and A. Nilsson. Wide-angle X-ray diffraction and molecular dynamics study of medium-range order in ambient and hot water. *Phys. Chem. Chem. Phys.*, 13:19997–20007, 2011. [16]

[123] C. Huang, K. T. Wikfeldt, T. Tokushima, D. Nordlund, Y. Harada, U. Bergmann, M. Niebuhr, T. M. Weiss, Y. Horikawa, M. Leetmaa, M. P. Ljungberg, O. Takahashi, A. Lenz, L. Ojamäe, A. P. Lyubartsev, S. Shin, L. G. M. Pettersson, and A. Nilsson. The inhomogeneous structure of water at ambient conditions. *Proceedings of the National Academy of Sciences*, 106(36):15214–15218, 2009. [16]

[124] S. Huotari, F. Albergamo, Gy. Vankó, R. Verbeni, and G. Monaco. Resonant inelastic hard x-ray scattering with diced analyzer crystals and position-sensitive detectors. *Review of Scientific Instruments*, 77(5):053102, 2006. [12]

[125] S. Huotari, Gy. Vankó, F. Albergamo, C. Ponchut, H. Graafsma, C. Henriquet, R. Verbeni, and G. Monaco. Improving the performance of high-resolution X-ray spectrometers with position-sensitive pixel detectors. *Journal of Synchrotron Radiation*, 12(4):467–472, 2005. [12]

[126] Simo Huotari, Tuomas Pylkkänen, Roberto Verbeni, Giulio Monaco, and Keijo Hämäläinen. Direct tomography with chemical-bond contrast. *Nature Materials*, 10(7):489 – 493, 2011. [13]

[127] H. Ikeno, F. M. F. de Groot, E. Stavitski, and I. Tanaka. Multiplet calculations of $L_{2,3}$ x-ray absorption near-edge structures for 3d transition-metal compounds. *Journal of Physics: Condensed Matter*, 21(10):104208, 2009. [31]

[128] Y. Inamura, Y. Katayama, W. Utsumi, and K.-i. Funakoshi. Transformations in the Intermediate-Range Structure of SiO_2 Glass under High Pressure and Temperature. *Phys. Rev. Lett.*, 93:015501, 2004. [48]

[129] J. Inkinen, A. Sakko, K. O. Ruotsalainen, T. Pylkkanen, J. Niskanen, S. Galambosi, M. Hakala, G. Monaco, S. Huotari, and K. Hämäläinen. Temperature dependence of CO_2 and N_2 core-electron excitation spectra at high pressure. *Phys. Chem. Chem. Phys.*, 15:9231–9238, 2013. [14]

[130] T. Irifune and M. Isshiki. Iron partitioning in a pyrolite mantle and the nature of the 410-km seismic discontinuity. *Nature*, 392(6677):702 – 705, 1998. [1]

[131] K. Ishii, T. Tohyama, and J. Mizuki. Inelastic X-ray Scattering Studies of Electronic Excitations. *Journal of the Physical Society of Japan*, 82(2):021015, 2013. [VI, 13]

[132] A. Jephcoat and P. Olson. Is the inner core of the earth pure iron? *Nature*, (6102):332 – 335, 1987. [1]

[133] N. Jiang, D. Su, and J. C. H. Spence. Comparison of Mg $L_{2,3}$ edges in MgO and $Mg(OH)_2$ - Importance of medium-range structure. *Ultramicroscopy*, 109(1):122 – 128, 2008. [53]

[134] H.H. Johann. Die Erzeugung lichtstarker Röntgenspektren mit Hilfe von Konkavkristallen. *Zeitschrift für Physik*, 69(3-4):185–206, 1931. [12]

[135] Y. Joly. Calculating X-ray absorption near-edge structure at very low energy. *Journal of Synchrotron Radiation*, 10(1):58–63, 2003. [18]

[136] L. Journel, L. El Khoury, T. Marin, R. Guillemin, S. Carniato, A. Avila, R. Delaunay, C. F. Hague, and M. Simon. Performances of a bent-crystal spectrometer adapted to resonant x-ray emission measurements on gas-phase samples. *Review of Scientific Instruments*, 80(9):093105, 2009. [12]

[137] I. Juurinen, T. Pylkkänen, K. O. Ruotsalainen, Ch. J. Sahle, G. Monaco, K. Hämäläinen, S. Huotari, and M. Hakala. Saturation Behavior in X-ray Raman Scattering Spectra of Aqueous LiCl. *The Journal of Physical Chemistry B*, 117(51):16506–16511, 2013. [14]

[138] W. S. Kai, H.-G. Liu, and A. Toriumi. Kinetic study of GeO disproportionation into a GeO_2/Ge system using x-ray photoelectron spectroscopy. *Applied Physics Letters*, 101(6), 2012. [103]

[139] H. E. King, Jr. and C. T. Prewitt. High-pressure and high-temperature polymorphism of iron sulfide (FeS). *Acta Crystallographica Section B*, 38(7):1877 – 1887, 1982. [2]

[140] Y.-C. King, T.-J. King, and C. Hu. Charge-trap memory device fabricated by oxidation of $Si_{1-x}Ge_x$. *Electron Devices, IEEE Transactions on*, 48(4):696 – 700, Apr 2001. [103]

[141] P Kirkpatrick and A. V. Baez. Formation of optical images by x-rays. *J. Opt. Soc. Am.*, 38(9):766–773, Sep 1948. [41]

[142] E. Kleymenov, J. A. van Bokhoven, C. David, P. Glatzel, M. Janousch, R. Alonso-Mori, M. Studer, M. Willimann, A. Bergamaschi, B. Henrich, and M. Nachtegaal. Five-element Johann-type x-ray emission spectrometer with a single-photon-counting pixel detector. *Review of Scientific Instruments*, 82(6):065107, 2011. [12]

[143] H. Kobayashi, M. Sato, T. Kamimura, M. Sakai, H. Onodera, N. Kuroda, and Y. Yamaguchi. The effect of pressure on the electronic states of FeS and Fe_7S_8 studied by Mössbauer spectroscopy. *Journal of Physics: Condensed Matter*, 9(2):515, 1997. [74]

[144] C. Kolczewski and K. Hermann. Ab initio DFT studies of oxygen K edge NEXAFS spectra for the V_2O_3 (0001) surface. *Theoretical Chemistry Accounts*, 114(1-3):60–67, 2005. [18]

[145] C. Kolczewski, R. Püttner, M. Martins, A. S. Schlachter, G. Snell, M. M. Sant'Anna, K. Hermann, and G. Kaindl. Spectroscopic analysis of small organic molecules: A comprehensive near-edge x-ray-absorption fine-structure study of C_6-ring-containing molecules. *The Journal of Chemical Physics*, 124(3), 2006. [18]

[146] D.C. Koningsberger and R. Prins. *X-ray absorption: Principles, applications, techniques of EXAFS, SEXAFS and XANES*. Wiley, 1987. [7]

[147] A. Kotani and Y. Toyozawa. Photoelectron Spectra of Core Electrons in Metals with an Incomplete Shell. *Journal of the Physical Society of Japan*, 37(4):912–919, 1974. [21, 30]

[148] M. H. Krisch, F. Sette, C. Masciovecchio, and R. Verbeni. Momentum Transfer Dependence of Inelastic X-Ray Scattering from the Li *K* Edge. *Phys. Rev. Lett.*, 78:2843–2846, 1997. [10, 14]

[149] K. M. Krishnan. Iron $L_{3,2}$ near-edge fine structure studies. *Ultramicroscopy*, 32(4):309 – 311, 1990. [54]

[150] T. Kroll, S. Bonhommeau, T. Kachel, H. A. Dürr, J. Werner, G. Behr, A. Koitzsch, R. Hübel, S. Leger, R. Schönfelder, A. K. Ariffin, R. Manzke, F. M. F. de Groot, J. Fink, H. Eschrig, B. Büchner, and M. Knupfer. Electronic structure of $LaFeAsO_{1?x}F_x$ from x-ray absorption spectroscopy. *Phys. Rev. B*, 78:220502, 2008. [25, 54]

[151] C. Krywka, C. Sternemann, M. Paulus, N. Javid, R. Winter, A. Al-Sawalmih, S. Yi, D. Raabe, and M. Tolan. The small-angle and wide-angle X-ray scattering set-up at beamline BL9 of DELTA. *Journal of Synchrotron Radiation*, 14(3):244 – 251, 2007. [45]

[152] I. Kupenko, L. Dubrovinsky, N. Dubrovinskaia, C. McCammon, K. Glazyrin, E. Bykova, T. Boffa Ballaran, R. Sinmyo, A. I. Chumakov, V. Potapkin, A. Kantor, R. Rüffer, M. Hanfland, W. Crichton, and M. Merlini. Portable double-sided laser-heating system for Mössbauer spectroscopy and X-ray diffraction experiments at synchrotron facilities with diamond anvil cells. *Review of Scientific Instruments*, 83(12):124501, 2012. [83, 84]

[153] I. Kupenko, C. McCammon, R. Sinmyo, C. Prescher, A.I. Chumakov, A. Kantor, R. Rüffer, and L. Dubrovinsky. Electronic spin state of Fe,Al-containing $MgSiO_3$ perovskite at lower mantle conditions. *Lithos*, 189(0):167 – 172, 2014. [83]

[154] S. K. Lee, P. J. Eng, and H.-k. Mao. Probing of Pressure-Induced Bonding Transitions in Crystalline and Amorphous Earth Materials: Insights from X-ray Raman Scattering at High Pressure. *Reviews in Mineralogy and Geochemistry*, 78(1):139 – 174, 2014. [16]

[155] S. K. Lee, P. J. Eng, H.-k. Mao, Y. Meng, M. Newville, M. Y. Hu, and J. Shu. Probing of bonding changes in B_2O_3 glasses at high pressure with inelastic X-ray scattering. *Nat Mater*, 4(11):851–854, November 2005. [16]

[156] S. K. Lee, P. J. Eng, H.-k. Mao, Y. Meng, and J. Shu. Structure of Alkali Borate Glasses at High Pressure: B and Li *K*-Edge Inelastic X-Ray Scattering Study. *Phys. Rev. Lett.*, 98:105502, 2007. [16]

[157] S. K. Lee, P. J. Eng, H.-k. Mao, and J. Shu. Probing and modeling of pressure-induced coordination transformation in borate glasses: Inelastic x-ray scattering study at high pressure. *Phys. Rev. B*, 78:214203, 2008. [16]

[158] S. K. Lee, J.-F. Lin, Y. Q. Cai, N. Hiraoka, P. J. Eng, T. Okuchi, H.-k. Mao, Y. Meng, M. Y. Hu, P. Chow, J. Shu, B. Li, H. Fukui, B. H. Lee, H. N. Kim, and C.-S. Yoo. X-ray Raman scattering study of $MgSiO_3$ glass at high pressure: Implication for triclustered $MgSiO_3$ melt in earth's mantle. *Proceedings of the National Academy of Sciences*, 105(23):7925–7929, 2008. [16, 51]

[159] F. Lehmkühler, A. Sakko, I. Steinke, C. Sternemann, M. Hakala, Ch. J. Sahle, T. Buslaps, L. Simonelli, S. Galambosi, M. Paulus, T. Pylkkänen, M. Tolan, and K. Hämäläinen. Temperature-Induced Structural Changes of Tetrahydrofuran Clathrate and of the Liquid Water/Tetrahydrofuran Mixture. *The Journal of Physical Chemistry C*, 115(43):21009–21015, 2011. [14]

[160] G. Lelong, L. Cormier, G. Ferlat, V. Giordano, G. S. Henderson, A. Shukla, and G. Calas. Evidence of fivefold-coordinated Ge atoms in amorphous GeO_2 under pressure using inelastic x-ray scattering. *Phys. Rev. B*, 85:134202, 2012. [16, 50]

[161] F. Li, Q. Cui, Z. He, T. Cui, C. Gao, Q. Zhou, and G. Zou. Brillouin scattering spectroscopy for a laser heated diamond anvil cell. *Applied Physics Letters*, 88(20):203507, 2006. [83]

[162] Y. Liang, C. R. Miranda, and S. Scandolo. Mechanical strength and coordination defects in compressed silica glass: Molecular dynamics simulations. *Phys. Rev. B*, 75:024205, 2007. [49]

[163] H.-P. Liermann, W. Morgenroth, A. Ehnes, A. Berghäuser, B. Winkler, H. Franz, and E. Weckert. The Extreme Conditions Beamline at PETRA III, DESY: Possibilities to conduct time resolved monochromatic diffraction experiments in dynamic and laser heated DAC. *Journal of Physics: Conference Series*, 215(1):012029, 2010. [84]

[164] J.-F. Lin, H. Fukui, D. Prendergast, T. Okuchi, Y. Q. Cai, N. Hiraoka, C.-S. Yoo, A. Trave, P. Eng, M. Y. Hu, and P. Chow. Electronic bonding transition in compressed SiO_2 glass. *Phys. Rev. B*, 75:012201, 2007. [16, 48]

[165] J.-F. Lin, V. V. Struzhkin, S. D. Jacobsen, M. Y. Hu, P. Chow, J. Kung, H. Liu, H.-k. Mao, and R. J. Hemley. Spin transition of iron in magnesiowustite in the Earth's lower mantle. *Nature*, 436(7049):377 – 380, 2005. [1, 74]

[166] J. Liu and Y. K. Vohra. Fluorescence emission from high purity synthetic diamond anvil to 370 GPa. *Applied Physics Letters*, 68(15):2049–2051, 1996. [15, 73]

[167] I. Llorens, E. Lahera, W. Delnet, O. Proux, A. Braillard, J.-L. Hazemann, A. Prat, D. Testemale, Q. Dermigny, F. Gelebart, M. Morand, A. Shukla, N. Bardou, O. Ulrich, S. Arnaud, J.-F. Berar, N. Boudet, B. Caillot, P. Chaurand, J. Rose, E. Doelsch, P. Martin, and P. L. Solari. High energy resolution five-crystal spectrometer for high quality fluorescence and absorption measurements on an x-ray absorption spectroscopy beamline. *Review of Scientific Instruments*, 83(6):–, 2012. [12]

[168] Y. Maeda. Visible photoluminescence from nanocrystallite Ge embedded in a glassy SiO_2 matrix: Evidence in support of the quantum-confinement mechanism. *Phys. Rev. B*, 51:1658–1670, 1995. [103]

[169] T. Manoubi, M. Tencé, and C. Colliex. Quantification of white lines in Electron Energy Loss Spectroscopy (EELS). *Ultramicroscopy*, 28(1 - 4):49 – 55, 1989. [56, 57]

[170] H.-k. Mao and R. J. Hemley. Experimental Studies of Earth's Deep Interior: Accuracy and Versatility of Diamond-Anvil Cells. *Philosophical Transactions: Mathematical, Physical and Engineering Sciences*, 354(1711):1315–1332, 1996. [73]

[171] H.-K. Mao and W.L. Mao. Theory and Practive - Diamond Anvil Cells and Probes for High P-T Mineral Physics Studies. In G. Schubert, editor, *Treatise on Geophysics*, pages 231 – 267. Elsevier, Amsterdam, 2007. [15, 73]

[172] H.-k. Mao, E. L. Shirley, Y. Ding, P. Eng, Y. Q. Cai, P. Chow, Y. Xiao, J. Shu, R. J. Hemley, C. Kao, and W. L. Mao. Electronic Structure of Crystalline ^{4}He at High Pressures. *Phys. Rev. Lett.*, 105:186404, 2010. [2, 16]

[173] W. L. Mao, H.-k. Mao, Y. Meng, P. J. Eng, M. Y. Hu, P. Chow, Y. Q. Cai, J. Shu, and R. J. Hemley. X-ray Induced Dissociation of H_2O and Formation of an O_2H_2 Alloy at High Pressure. *Science*, 314(5799):636–638, 2006. [16]

[174] A. Mattila, T. Pylkkänen, J.-P. Rueff, S. Huotari, G. Vankó, M. Hanfland, M. Lehtinen, and K. Hämäläinen. Pressure induced magnetic transition in siderite $FeCO_3$ studied by x-ray emission spectroscopy. *Journal of Physics: Condensed Matter*, 19(38):386206, 2007. [1, 72, 74, 101]

[175] A. Mattila, J. A. Soininen, S. Galambosi, T. Pylkkänen, S. Huotari, N. D. Zhigadlo, J. Karpinski, and K. Hämäläinen. Electron-hole counts in Al-substituted MgB_2 superconductors from x-ray Raman scattering. *Phys. Rev. B*, 78:064517, 2008. [14]

[176] C. McCammon. Perovskite as a possible sink for ferric iron in the lower mantle. *Nature*, 387(6634):694 – 696, 1997. [1, 2]

[177] C.A McCammon, D.J. Frost, J.R Smyth, H.M.S. Laustsen, T. Kawamoto, N.L. Ross, and P.A. van Aken. Oxidation state of iron in hydrous mantle phases: implications for subduction and mantle oxygen fugacity. *Physics of the Earth and Planetary Interiors*, 143 - 144:157 – 169, 2004. [1, 54, 72]

[178] Paul F. McMillan. New materials from high-pressure experiments. *Nat Mater*, 1(1):19–25, 2002. [2]

[179] C. Meade, R. J. Hemley, and H. K. Mao. High-pressure x-ray diffraction of SiO_2 glass. *Phys. Rev. Lett.*, 69:1387 – 1390, 1992. [48]

[180] Y. Meng, H.-k. Mao, P. J. Eng, T. P. Trainor, M. Newville, M. Y. Hu, C. Kao, J. Shu, D. Hausermann, and R. J. Hemley. The formation of sp^3 bonding in compressed BN. *Nature Materials*, 3(2):111–114, 2004. [14, 16]

[181] Y. Meng, G. Shen, and H.-k. Mao. Double-sided laser heating system at HPCAT for in situ x-ray diffraction at high pressures and high temperatures. *Journal of Physics: Condensed Matter*, 18(25):S1097, 2006. [83, 84, 85, 99]

[182] S. Miao, M. Kocher, P. Rez, B. Fultz, R. Yazami, and C. C. Ahn. Local Electronic Structure of Olivine Phases of Li_xFePO_4. *The Journal of Physical Chemistry A*, 111(20):4242–4247, 2007. [54]

[183] P. S. Miedema, P. Ngene, A. M. J. van der Eerden, T.-C. Weng, D. Nordlund, D. Sokaras, R. Alonso-Mori, A. Juhin, P. E. de Jongh, and F. M. F. de Groot. In situ X-ray Raman spectroscopy of $LiBH_4$. *Phys. Chem. Chem. Phys.*, 14:5581–5587, 2012. [14]

[184] L. C. Ming and W. A. Bassett. Laser heating in the diamond anvil press up to 2000°C sustained and 3000°C pulsed at pressures up to 260 kilobars. *Review of Scientific Instruments*, 45(9):1115 – 1118, 1974. [84]

[185] J. Miot, K. Benzerara, M. Obst, A. Kappler, F. Hegler, S. Schädler, C. Bouchez, F. Guyot, and G. Morin. Extracellular iron biomineralization by photoautotrophic iron-oxidizing bacteria. *Appl. Environ. Microbiol.*, 75(17):5586 – 5591, 2009. [2]

[186] L. Miyagi, W. Kanitpanyacharoen, S. V. Raju, P. Kaercher, J. Knight, A. MacDowell, H.-R. Wenk, Q. Williams, and E. Z. Alarcon. Combined resistive and laser heating technique for in situ radial X-ray diffraction in the diamond anvil cell at high pressure and temperature. *Review of Scientific Instruments*, 84(2):025118, 2013. [83]

[187] Y. Mizuno and Y. Ohmura. Theory of X-Ray Raman Scattering. *Journal of the Physical Society of Japan*, 22(2):445–449, 1967. [5, 9, 11, 13]

[188] P. Moreau and F. Boucher. Revisiting lithium K and iron $M_{2,3}$ edge superimposition: The case of lithium battery material LiFePO4. *Micron*, 43(1):16 – 21, 2012. [2]

[189] M. Munõz, V. De Andrade, O. Vidal, E. Lewin, S. Pascarelli, and J. Susini. Redox and speciation micromapping using dispersive X-ray absorption spectroscopy: Application to iron in chlorite mineral of a metamorphic rock thin section. *Geochemistry, Geophysics, Geosystems*, 7(11):–, 2006. [2]

[190] B. Mysen and P. Richet. *Silicate Glasses and Melts: Properties and Structure*. Developments in Geochemistry. Elsevier Science, 2005. [48]

[191] B. O. Mysen. Relations Between Structure, Redox Equilibria of Iron, and Properties of Magmatic Liquids. In L. L. Perchuk and I. Kushiro, editors, *Physical Chemistry of Magmas*, volume 9 of *Advances in Physical Geochemistry*, pages 41 – 98. Springer New York, 1991. [2]

[192] H. Nagasawa, S. Mourikis, and W. Schülke. X-Ray Raman Spectrum of Li, Be and Graphite in a High-Resolution Inelastic Synchrotron X-Ray Scattering Experiment. *Journal of the Physical Society of Japan*, 58(2):710–717, 1989. [11, 14]

[193] H. Nagasawa, S. Mourikis, and W. Schülke. Momentum-Transfer Dependence of the Near Edge Structure of Li. *Journal of the Physical Society of Japan*, 66(10):3139–3146, 1997. [10, 14]

[194] K. P. Nagle, G. T. Seidler, E. L. Shirley, T. T. Fister, J. A. Bradley, and F. C. Brown. Final-state symmetry of Na 1*s* core-shell excitons in NaCl and NaF. *Phys. Rev. B*, 80:045105, 2009. [15]

[195] S.-I. Nakai, H. Nakamori, A. Tomita, K. Tsutsumi, H. Nakamura, and C. Sugiura. Soft-x-ray $M_{2,3}$ absorption spectra of some transition-metal halides. *Phys. Rev. B*, 9:1870–1873, 1974. [30]

[196] O. Narygina, L.S. Dubrovinsky, H. Samuel, C.A. McCammon, I. Yu. Kantor, K. Glazyrin, S. Pascarelli, G. Aquilanti, and V.B. Prakapenka. Chemically homogeneous spin transition zone in Earth's lower mantle. *Physics of the Earth and Planetary Interiors*, 185(3 - 4):107 – 111, 2011. [72, 83]

[197] O. Narygina, M. Mattesini, I. Kantor, S. Pascarelli, X. Wu, G. Aquilanti, C. McCammon, and L. Dubrovinsky. High-pressure experimental and computational XANES studies of $(Mg,Fe)(Si,Al)O_3$ perovskite and (Mg,Fe)O ferropericlase as in the Earth's lower mantle. *Phys. Rev. B*, 79:174115, 2009. [2]

[198] M. R. Neupane, R. K. Lake, and R. Rahman. Core size dependence of the confinement energies, barrier heights, and hole lifetimes in Ge-core/Si-shell nanocrystals. *Journal of Applied Physics*, 110(7), 2011. [103]

[199] M. Newville. Fundamentals of XAFS. *Consortium for Advanced Radiation Sources, University of Chicago (USA)[http://xafs. org]*, 2004. [VI, 5]

[200] M. Newville, S. R. Sutton, M. L. Rivers, and P. Eng. Micro-beam X-ray absorption and fluorescence spectroscopies at GSECARS: APS beamline 13ID. *Journal of Synchrotron Radiation*, 6(3):353 – 355, 1999. [2]

[201] A. Nilsson and L.G.M. Pettersson. Perspective on the structure of liquid water. *Chemical Physics*, 389(1-3):1–34, 2011. [16]

[202] M. Nogami and Y. Abe. Sol-gel method for synthesizing visible photoluminescent nanosized Ge-crystal doped silica glasses. *Applied Physics Letters*, 65(20):2545–2547, 1994. [103]

[203] A. Nyrow, C. Sternemann, Ch. J. Sahle, A. Hohl, M. Zschintzsch-Dias, A. Schwamberger, K. Mende, I. Brinkmann, M. Moretti Sala, R. Wagner, A. Meier, F. Völklein, and M. Tolan. Structural changes in amorphous Ge_xSiO_y on the way to nanocrystal formation. *Nanotechnology*, 24(16):165701, 2013. [X, 2, 15, 49, 51, 103, 104, 105, 106]

[204] A. Nyrow, C. Sternemann, M. Wilke, R.A. Gordon, K. Mende, H. Yavaş, L. Simonelli, N. Hiraoka, Ch.J. Sahle, S. Huotari, G.B. Andreozzi, A.B. Woodland, M. Tolan, and J.S. Tse. Iron speciation in minerals and glasses probed by $M_{2/3}$-edge x-ray raman scattering spectroscopy. *Contributions to Mineralogy and Petrology*, 167(5):1012, 2014. [VIII, XI, 61, 62, 64, 66, 68, 70]

[205] A. Nyrow, J. S. Tse, N. Hiraoka, S. Desgreniers, T. Büning, K. Mende, M. Tolan, M. Wilke, and C. Sternemann. Pressure induced spin transition revealed by iron $M_{2,3}$-edge spectroscopy. *Applied Physics Letters*, 104(26):262408, 2014. [VIII, IX, 72, 75, 77]

[206] Institute of Experimental Mineralogy; Russian Academy of Science. Crystallographic and crystallochemical database for minerals and their structural analogues. `http://database.iem.ac.ru/mincryst/`, April 2014. [VII, 46]

[207] T. Okuchi. Hydrogen Partitioning into Molten Iron at High Pressure: Implications for Earth's Core. *Science*, 278(5344):1781 – 1784, 1997. [1]

[208] W. Olovsson, I. Tanaka, T. Mizoguchi, P. Puschnig, and C. Ambrosch-Draxl. All-electron Bethe-Salpeter calculations for shallow-core x-ray absorption near-edge structures. *Phys. Rev. B*, 79:041102, 2009. [53]

[209] S. Ono, Y. Ohishi, and T. Kikegawa. High-pressure study of rhombohedral iron oxide, FeO, at pressures between 41 and 142 GPa. *Journal of Physics: Condensed Matter*, 19(3):036205, 2007. [1, 74]

[210] S. Ono, Y. Ohishi, and T. Kikegawa. High-pressure study of rhombohedral iron oxide, FeO, at pressures between 41 and 142 GPa. *Journal of Physics: Condensed Matter*, 19(3):036205, 2007. [1]

[211] A. Pacella, G. B. Andreozzi, J. Fournier, L. Stievano, F. Giantomassi, G. Lucarini, M. R: Rippo, and A. Pugnaloni. Iron topochemistry and surface reactivity of amphibole asbestos: relations with in vitro toxicity. *Analytical and Bioanalytical Chemistry*, 402(2):871 – 881, 2012. [2]

[212] D. C. Paine, C. Caragianis, T. Y. Kim, Y. Shigesato, and T. Ishahara. Visible photoluminescence from nanocrystalline Ge formed by H_2 reduction of $Si_{0.6}Ge_{0.4}O_2$. *Applied Physics Letters*, 62(22):2842–2844, 1993. [103]

[213] H. Palme and A. Jones. 1.03 - Solar System Abundances of the Elements. In Heinrich D. Holland and Karl K. Turekian, editors, *Treatise on Geochemistry*, pages 41 – 61. Pergamon, Oxford, 2003. [1]

[214] C. J. Park, K. H. Cho, W.-C. Yang, H. Y. Cho, S.-H. Choi, R. G. Elliman, J. H. Han, and C. Kim. Large capacitance-voltage hysteresis loops in SiO_2 films containing Ge nanocrystals produced by ion implantation and annealing. *Applied Physics Letters*, 88(7), 2006. [103]

[215] M. P. Pasternak, R. D. Taylor, R. Jeanloz, X. Li, J. H. Nguyen, and C. A. McCammon. High Pressure Collapse of Magnetism in $Fe_{0.94}O$: Mössbauer Spectroscopy Beyond 100 GPa. *Phys. Rev. Lett.*, 79:5046 – 5049, 1997. [72]

[216] J. H. Paterson and O. L. Krivanek. ELNES of 3d transition-metal oxides: II. Variations with oxidation state and crystal structure. *Ultramicroscopy*, 32(4):319 – 325, 1990. [54]

[217] V. Petkov, Y. Ren, and M. Suchomel. Molecular arrangement in water: random but not quite. *Journal of Physics: Condensed Matter*, 24(15):155102, 2012. [16]

[218] J.-P. Poirier. Light elements in the Earth's outer core: A critical review. *Physics of the Earth and Planetary Interiors*, 85(3 - 4):319 – 337, 1994. [1]

[219] P. Postorino, R. H. Tromp, M-A. Ricci, A. K. Soper, and G. W. Neilson. The interatomic structure of water at supercritical temperatures. *Nature*, 366(6456):668–670, 1993. [16]

[220] T. Pylkkänen, V. M. Giordano, J.-C. Chervin, A. Sakko, M. Hakala, J. A. Soininen, K. Hämäläinen, G. Monaco, and S. Huotari. Role of Non-Hydrogen-Bonded Molecules in the Oxygen K-Edge Spectrum of Ice. *The Journal of Physical Chemistry B*, 114(11):3804–3808, 2010. PMID: 20187617. [14]

[221] T. Pylkkänen, J. Lehtola, M. Hakala, A. Sakko, G. Monaco, S. Huotari, and K. Ha?ma?la?inen. Universal Signature of Hydrogen Bonding in the Oxygen K-Edge Spectrum of Alcohols. *The Journal of Physical Chemistry B*, 114(41):13076–13083, 2010. [14]

[222] T. Pylkkänen, A. Sakko, M. Hakala, K. Hämäläinen, G. Monaco, and S. Huotari. Temperature Dependence of the Near-Edge Spectrum of Water. *The Journal of Physical Chemistry B*, 115(49):14544–14550, 2011. [14]

[223] J. J. Rehr and R. C. Albers. Theoretical approaches to x-ray absorption fine structure. *Rev. Mod. Phys.*, 72:621–654, 2000. [VIII, 7, 52]

[224] J. J. Rehr, J. J. Kas, Prange M. P., Sorini A. P., Takimoto Y., and Vila F. Ab initio theory and calculations of X-ray spectra. *Comptes Rendus Physique*, 10(6):548 – 559, 2009. [VIII, 18, 52]

[225] S. Rossano, E. Balan, G. Morin, J.-P. Bauer, G. Calas, and C. Brouder. ^{57}Fe Mössbauer spectroscopy of tektites. *Physics and Chemistry of Minerals*, 26(6):530 – 538, 1999. [71]

[226] J. P. Rueff, Y. Joly, F. Bartolome, M. Krisch, J. L. Hodeau, L. Marques, M. Mezouar, A. Kaprolat, M. Lorenzen, and F. Sette. X-ray Raman scattering from the carbon K edge in polymerized C_{60}: experiment and theory. *Journal of Physics: Condensed Matter*, 14(45):11635, 2002. [14]

[227] J.-P. Rueff, C.-C. Kao, V. V. Struzhkin, J. Badro, J. Shu, R. J. Hemley, and H. K. Mao. Pressure-Induced High-Spin to Low-Spin Transition in FeS Evidenced by X-Ray Emission Spectroscopy. *Phys. Rev. Lett.*, 82:3284 – 3287, 1999. [IX, 1, 74, 76, 77, 78]

[228] Ch. J. Sahle, C. Sternemann, C. Schmidt, S. Lehtola, S. Jahn, L. Simonelli, S. Huotari, M. Hakala, T. Pylkkänen, A. Nyrow, K. Mende, M. Tolan, K. Hämäläinen, and M. Wilke. Microscopic structure of water at elevated pressures and temperatures. *Proceedings of the National Academy of Sciences*, 2013. [2, 16, 83]

[229] Ch. J. Sahle, C. Sternemann, H. Sternemann, J. S. Tse, S. Gordon, R. A. Desgreniers, S. Maekawa, S. Yamanaka, F. Lehmkühler, D. C. F. Wieland, K. Mende, S. Huotari, and M. Tolan. The Ba 4d-4f giant dipole resonance in complex Ba/Si compounds. *Journal of Physics B: Atomic, Molecular and Optical Physics*, 47(4):045102, 2014. [65]

[230] Ch. J. Sahle, M. Zschintzsch, C. Sternemann, J. von Borany, A. Mücklich, A. Nyrow, N. M. Jeutter, R. Wagner, R. Frahm, and M. Tolan. Influence of hydrogen on thermally induced phase separation in GeO/SiO_2 multilayers. *Nanotechnology*, 22(12):125709, 2011. [103, 104]

[231] A. Sakko, S. Galambosi, J. Inkinen, T. Pylkkänen, M. Hakala, S. Huotari, and K. Hämäläinen. Inelastic X-ray scattering and vibrational effects at the K-edges of gaseous N_2, N_2O, and CO_2. *Phys. Chem. Chem. Phys.*, 13:11678–11685, 2011. [14, 107]

[232] A. Sakko, M. Hakala, J. A. Soininen, and K. Hämäläinen. Density functional study of x-ray Raman scattering from aromatic hydrocarbons and polyfluorene. *Phys. Rev. B*, 76:205115, 2007. [14]

[233] A. Sakko, C. Sternemann, Ch. J. Sahle, H. Sternemann, O. M. Feroughi, H. Conrad, F. Djurabekova, A. Hohl, G. T. Seidler, M. Tolan, and K. Hämäläinen. Suboxide interface in disproportionating *a*-SiO studied by x-ray Raman scattering. *Phys. Rev. B*, 81:205317, 2010. [X, 15, 49, 51, 104, 105, 106, 107]

[234] A. Salamat, R. A. Fischer, R. Briggs, M. I. McMahon, and S. Petitgirard. In situ synchrotron X-ray diffraction in the laser-heated diamond anvil cell: Melting phenomena and synthesis of new materials. *Coordination Chemistry Reviews*, 2014. [83]

[235] A. San-Miguel, P. Mélinon, D. Connétable, X. Blase, F. Tournus, E. Reny, S. Yamanaka, and J. P. Itié. Pressure stability and low compressibility of intercalated cagelike materials: The case of silicon clathrates. *Phys. Rev. B*, 65:054109, 2002. [2]

[236] C. Sanloup, J. W. E. Drewitt, Z. Konopkova, P. Dalladay-Simpson, D. M. Morton, N. Rai, W. van Westrenen, and W. Morgenroth. Structural change in molten basalt at deep mantle conditions. *Nature*, 503(7474):104 – 107, 2013. [100, 102]

[237] C. Sanloup, J.W.E. Drewitt, C. Crepisson, Y. Kono, C. Park, C. McCammon, L. Hennet, S. Brassamin, and A. Bytchkov. Structure and density of molten fayalite at high pressure. *Geochimica et Cosmochimica Acta*, 118(0):118 – 128, 2013. [100, 102]

[238] S. Satō and Y. Ohmura. Inelastic Scattering of γ-Rays by K-Shell Electrons of Metallic Copper and Iron. I. Scattering by A^2-Term. *Journal of the Physical Society of Japan*, 57(1):342–352, 1988. [6]

[239] S. K. Saxena and L. S. Dubrovinsky. Iron phases at high pressures and temperatures: Phase transition and melting. *American Mineralogist*, 85:372, 2000. [85]

[240] S. K. Saxena, L. S. Dubrovinsky, P. Häggkvist, Y. Cerenius, G. Shen, and H. K. Mao. Synchrotron X-ray Study of Iron at High Pressure and Temperature. *Science*, 269(5231):1703 – 1704, 1995. [85]

[241] N. Schell, R. O. Simmons, A. Kaprolat, W. Schülke, and E. Burkel. Electronic Excitations in hcp ^{4}He at 61.5 Mpa and 4.3 K Studied by Inelastic X-Ray Scattering Spectroscopy. *Phys. Rev. Lett.*, 74:2535–2538, 1995. [2, 16]

[242] R. Schmid, M. Wilke, R. Oberhänsli, K. Janssens, G. Falkenberg, L. Franz, and A. Gaab. Micro-XANES determination of ferric iron and its application in thermobarometry. *Lithos*, 70(3 - 4):381 – 392, 2003. [2]

[243] C. Schmidt and K. Rickers. In-situ determination of mineral solubilities in fluids using a hydrothermal diamond-anvil cell and SR-XRF: Solubility of AgCl in water. *American Mineralogist*, 88(2 - 3):288 – 292, 2003. [16, 83]

[244] W. Schülke. Inelastic x-ray scattering. *Nuclear Instruments and Methods in Physics Research Section A: Accelerators, Spectrometers, Detectors and Associated Equipment*, 280(2-3):338–348, 1989. [VI, 5]

[245] W. Schülke. *Electron Dynamics by Inelastic X-Ray Scattering*. Oxford Series on Synchrotron Radiation. Oxford Univ. Press, Oxford, 2007. [VI, 2, 5, 6, 7, 8, 9, 10, 11, 12, 13, 16, 56]

[246] W. Schulke, A. Kaprolat, K. J. Gabriel, N. Schell, E. Burkel, and R. O. Simmons. First inelastic x-ray scattering spectroscopy measurements of the dynamic structure factor S(q, ω) of electrons in a solid noble gas (He). *Review of Scientific Instruments*, 66(2):1578–1580, 1995. [2, 16]

[247] W. Schülke, H. Nagasawa, S. Mourikis, and P. Lanzki. Dynamic structure of electrons in Li metal: Inelastic synchrotron x-ray scattering results and interpretation beyond the random-phase approximation. *Phys. Rev. B*, 33:6744–6757, 1986. [13]

[248] W. Schülke, H. Schulte-Schrepping, and J. R. Schmitz. Dynamic structure of electrons in Al metal studied by inelastic x-ray scattering. *Phys. Rev. B*, 47:12426–12436, 1993. [4]

[249] E. Schultz, M. Mezouar, W. Crichton, S. Bauchau, G. Blattmann, D. Andrault, G. Fiquet, R. Boehler, N. Rambert, B. Sitaud, and P. Loubeyre. Double-sided laser heating system for in situ high pressure-high temperature monochromatic x-ray diffraction at the ESRF. *High Pressure Research*, 25(1):71 – 83, 2005. [84, 85]

[250] G. Schütz, W. Wagner, W. Wilhelm, P. Kienle, R. Zeller, R. Frahm, and G. Materlik. Absorption of circularly polarized x rays in iron. *Phys. Rev. Lett.*, 58:737 – 740, 1987. [54]

[251] K. Schwarz and P. Blaha. Solid state calculations using WIEN2k. *Computational Materials Science*, 28(2):259 – 273, 2003. [18]

[252] S. Sen Gupta, J. A. Bradley, M. W. Haverkort, G. T. Seidler, A. Tanaka, and G. A. Sawatzky. Coexistence of bound and virtual-bound states in shallow-core to valence x-ray spectroscopies. *Phys. Rev. B*, 84:075134, 2011. [65]

[253] S. Shin, S. Suga, H. Kanzaki, S. Shibuya, and T. Yanaguchi. Multiplet structures of the inner core absorption spectra of $KMnF_3$ and $KCoF_3$ measured by synchrotron radiation. *Solid State Communications*, 38(12):1281 – 1284, 1981. [30]

[254] S. Shin, S. Suga, M. Taniguchi, H. Kanzaki, S. Shibuya, and T. Yamaguchi. Final State Interactions of Inner Core Absorption Excitation in Transition Metal Halides. *Journal of the Physical Society of Japan*, 51(3):906–914, 1982. [30]

[255] Yu.V. Shvyd'ko, J.P. Hill, C.A. Burns, D.S. Coburn, B. Brajuskovic, D. Casa, K. Goetze, T. Gog, R. Khachatryan, J.-H. Kim, C.N. Kodituwakku, M. Ramanathan, T. Roberts, A. Said, H. Sinn, D. Shu, S. Stoupin, M. Upton, M. Wieczorek, and H. Yavas. MERIX - Next generation medium energy resolution inelastic x-ray scattering instrument at the APS. *Journal of Electron Spectroscopy and Related Phenomena*, 188(0):140 – 149, 2013. [12]

[256] J. C. Slater. The Theory of Complex Spectra. *Phys. Rev.*, 34:1293–1322, 1929. [20]

[257] J.R. Smyth, C.M. Holl, F. Langenhorst, H.M.S. Laustsen, G.R. Rossman, A. Kleppe, C.A. McCammon, T. Kawamoto, and P.A. van Aken. Crystal chemistry of wadsleyite II and water in the Earth's interior. *Physics and Chemistry of Minerals*, 31(10):691 – 705, 2005. [1]

[258] V. N. Sobolev, C. A. McCammon, L. A. Taylor, G. A. Snyder, and N. V. Sobolev. Precise Mössbauer milliprobe determination of ferric iron in rock-forming minerals and limitations of electron microprobe analysis. *American Mineralogist*, 84(1 - 2):78 – 85, 1999. [2]

[259] J. A. Soininen, A. L. Ankudinov, and J. J. Rehr. Inelastic scattering from core electrons: A multiple scattering approach. *Phys. Rev. B*, 72:045136, 2005. [9, 10]

[260] J A Soininen, K Hämäläinen, W A Caliebe, C-C Kao, and Eric L Shirley. Core-hole-electron interaction in x-ray Raman scattering. *Journal of Physics: Condensed Matter*, 13(35):8039, 2001. [14]

[261] J A Soininen, A Mattila, J J Rehr, S Galambosi, and K Hämäläinen. Experimental determination of the core-excited electron density of states. *Journal of Physics: Condensed Matter*, 18(31):7327, 2006. [10]

[262] D. Sokaras, D. Nordlund, T.-C. Weng, R. Alonso Mori, P. Velikov, D. Wenger, A. Garachtchenko, M. George, V. Borzenets, B. Johnson, Q. Qian, T. Rabedeau, and U. Bergmann. A high resolution and large solid angle x-ray Raman spectroscopy end-station at the Stanford Synchrotron Radiation Lightsource. *Review of Scientific Instruments*, 83(4):043112, 2012. [12]

[263] E.I. Solomon and A.B.P. Lever. *Inorganic Electronic Structure and Spectroscopy: Methodology*. Inorganic Electronic Structure and Spectroscopy. Wiley, 2006. [31]

[264] A. K. Soper. Water: Two Liquids Divided by a Common Hydrogen Bond. *The Journal of Physical Chemistry B*, 115:14014–14022, 2011. [16]

[265] A.K. Soper. The radial distribution functions of water and ice from 220 to 673 K and at pressures up to 400 MPa. *Chemical Physics*, 258:121–137, 2000. [16]

[266] S. Speziale, A. Milner, V. E. Lee, S. M. Clark, M. P. Pasternak, and R. Jeanloz. Iron spin transition in Earth's mantle. *Proceedings of the National Academy of Sciences of the United States of America*, 102(50):17918 – 17922, 2005. [1, 72, 74]

[267] E. Stavitski and F. M.F. de Groot. The CTM4XAS program for EELS and XAS spectral shape analysis of transition metal L edges. *Micron*, 41(7):687 – 694, 2010. [31, 32, 64]

[268] C Sternemann, Ch J Sahle, K Mende, C Schmidt, A Nyrow, L Simonelli, M Moretti Sala, M Tolan, and M Wilke. X-ray Raman scattering: An exciting tool for the study of matter at conditions of the Earth's interior. *Journal of Physics: Conference Series*, 425(20):202011, 2013. [2, 15, 16, 83]

[269] C. Sternemann, J. A. Soininen, S. Huotari, G. Vankó, M. Volmer, R. A. Secco, J. S. Tse, and M. Tolan. X-ray Raman scattering at the L edges of elemental Na, Si, and the N edge of Ba in Ba_8Si_{46}. *Phys. Rev. B*, 72:035104, 2005. [15]

[270] C. Sternemann, J.A. Soininen, M. Volmer, A. Hohl, G. Vankó, S. Streit, and M. Tolan. X-ray Raman scattering at the Si $L_{II,III}$-edge of bulk amorphous SiO. *Journal of Physics and Chemistry of Solids*, 66(12):2277 – 2280, 2005. [15]

[271] C. Sternemann, H. Sternemann, S. Huotari, F. Lehmkühler, M. Tolan, and J. S. Tse. The barium giant dipole resonance in barite: a study of soft X-ray absorption edges using hard X-rays. *J. Anal. At. Spectrom.*, 23:807–813, 2008. [15]

[272] C. Sternemann, M. Volmer, J. A. Soininen, H. Nagasawa, M. Paulus, H. Enkisch, G. Schmidt, M. Tolan, and W. Schülke. Momentum-transfer dependence of x-ray Raman scattering at the Be K-edge. *Phys. Rev. B*, 68:035111, 2003. [10]

[273] H. Sternemann, J. A. Soininen, C. Sternemann, K. Hämäläinen, and M. Tolan. Near-edge structure of nonresonant inelastic x-ray scattering from L-shell core levels studied by a real-space multiple-scattering approach. *Phys. Rev. B*, 75:075118, 2007. [9, 10, 15]

[274] H. Sternemann, C. Sternemann, G. T. Seidler, T. T. Fister, A. Sakko, and M. Tolan. An extraction algorithm for core-level excitations in non-resonant inelastic X-ray scattering spectra. *Journal of Synchrotron Radiation*, 15(2):162–169, 2008. [15, 56, 61, 62, 63]

[275] H. Sternemann, C. Sternemann, J. S. Tse, S. Desgreniers, Y. Q. Cai, G. Vankó, N. Hiraoka, A. Schacht, J. A. Soininen, and M. Tolan. Giant dipole resonance of Ba in Ba_8Si_{46}: An approach for studying high-pressure induced phase transitions of nanostructured materials. *Phys. Rev. B*, 75:245102, 2007. [15]

[276] D. J. Stevenson. A planetary perspective on the deep earth. *Nature*, 451(7176):261 – 265, 2008. [83]

[277] L. Stixrude, E. Wasserman, and R. E. Cohen. Composition and temperature of Earth's inner core. *Journal of Geophysical Research: Solid Earth*, 102(B11):24729 – 24739, 1997. [1]

[278] S. Suga, S. Shin, M. Taniguchi, K. Inoue, M. Seki, I. Nakada, S. Shibuya, and T. Yamaguchi. Reflectance spectra of $ZnCr_2Se_4$ spinel from 4 to 100 ev measured with synchrotron radiation: Band structure, covalency, and final-state interactions. *Phys. Rev. B*, 25:5486–5491, 1982. [30]

[279] S. Sugano, Y. Tanabe, and H. Kamimura. *Multiplets of transition-metal ions in crystals*. Pure and applied physics. Academic Press, 1970. [28]

[280] T. Suzuki. X-Ray Raman Scattering Experiment. I. *Journal of the Physical Society of Japan*, 22(5):1139–1150, 1967. [7, 14]

[281] T. Suzuki, T. Kishimoto, T. Kaji, and T. Suzuki. X-ray raman scattering. ii. experiment with cr k_α radiation. *Journal of the Physical Society of Japan*, 29(3):730–736, 1970. [14]

[282] T. Suzuki and H. Nagasawa. X-Ray Raman Scattering. III. The Angular Dependence of the Scattering Intensity. *Journal of the Physical Society of Japan*, 39(6):1579–1585, 1975. [11, 13, 14]

[283] J. Taftøand O. L. Krivanek. Site-Specific Valence Determination by Electron Energy-Loss Spectroscopy. *Phys. Rev. Lett.*, 48:560 – 563, 1982. [54]

[284] H. Tan, J. Verbeeck, A. Abakumov, and G. van Tendeloo. Oxidation state and chemical shift investigation in transition metal oxides by EELS. *Ultramicroscopy*, 116(0):24 – 33, 2012. [2]

[285] B.-K. Teo and P. A. Lee. Ab initio calculations of amplitude and phase functions for extended x-ray absorption fine structure spectroscopy. *Journal of the American Chemical Society*, 101(11):2815–2832, 1979. [13]

[286] B.T. Thole, G. Van Der Laan, and P.H. Butler. Spin-mixed ground state of Fe phthalocyanine and the temperature-dependent branching ratio in X-ray absorption spectroscopy. *Chemical Physics Letters*, 149(3):295–299, 1988. [30]

[287] A. C. Thompson and D. Vaughan, editors. *X-ray Data Booklet*. Lawrence Berkeley National Laboratory, University of California, second edition, 2001. [4, 13, 31, 33, 51, 54, 60, 64, 104, 105]

[288] P. Thy and G.E. Lofgren. Experimental constraints on the low-pressure evolution of transitional and mildly alkalic basalts: the effect of Fe-Ti oxide minerals and the origin of basaltic andesites. *Contributions to Mineralogy and Petrology*, 116(3):340–351, 1994. [44]

[289] K. Tohji and Y. Udagawa. Novel approach for structure analysis by x-ray Raman scattering. *Phys. Rev. B*, 36:9410–9412, 1987. [13, 14]

[290] K. Tohji and Y. Udagawa. X-ray Raman scattering as a substitute for soft-x-ray extended x-ray-absorption fine structure. *Phys. Rev. B*, 39:7590–7594, 1989. [14]

[291] J. S. Tse, R. Flacau, S. Desgreniers, T. Iitaka, and J. Z. Jiang. Electron density topology of high-pressure Ba_8Si_{46} from a combined Rietveld and maximum-entropy analysis. *Phys. Rev. B*, 76:174109, 2007. [2]

[292] J. S. Tse, M. Hanfland, R. Flacau, S. Desgreniers, Z. Li, K. Mende, K. Gilmore, A. Nyrow, M. Moretti Sala, and C. Sternemann. Pressure-Induced Changes on The Electronic Structure and Electron Topology in the Direct FCC → SH Transformation of Silicon. *The Journal of Physical Chemistry C*, 118(2):1161–1166, 2014. [2, 16]

[293] J. S. Tse, L. Yang, S. J. Zhang, C. Q. Jin, Ch. J. Sahle, C. Sternemann, A. Nyrow, V. Giordano, J. Z. Jiang, S. Yamanaka, S. Desgreniers, and C. A. Tulk. Pressure-induced electron topological transitions in Ba-doped Si clathrate. *Phys. Rev. B*, 84:184105, 2011. [16]

[294] P. A. van Aken and B. Liebscher. Quantification of ferrous/ferric ratios in minerals: new evaluation schemes of Fe L_{23} electron energy-loss near-edge spectra. *Physics and Chemistry of Minerals*, 29(3):188 – 200, 2002. [56, 57]

[295] P. A. van Aken, B. Liebscher, and V. J. Styrsa. Quantitative determination of iron oxidation states in minerals using Fe $L_{2,3}$-edge electron energy-loss near-edge structure spectroscopy. *Physics and Chemistry of Minerals*, 25(5):323–327, 1998. [3, 54, 55, 56, 57, 58, 76]

[296] P. A. van Aken, V. J. Styrsa, B. Liebscher, A. B. Woodland, and G. J. Redhammer. Microanalysis of $Fe^{3+}/\sum Fe$ in oxide and silicate minerals by investigation of electron energy-loss near-edge structures (ELNES) at the Fe $M_{2,3}$ edge. *Physics and Chemistry of Minerals*, 26(7):584 – 590, 1999. [2, 60, 67, 76]

[297] G. van Der Laan. $M_{2,3}$ absorption spectroscopy of 3d transition-metal compounds. *Journal of Physics: Condensed Matter*, 3(38):7443–7454, 1991. [31, 60, 64, 78, 81]

[298] G. van der Laan and I. W. Kirkman. The 2p absorption spectra of 3d transition metal compounds in tetrahedral and octahedral symmetry. *Journal of Physics: Condensed Matter*, 4(16):4189, 1992. [31]

[299] L. van Hove. Correlations in Space and Time and Born Approximation Scattering in Systems of Interacting Particles. *Phys. Rev.*, 95:249–262, 1954. [8]

[300] R. Verbeni, M. Kocsis, S. Huotari, M. Krisch, G. Monaco, F. Sette, and G. Vanko. Advances in crystal analyzers for inelastic X-ray scattering. *Journal of Physics and Chemistry of Solids*, 66(12):2299 – 2305, 2005. [12]

[301] R. Verbeni, T. Pylkkänen, S. Huotari, L. Simonelli, G. Vankó, K. Martel, C. Henriquet, and G. Monaco. Multiple-element spectrometer for non-resonant inelastic X-ray spectroscopy of electronic excitations. *Journal of Synchrotron Radiation*, 16(4):469–476, 2009. [12, 13, 39]

[302] J. Vinson, J. J. Rehr, J. J. Kas, and E. L. Shirley. Bethe-Salpeter equation calculations of core excitation spectra. *Phys. Rev. B*, 83:115106, 2011. [18]

[303] L. Vočadlo. 2.05 - Mineralogy of the Earth - The Earth's Core: Iron and Iron Alloys. In G. Schubert, editor, *Treatise on Geophysics*, pages 91 – 120. Elsevier, Amsterdam, 2007. [1]

[304] H. Wang, G. Peng, L. M. Miller, E. M. Scheuring, S. J. George, M. R. Chance, and S. P. Cramer. Iron L-Edge X-ray Absorption Spectroscopy of Myoglobin Complexes and Photolysis Products. *Journal of the American Chemical Society*, 119(21):4921–4928, 1997. [54]

[305] J. P. Wang, N. Ji, X. Liu, Y. Xu, C. Sanchez-Hanke, Y. Wu, F. M. F. De Groot, L. F. Allard, and E. Lara-Curzio. Fabrication of Fe_16N_2 Films by Sputtering Process and Experimental Investigation of Origin of Giant Saturation Magnetization in Fe_16N_2. *IEEE Transactions on Magnetics*, 48(5):1710–1717, 2012. [54]

[306] B.E. Warren. *X-ray Diffraction*. Addison-Wesley series in metallurgy and materials engineering. Dover Publications, 1969. [45]

[307] E. C. Wasinger, F. M. F. de Groot, B. Hedman, K. O. Hodgson, and E. I. Solomon. L-edge X-ray Absorption Spectroscopy of Non-Heme Iron Sites:?Experimental Determination of Differential Orbital Covalency. *Journal of the American Chemical Society*, 125(42):12894–12906, 2003. PMID: 14558838. [36]

[308] N. Watanabe, H. Hayashi, Y. Udagawa, K. Takeshita, and H. Kawata. Anisotropy of hexagonal boron nitride core absorption spectra by x-ray raman spectroscopy. *Applied Physics Letters*, 69(10):1370–1372, 1996. [14]

[309] T. Watanuki, O. Shimomura, T. Yagi, T. Kondo, and M. Isshiki. Construction of laser-heated diamond anvil cell system for in situ x-ray diffraction study at SPring-8. *Review of Scientific Instruments*, 72(2):1289 – 1292, 2001. [84]

[310] E. Welter, P. Machek, G. Dräger, U. Brüggmann, and M. Fröba. A new X-ray spectrometer with large focusing crystal analyzer. *Journal of Synchrotron Radiation*, 12(4):448–454, 2005. [12]

[311] Ph. Wernet, D. Nordlund, U. Bergmann, M. Cavalleri, M. Odelius, H. Ogasawara, L. Å. Näslund, T. K. Hirsch, L. Ojamäe, P. Glatzel, L. G. M. Pettersson, and A. Nilsson. The Structure of the First Coordination Shell in Liquid Water. *Science*, 304(5673):995–999, 2004. [11, 14, 16]

[312] Ph. Wernet, D. Testemale, J.-L. Hazemann, R. Argoud, P. Glatzel, L. G. M. Pettersson, A. Nilsson, and U. Bergmann. Spectroscopic characterization of microscopic hydrogen-bonding disparities in supercritical water. *The Journal of Chemical Physics*, 123(15):–, 2005. [16]

[313] W. B. White and L. K. Kenneth. Optical absorption spectra of iron in the rock-forming silicates. *American Mineralogist*, 51:774–791, 1966. [1]

[314] E. Wigner. Einige Folgerungen aus der Schrödingerschen Theorie für die Termstrukturen. *Zeitschrift für Physik*, 43(9-10):624 – 652, 1927. [24]

[315] M. Wilke and H. Behrens. The dependence of the partitioning of iron and europium between plagioclase and hydrous tonalitic melt on oxygen fugacity. *Contributions to Mineralogy and Petrology*, 137(1-2):102–114, 1999. [1]

[316] M. Wilke, F. Farges, P.-E. Petit, G. E. Brown, and F. Martin. Oxidation state and coordination of fe in minerals: An Fe K-XANES spectroscopic study. *American Mineralogist*, 86(5 - 6):714 – 730, 2001. [2, 43]

[317] M. Wilke, G. M. Partzsch, R. Bernhardt, and D. Lattard. Determination of the iron oxidation state in basaltic glasses using XANES at the k-edge. *Chemical Geology*, 220(1 - 2):143 – 161, 2005. [44]

[318] M. Wilke, C. Schmidt, F. Farges, V. Malavergne, L. Gautron, A. Simionovici, M. Hahn, and P.-E. Petit. Structural environment of iron in hydrous aluminosilicate glass and melt-evidence from X-ray absorption spectroscopy. *Chemical Geology*, 229(1 - 3):144 – 161, 2006. Physics, Chemistry and Rheology of Silicate Melts and Glasses. [2]

[319] K. C. Williams. The $M_{IV,V}$ spectra of ^{63}Eu. *Proceedings of the Physical Society*, 87(4):983, 1966. [30]

[320] Q. Williams and R. Jeanloz. Spectroscopic Evidence for Pressure-Induced Coordination Changes in Silicate Glasses and Melts. *Science*, 239(4842):902 – 905, 1988. [48]

[321] A.B. Woodland and P.J. Jugo. A complex magmatic system beneath the deves volcanic field, Massif Central, France: evidence from clinopyroxene megacrysts. *Contributions to Mineralogy and Petrology*, 153(6):719–731, 2007. [44]

[322] W. Xiong, J. Peng, and Y. Hu. Use of x-ray absorption near edge structure (XANES) to identify physisorption and chemisorption of phosphate onto ferrihydrite-modified diatomite. *Journal of Colloid and Interface Science*, 368(1):528 – 532, 2012. [2, 60, 67]

[323] J. A. Xu, H. K. Mao, and P. M. Bell. High-Pressure Ruby and Diamond Fluorescence: Observations at 0.21 to 0.55 Terapascal. *Science*, 232(4756):1404–1406, 1986. [15, 73]

[324] Y. Yao, B. Zhang, M.A. Green, G. Conibeer, and S.K. Shrestha. Photovoltaic effect in Ge nanocrystals/c-silicon heterojunctions devices. In *Photovoltaic Specialists Conference (PVSC), 2010 35th IEEE*, pages 001889 – 001893, June 2010. [103]

[325] C.D. Yin, M. Okuno, H. Morikawa, and F. Marumo. Structure analysis of $MgSiO_3$ glass. *Journal of Non-Crystalline Solids*, 55(1):131 – 141, 1983. [51]

[326] C. S. Yoo, J. Akella, A. J. Campbell, H. K. Mao, and R. J. Hemley. Phase Diagram of Iron by in Situ X-ray Diffraction: Implications for Earth's Core. *Science*, 270(5241):1473 – 1475, 1995. [85]

[327] M. Zacharias, F. Stolze, T. Drüsedau, and W. Bock. The Preparation of Amorphous $Si_xGe_yO_z$ Alloy Films by Sputtering. Preparation Conditions, Chemical Composition, and Vibrational Properties. *physica status solidi (b)*, 189(2):409 – 416, 1995. [103]

[328] A. Zerr and R. Boehler. Melting of (Mg, Fe)SiO3-Perovskite to 625 Kilobars: Indication of a High Melting Temperature in the Lower Mantle. *Science*, 262(5133):553 – 555, 1993. [1]

[329] A. Zerr and R. Boehler. Constraints on the melting temperature of the lower mantle from high-pressure experiments from MgO and magnesiowüstite. *Nature*, 371:506 – 508, 1994. [1]

[330] C.-S. Zha, H.-k. Mao, and R. J. Hemley. Elasticity of MgO and a primary pressure scale to 55 GPa. *Proceedings of the National Academy of Sciences*, 97(25):13494–13499, 2000. [73]

[331] C.-S. Zha, H.-k. Mao, and R. J. Hemley. Elasticity of dense helium. *Phys. Rev. B*, 70:174107, 2004. [73]

[332] B. Zhang, S. Shrestha, P. Aliberti, M. A. Green, and G. Conibeer. Synthesis and structural properties of Ge nanocrystals in multilayer superlattice structure. *Proc. SPIE*, 7411:741103–741103–10, 2009. [103]

[333] J. Zhao, W. Sturhahn, J.-f. Lin, G. Shen, E. E. Alp, and H.-k. Mao. Nuclear resonant scattering at high pressure and high temperature. *High Pressure Research*, 24(4):447 – 457, 2004. [84, 85]

[334] F. Zheng, W. K. Choi, F. Lin, S. Tripathy, and J. X. Zhang. Stress tuning of ge nanocrystals embedded in dielectrics. *The Journal of Physical Chemistry C*, 112(25):9223 – 9228, 2008. [103]

[335] L F Zhu, L S Wang, B P Xie, K Yang, N Hiraoka, Y Q Cai, and D L Feng. Inelastic x-ray scattering study on the single excitations of helium. *Journal of Physics B: Atomic, Molecular and Optical Physics*, 44(2):025203, 2011. [14]

[336] M. Zschintzsch, N. M. Jeutter, J. von Borany, M. Krause, and A. Mücklich. Reactive dc magnetron sputtering of (GeO_x-SiO_2) superlattices for Ge nanocrystal formation. *Journal of Applied Physics*, 107(3), 2010. [103, 104]

[337] M. Zschintzsch, C. J. Sahle, J. von Borany, C. Sternemann, A. Mücklich, A. Nyrow, A. Schwamberger, and M. Tolan. Ge-Si-O phase separation and Ge nanocrystal growth in Ge:SiO_x/SiO_2 multilayers - a new dc magnetron approach. *Nanotechnology*, 22(48):485303, 2011. [103, 104]

Publication list

- **A. Nyrow**, J.S. Tse, N. Hiraoka, S. Desgreniers, T. Büning, K. Mende, M. Tolan, M. Wilke, and C. Sternemann (2014) *submitted to Applied Physics Letters*: "Pressure induced spin transition revealed by iron $M_{2,3}$-edge spectroscopy"

- **A. Nyrow**, C. Sternemann, M. Wilke, R. A. Gordon, K. Mende, H. Yavaş, L. Simonelli, N. Hiraoka, Ch. J. Sahle, S. Huotari, G. B. Andreozzi, A. B. Woodland, M. Tolan, J. S. Tse (2014). *Contrib. Mineral. Petrol.* 167:1012: "Iron speciation in minerals and glasses probed by $M_{2/3}$-edge X-ray Raman scattering spectroscopy"

- J. S. Tse, M. Hanfland, R. Flacau, S. Desgreniers, Z. Li, K. Mende, K. Gilmore, **A. Nyrow**, M. Moretti Sala and C. Sternemann (2014) *J. Phys. Chem. C* 118, 1161-1166: "Pressure-Induced Changes on The Electronic Structure and Electron Topology in the Direct FCC $\rightarrow$ SH Transformation of Silicon"

- Ch. J. Sahle, C. Sternemann, C. Schmidt, S. Lehtola, S. Jahn, L. Simonelli, S. Huotari, M. Hakala, T. Pylkkänen, **A. Nyrow**, K. Mende, M. Tolan, K. Hämäläinen and M. Wilke (2013). *PNAS* 110(16), 6301-6306: "Microscopic structure of water at elevated pressures and temperatures"

- **A. Nyrow**, C. Sternemann, Ch. J. Sahle, A. Hohl, M. Zschintzsch-Dias, A. Schwamberger, K. Mende, I. Brinkmann, M. Moretti Sala, R. Wagner, A. Meier, F. Völklein and M. Tolan (2013). *Nanotechnology* 24, 165701: "Structural changes in amorphous Ge_xSiO_y on the way to nanocrystal formation"

- C. Sternemann, Ch. J. Sahle, K. Mende, C. Schmidt, **A. Nyrow**, L. Simonelli, M. Moretti Sala, M. Tolan and M. Wilke (2013). *Journal of Physics: Conference Series* 425, 202011: "X-ray Raman scattering: An exciting tool for the study of matter at conditions of the Earth's interior"

- J. Möller, M. Cebi, M. A. Schroer, M. Paulus, P. Degen, Ch. J. Sahle, D. C. F. Wieland, S. Leick, **A. Nyrow**, H. Rehage and M. Tolan (2011). *Phys. Chem. Chem. Phys.* 13, 20354-20360: "Dissolution of iron oxide nanoparticles inside polymer nanocapsules"

- J. S. Tse, L. Yang, S. J. Zhang, C. Q. Jin, Ch. J. Sahle, C. Sternemann, **A. Nyrow**, V. Giordano, J. Z. Jiang, S. Yamanaka, S. Desgreniers, and C. A. Tulk (2011). *PRB* 84, 184105: "Pressure-induced electron topological transitions in Ba-doped Si clathrate"

- Ch. J Sahle, M. Zschintzsch, C. Sternemann, J. von Borany, A. Mücklich, **A. Nyrow**, N. M. Jeutter, R. Wagner, R. Frahm and M. Tolan (2011). *Nanotechnology* 22, 125709: "Influence of hydrogen on thermally induced phase separation in GeO/SiO_2 multilayers"

- M.Zschintzsch, Ch. J. Sahle, J.von Borany, C. Sternemann, A. Mücklich, **A. Nyrow**, A. Schwamberger and M. Tolan (2011). *Nanotechnology* 22, 485303: "Ge-Si-O phase separation and Ge nanocrystal growth in $Ge:SiO_x/SiO_2$ multilayers - a new dc magnetron approach"

- F. Lehmkühler, A. Sakko, C. Sternemann, M. Hakala, K. Nygard, C.J. Sahle, S. Galambosi, I. Steinke, S. Tiemeyer, **A. Nyrow**, T Buslaps, D. Pontoni, M. Tolan, K. Hämäläinen (2010). *J. Phys. Chem. Lett.* 1, 2832-2836: "Anomalous Energetics in Tetrahydrofuran Clathrate Hydrate Revealed by X-ray Compton Scattering"

Acknowledgments

First of all, I would like to thank Prof. Dr. M. Tolan for the possibility to do a PhD in his group. I also thank the BMBF (projects 05K10PEC and 05K13PE2) for financial support.
My deepest gratitude is to Dr. C. Sternemann for the invaluable support during the last years. Many thanks for his outstanding patience, optimism, and for giving me the freedom to present my results at numerous conferences and for getting experience to work at different synchrotron radiation sources.
For many discussions, support during beam times, for providing samples, managing sample characterization, and for many other things, which contributed to the project I kindly thank PD Dr. M. Wilke. I also thank Dr. H.-J. Reichmann, Dr. S. Speziale, and Dr. C. Schmidt for helping me to get experience with high pressure instrumentation and laser applications.
I kindly thank to Prof. Dr. J. S. Tse for the possibility to perform high pressure experiments and for the fruitful cooperation during the last years. Furthermore, I would like to thank Prof. Dr. S. Desgreniers for the experimental support.
Experiments at large synchrotron radiation facilities require help of many people. Thus, my appreciation is to Dr. Sternemann, K. Mende, T. Büning and everybody who helped me during my experiments. I kindly thank Dr. N. Hiraoka (SPring-8), Dr. R. A. Gordon (APS), and Dr. L. Simonelli (ESRF) for the beamline support. I especially thank K. Mende for numerous discussions.
I kindly thank to Dr. H. Yavaş for the possibility to get a deeper insight into the XRS instrumentation and for the possibility to be one of those, who performed first XRS experiments at the new beamline P01 at PETRA III. I also thank to F.-U. Dill for the technical support.
I would like to thank to Dr. Ch. J. Sahle (University of Helsinki) for giving me a possibility to get experience with x-ray Raman scattering. I also thank Dr. S. Huotari (University of Helsinki) for the support with calculations.
Construction of the laser heating setup was a big challenge for me and could not have been accomplished without the support of many different people. Thus, I would like to thank to Dr. W. Morgenroth, Dr. Z. Konopkova, A. Ehnes (DESY), Dr. Y. Ohishi from beamline ID10XU at SPring-8, Dr. M. Mezouar, Dr. G. Garbarino, Dr. S. Petitgirard from beamline ID27 at the ESRF, Dr. L. Bayarjargal (Universität Frankfurt), Dr. H.-J. Reichmann, Dr. S. Speziale (GFZ Potsdam), Prof. Dr. L. Dubrovinsky (Bayerisches Geoinstitut, Bayreuth) and to many other people for giving numerous advises and for providing other support.
Ich möchte mich außerdem bei der mechanischen Werkstatt der TU Dortmund für das Herstellen zahlreicher Komponenten der Laserheizung bedanken.

Ich danke allen, die diese Arbeit Korrektur gelesen haben und ich möchte mich bei der ganzen Arbeitsgruppe für die sehr angenehme Atmosphäre bedanken. Zahlreiche Lehrstuhlausflüge und Sportaktivitäten bleiben unvergessen.
Mein größter Dank geht an meine Familie und an Victoria S. für die moralische Unterstützung. Diese Arbeit ist auch euer Verdienst.

Hiermit erkläre ich an Eides statt, dass ich die vorliegende Arbeit ausschließlich unter Verwendung der angegebenen Hilfmittel und unter Beratung meiner wissenschaftlichen Betreuer angefertigt habe. Ich habe keine anderen als die angegebenen Quellen und Hilfsmittel benutzt sowie wörtliche und sinngemäße Zitate kenntlich gemacht. Die Arbeit wurde weder ganz noch in Teilen an anderer Stelle im Rahmen eines Prüfungsverfahrens vorgelegt.

Ort, Datum	Unterschrift